https://doi.org/10.15388/vu.thesis.676
https://orcid.org/0000-0003-2923-0347

VILNIUS UNIVERSITY
CENTER FOR PHYSICAL SCIENCE AND TECHNOLOGY

Sonata Adomavičiūtė-Grabusovė

Enhancing Vibrational Spectra of Biomolecules Using Non-standard Substrates and Materials

DOCTORAL DISSERTATION

Natural Sciences,
Physics (N 002)

VILNIUS 2024

The dissertation was prepared between 2019 and 2024 at Vilnius University. The research was supported by Research Council of Lithuania.

Academic supervisor –
Prof. Dr. Valdas Šablinskas (Vilnius University, Natural sciences, Physics, N 002).

This doctoral dissertation will be defended in a public meeting of the Dissertation Defence Panel:

Chairman – Prof. Dr. Vidmantas Gulbinas (Center for Physical Sciences and Technology, Natural sciences, Physics, N 002).
Members: (members listed in alphabetical order of surnames)
Prof. Dr. Saulius Bagdonas (Vilnius University, Natural sciences, Physics, N 002),
Prof. Dr. Andrzej Kudelski (University of Warsaw, Poland, Natural sciences, Chemistry, N 003),
Prof. Dr. Liutauras Marcinauskas (Kaunas University of Technology, Natural sciences, Physics, N 002),
Dr. Šarūnas Svirskas (Vilnius University, Natural sciences, Physics, N 002).

The dissertation shall be defended at a public meeting of the Dissertation Defence Panel at 14 hour on 24th of October 2024 in meeting room A101 of the Center for Physical Sciences and Technology.
Address: Saulėtekio av. 3, Vilnius, Lithuania
Tel. +370 5 264 9211; e-mail: office@ftmc.lt

The text of this dissertation can be accessed at the libraries of Vilnius University and Center for Physical Sciences and Technology, as well as on the website of Vilnius University:
www.vu.lt/lt/naujienos/ivykiu-kalendorius

https://doi.org/10.15388/vu.thesis.676
https://orcid.org/0000-0003-2923-0347

VILNIAUS UNIVERSITETAS
FIZINIŲ IR TECHNOLOGIJOS MOKSLŲ CENTRAS

Sonata Adomavičiūtė-Grabusovė

Biomolekulių virpesinių spektrų stiprinimas naudojant nestandartinius substratus ir dangas

DAKTARO DISERTACIJA

Fiziniai mokslai,
Fizika (N 002)

VILNIUS 2024

Disertacija rengta 2019–2024 metais Vilniaus universitete.
Mokslinius tyrimus rėmė Lietuvos mokslo taryba.

Mokslinis vadovas – prof. dr. Valdas Šablinskas (Vilniaus universitetas, gamtos mokslai, fizika, N 002).

Gynimo taryba:

Pirmininkas – prof. dr. Vidmantas Gulbinas (Fizinių ir technologijos mokslų centras, gamtos mokslai, fizika, N 002).
Nariai:
prof. dr. Saulius Bagdonas (Vilniaus universitetas, gamtos mokslai, fizika, N 002),
prof. dr. Liutauras Marcinauskas (Kauno technologijos universitetas, gamtos mokslai, fizika, N 002),
Prof. dr. Andrzej Kudelski (Varšuvos universitetas, Lenkija, gamtos mokslai, chemija, N 003),
dr. Šarūnas Svirskas (Vilniaus Universitetas, gamtos mokslai, fizika, N 002).

Disertacija ginama viešame Gynimo tarybos posėdyje 2024 m. spalio mėn. 24 d. 14 val. Fizinių ir technologijos mokslų centro A101 auditorijoje. Adresas: Saulėtekio al. 3, A101, Vilnius, Lietuva; tel. +370 5 264 9211; e-mail: office@ftmc.lt

Disertaciją galima peržiūrėti Vilniaus universiteto ir Fizinių ir technologijos mokslų centro bibliotekose ir VU interneto svetainėje adresu:
https://www.vu.lt/naujienos/ivykiu-kalendorius

LIST OF ABBREVIATIONS

1D – One-dimensional
2D – Two-dimensional
4-MBA – 4-mercaptobenzoic Acid
AEF – Analytical Enhancement Factor
Ag-PVP – Silver Polyvinylpyrrolidone Nanoparticles
ARM – Anti-reflection Microstructure
ATR – Attenuated Total Reflection
CT – Charge-transfer
DFT – Density Functional Theory
EDX – Energy-Dispersive X-ray
EF – Enhancement Factor
FTIR – Fourier Transform Infrared
HOMO – Highest Occupied Molecular Orbital
LUMO – Lowest Unoccupied Molecular Orbital
LOD – Limit of Detection
LSP – Localized Surface Plasmon
LSPR – Localized Surface Plasmon Resonance
PIR – Polycrystalline Infrared
PLAL – Pulsed Laser Ablation in Liquids
PVP – Polyvinylpyrrolidone
SEIRA – Surface Enhanced Infrared Absorption
SEM – Scanning Electron Microscopy
SERS – Surface Enhanced Raman Scattering
SEVS – Surface Enhanced Vibrational Spectroscopy
SNR – Signal-to-noise Ratio
SPP – Surface Plasmon-polariton
TD-DFT – Time-dependent Density Functional Theory
UV-Vis-NIR – Ultraviolet-Visible-Near infrared
VOCs – Volatile Organic Compounds
XRD – X-ray Diffraction

CONTENTS

INTRODUCTION

Vibrational spectroscopy is a versatile analytical tool that has acquired its highest significance in analysis of materials,[1,2] but is also commonly employed in various areas such as environmental science,[3,4] clinical diagnostics,[5,6] food safety,[7] pathogen identification,[8] etc.[9] It is a non-destructive technique that discloses a unique "fingerprint" for each molecule, allowing for the identification and structural determination of compounds. The ultimate versatility of vibrational spectroscopy lies in its capability to distinguish between different chemical compounds,[10] even those very similar to each other, for example isomers or conformers.[11–13] Therefore, it is considered as a fundamental tool that shows promising potential in biological analysis because of its non-invasive nature and precision. This includes applications in detecting pesticide residues,[14] identifying viruses,[15–17] recognizing cancerous tissues,[18,19] and even in bioimaging.[20] Vibrational spectroscopy stands out from other analytical methods, for example, chromatography and immunoassay due to its fast execution, high sensitivity, and non-destructiveness of the sample, which is very important for sensitive biological samples. It is highly adaptable for analyzing solids, liquids, and gases.[21] Namely, vibrational spectroscopy consists of two broad branches, both dealing with changes in intermolecular bond angles or lengths: Raman scattering and infrared absorption spectroscopies. These approaches employ different excitation sources, optical components, detectors, and the mechanisms of the fundamental processes themselves. Although the methodologies of the two spectroscopy types are distinct, the information obtained is similar and usually complementary.[21] Therefore, the specific tools, methods, obstacles and challenges in enhancing and improving the spectral signal vary slightly for each spectroscopy type.

Advancements in vibrational spectroscopy can be achieved by minimizing spectral signal losses attributable to the methodology used. For instance, *in situ* vibrational spectroscopy techniques, which involve the usage of optical fibers, can generate losses due to (i) absorption and scattering by the fiber material or (ii) signal transmittance across several interfaces (reflection).[22,23] Alternatively, advancements can also be realized by enhancing the spectral signal generated by the molecules themselves. A well-known method that boosts capabilities of conventional spectroscopy is the markedly enhanced spectral signal resulting from an intensified electric field around the plasmonic surface. This effect is widely known as surface enhanced Raman scattering (SERS) or surface enhanced infrared absorption (SEIRA) spectroscopies. They are collectively known as surface enhanced vibrational spectroscopies

(SEVS). SERS, primarily obtained using plasmonic metal nanoparticles or nano-structured substrates (Ag, Au, Cu, and in the ultraviolet range - Al, In, Pd, etc.[24–27]), has undergone profound development since its discovery in the 1970s.[28–30] It shows applicability in fields of biodetection, detecting pesticide residues, identifying viruses, recognizing cancerous tissues, and even in bioimaging as well as detection of non-biological samples. This ongoing interest in SERS spectroscopy can be attributed to several factors. Firstly, the enhancement of the SERS signal is directly proportional to the fourth power of the electric field, denoted as E^4, which is associated with the Raman effect.[27,31,32] This relationship underscores the significant amplification of the signal that can be achieved. Secondly, metal nanoparticles are crucial in this enhancement process due to their localized surface plasmon resonance (LSPR). The LSPR phenomenon is particularly important because when the plasmon resonance frequency of the nanoparticles aligns with the Raman excitation frequency, it leads to a substantial increase in the Raman signal. Lastly, both of these conditions result in SERS achieving an exceptionally high enhancement factor.[31,33–36]

Similarly, an analogous enhancement was observed for SEIRA spectroscopy in the 1980s,[37] which was recognized and developed using metal nanoparticles. While the infrared absorption cross-section is markedly larger than that of Raman scattering,[38–40] the enhancement observed in SEIRA is comparatively modest, amplifying the electric field by two orders of magnitude.[31] Nonetheless, this enhancement, although not as pronounced as in Raman spectroscopy, holds great promise for advancing the capabilities of infrared spectroscopy. Importantly, the underlying mechanisms of enhancement are similar in both SERS and SEIRA techniques.[41] Generally, the enhancement arises from the electric field being intensified near the molecular species, which is a result of the oscillation of free charges within the plasmonic material. In infrared spectroscopy, these plasmonic materials and the excitation mechanisms of plasmons may differ.

Nonetheless, SEIRA and SERS techniques still encounter some problems concerning enhancing materials, and for better usage of these techniques, some obstacles still have to be overcome. In brief, one of the major challenges for SERS is the non-reproducibility of signal intensity that impedes its more automated application in biomedicine. Consequently, considerable effort is being directed toward developing SERS substrates that offer more reproducible spectral intensity while maintaining a high enhancement factor. Such advancements would facilitate the broader application of SERS in scientific research as well as in medical diagnostics.

SEIRA spectroscopy holds several key challenges. The main challenge is considerably lower enhancement factor achieved with SEIRA, which necessitates the development of suitable materials that can excite plasmonic resonances in the infrared range and are also cost-effective.[42] Another critical aspect of SEIRA is that the technique should be adapted for broader usage in real-life conditions.

In this thesis both vibrational spectroscopy types will be utilized to improve the signal obtained from molecules of biological interests. This includes improving the reproducibility and specificity of SERS substrates. This also includes expanding the applicability of the SEIRA technique for direct and remote sensing applications, in conjunction with enhancing optical fiber performance for *in situ* research.

GOAL OF THE DISSERTATION

The goal of this dissertation is to investigate several kinds of material manipulation to either improve the existing or identify novel substrates that could be utilized to boost the SEVS efficacy for biological-interest molecules.

TASKS OF THE WORK

In order to achieve the research goal, the following tasks were set:

- To explore the magnetic and plasmonic properties of hybrid nanoparticles to enhance SERS performance for detection of adenine biomolecules.
- To explore the potential of $Ti_3C_2T_x$ MXene for application in SERS spectroscopy, focusing on the interaction between MXene and salicylic acid.
- To form anti-reflection microstructures at room temperature on the optical fiber end faces to enhance signal transmittance over a broad wavelength range for application in infrared spectroscopy.
- To expand the capabilities of SEIRA spectroscopy for *in situ* application by combining SEIRA with fiber-based technology for the detection of naphthalene impurities in water.

NOVELTY AND IMPORTANCE OF THE WORK

This thesis shows the important role of SEVS techniques in advancing spectroscopy, despite the challenges that persist in optimizing these methods. As a response to many of the persistent challenges in advancing these techniques, this research focuses on several kinds of material manipulation to either improve the existing or identify novel substrates that could be utilized to boost the SEVS efficiency. This thesis employs both SEIRA and SERS methods to enhance the detection of biologically relevant molecules.

A very important issue in SERS spectroscopy that still needs to be overcome is the inconsistency in signal intensity, which currently limits its automated application in biomedical analysis.[43–45] To mitigate this, research is actively focused on developing substrates that not only retain high enhancement factors but also yield reproducible spectral intensities.[46] Such progress promises to widen the scope of SERS in both scientific inquiry and medical diagnostics. Other issues include chemical contamination[47–49] and poor specificity for certain molecules.[50]

In this thesis, the use of hybrid metal magneto-plasmonic nanoparticles, synthesized *via* the pulsed laser ablation in liquids (PLAL) methods, to improve SERS performance, is explored. These nanoparticles address two primary SERS substrate issues: signal reproducibility and chemical contamination, which often result in spectral residues.[47–49] By integrating magnetic and plasmonic properties, these nanoparticles can be controllably arranged on the substrate, enhancing the reproducibility of the SERS signal for biomolecule detection and analysis. The research presented in this thesis aims to confirm the magnetic and plasmonic attributes of the nanoparticles for biomolecule study, potentially leading to more consistent and reliable SERS-based sensors, especially valuable in biochemistry and medical diagnostics.

A significant focus of the thesis is the potential application of $Ti_3C_2T_x$ MXene in SERS spectroscopy. The interaction between MXene and salicylic acid revealed an enhancement in spectral bands, particularly those corresponding to out-of-plane vibrational modes. This suggests that $Ti_3C_2T_x$ MXene could act as a two-dimensional sensor with chemical enhancement properties, offering heightened selectivity for target molecules and more reproducible SERS signals.[50]

SEIRA spectroscopy, on the other hand, faces its own set of challenges, notably a lower enhancement factor (EF) from easily-fabricated polydisperse metal island films. The high enhancement factor SEIRA technology necessitates the use of materials capable of effectively exciting plasmonic resonances in the infrared range in a broad plasmon bandwidth.[42] Which

usually demands sophisticated nanostructure fabrication techniques like electron beam lithography.[51,52] As most advances in the SEIRA field are focused on substrate formation and the achievement of a high enhancement factor, little research is concentrated on the SEIRA integration into real-life applications.[53]

This thesis suggests an approach that links the SEIRA effect with an infrared fiber probe attachment, employing polycrystalline infrared (PIR) fiber loops to facilitate attenuated total reflection (ATR) based SEIRA spectroscopy. The aim is to extend applicability of SEIRA to direct and remote sensing, especially where traditional methods are inadequate, such as identifying low-solubility compounds in aqueous environments. In this thesis the detection of naphthalene in water, unachievable with standard infrared absorption techniques, is demonstrated highlighting an enhancement in SEIRA application.

The thesis also delves into the engineering of optical fiber surfaces to boost the transmission of PIR fiber end faces. Techniques such as imprinting microstructures and profiling were employed to modify the fiber ends. A key aspect of this research is the formation of anti-reflective microstructures (ARMs) at room temperature, bypassing the need for higher temperatures that are typically required. The findings offer straightforward strategies to enhance optical fiber performance, potentially benefiting various technological and scientific applications.

KEY STATEMENTS FOR DEFENCE:

1. Raman signal enhancement for adenine biomolecules can be effectively realized, reaching 10^4, using hybrid nanoparticles with plasmonic and magnetic properties, allowing arrangement of the nanoparticles in a controllable manner.
2. The $Ti_3C_2T_x$ MXene substrate enables a notable Raman signal enhancement for salicylic acid, equal to 220, attributable to the inherent chemical enhancement origin.
3. The enhancement of the infrared absorption signal of naphthalene in water, equal to 90, can be achieved using silver nanoparticles deposited onto the optical fiber attenuated-total-reflection loop.
4. The fiber-based infrared absorption signal can be enhanced by microstructuring the optical fiber ends, improving signal transmission by up to 25 % through the reduction of Fresnel reflection from interfaces.

LAYOUT OF THE DISSERTATION

The dissertation is organized into several distinct sections:

- Brief Introduction to the Research Fields. This section provides a concise overview of the research field, emphasizing the fundamental principles of surface-enhanced vibrational spectroscopies. It also showcases the latest advancements and the driving ambitions behind research on the substrates in the field.
- Research Fields. This segment details various methods employed throughout the thesis. While the overarching aim of enhancing the performance of vibrational spectroscopy unifies the thesis, the employed methods vary. Therefore, the research fields are subdivided into four subsections. Each subsection begins with 1) motivation for the study and introduction to the topic, followed by 2) the implemented methodologies, and 3) the main results and key findings.
- The dissertation finalizes with Conclusions covering all thesis fields.

CONTRIBUTION OF THE AUTHOR AND CO-AUTHORS

In the **I publication** *"Magneto-Plasmonic Nanoparticles Generated by Laser Ablation of Layered Fe/Au and Fe/Au/Fe Composite Films for SERS Application"*, the thesis author planned and conducted all SERS measurements and electronic extinction spectral measurements; contributed to writing the initial version of the publication. The main co-authors of this publication are: prof. G. Niaura and prof. V. Šablinskas – supervised and contributed to the preparation of the publication; dr. L. Mikoliūnaitė – preparation of the publication; dr. E. Stankevičius, V. Petrikaitė, dr. R. Trusovas, dr. M. Talaikis – performed experiments and formal analysis; dr. M. Talaikis also performed computational calculations.

In other (**II – VI**) **publications**, the author of this thesis planned and conducted most of the experiments (including SERS, SEIRA, Raman, electronic extinction, transmission spectral measurements, etc.); analyzed obtained results, and created their graphical representations; performed computational calculations and presented visualized results, prepared the publications.

The main co-authors of other (**II – VI) publications** are: prof. V. Šablinskas, prof. A. Ramanavičius, dr. V. Artyushenko – supervised and contributed to the preparation of the publications; dr. V. Artyushenko

provided silver halide PIR fibers and ATR loop probe; dr. S. Ramanavičius and dr. A. Popov – synthesized $Ti_3C_2T_x$ MXene and performed EDX, XRD, SEM analysis; dr. O. Bibikova, dr. T. Sakharova, K. Shevchuk, A. S. Novikov – contributed to the preparation and editing of the publications; J. Hinkel – performed one-dimensional profiling of fiber end faces and transmission calculations using COMSOL software; dr. M. Velička – helped with SERS measurements, experiment planning, publication preparation and conducted the deconvolution of the human serum SERS spectra in the **VI publication**: *"Detection of aspirin traces in blood by means of surface-enhanced Raman scattering spectroscopy"*.

APPROBATION OF THE RESEARCH RESULTS

This thesis presents 6 scientific publications that address distinct challenges in SEVS and provide perspectives for substrate research and the analysis of biologically relevant molecules. **I publication** corresponds to the first thesis assignment, **II and III publications**: "*Selective Enhancement of SERS Spectral Bands of Salicylic Acid Adsorbate on 2D Ti3C2Tx-Based MXene Film"* and *"Monitoring $Ti_3C_2T_x$ MXene Degradation Pathways Using Raman Spectroscopy"*. – the second, **IV publication**: "*Microstructuring of the end-surface for silver halide polycrystalline fibers to suppress Fresnel reflection"* – the third. **V publication**: "*Development of Silver Halide Fiber-Based SEIRA Approach for Detection of Pollutants in Aqueous Environment"* has been submitted to the ACS Applied Nano Materials. The results of this publication are presented at conferences and align with the fourth thesis assignment. Although **VI publication** does not directly correspond to a thesis assignment, it demonstrates the potential of the SEVS method for analyzing complex biological fluids. It was used to establish a method for practical application. Copies of all publications are provided at the end of the dissertation.

LIST OF PUBLICATIONS

LIST OF PUBLICATIONS RELATED TO THE DISSERTATION

I. Mikoliunaite, L.; Stankevičius, E.; **Adomavičiūtė-Grabusovė, S**.; Petrikaitė, V.; Trusovas, R.; Talaikis, M.; Skapas, M.; Zdaniauskienė, A.; Selskis, A.; Šablinskas, V.; Niaura, G. *Magneto-Plasmonic Nanoparticles Generated by Laser Ablation of Layered Fe/Au and Fe/Au/Fe Composite Films for SERS Application.* Coatings, 2023, 13, 1523. DOI: 10.3390/coatings13091523.

II. **Adomavičiūtė-Grabusovė, S.**; Ramanavičius, S.; Popov, A.; Šablinskas, V.; Gogotsi, O.; Ramanavičius, A. *Selective Enhancement of SERS Spectral Bands of Salicylic Acid Adsorbate on 2D Ti3C2Tx-Based MXene Film*. Chemosensors, 2021, 9, 223. DOI: 10.3390/chemosensors9080223.

III. **Adomaviciute-Grabusove**, **S.;** Popov, A.; Ramanavicius, S.; Sablinskas, V.; Shevchuk, K.; Gogotsi, O.; Baginskiy, I.; Gogotsi, Y.; Ramanavicius, A. *Monitoring $Ti_3C_2T_x$ MXene Degradation Pathways Using Raman Spectroscopy.* ACS Nano, 2024. DOI: 10.1021/acsnano.4c02150.

IV. **Adomavičiūtė-Grabusovė, S.;** Hinkel, J.; Usenov, I.; Novikov, A.S.; Sakharova, T.; Döhler, T.; Geißler, U.; Feliksberger, E.; Artyushenko, V. *Microstructuring of the end-surface for silver halide polycrystalline fibers to suppress Fresnel reflection,* Opt. Mater. Express, 2022, 12, 34-48. DOI: 10.1364/OME.439904.

V. **Adomaviciute-Grabusove, S.;** Bibikova, O.; Sakharova, T.; Artyushenko, V.; Sablinskas, V. *Development of Silver Halide Fiber-Based SEIRA Approach for Detection of Pollutants in Aqueous Environment.* ACS Applied Nano Materials (submitted 2024, May 25).

VI. **Adomavičiūtė, S.;** Velička, M.; Šablinskas, V. *Detection of aspirin traces in blood by means of surface-enhanced Raman scattering spectroscopy*. Journal of Raman Spectroscopy, 2020, 51(6), 919-931. DOI: 10.1002/jrs.5853.

OTHER PUBLICATIONS WITHOUT A CITATION INDEX

1. Šablinskas, Valdas, et al. "Magneto-plasmonic nanoparticles for SERS." Plasmonics: Design, Materials, Fabrication, Characterization, and Applications XIX. Vol. 11797. International Society for Optics and Photonics, 2021. DOI: 10.1117/12.2597199.

2. Adomavičiūtė, Sonata, Martynas Velička, and Valdas Šablinskas. "Screening of usage of OCT drugs by means of SERS spectroscopy." Plasmonics in Biology and Medicine XVI. Vol. 10894. International Society for Optics and Photonics, 2019. DOI: 10.1117/12.2508276.

3. Adomaviciute, Sonata, Velicka, Martynas, Sablinskas, Valdas. "Fiber based SERS studies of cancerous tissues: toward clinical trials. " Plasmonics in Biology and Medicine XVII vol. 11257. International Society for Optics and Photonics, 2020. DOI: 10.1117/12.2543029.

4. Velicka, Martynas, Adomaviciute, Sonata, Sablinskas, Valdas. "Application of label-free SERS and EC-SERS for detection of traces of drugs in biological fluids." Submitted to Proceedings of SPIE. Plasmonics in Biology and Medicine XVII, vol. 11257. International Society for Optics and Photonics, 2020. DOI: 10.1117/12.2542306.

LIST OF CONFERENCES RELATED TO THE DISSERTATION

1. Sonata Adomavičiūtė-Grabusovė, Marius Balodis, Valdas Sablinskas, Viacheslav Artyushenko. Surface Enhanced Raman Scattering (SERS) and Infrared Absorption (SEIRA) Spectroscopies for *in situ* Imaging of Biomolecules // 4th Baltic Biophysics Conference. Kaunas, Lithuania, October 3 – 4th, 2024. Oral presentation.

2. Sonata Adomaviciute-Grabusove, Olga Bibikova, Tatiana Sakharova, Viacheslav Artyushenko, Valdas Sablinskas. Advancing SEIRA Spectroscopy for *in situ*: Fiber-Based Detection of Naphthalene with Ag-PVP Nanoparticles // Advanced Materials and Technologies. Palanga, Lithuania, August 26 – 30th, 2024. Poster presentation.

3. Sonata Adomaviciute Grabusove, Martynas Talaikis, Evaldas Stankevicius, Vita Petrikaite, Romualdas Trusovas, Justinas Ceponkus, Lina Mikoliunaite, Algirdas Selskis, Arūnas Želvys, jankevičius Feliksas, Valdas Sablinskas, Gediminas Niaura. Advanced SERS Substrate of Magnetoplasmonic Nanoparticles for Cancerous Kidney Diagnostics // European Materials Research Society Spring Meeting. Strasbourg, France, May 29th – June 3rd, 2023. Oral presentation.

4. Evaldas Stankevičius, Vita Petrikaitė, Ilja Ignatjev, Romualdas Trusovas, Sonata Adomavičiūtė-Grabusovė, Valdas Šablinskas, Martynas Talaikis, Justinas Čeponkus, Lina Mikoliūnaitė, Algirdas Selskis, Gediminas Niaura. Hybrid Gold-Silver Nanoparticles Synthesis Using a Nanosecond Laser Treatment and Their Use in Raman Spectroscopy // Lasers in Manufacturing Conference. Munich, Germany, June 26 – 29th, 2023. Poster presentation.

5. Sonata Adomavičiūtė-Grabusovė, Jonas Hinkel, Iskander Usenov, Alexander S. Novikov, Tatiana Sakharova, Torsten Döhler, Ute Geißler, Elena Feliksberger, Viacheslav Artyushenko. Imprinting and Profiling of Silver Halide Polycrystalline Fiber End Faces to Create Moth-eye Anti-reflective Microstructures to Reduce Fresnel Reflection Losses // SPIE Optics + Optoelectronics. Prague, Czech Republic, April 24 – 25th, 2023. Poster presentation.

6. Simonas Ramanavičius, Anton Popov, Sonata Adomavičiute-Grabusove, Martynas Talaikis, Valdas Sablinskas, Arunas Ramanavicius, Gediminas Niaura. Formation of 2D MXene Structures with Tunable properties for application in the design of SERS substrates // The 4th International Online Conference on Nanomaterials. Virtual, April 24th – May 4th, 2023. Poster presentation.

7. Sonata Adomaviciute Grabusove, Evaldas Stankevicius, Vita Petrikaite, Romualdas Trusovas, Martynas Talaikis, Arunas Zelvys, Valdas Sablinskas, Gediminas Niaura. Dual *vs* Triple composition of magneto-plasmonic nanoparticle arrays generated by laser ablation: effect on reliability for SERS applications // 12th International Colloids Conference. Palma, Spain, 2023. Poster presentation.

8. Adomaviciute-Grabusove, S., Sablinskas, V., Ceponkus, J., Stankevicius, E., Petrikaite,V, Zdaniauskiene, A., Selskis, A., Niaura, G. SERS performance of laser-ablated magneto-plasmonic nanoparticles // European Materials Research Society Spring Meeting. Virtual, May 30th – June 3rd, 2022. Oral presentation.

9. Aliona Klimovich, Sonata Adomavičiūtė-Grabusovė, Hamza Rehman, Polina Kuzhir, Ieva Matulaitienė. Surface-enhanced Raman Spectroscopy of Potential Induced Changes in Human Urotensin II // Chemistry and Chemical Technology. Kaunas, Lithuania, October 14th, 2022. Poster presentation.

10. Sonata Adomaviciute, Martynas Velicka, Valdas Sablinskas. Diagnostic studies of traces of OTC drugs in blood by SERS spectroscopy // 43-ioji Lietuvos nacionalinė fizikos konferencija. Kaunas, Lithuania, October 3rd –5th, 2019. Poster presentation

11. Sonata Adomaviciute, Martynas Velicka, Valdas Sablinskas. Traces of paracetamol in blood as studied by means of colloidal SERS // Open Readings 2019. 62nd International Conference for Students of Physics and Natural Sciences. Vilnius, Lithuania, March 19–22nd, 2019. Oral presentation.

LIST OF PUBLICATIONS UNRELATED TO THE DISSERTATION

1. Velička, M.; Zacharovas, E.; **Adomavičiūtė, S**.; Šablinskas, V. *Detection of caffeine intake by means of EC-SERS spectroscopy of human saliva*. Spectrochimica Acta Part A: Molecular and Biomolecular Spectroscopy 2021 246, 118956. DOI: 10.1016/j.saa.2020.118956

2. Golubewa, L.; Klimovich, A.; Timoshchenko, I.; Padrez, Y.; Fetisova, M.; Rehman, H.; Karvinen, P.; Selskis, A.; **Adomaviciute-Grabusovė, S**; Matulaitiene. I.; Ramanavicius, A; Karpicz. R.; Kulahava, T.; Svirko, I.; Kuzhir, P. *Stable and Reusable Lace-like Black Silicon Nanostructures Coated with Nanometer-Thick Gold Films for SERS-Based Sensing*. ACS Applied Nano Materials 2023, 6(6), 4770-4781. DOI: 10.1021/acsanm.3c00281

1. INTRODUCTION TO THE RESEARCH FIELDS

The interaction of electromagnetic radiation with the molecules manifests in several ways. The electromagnetic radiation can be scattered or absorbed. Scattering can also be different, the radiation can be scattered elastically (when the frequency of the incident and scattered radiation does not change, only the direction), known as Rayleigh, Mie scattering or inelastically – Raman, Brillouin scattering. Molecules of different materials interact slightly differently with electromagnetic radiation, depending on functional groups, the number of atoms, orbital overlap, etc. This can be seen in the absorption and/or Raman scattering spectra, which are specific to each molecule. Based on these, a qualitative analysis of materials can be precisely performed. If the spectral markers of the specific molecules are known, a quantitative analysis can also be done.

Infrared absorption depends on the interaction between molecules and electromagnetic radiation (specifically, middle infrared radiation: 400 – 4000 cm^{-1}). Absorption occurs at specific vibrational energy levels. Infrared spectroscopy relies on the unique movements of atoms within the molecule. When a photon has a frequency that matches the vibrational frequency of a molecule, it is absorbed. This leads to an increase in the amplitude of the molecular vibrations, which is similar to the resonance effect. In simple terms, the incident radiation I_0 decreases exponentially due to absorption, which is dependent on the length of the sample l and the attenuation constant μ:

$$I = I_0 e^{-\mu l}. \qquad (1.1.1)$$

The attenuation constant varies for each type of molecule, and it is dependent on the changes in the molecular dipole moment during each normal vibration.

Raman scattering, discovered in 1928, is an inelastic two-photon process. The incident photon is 'absorbed,' exciting the molecule to a virtual level, and a photon of a different frequency is emitted. Sometimes, instead of saying the photon is absorbed, it is said that the molecule is perturbed by the intense electric field in the incident radiation, because the photon is not absorbed in the traditional sense. After scattering, the material remains in a changed energy state at an excited vibrational level. The shift in Raman scattering depends on the energy difference between the excited and unexcited vibrational levels. During conventional Raman scattering a high-power, monochromatic radiation source, such as a laser, is required for this process. The efficiency of the process can be described by the effective cross-section.

It is the ratio of the radiation strength or power generated by the molecule to the power of the radiation causing the process. The effective cross-section of Raman scattering (σ_R) is 10^{10} times smaller than the absorption cross-section of infrared radiation ($\sigma_{IR} \approx 10^{31}$ cm^2 sr^{-1}). The efficiency of Raman scattering is very low, scattering 10^{-5} of the intensity of the incident radiation. The intensity of the scattered light, knowing the effective cross-section, can be described as dependent on the intensity of the incident radiation I_0, and the effective cross-section σ at a certain angle Ω:[32]

$$I = I_0 d\sigma/d\Omega. \qquad (1.1.2)$$

Raman scattering spectroscopy is a method known for its molecular specificity; however, it is not particularly efficient. Its efficiency depends on the intensity of the electric field interacting with the molecule. While increasing the radiation intensity that excites the scattering can enhance efficiency, this raises the risk of sample damage. Thus, it is not possible to greatly increase the efficiency of Raman scattering. In 1974, the method of SERS was discovered,[28–30] which enables the amplification of both the intensity and efficiency of Raman scattering, thereby increasing spectral sensitivity to molecules at low concentrations.

1.1. Surface Enhanced Raman Scattering Spectroscopy

In SERS spectroscopy, specific resonance conditions lead to a remarkable increase in the enhancement factor of Raman signal.[26,31,33,35] The effect of Raman scattering enhancement near the surface of plasmonic metal nanostructures is conditioned by several effects. It is now believed that the enhancement consists of two mechanisms. The largest contribution to this Raman scattering enhancement comes from the electromagnetic enhancement component. It has been determined that the reason for the significant electromagnetic enhancement is the resonant phenomena of surface plasmons created in the metal.[26,54] In nano-sized structures, the surface plasmon-polariton (SPP) wave (a coupled wave of a surface plasmon, which is the charge motion in the metal, and a polariton, which is the electromagnetic wave in the dielectric)[54] is limited by the nanoparticle dimensions – the wave does not spread across the surface and is rather localized. When the size of the nanostructure is half the length of the SPP wave, scattering can lead to the formation of standing SPP waves. In nanoparticles, these modes are called localized surface plasmons (LSP), which are excited by an electromagnetic wave of a certain frequency that coincides with the frequency of the free

electron oscillations in the nanoparticle. Structures with curved surface geometry (including nanoparticles) are characterized by an effective force that maintains oscillating electrons, causing electron resonance on the surface (LSPR).[32,54] This is manifested by corresponding LSPR extinction bands.

The surface plasmon resonance occurring on the surface of noble metal nanoparticles can be explained by imagining a flat electromagnetic wave falling onto a spherical metal nanoparticle. Solutions for such a system were described by G. Mie, and they are called Mie scattering.[55] By solving Maxwell's equations at the boundary of metal (index *m*) and dielectric (index *d*) and applying boundary conditions, a condition is obtained that must be satisfied to form LSP:[32,54]

$$\varepsilon_m(\omega) = -2\varepsilon_d. \qquad (1.1.3)$$

That is, the dielectric permittivity of the material into which the radiation falls (in this case, metal) must be of opposite sign and twice as large as that of the material from which the radiation falls. The conditions also must be satisfied: $2|\varepsilon_d| > \varepsilon_m; \varepsilon_m < 0$. Metals have negative dielectric permittivity in the ultraviolet-visible (UV-Vis) range. The 'free' electrons (plasmons) in them interact weakly with ions and can oscillate relative to them. Therefore, if the frequency of the incident radiation is not higher than the frequency of the free electrons, or plasmons, the metal plasmons adapt and reflect the radiation. Their dielectric permittivity is described by the Drude model, and by calculating the imaginary part (damping coefficient - γ), the Drude – Sommerfeld model:[56,57]

$$\varepsilon_m(\omega) = 1 - \left(\frac{\omega_p^2}{\omega^2}\right) \rightarrow 1 - \frac{\omega_p^2}{\omega_p^2 + i\gamma\omega}, \qquad (1.1.4)$$

and depends on the frequency of the external electromagnetic field ω and the oscillation frequency of free electrons in metal ω_p.

$$\omega_p^2 = (ne^2)/(\varepsilon_0 m_f). \qquad (1.1.5)$$

The frequency of plasmon oscillations depends on the concentration of electrons, n, and the effective mass, m_f. Here e is the charge of an electron. Of course, all metals have their own characteristic plasmon oscillation frequency, but when talking about SERS, usually only a few are examined – Ag, Au, Al and Cu. Nonetheless, this equation shows that some materials might also possess plasmon oscillations and be used as a SERS substrate.

Since the plasmon frequency depend on the concentration of electrons n, so does the LSPR.

1.2. SERS of Biological Tissues

The SERS spectroscopy has proven to be efficient for biological sample analyzation.[43,44] SERS has been successfully used to detect biomolecules,[58–61] pathogens,[62] cancer cells,[63,64] *in vivo* tumor imaging,[65,66] etc. The simple and convenient principle of SERS measurements is provided in **Figure 1.1.1**. Usually, the biological tissue or fluid is placed on top or bottom of the nanoparticle substrate, depending on the sample and substrate used. The label-free (unfunctionalized) SERS method offers selectivity for certain molecules, and in complex biological samples, this is advantageous.[61] SERS spectra are primarily influenced by biomolecules that strongly adhere to SERS-active metal surfaces, therefore SERS is very good for detection of trace components, such as metabolites that have a strong attraction to surfaces.

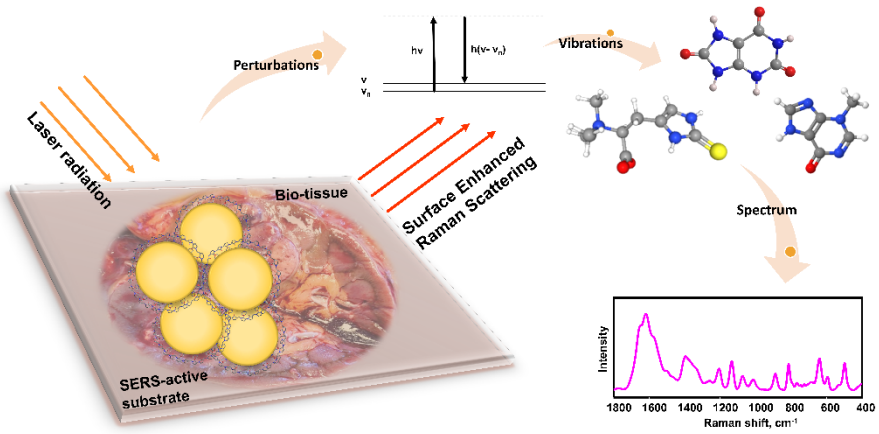

Figure 1.1.1. Schematic representation of SERS method application for biological samples.

The selectivity of the SERS method is demonstrated in the **VI publication**. In this publication, whole human blood and blood serum were investigated using SERS spectroscopy and a search for spectral markers of the aspirin metabolite in human blood samples was conducted.

The whole blood SERS spectrum consists of a complex distribution of macromolecules such as structural proteins, carotenoid,[67] and metabolites like uric acid, hypoxanthine, and amino acids.[43,67–69] This makes the assignment of spectral bands in the SERS spectra challenging and often contradictory. SERS spectra of whole blood depend heavily on the excitation wavelength used. For

the 515 nm wavelength, mostly resonance Raman spectral bands of the heme group in erythrocytes are observed.[70] When blood is excited with a 785 nm wavelength laser, the SERS spectrum obtained is similar to that of plasma,[68] indicating that the SERS spectral bands of blood arise from the vibrational modes of small molecules present in serum. In the SERS spectra of blood, excited using a 785 nm wavelength laser, characteristic bands of uric acid, hypoxanthine, human serum albumin, and hemoglobin can be detected.[69]

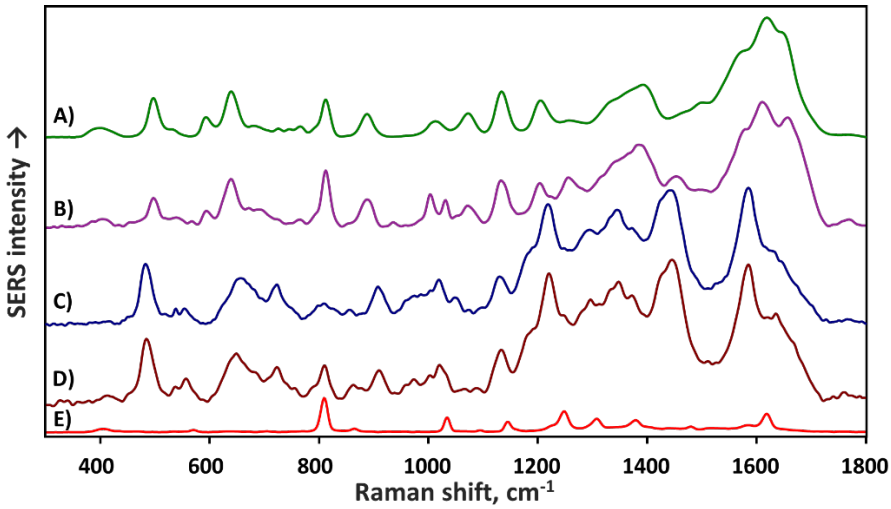

Figure 1.1.2. SERS spectra of 20 times diluted fresh human serum (A); mixture of human serum with 5 mM salicylic acid solution (B); 20 times diluted whole blood (C); mixture of whole blood with 5 mM salicylic acid solution (D); 1 mM salicylic acid solution.

The SERS spectra of whole human blood, its serum, and their mixtures with a 5 mM concentration of salicylic acid are shown in **Figure 1.1.2**. The whole blood and serum were diluted 20 times prior to spectral measurements using deionized water. The presence of salicylic acid in whole blood can be determined by the appearance of a spectral band at 809 cm^{-1}, corresponding to the normal vibration related to ring stretching and (C─COO) scissor vibration. It is important to note that there is significant spectral variation in the SERS spectrum of blood in this region (Supporting Information in the **VI publication**). Therefore, when the concentration of salicylic acid in blood is below 5 mM, it is not possible to confirm its presence.

The cells and clotting factors (fibrinogen, prothrombin, etc.) that participate in the coagulation process are removed in human blood serum. However, more than 4000 different components remain in it.[71] Human serum albumin is the most common protein in plasma and serum (35 – 50 mg/l),[72] making up approximately 60 % of the total amongst other protein: globulin,

enzymes, hormones, etc.[73] Under normal conditions, the concentration of uric acid in blood serum ranges from 140 μM to 420 μM. Nevertheless, in SERS spectra of human serum, mostly SERS bands of uric acid and hypoxanthine are observed, as these molecules show great affinity towards silver or gold nanoparticle surfaces (**Figure 1.1.3**).

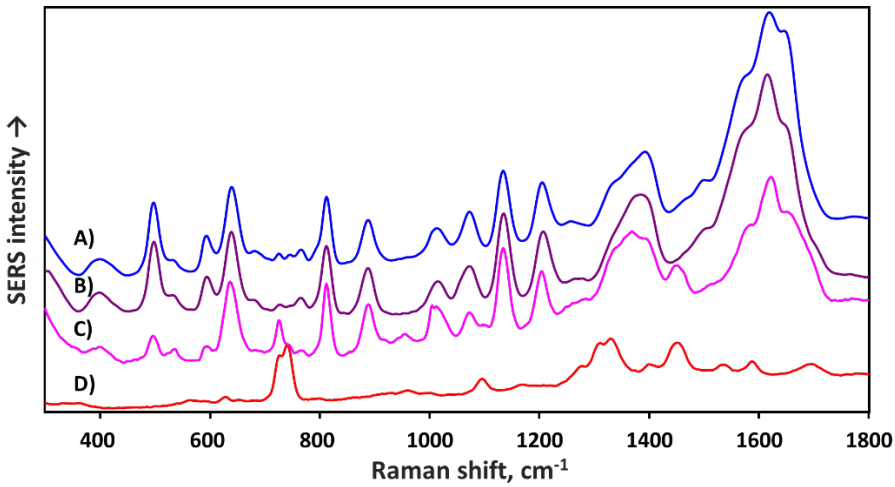

Figure 1.1.3. SERS spectra of fresh human serum (A); 0.1 mM uric acid solution (B); week old human serum (C) and 1 mM hypoxanthine solution (D).

When the concentration of salicylic acid in serum is high (5 mM – **Figure 1.1.2**), the spectral band of salicylic acid located at 1032 cm^{-1} is prominent. In cases of low salicylic acid concentration, the intensity of this spectral band decreases and can only be detected as a shoulder of the serum spectral band at 1012 cm^{-1} (**Figure 1.1.4**). Another spectral marker that appears to be prominent for salicylic acid concentrations from 0.15 to 0.5 mM. is the intensity of the serum spectral band at 1012 cm^{-1}. The intensity in this band increases with rising concentrations of salicylic acid, which is thought to be caused by a more intense spectral band at 1003 cm^{-1}, associated with asymmetric ring vibrations in phenylalanine. It was shown that changes in serum pH, related to the presence of salicylic acid, may cause these changes in human serum spectra (possibly due to hindered adsorption of uric acid on the nanoparticle surface). Different molecular structures and binding sites influence the adsorption affinity of molecules differently when sample conditions, such as pH, change. SERS is a surface-sensitive spectroscopy, meaning the Raman signal is enhanced only for molecules adsorbed or close to the surface of nanoparticles. Since nanoparticles are relatively stable and their surface area does not change, molecules compete for adsorption. Solution

properties, such as pH or an electrostatic field on the nanoparticle surface, may enhance the adsorption of certain molecules. Based on the intensity changes of spectral bands at 1012 cm^{-1} and 1003 cm^{-1}, salicylic acid at a concentration of 0.15 mM can be detected, corresponding to an overall concentration of 3 mM in undiluted serum.

The research presented in the **VI publication** demonstrated that label-free colloidal SERS using a near-infrared laser excitation wavelength (1064 nm) can effectively detect salicylic acid, a metabolite of aspirin, in human blood and its derivatives. Serum was identified as the optimal medium for salicylic acid detection due to fewer interfering constituents compared to whole blood, achieving a detection limit of 3 mM of salicylic acid, corresponding to mild toxicity levels. A calibration curve was created, showing nonlinearity due to competing adsorption between salicylic acid and uric acid. It was discovered that increasing salicylic acid concentration significantly affects uric acid adsorption, enhancing the detection of salicylic acid and other molecules like phenylalanine. The intensity of the SERS band of phenylalanine at 1003 cm^{-1} was identified as a reliable indirect spectral marker for SA concentration, more so than the direct marker at 1031 cm^{-1}. These findings highlight the potential of SERS for fast, sensitive salicylic acid detection in blood, with implications for point-of-care analysis and rapid clinical decision-making.

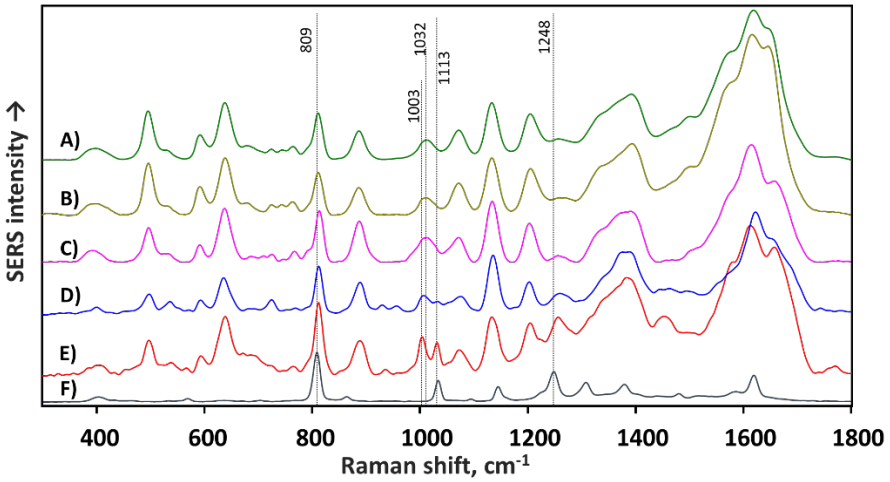

Figure 1.1.4. SERS spectra of 20 times diluted blood serum (A); blood serum mixtures with varying concentrations of salicylic acid: 0.15 mM (B), 0.5 mM (C), 2.5 mM(D), 5 mM (E); 1 mM salicylic caid solution (F).

While the proposed method for detecting aspirin usage is not yet sensitive enough to replace standard drug testing methods like liquid chromatography tandem mass spectrometry and gas chromatography tandem mass

spectrometry, it offers several advantages. This method can be applied faster and more easily, saving time and resources. Additionally, the hardware required for SERS analysis and its maintenance is cheaper than that for liquid chromatography or mass spectrometry devices, making it more accessible for clinics and medical centers.

1.3. SERS Substrates

In general, materials that have been shown to improve the Raman scattering signal can be categorized into several types. These include I) metal SERS substrates, which are typically noble metals like gold, silver, or copper. These metals have surface plasmon resonances that can amplify the Raman signal. II) Semiconductor nanomaterials, which are certain semiconductors that exhibit properties enhancing Raman signals due to their electronic and optical characteristics.[45] III) Nanocomposites of metallic and semiconducting materials, which combine metals with semiconductors at the nanoscale to create synergistic effects that further boost the Raman signal and offer additional advantages.[46,74]

1.3.1. Metal nanostructures as SERS substrate

Metals are known to exhibit the highest enhancement factors and are commonly utilized. As previously mentioned, typical metals used include Ag, Au, and Cu. These can be employed to create monometallic nanoparticles, hybrid metal substrates,[75] or be combined with semiconducting materials for nanocomposites.[76] However, here they are referred to as metal SERS substrates because the most significant enhancement is derived from the noble metals that possess LSPR within the visible range. When LSPR is stimulated in a nanoscale structure through irradiation, it generates a potent electromagnetic field. This field can significantly amplify the Raman signal of reporter molecules due to the field intensity, leading to a dramatic enhancement in the signal, potentially increasing by a factor ranging from 10^3 to 10^9.[46] This factor can be even higher, reaching 10^{15} if reporter molecules that possess absorption in the excitation range are used, i.e. dye molecules. In this scenario, an additional enhancement is achieved through the Resonance Raman effect.[77] It is widely accepted now that the electromagnetic enhancement mechanism plays a key role, alongside possible chemical contributions, in this substantial enhancement of the Raman signal.

While metal SERS substrates are widely used due to their strong enhancement effects, they do come with several inherent disadvantages:

- High preparation cost: The synthesis of noble metal nanoparticles often requires expensive materials and sophisticated equipment.
- Susceptibility to oxidation: Metals like silver can easily oxidize, which can alter their surface properties and affect the enhancement capabilities.
- Tendency to agglomerate: Nanoparticles form larger clusters that may not exhibit the desired plasmonic properties and drastically change the enhancement factor.
- Poor stability: The physical and chemical properties of nanoparticles can change over time or under different conditions, leading to inconsistent results.
- Low signal reproducibility: Due to the factors above, it can be challenging to get consistent SERS signals, which is crucial for quantitative analysis.

Researchers are actively working on overcoming these challenges by developing new types of substrates and improving the synthesis methods to make SERS a more reliable and accessible technique.

In brief, one of the major challenges for SERS is the non-reproducibility of signal intensity. Consequently, considerable effort is being directed toward developing SERS substrates that offer more reproducible spectral intensity while maintaining a high enhancement factor. Such advancements would facilitate the broader application of SERS in scientific research as well as in medical diagnostics.

1.3.2. Semiconductor SERS substrates

Semiconductor SERS substrates are becoming more popular for research, analysis and developing applications. These materials do not provide such high enhancement factors but are valued for their distinctive properties, such as high surface area and strong interaction with light, which make them excellent candidates for enhancing Raman signals.[50] Furthermore, the high selectivity attributed to the Charge-transfer (CT) mechanism in non-noble metal SERS substrates enables the differentiation of specific molecules within complex environments.[78,79] Consequently, non-noble metal nanomaterials emerge as promising candidates for SERS substrates, presenting significant potential for application in SERS detection.

While electromagnetic enhancement mechanism of the SERS signal is the predominant contributor to SERS sensitivity, overshadowing the chemical enhancement mechanism is not the less important. Typically, electromagnetic enhancement reaches up to $10^3 – 10^9$ times.[46] Chemical enhancement reaches

only about 100 times.[32,50,80] The observable and unwanted 'hot spot' effect in SERS substrates, where the intensity significantly varies across different spots of the sample, is due to the electromagnetic enhancement mechanism. This occurs when the analyte molecule is positioned between two nanoparticles.[32,54] The random distribution of these hot spots leads to variations in the absolute intensity of the SERS bands. The chemical enhancement mechanism contributes to a more uniform substrate in terms of the intensity changes in the Raman bands.

Chemical enhancement in SERS originates from alterations in molecular polarizability and the Raman cross-section of vibrational modes due to the interaction with a substrate. This interaction, through physisorption or chemisorption, modifies the shape and electronic configuration of the molecule.

There are two primary mechanisms of chemical enhancement: (i) non-resonant chemical effect and (ii) resonant charge transfer chemical effect. The non-resonant chemical effect occurs when the molecular orbitals are distant from the Fermi level of metal, not creating new electronic states but changing the electronic and geometric structure of the molecule. This transformation affects the Raman shifts and intensities of vibrational modes. The more significant and usually investigated resonant effect, or CT mechanism happens when the metal – molecule interaction creates a CT state. Energy levels between the Highest Occupied Molecular Orbital (HOMO) and Lowest Unoccupied Molecular Orbital (LUMO) of the molecule and the Fermi level of metal redistribute, and the electronic level of the molecule can be excited not directly by transferring an electron from LUMO to HOMO orbitals, but through the CT complex involving the Fermi level of metal. [32] Then, the energy of the exciting radiation frequency can be close to the energy required for electronic excitation. The formed CT complex between the nanoparticle and the molecule can increase the Raman scattering process up to 100 times. Even if the energy of the exciting wave frequency cannot excite electronic absorption, a surface complex is created between the adsorbed molecule and the nanoparticle surface – selection rules for enhanced vibrations appear. Those vibrations whose polarizability changes perpendicular to the direction of the nanoparticle surface are most enhanced.

The selection rules for Raman scattering are derived based on the postulates of quantum mechanics. Molecular vibrations are seen in Raman scattering spectra when at least one of the components of the polarizability tensor changes[32,54]. In the case of SERS, additional selection rules appear. Since even a small distance from the surface of the nanoparticle weakens the electromagnetic field enhancement,[32,54] the intensities of the vibrational

modes of the functional groups of the molecule that are oriented or adsorbed onto the nanoparticle are most enhanced. The vibrations whose translational moment coincides with the direction of plasmon oscillations – perpendicular to the nanoparticle surface – are most enhanced.

Common semiconductor materials for SERS are ZnO, TiO_2, CdSe,[81] Ta_2O_5,[82] organic semiconducting materials and two-dimensional semiconductor materials (e.g., graphene, MoS_2, h-BN, MXene, etc.).[83,84] Two-dimensional materials like graphene, hexagonal boron nitride (h-BN), and molybdenum disulfide (MoS_2) have shown unique Raman enhancement effects in previous research, indicating their potential as substrates for Raman enhancement.[85] The ability of these materials to improve Raman scattering signals opens up new possibilities for sensitive detection and analysis in scientific and medical diagnostics. Graphene is known to achieve a SERS enhancement factor of one or two orders of magnitude. The enhancement can be controlled by the surface structure and the number of graphene layers. It is believed to exhibit chemical effects and, importantly, is advantageous for molecules considered to be non-absorbing, which usually do not form a covalent bond with metal nanostructures. Therefore, achieving SERS for similar molecules using metal nanostructures is complicated. For example, SERS investigation of molecules that typically interact *via* π-π stacking or hydrophobic interactions, such as naphthalene (investigated in this work) and other aromatic compounds, present challenges.[46] $Ti_3C_2T_x$ layered structures, known as MXene, have been compared to graphene in various aspects.[86]

1.3.3. Hybrid SERS substrates

One of the most employed hybrid SERS substrates for biological tissue analysis is known as "shell-isolated" nanoparticles (or SHINERS).[87] These are created by coating metal nanoparticles, typically gold or silver, with a thin layer of SiO_2 (2-5 nm). This SiO_2 layer is advantageous because it prevents the adsorption of molecules. Consequently, these nanoparticles can be used to obtain more "objective" spectra by preventing the adsorption of commonly SERS-active molecules. By using Au-core silica-shell nanoparticles for SERS applications, the shell surface can be varied in composition and morphology, which prevents direct interaction between the Au core and the analytes. This reduces signal alteration and allows the enhancement effect to be controlled by adjusting the shell thickness.

Graphene and its derivatives, such as graphene oxide and reduced graphene oxide, have also been extensively studied and have emerged as promising materials for SERS substrates due to their unique properties.[88–90]

As a multifunctional layered material, graphene can also serve as a protective shell for noble metal nanoparticles. Firstly, their distinctive structure promotes interactions with analytes through π-π stacking and hydrophobic interactions, enhancing the adsorption of non-thiolated molecules. Graphene shell of the hybrid nanoparticles offers the additional benefit of fluorescence quenching, further improving SERS efficacy.[90] For instance, a graphene-coated AgCu nanoparticle showed excellent potential for imaging.[88] Additionally, polymers like dopamine have been suggested as promising candidates for coating nanoparticles due to their flexible properties.[91,92]

Hybrid nanoparticle substrates have demonstrated significant advantages for SERS over the past decade, thanks to their high surface-to-volume ratio, surface control, biocompatibility and stability of SERS substrates. These materials have been explored as SERS substrates due to their remarkable properties, including enhanced photogeneration rates, plasmon-induced "hot electrons," and improved conductivity. In brief, the core-shell structure offers two main advantages: it combines the distinct properties of both the core and the shell, and it allows for the incorporation of tags in the inner gap, which is useful as an internal standard for quantitative detection.[76]

Numerous studies have explored colloidal solutions of nanoparticles hybridized with other materials. Among nanocomposite material substrates, a wide range of materials have been investigated, including hexagonal boron nitride (h-BN), and MXene layers incorporated with decorated Ag, Au, or Pd nanoparticles.[93] For example, h-BN has been shown to reduce the oxidation of plasmonic metals in hybrid substrates and increase their shelf-life.[94] Although the applicability of these materials is still under ongoing research, the results seem very promising.

1.4. Surface Enhanced Infrared Absorption Spectroscopy

SEIRA spectroscopy is a technique that amplifies the infrared absorption signals of molecules when they are placed at the interface to metals, metal oxides, or semiconductor materials. The SEIRA enhancement, while not as substantial as that seen in SERS spectroscopy, is nonetheless significant and offers exciting prospects for the advancement of infrared spectroscopic techniques. While SERS depends on changes in the polarizability of the molecule, SEIRA relies on changes in the dipole moment. SEIRA is particularly useful for studying molecules at metal interfaces.

Compared to conventional infrared spectroscopy, SEIRA can enhance the infrared absorption signals by several orders of magnitude (commonly, two orders of magnitude)[31] enabling the detection of as few as 1000, or 500

molecules. This is a substantial improvement over the typical detection limit of sub-micromolar levels found in standard infrared spectroscopy. The chemical resolution inherent to infrared spectroscopy, combined with its non-destructive and label-free nature, makes SEIRA a powerful tool for a wide range of chemical and biophysical applications. Moreover, SEIRA can be performed with various metal electrodes in a spectroelectrochemical setup, making it an ideal technique for monitoring heterogeneous electrocatalytic chemical reactions *in situ* and providing mechanistic insights *via* the detected infrared spectra[3].

In non-resonant SEIRA technique, electromagnetic enhancement is achieved through dielectric modulation. Molecular vibrations, which involve shifts in charge distribution, act like oscillating dipoles. At the interface with a metal or dielectric, these oscillations induce similar dipole movements within the material surface, altering its dielectric function. This change can affect the optical characteristics of material, such as transmittance and reflectivity, at the molecular vibration frequencies, enabling the material to amplify the absorption of incident infrared radiation. This broad spectral enhancement, usually in tens order is most effective for molecules within 10 nm of the material surface and aligns with predictions from effective medium theories like Bruggemann approximation.

Resonant SEIRA involves electromagnetic enhancement through plasmon resonance. Incident infrared light excites surface plasmon polaritons, a collective oscillation of free charges in the particle, creating oscillating dipoles that produce a localized electromagnetic field (or near field) on the material surface. This effect is very similar to SERS. While enhancement in non-resonant SEIRA is minimal due to plasmon damping, resonant SEIRA can significantly amplify the electric field in the particles if their geometry resembles a nanoantenna and matches the resonance conditions of the infrared light. This LSPR leads to a near field that is exponentially stronger enhancing infrared spectra by over 10^4 times within a narrow spectral range. This enhancement decays exponentially from the surface. Unlike non-resonant SEIRA, the resonance frequency and the wavenumber range of enhancement can be adjusted by altering the shape and size of the nanoantennas. Furthermore, when multiple nanoantennas are positioned in specific orientations and distances without touching, their LSPRs can interact, creating an intense near field at the gaps (hot spots), resulting in the highest enhancement levels. Nonetheless, this resonant SEIRA effect, though producing very high (similar to SERS) enhancement, is limited to only a narrow spectral range and does not cover the entire middle infrared range

(400 – 4000 cm^{-1}). For a more diverse SEIRA substrate, non-resonant SEIRA should be considered.

While the technique is effective in controlled laboratory settings, it encounters limitations in practical scenarios. Most advances in the SEIRA field focus on substrate formation and achieving a high enhancement factor, with little research dedicated to integrating SEIRA into real-life applications. However, incorporating optical fibers into Fourier Transform Infrared (FTIR) spectrometers opens new opportunities for in situ sample analysis, effectively bridging the gap between traditional spectroscopic methods and field applications.

1.5. SEIRA Substrates

The advancements in SEIRA field have been rather slow for the last 30 years following 1980, with two main factors impeding its progress. Firstly, SEIRA was noticed from the metal island generated enhancement. The enhancement achieved with this approach was approximately 20.[95] SEIRA reliance on metal island films for enhancement is based on a non-resonant mechanism that does not align plasmon resonance with the infrared spectrum. Consequently, the enhancement factors have been modest, generally between 10 and 100,[31] in comparison to the enhancement seen in SERS during the same timeframe. Secondly, the structural inconsistency of metal island films created through gas-phase or electrochemical deposition leads to an unpredictable SEIRA signal.[42]

The LSPR of metals lies in the visible range, whereas the working range of infrared absorption spectroscopy is (3 – 17 μm) far beyond the LSPR of metals. Thus, the LSPR wavelength can either be shifted to the infrared range using metamaterials. These engineered materials, characterized by their subwavelength periodic structures, can manipulate electromagnetic waves in ways that natural materials cannot. LSPR in the infrared spectrum was successfully achieved by designing plasmonic nanoantennas.[96] These nanoantennas generate enhanced-intensity electromagnetic hotspots, fostering interactions with adjacent analyte molecules and improving SEIRA sensitivity. This leads to a resonant SEIRA method that benefits from high enhancement factors.

In general, resonant SEIRA enhancement has been achieved using metal nanostructures, particularly through the tuning of plasmonic resonances in metal antennas to the infrared range.[96–100] For further improvement, an array of plasmonic nanoantennas for the ultra-sensitive spectral detection of protein monolayers has been demonstrated[101] together with the dipolar resonances in

coupled nanoshell structures within the mid-infrared region.[102] These arrayed nanoantennas are capable of exciting collective electron resonances, leading to greater local field enhancements and more defined spectral responses. Importantly, the underlying mechanisms of enhancement in infrared spectroscopy are related to those in Raman spectroscopy in this case. The electric field enhancement near molecular species is attributed to the oscillation of free charges within the plasmonic material in resonant SEIRA (and effective medium theory in non-resonant SEIRA).

Despite these improvements, the drawback of resonant SEIRA is the limited LSPR wavenumber range. This means that only a few spectral markers can be highly enhanced with these substrates or within a narrow wavelength range. Besides, the fabrication of such metamaterial substrates is challenging.

Additionally, for infrared spectroscopy, materials like III–V group semiconductors,[103] graphene nanostructures,[104] and hexagonal boron nitride[105] can also be employed.

2. RESEARCH FIELDS

In this section, the research conducted during the doctoral studies is presented, highlighting the innovative aspects and key findings. The results discussed in this chapter are derived from publications included in the thesis. This section is organized into four subsections, each covering different methods and substrates used for signal enhancement: 1) Signal Enhancement Using Magneto-plasmonic Nanoparticles; 2) Signal Enhancement Using Two-dimensional MXene Substrate for SERS Applications; 3) Signal Enhancement in Infrared Absorption-Based Remote Sensors (Parts 3 and 4).

2.1. Signal Enhancement Using Magneto-plasmonic Nanoparticles

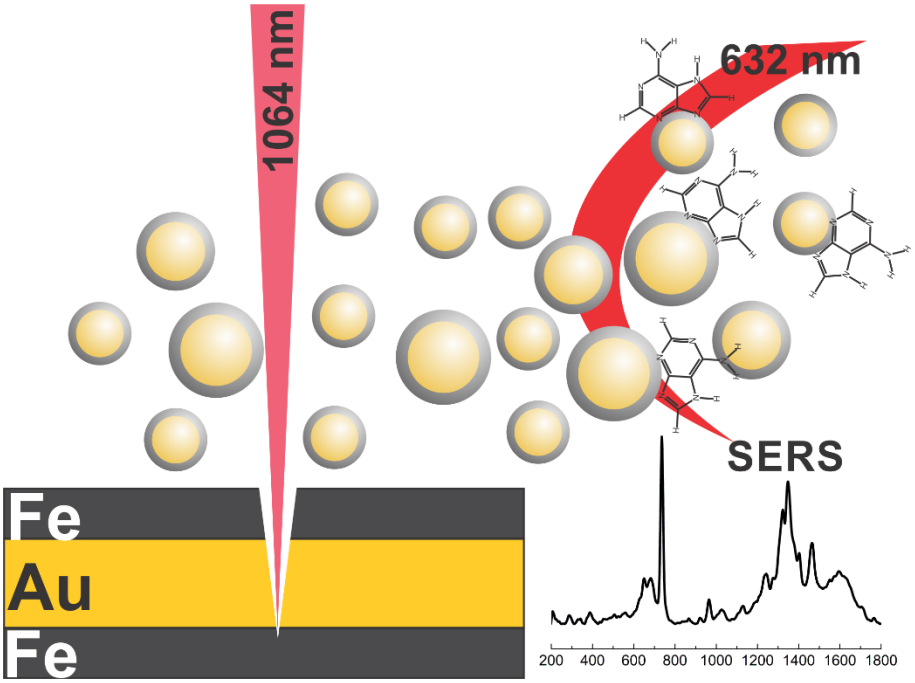

In this subsection results from the **I publication** are presented addressing the first thesis assignment and supporting the initial key statement for defense. This assignment delves into the investigation of hybrid metal magneto-plasmonic nanoparticles for enhanced SERS performance. The PLAL method was employed to generate high-purity nanoparticles. The employed PLAL method and magneto-plasmonic nanoparticles addresses two major issues of SERS substrates: signal reproducibility and chemical contamination, both of which lead to spectral residues. By combining magnetic and plasmonic properties, these nanoparticles can be precisely manipulated without compromising their ability to enhance the Raman signal, which is crucial for the detection and analysis of biomolecules. The goal behind this research was to ascertain the magnetic and plasmonic properties of hybrid nanoparticles for biomolecule investigation. The dual functionality of these nanoparticles could potentially lead to more consistent and reliable SERS-based sensors. This would be particularly beneficial in the field of biochemistry and medical diagnostics, where precise and reproducible measurements are essential.

2.1.1. Motivation

The idea behind these hybrid nanoparticles is that they possess a plasmonic part (noble metals such as Au, Ag) that generates LSPR and enhances the Raman signal alongside the magnetic part (elements like Fe, Co, or Ni) that can be controlled *via* magnetic forces, showcasing both magnetic and plasmonic characteristics simultaneously. The advantages of these nanoparticles have been demonstrated in medical applications.[106–108] Specifically in phototherapy,[109] magnetic resonance imaging,[110] treatment of brain disease[111] and cancer[112] apart from application in SERS.[60,113–115] The controllable hot-spots due to the magnetic properties of these nanoparticles in a dynamic approach were achieved,[116] as well as the magnetic manipulation of nanocrescent particles,[60] thus showing the ability to manipulate these particles *via* an external magnetic field. Nevertheless, since the SERS method is extremely sensitive to various impurities, contamination, etc. the commonly employed magneto-plasmonic nanoparticle synthesis methods might hinder application of these nanoparticles for SERS.

Conventional chemical synthesis methods for obtaining magneto-plasmonic nanoparticles involve several steps and contain a number of additional reagents, solvents, catalysts and merging polymers[108,109,111] and create various by-products.[117] These additional chemical components sometimes interfere with the SERS signal from sample molecules and generate spectral residues.[49] The surfactants that coat nanoparticles and ensure stability can also produce spectral residues.[47,48]

The need for alternative nanoparticle production methods arises from the desire to reduce the use of excess chemical components, produce high-purity nanoparticles and simplify synthesis methods for application in SERS. One of these methods is direct laser-ablation.[117,118] This method ensures the production of chemically clean nanoparticles. PLAL is a prevalent method for producing these nanoparticles.[114,119] It involves directing a pulsed laser onto a solid target submerged in a liquid. The appeal of PLAL lies in its chemical cleanliness and the absence of a need for additional reagents.[120]

Using solid targets composed of Au and Fe, magneto-plasmonic Fe/Au alloy nanoparticles can be effectively produced through ablation in solvents like ethanol[121] and acetone.[122,123] The process of creating alloy and core-shell nanoparticles *via* the ablation of layered films has been explored by Amendola et al.[118] It has been observed that ablation with nanosecond-duration lasers results in a greater proportion of core-shell nanoparticles compared to ablation with picosecond lasers. This is attributed to the differing durations of interaction between the laser radiation and the plasma plume generated during

the ablation process. In recent studies, researchers have also shown that Fe/Au nanoparticles can be synthesized by employing laser ablation on a bulk alloy target. This method allows for the control over the nanoparticle composition and size, contributing to the advancement of nanotechnology applications.[121]

The configuration of these nanoparticles can vary, presenting either a noble metal shell with a magnetic core or the reverse arrangement.[108,111] In case of chemical synthesis methods other configurations might occur.[108,109,112] The successful incorporation magneto-plasmonic nanoparticles produced by the PLAL method for application in SERS have been reported by Amendola group.[121,124]

2.1.2. Methods

Target preparation. Ablation targets were prepared by sequentially magneto sputtering Fe and Au layers on the thin soda-lime glass surface. Different layer composition was obtained: Fe50/Au150, Fe100/Au150, Fe50/Au150/Fe25, Fe50/Au150/Fe50.

Ablation. Using a picosecond Nd:YAG laser Atlantic (Ekspla, Vilnius, Lithuania) equipped with 1064 nm laser. Laser parameters were as follows: 10 ps pulse duration, 100 kHz pulse repetition rate, laser power – 5 W, and the laser fluence was ~1.3 J/cm^2. The galvanoscanner hurrySCAN (ScanLab, Puchheim, Germany) with a 160 mm focal distance focusing objective was used to scan the target inside the chamber, filled with acetone. Scanning was performed over a hatch pattern with 50 μm distance between lines and 500 mm/s scanning speed.

Substrate preparation. Substrates for SERS measurements were prepared as follows: The Nd magnet was wrapped in aluminum foil, cleaned with ethanol, dried, and immersed in a colloid of generated Au/Fe nanoparticles for 60 s. The extracted magnet was washed with deionized water and dried.

SERS measurements. The plasmonic properties of the generated nanoparticles were verified by measuring the SERS spectra of the test molecules. A 0.1 mM water solution of adenine was selected to evaluate the SERS enhancement. One drop (25 μl) of a 0.1 mM adenine solution was dripped on the previously prepared SERS substrate. Adenine molecules covered an area of ≈ 0.25 cm^2 after drying. SERS spectra were measured in a water solution containing adenine. The SERS spectra were measured using a MonoVista CRS+ spectrometer (S&I, Warstein, Germany) with an integrated optical microscope with a 100×/0.80 NA objective. An excitation wavelength of 632.8 nm was used, and the laser beam was focused on an area of

approximately 1 μm^2 on the sample. The Raman spectra of the magneto-plasmonic nanoparticle substrate were measured at a power of 0.8 mW.

Nanoparticle characterization. Nanoparticle images were obtained using scanning electron microscopy (SEM) using a dual-beam system, Helios Nanolab 650 (*Thermo Scientific*, The Netherlands), and a transmission electron microscope (TEM), FEI Tecnai G2 F20 X-TWIN (*Thermo Scientific*, The Netherlands) with EDAX (Amtek, USA) attachment providing energy dispersive spectroscopy (EDX) measurements.

2.1.3. Main results and key points

Magneto-plasmonic nanoparticle characterization. Laser ablation of layered structures was performed in deionized water, acetone, and isopropanol. Nanoparticles formed in deionized water aggregated quickly after ablation, making them unsuitable for further experiments. While isopropanol offered moderate stability, acetone proved to be the best solvent, therefore it was chosen. The instability in water is conditioned by the magnetic nature of these nanoparticles.

The hybrid nature of the magneto-plasmonic nanoparticles, ablated in acetone, was confirmed by TEM images (**Figure 2.1.1**) and EDX analysis (**Figure 2.1.2**). The TEM images reveal spherical hybrid nanoparticles with an Au core and Fe shell, alongside homogeneous nanoparticles. The size distribution of nanoparticles ablated from the Fe50/Au150/Fe25 sample was 46 ± 12 nm while the Fe50/Au150 sample showed 59 ± 28 nm. Wider size distribution and larger nanoparticles were noticed for the Fe50/Au150 sample. The EDX analysis supports the Au core and Fe shell composition, with the Fe shell thickness estimated at approximately 6 – 10 nm, aligning with our previous results.[125] Notably, the metal layer composition (whether Fe/Au or Au/Fe) does not affect the core/shell structure of the magneto-plasmonic nanoparticles. This is because during PLAL both metals are vaporized making plasma plume which forms cavitation bubble in the liquid. Within this bubble, the vaporized metals cool and condense into nanoparticles.[117]

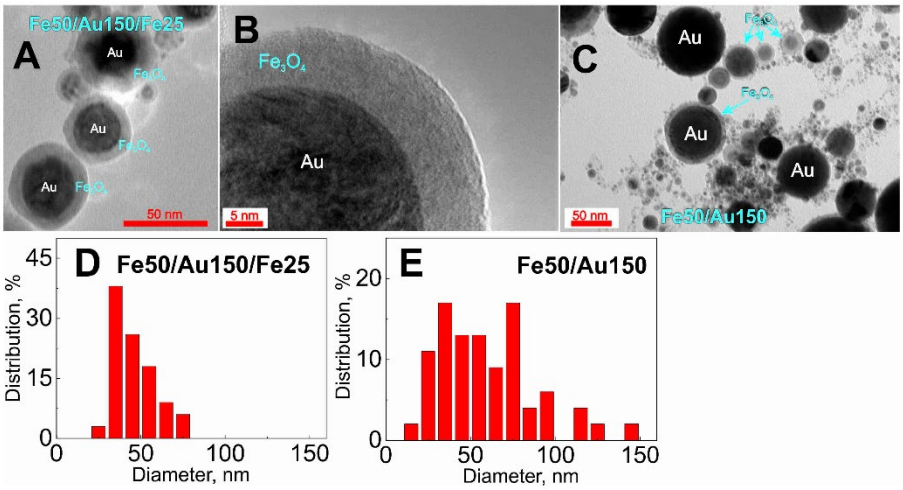

Figure 2.1.1. TEM images of magneto-plasmonic nanoparticles generated from Fe50/Au150/Fe25 target at different magnifications: 50 nm scale bar (**A**) and 5 nm scale bar (**B**) and nanoparticles from Fe50/Au150 target (**C**). The size distribution of nanoparticles is presented below: for Fe50/Au150/Fe25 (**D**) and for Fe50/Au150 (**E**).

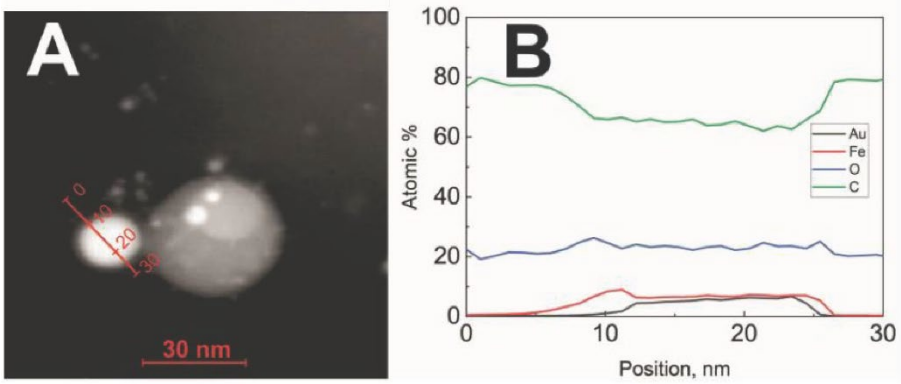

Figure 2.1.2. TEM image of the analyzed nanoparticle (**A**); EDX analysis of the composition of magneto-plasmonic core-shell nanoparticles generated from Fe50/Au150/Fe25 target (**B**).

Magnetic properties. The magnetic properties can be determined based on the nanoparticle response to a neodymium (Nd) magnet and magnetization measurements. After preparing SERS substrates by drying them under a magnetic field, SEM images (**Figure 2.1.3**) display nanoparticles on aluminum foil aligned with the magnetic field lines. The size of these nanoparticles varies up to several hundred nanometers.

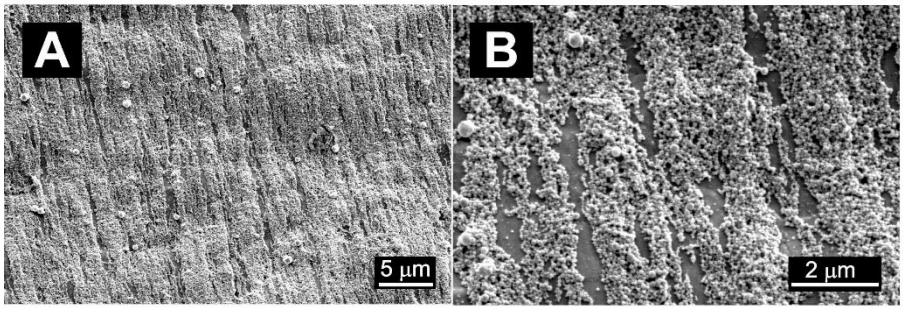

Figure 2.1.3. SEM images of magneto-plasmonic nanoparticles (Fe50/Au150/Fe25) concentrated by a magnetic field on an aluminum foil substrate. Two magnifications are presented: a scale bar of 5 µm (**A**) and 2 µm (**B**).

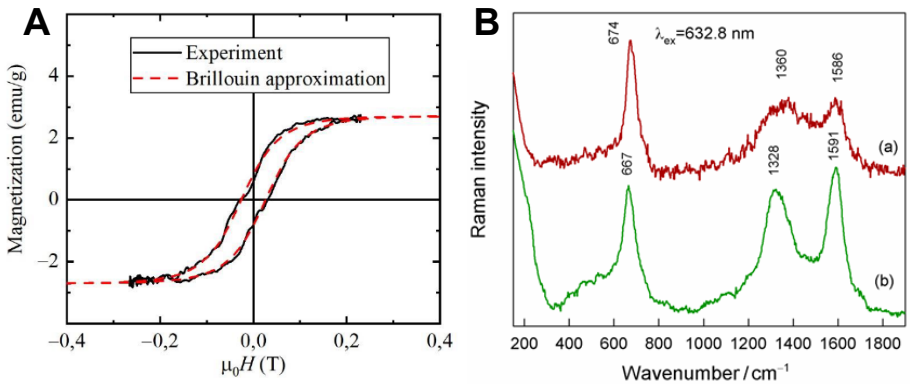

Figure 2.1.4. The hysteresis loop of the laser ablated magneto-plasmonic nanoparticles (Fe50/Au150/Fe25) (black), approximation with Brillouin function (red) (**A**) and Raman spectra of nanoparticles prepared by laser-ablation from (a) Fe50/Au150/Fe25 and (b) Fe50/Au150 films (**B**). Intensities are normalized to the intensity of the Fe_3O_4 band near 674/666 cm^{-1}. The excitation wavelength is 632.8 nm (0.8 mW).

Furthermore, we conducted magnetization studies on the synthesized nanoparticles using a pulsed magnetic field, with a duration of about 4 ms and a strength of up to 0.5 T. The results revealed the weak magnetic properties of the sample, with coercivity at approximately 26 mT, saturation of mass magnetization near 2.7 emu/g, and remanent magnetization around 1 emu/g (**Figure 2.1.4 A**). The magnetization calculations, which include the mass of the gold component, account for the low residual magnetization.[113] The weak magnetization is primarily due to gold's diamagnetic nature and its comparatively high concentration in the nanoparticles. This characteristic is advantageous for SERS applications, as the thin Fe outer layer is unlikely to significantly reduce the SERS signal of analytes. The high coercivity observed

is linked to the presence of larger nanoparticles, specifically in the 200 – 300 nm range, confirming a broad size and composition distribution.

Spectral properties. The Raman spectra of the bare Fe50/Au150/Fe25 and Fe50/Au150 samples reveal the presence of magnetite (Fe_3O_4) as shown in **Figure 2.1.4 B**. Magnetite can be identified by the band at 667 – 674 cm^{-1} associated with the symmetric stretching vibration of Fe–O bonds.[126] Importantly, no bands characteristic of maghemite (γ-Fe_2O_3 identified by broad peaks at 350, 500, and 700 cm^{-1}) or hematite (α-Fe_2O_3 identified by intense and narrow bands at 412 and 290 cm^{-1}) are visible in the spectrum.[127] The broad spectral features around 1586 – 1591 and 1328 – 1360 cm^{-1} represent the G and D vibrational bands of carbon materials, respectively.[128,129] These bands are resonantly enhanced, indicating that even minimal carbon content can yield pronounced Raman signals. This carbon likely formed during the laser ablation process in acetone solvent [126]. No link was found between intensities of the carbon bands and the composition of the laser-ablated targets. The more pronounced magnetite band in the Fe50/Au150/Fe25 sample is attributed to the initially higher iron content in the target.

SERS measurements of adsorbed adenine. Finally, plasmonic properties were ascertained by measuring SERS spectra of 0.1 mM aqueous solution of adenine adsorbed on the magneto-plasmonic nanoparticle substrates (**Figure 2.1.5**). Since the best SERS performance was obtained from dual Fe100/Au150 and Fe50/Au150 samples, only these SERS spectra are presented. Less intense adenine bands were visible using other nanoparticle samples. Comparison of SERS obtained from magneto-plasmonic nanoparticles *vs* pure Au nanoparticles reveal difference of relative adenine bands.

This indicates that adenine molecules absorb onto the magnetite surface of the magneto-plasmonic nanoparticles. The prominent spectral band at 736 cm^{-1} is identified as the ring breathing mode. The distinct SERS band, ranging from 1454 – 1464 cm^{-1}, was assigned to the ν(N1–C6) + β(C2H) + ν(C2–N3) + δ(NH2) vibrational mode. A notable frequency shift of this band from 1454 on Au cm^{-1} to 1464 cm^{-1} on magneto-plasmonic nanoparticles suggests the NH_2 interaction with the magneto-plasmonic nanoparticle surface. Low-frequency SERS analysis (**Figure 2.1.5 B**) reveals insights of adenine bonding with nanoparticles. Adenine adsorbed on laser-ablated Au nanoparticles exhibits a broad band at 200 cm^{-1}, while on magneto-plasmonic nanoparticles, a band at 295 cm^{-1} and a feature near 218 cm^{-1} are present. We indicate these features to N–Fe_3O_4 bonding. These findings are corroborated by Density Functional Theory (DFT) studies (presented in the **I publication**),

which also predict two low-frequency modes of adenine adsorbed on the magnetite surface (between 150 – 216 cm^{-1} and 243 – 263 cm^{-1}). The aforementioned spectral band at 1464 cm^{-1} was predicted to shift by 14 cm^{-1} upon adsorption on magnetite and by 22 cm^{-1} on Au, with observed shifts of 19 and 29 cm^{-1}, respectively. A significant blueshift was calculated for the 941 cm^{-1} band (associated with rocking NH_2 vibration) of adenine adsorbed on both Au (by 31 cm^{-1}) and magnetite (by 37 cm^{-1}) surfaces, with an experimental observation of 25 cm^{-1}.

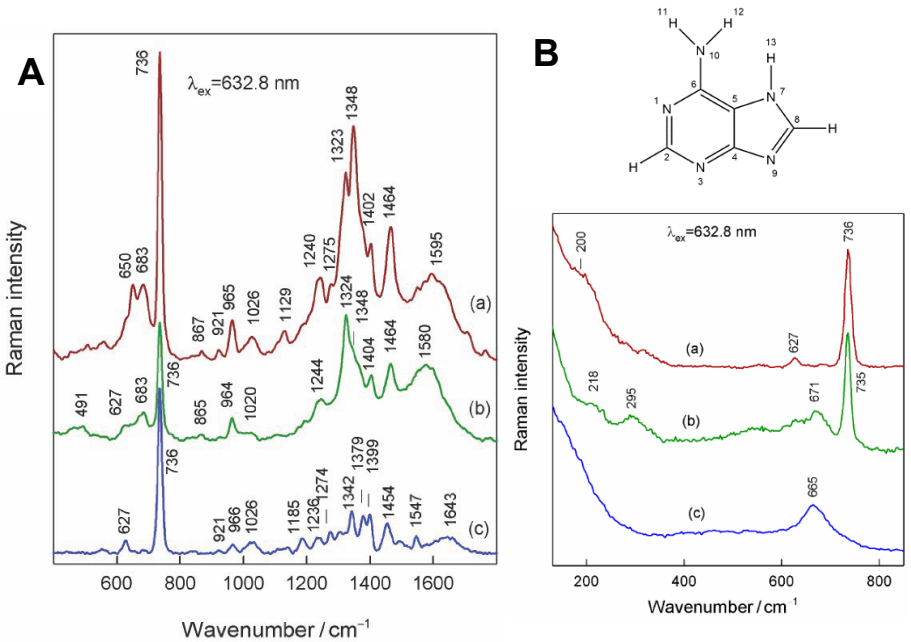

Figure 2.1.5. SERS spectra of 0.1 mM aqueous solution of adenine on magneto-plasmonic nanoparticle substrate and on gold nanoparticle substrate produced by laser ablation of (a) Fe100/Au150, (b) Fe50/Au150, and (c) bulk Au target (**A**). SERS spectra in the low-frequency region (130 – 850 cm^{-1}) (**B**). The excitation wavelength is 632.8 nm (2.5 mW).

SERS enhancement factor. The EF for the SERS substrate with Fe100/Au150 sample coating, using 4-mercaptobenzoic acid (4-MBA) as the reporter molecule, was calculated for a 632.8 nm excitation wavelength. The 4-MBA molecule was chosen because it forms a monolayer on the surface of gold nanoparticles. The resulting EF value was 5.8 (±2.8) × 10^4 for the 633 nm wavelength (**Figure 2.1.6**). The EF for adenine was also assessed but not included in publication due to complexities. It is challenging to accurately assess the concentration of adenine, confirm monolayer adsorption, and rule out the incidental formation of hot-spots. These factors can complicate the

calculation of EF. Nonetheless, the analytical EF in this case was calculated: Fe100/Au150 – 8.94×10^4; Fe50/Au150 – 3.44×10^4; Fe50/Au150/Fe25 – 3.76×10^4.

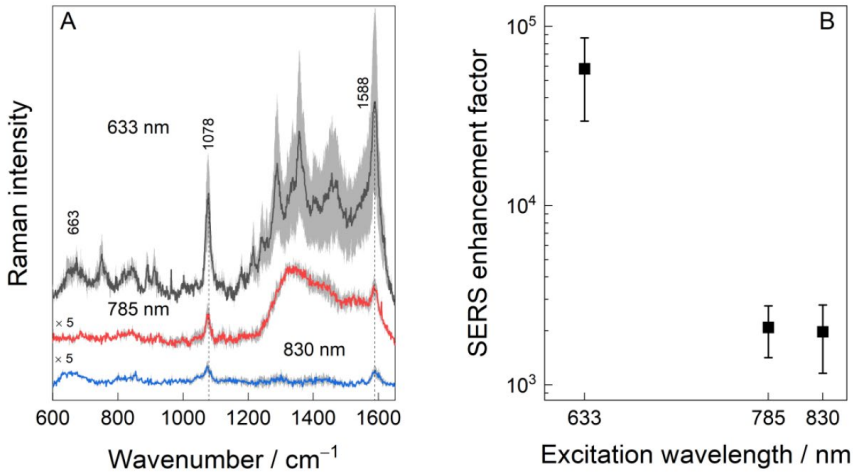

Figure 2.1.6. SERS spectra of 4-MBA molecule obtained using magneto-plasmonic nanoparticles at 633, 785, and 830 nm laser radiations (**A**). Shaded areas represent the standard deviation from 9 measurements. SERS enhancement factors calculated for different laser excitations (**B**).

Key points:

- The Fe-shell and Au-core nanoparticles are produced by the PLAL method, involving target ablation in acetone, resulting in a broad size and composition distribution.
- Hybrid magneto-plasmonic nanoparticles exhibit weak magnetic properties, with remanent magnetization around 1 emu/g, attributed to the high amount of Au in the nanoparticles.
- Raman spectra of magneto-plasmonic nanoparticles are characterized by wide D and G spectral bands at 1586–1591 cm^{-1} and 1328–1360 cm^{-1}, respectively and a magnetite spectral band at 667–674 cm^{-1}.
- The EF was calculated to be 5.8 (±2.8) × 10^4 for 4-MBA molecules using a 633 nm excitation wavelength.
- Based on SERS spectra and DFT calculations adenine adsorbs onto the magnetite shell of magneto-plasmonic nanoparticles; this can be distinguished from adsorption on Au surface *via* spectral markers: low-frequency bands at 295 cm^{-1} and 218 cm^{-1}; the redshift of the 1483 cm^{-1} band to 1464 cm^{-1} (less than on the Au surface).

2.2. Signal Enhancement Using Two-dimensional MXene Substrate for SERS Application

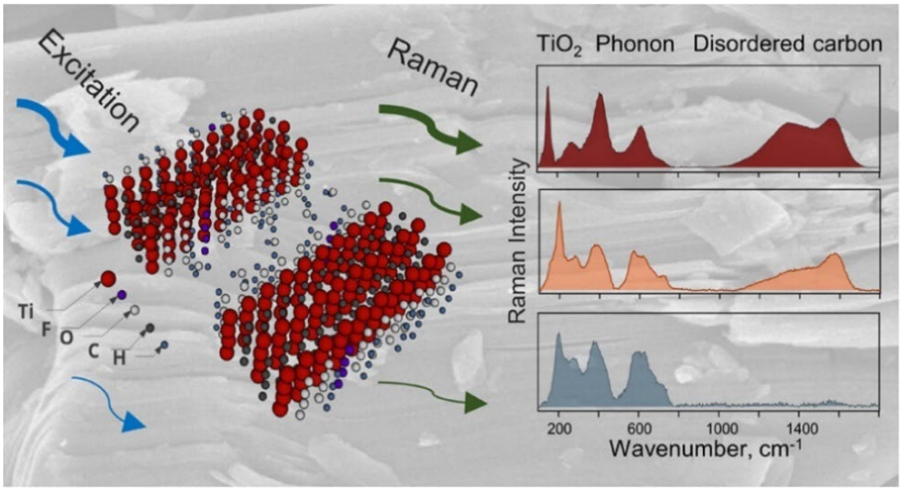

In this subsection results from the **II** and **III publications** are presented addressing the second thesis assignment and supporting the second key statement for defense. The primary objective of this study was to explore the potential of $Ti_3C_2T_x$ MXene in SERS spectroscopy. Study focused on the interaction between MXene and salicylic acid, where an enhancement in the spectral bands of salicylic acid, especially those corresponding to out-of-plane vibrational modes was observed. This enhancement is attributed to the chemical mechanism of the $Ti_3C_2T_x$ MXene, indicating the possibility for MXene to serve as a two-dimensional sensor with chemical enhancement capabilities. Such sensors typically offer greater selectivity for target molecules and more consistent signals.

Furthermore, other study highlighted the effectiveness of Raman spectroscopy in identifying the degradation mechanisms of $Ti_3C_2T_x$ MXene, providing essential insights for the creation of more efficient and reliable sensor devices within this material family.

2.2.1. Motivation

MXenes, a novel class of two-dimensional materials, have been on the rise since the unveiling of $Ti_3C_2T_x$ in 2011.[130] These materials, which include carbides, nitrides, oxycarbides, and carbonitrides of transition metals, follow the formula $M_{n+1}X_nT_x$ (where n = 1, 2, 3 or 4, M depicts a transition metal, e.g., Ti, V, Nb, Mo; X represents C and/or N (O substitution is possible); T_x – surface functional groups, e.g., –OH, –F, =O, etc.). MXenes are produced by etching out the 'A' element from their MAX phase precursors, leading to the release of two-dimensional MX layers. These layers are then isolated through intercalation or sonication to produce individual two-dimensional MXenes. $Ti_3C_2T_x$, in particular, is distinguished for its cost-effective production, high conductivity, hydrophilicity, and redox-active surfaces.[131–133] Further investigations are also directed toward efficiently producing different MXene types that can yield defect-free two-dimensional MXene layers.[132,134]

MXenes are interesting and widely investigated materials partly due to their extensive applicability in various sectors. This includes energy storage[133,135] and conversion technologies,[131,135,136] as well as creation of sensors,[137–143] electronic parts,[144,145] and various nanocomposites.[133] The sensitivity of MXene to environmental and structural changes makes it an excellent sensor material. It can either operate independently as a sensor[137–140] or be incorporated as an essential element within nanocomposites designed for sensing purposes.[139,141–143] The unique optical,[146] electronic,[135] and chemical characteristics[147] of MXene are influenced by structural modifications, such as changes in the oxidation state of the material[135,146,148] and the incorporation of amorphous carbon or TiO_2 nanoparticles.[149–151] Importantly, MXenes exhibit metal-like properties, due to a high density of charge carriers.[152–155] The concentration of free charge carriers in $Ti_3C_2T_x$ MXene is reported to be 2×10^{21} cm^{-3},[156] compared to approximately 6×10^{22} cm^{-3} in noble metal nanoparticles[157] and 3×10^{13} cm^{-2} in graphene.[158,159] The concentration of free electrons in MXene induces a plasmonic effect as plasmon frequency is dependent on electron density.[157] Generally, materials exhibit plasmonic activity due to the real and negative part of the dielectric function, which is observed in the near-infrared range for MXenes. This suggests that surface plasmons in MXenes are excited at longer (NIR) wavelengths.

To date, enhanced resonance Raman spectra have been observed for dye molecules like rhodamine 6G, crystal violet, methylene blue, and malachite green,[160–162] which absorb within the excitation range and are adsorbed onto $Ti_3C_2T_x$ MXene surface. Enhancement has also been observed for non-

absorbing molecules.[160,163] This enhancement is primarily attributed to a chemical mechanism stemming from the energy level coupling between the MXene and the target molecules.[160,161,163]

Furthermore, it has been established that certain molecules, when complexed with $Ti_3C_2T_x$ MXenes, engage in charge transfer.[164,165] Our findings indicate that the interaction between salicylic acid and $Ti_3C_2T_x$ MXene leads to a chemical enhancement in SERS, facilitated by charge transfer. This interaction particularly amplifies asymmetric vibrational modes, as evidenced in the salicylic acid adsorbed on MXene, where the less symmetric out-of-plane vibrations are significantly enhanced.

Overall, the chemical enhancement mechanism typically results in a modest increase, not surpassing two orders of magnitude.[80] Sensors utilizing this mechanism are expected to be more specific and exhibit uniform signal intensity. The phenomenon of hot-spots in SERS substrates, where intensity significantly varies across different sample spots, is due to the electromagnetic enhancement mechanism. This occurs when the analyte molecule is positioned between two nanoparticles. The chaotic arrangement of these hot-spots leads to fluctuations in the absolute intensity of the SERS bands. Conversely, the chemical enhancement mechanism contributes to a more homogeneous substrate, resulting in minimal variation in the intensity of the Raman bands.[80]

Although $Ti_3C_2T_x$ MXene has shown potential for use as sensors in various molecule detection and analysis applications, particularly in SERS sensors, it also exhibits sensitivity to exposure to temperature, oxygen, water, etc.[149,153,166–168] Therefore, spectral markers for MXene lattice alterations themselves are as important as spectral markers for target molecule detection to gain an in-depth understanding of MXene lattice disruptions.

2.2.2. Methods

Synthesis of $Ti_3C_2T_x$ MXene substrates. Two different synthesis methods were employed for multilayered and single-layered $Ti_3C_2T_x$ MXene. Multilayered MXene was prepared by etching 0.1 g of Ti_2AlC_3 MAX phase in 10 mL of 5 wt. % hydrofluoric acid solution. Solution was stirred for 24 h at 25 °C temperature. After this step, the solution was centrifuged until the pH of solution became neutral.

For single-layered $Ti_3C_2T_x$ MXene, 0.1 g of Ti_3AlC_2 was etched in 9 M HCl with 1 g LiF, stirred at 200 rpm for 48h at 35°C. Centrifugation was repeated until a dark supernatant indicated delamination, single-layered MXene was then collected. Substrates for lattice degradation study were

prepared by drop-casting 0.01 g/mL single-layered MXene solution on microscope glass. Finally, the multilayered and single-layered MXene films on a microscope glass slide were prepared for SERS measurements.

Characterization of $Ti_3C_2T_x$ MXene samples. The $Ti_3C_2T_x$ MXene were assessed using a Helios Nanolab 650 SEM (FEI, Netherlands), which is equipped with an EDX spectrometer X-Max (Oxford Instruments, Abingdon, U.K.). Furthermore, the crystalline structure was assessed through X-ray Diffraction (XRD) analysis. This was performed with a MiniFlex II diffractometer (Rigaku, Tokyo, Japan), utilizing Ni-filtered Cu Kα radiation. The analysis was conducted in a Bragg-Brentano (θ/2θ) configuration, scanning a 2θ range from 5 to 60°. The increments were set at a step width of 0.02°, and the sweep progressed at a rate of 1° per minute.

Visible – near-infrared (Vis-NIR) absorption spectra were acquired with dual-channel Lambda 1050 spectrometer (PerkinElmer, USA) in the range 350 – 2300 nm with 5 nm resolution.

MonoVista CRS+ Raman microscope system (S&I GmbH, Germany) equipped with four excitation lasers (457 nm, 532 nm, 633 nm and 785 nm) and a liquid nitrogen cooled CCD detector was used for acquiring the spectra. Diameter of the focused laser beam on the sample was ≈ 1 μm and its power density on the sample was ≈ 20 kW/cm^2 (for 633 nm excitation) and ≈ 45 kW/cm^2 (for 785 nm excitation), unless stated otherwise. Before the measurements, the spectrometer was calibrated to a fundamental vibrational band at 520.7 cm^{-1} of silicon wafer. Fourier transform MultiRAM spectrometer (Bruker, Germany) equipped with liquid-nitrogen-cooled Ge diode detector was used for the calculations of enhancement factor for salicylic acid adsorbed on $Ti_3C_2T_x$ MXene with 1064 nm excitation wavelength.

SERS measurements of salicylic acid adsorbed on MXene film. Solution of salicylic acid in water with concentration equal to 2 mM was prepared. Two drops (5 μl each) of the solution were dried on the glass substrate covered by the $Ti_3C_2T_x$ MXene film. Presented SERS spectra of salicylic acid were recorded on 20 randomly chosen positions on the MXene surface and averaged. The standard deviation for the spectral intensity of salicylic acid on MXene substrate was calculated while applying 3 s acquisition time.

Computational study. Theoretical calculations of structure and vibrational spectra of crystalline salicylic acid were performed by means of quantum chemistry calculations implemented in Gaussian 09W software package. The salicylic acid dimer was chosen to resemble the crystalline structure of solid-state salicylic acid. The DFT calculations using

B3LYP/6311++G functional were performed. For the investigation of the salicylic acid–MXene complex, the 2 × 2 × 1 supercell expansion of $Ti_3C_2(OH)_2$ MXene crystal structure (of 20 atoms) was built and optimized. Initially geometry optimization was performed separately for salicylic acid (B3LYP/6311++G) and $Ti_3C_2(OH)_2$ cluster (B3LYP/LanL2DZ) and for their complex afterwards (B3LYP/LanL2DZ). No virtual frequencies were present after the complex optimization. Time-dependent density functional theory (TD-DFT) excited-state calculations using the B3LYP/LanL2DZ level of theory were performed to assess the redistribution of electronic energy levels and predict the Vis-NIR absorption spectra.

2.2.3. Main results and key points

Assessment of successful $Ti_3C_2T_x$ MXene synthesis was confirmed using SEM and EDX analysis. SEM images reveal stacked lamellar structures within the multilayered $Ti_3C_2T_x$ MXene (see **Figure 2.2.1 A** and **2.2.1 B**). The etching process using a 5 wt.% HF solution resulted in the formation of multilayered MXene whose structure closely resembles that of the MAX phase, albeit with slightly separated MXene layers. Different etching process using 9 M HCl with 1 g LiF, produced single-layered $Ti_3C_2T_x$ MXene flakes, as depicted in **Figure 2.2.1 C** and **2.2.1 D**.

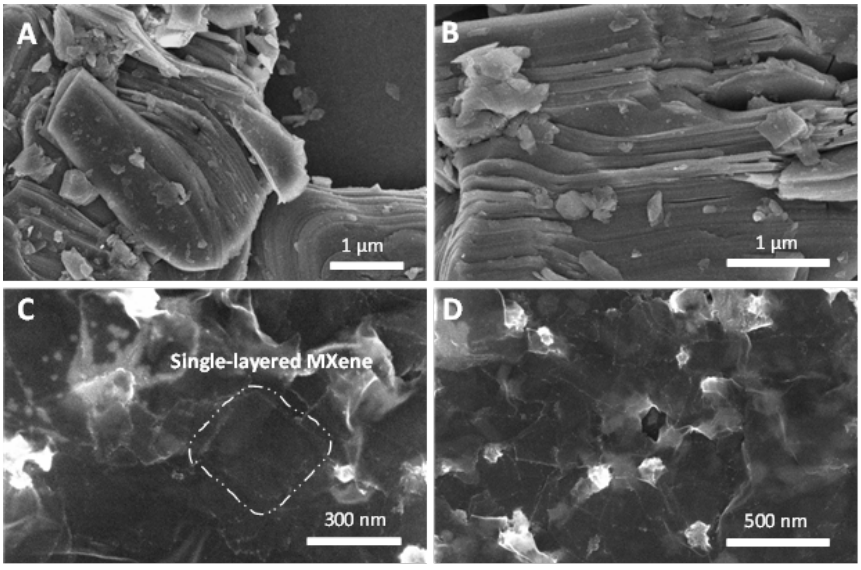

Figure 2.2.1. SEM images of multilayered powder (**A, B**) and delaminated single-layered films of (**C, D**) $Ti_3C_2T_x$ MXene.

Confirmation of MXene synthesis *via* XRD analysis was provided as depicted in **Figure 2.2.2 B** Notably, the (002) peak of Ti_3AlC_2 (MAX phase) exhibits a significant shift from 9.5° to 7.3° in the $Ti_3C_2T_x$ samples. The presence of a distinct and sharp (002) peak is a recognized signature of MXene.[169] The distinction between multilayered and single-layered MXene is marked by the (002) peak shifting to 7.0° for the former and 7.1° for the latter. The XRD pattern for multilayered MXene, shown in **Figure 2.2.2 B**, closely resembles the MAX phase between 33° to 44°, which may suggest that the etching or washing was not fully completed. In contrast, the single-layered MXene shows two extra diffraction peaks at 38.7° and 45°, consistent with the standard XRD data for LiF (00-004-0857), indicating that some LiF remains after the washing process. This LiF is concentrated at the top of the sample (as visible from EDX analysis in the Supporting Information of the **III publication**). This is likely due to the complete etching of the single-layered samples but incomplete washing out of the LiF remnants. LiF does not produce a Raman signal and does not interfere with our further study.

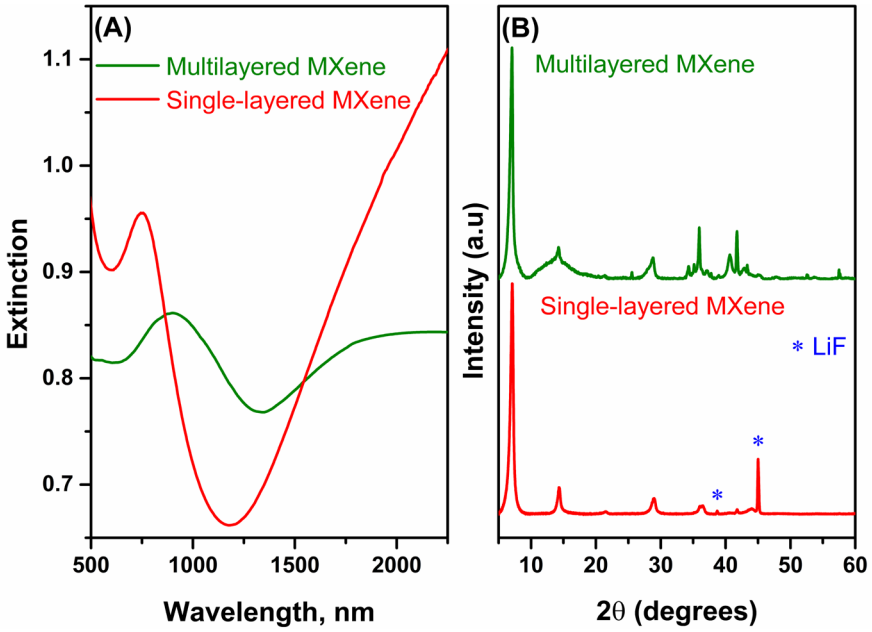

Figure 2.2.2. Comparison between the multilayered and single-layered MXene samples. (**A**) Vis-NIR absorption spectrum and (**B**) XRD patterns of multilayered and delaminated single-layered MXene.

The single-layered MXene Vis-NIR spectrum displays an extinction band at approximately 750 nm (equivalent to 1.65 eV) with a full width at half maximum of 195 nm (**Figure 2.2.2 A)**. The origin of this spectral band is

attributed to an interband transition of delaminated MXene.[144,170–173] MXene is supposed to have plasmon resonance but plasmonic activity results from the real part of the dielectric function. This occurs only in the near-infrared range, implying that surface plasmons may be excited at longer wavelengths.[172,173] Typically, plasmonic and electronic transition overlap results in a broad plasmon resonances, which may be the case for $Ti_3C_2T_x$ MXene.[54,174] Multilayered MXene shows reduced extinction in this domain, likely due to its lower charge-carrier density and distinct surface functional groups compared to single-layered MXene.

Based on Vis-NIR, SEM, and XRD analyses, $Ti_3C_2T_x$ MXene was successfully produced from the Ti_3AlC_2 precursor, and the resulting properties and composition of MXene differ across different synthesis/etching routes.

Raman investigation of MXene. Raman spectroscopy might yield insightful details regarding the composition of MXene films.[153,166,175–178] The positions of Raman spectral bands primarily result from vibrations of the $Ti_3C_2T_x$ lattice and surface groups.[153,175,176] By examining spectral changes, we can distinguish different surface groups[175,176,179,180] that might determine the interactions with target molecules and MXene lattice decomposition byproducts such as amorphous carbon and TiO_2 nanoparticles.[176–178] The emergence of these byproducts may be attributed to factors such as intense laser power exposure,[146,176] thermal processes, or anticipated chemical reactions.[149,153,166–168] Notably, the detected markers are instrumental in pinpointing both the byproducts and the underlying mechanisms at play in MXene-based SERS sensors.

Raman spectra of an $Ti_3C_2T_x$ MXene film on a glass plate were obtained using different excitation wavelengths: 457, 532, 633, and 785 nm (**Figure 2.2.3 A**). When comparing the Raman spectra of single-layered MXene collected using different excitation wavelengths, notable changes are observed primarily under pre-resonance conditions. The spectrum obtained with 785 nm excitation differs due to the appearance of new bands. The appearance of new spectral bands can be explained by the resonant condition of excitation (extinction band, arising from interband transition, at 750 nm is visible in Vis-NIR spectrum of MXene – **Figure 2.2.2**). These include the band at 122 cm^{-1} ('skeleton vibration', which is associated with the in-plane vibrational mode of all atomic groups), 513 cm^{-1} (associated with the out-of-plane ω_6 mode of $Ti_3C_2(OH)_2$), and 722 cm^{-1} (associated with the out-of-plane ω_3 mode of mainly $Ti_3C_2O_2$) bands.[179,180]

$Ti_3C_2T_x$ MXene has been shown to exhibit sensitivity to exposure to radiation,[146,176] oxygen, water, etc.[149,153,166–168] Consequently, spectral markers for MXene lattice alterations were investigated through photo-induced lattice

degradation, in search of related markers. Such markers are important for gaining an in-depth understanding of MXene lattice disruptions or possible interactions with target molecules. Subtle changes in MXene lattice composition were observed at lower laser power densities of 60 – 160 kW/cm^2 (for Figures concerning photo-induced and heat-induced degradation, refer to the **III publication**). I) Initially, a blueshift in the 200 cm^{-1} band was detected, signaling the reduction of interlayered molecules, including water. II) As the power density escalated, a notable blueshift in the 370 cm^{-1} band occurred. This suggests a diminishing presence of –(OH) surface groups, a hypothesis observed in other studies as well. III) Concurrently, a redshift in the 620 cm^{-1} band emerged at higher power densities, indicative of oxidation processes. Oxidation is also indicative by the initial blueshift of the 370 cm^{-1} band, although it manifested solely at lower power densities. These spectral markers indicate changes in surface groups, allowing us to pinpoint when these changes initiate. The apparent signs of substantial lattice degradation can be observed by the IV) appearance of D and G carbon bands due to the formation of C–C bonds (over 160 kW/cm^2) and V) the formation of TiO_2 nanoparticles (over 390 kW/cm^2).

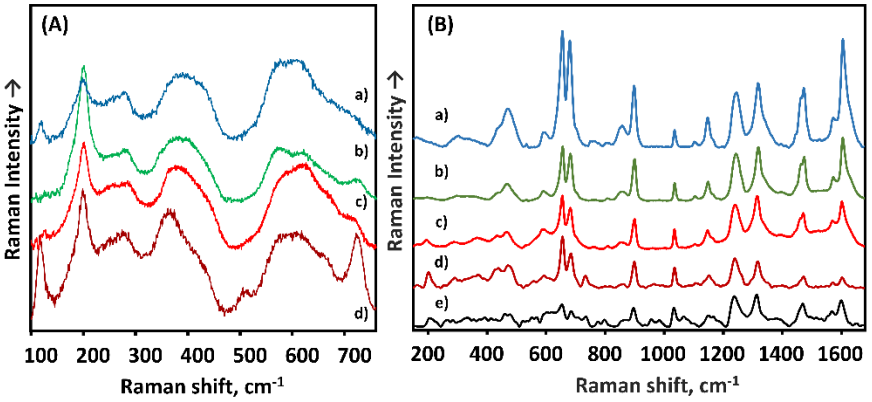

Figure 2.2.3. Raman spectra of single-layered $Ti_3C_2T_x$ MXene (**A**) and salicylic acid adsorbed on MXene (**B**) obtained with different excitation wavelengths: 457 nm (a), 532 nm (b), 633 nm (c), 785 nm (d), 1064 nm (e).

At excitation powers reaching 160 kW/cm^2, the formation of amorphous carbon and hydrocarbons is initiated. This is evidenced by the presence of broad G and D bands, observable at 1582 cm^{-1} and 1396 cm^{-1}, respectively. The G band is indicative of C-C bond vibrations within all sp^2-hybridized carbon structures, whereas the D band is characteristic of disordered carbon ring systems.[181] The culmination and most rapid phase of MXene degradation

is marked by the creation of TiO_2 nanoparticles, a process that was detected at an excitation power density of 390 – 550 kW/cm^2. The TiO_2 that evolves from MXene manifests in two distinct crystalline forms: anatase and rutile.[182–184] The anatase variant emerges initially, owing to its lower energy formation threshold. This anatase form is discernible by a pronounced band at 154 cm^{-1}, corresponding to the E*g* vibrational mode, a definitive signature of this crystal structure.[182–184] Due to this, lasers with considerably low excitation power (≈ 20 kW/cm^2) were used when measuring the spectra of salicylic acid adsorbed on MXene. For a comprehensive overview of $Ti_3C_2T_x$ MXene bands and their tentative assignments, refer to **Table 2.2.1**.

Table 2.2.1. Experimentally observed Raman bands of single-layered and multilayered $Ti_3C_2T_x$ MXene.

Vibrational frequency, cm^{-1}				MXene type[179,180]
Single-layered		Multilayered		
633 nm	785 nm	633 nm	785 nm	
122	122[a]	122	123[a]	complex[179]
154	154	154	154	-
200	201	211	210	complex[179]
256	258	258w	258	$Ti_3C_2F_2$[179,180]
283	283	284	283	$Ti_3C_2(OH)_2$[179]
372	372[a]	370	371[a]	complex[180]
450	-	452	-	$Ti_3C_2(OH)_2$[179]
511	513[a]	505w	512[a]	$Ti_3C_2(OH)_2$[179]
590	584	590	585	$Ti_3C_2O_2$[179,180]
626	617	621	616	complex[180]
667	667	667	668	$Ti_3C_2(OH)_2$[179,180]
712	722[a]	734	737[a]	$Ti_3C_2O_2$[179]
1396	1396	-	-	
1582	1582	1562	1561	

[a] Increased intensity in spectral band compared to 633 nm excitation.
[W] Not prominent or weak band.
complex – two or more different MXene types.

SERS spectra of salicylic acid on $Ti_3C_2T_x$ MXene. The SERS activity of $Ti_3C_2T_x$ MXene was noticed for salicylic acid molecule. It is noteworthy that a similar interaction of salicylic acid with MXene occurred in both multilayered and single-layered forms. However, the single-layered MXene demonstrated a superior enhancement effect, likely attributable to the greater surface area available for interaction. Therefore, further study was performed with single-layered $Ti_3C_2T_x$ MXene.

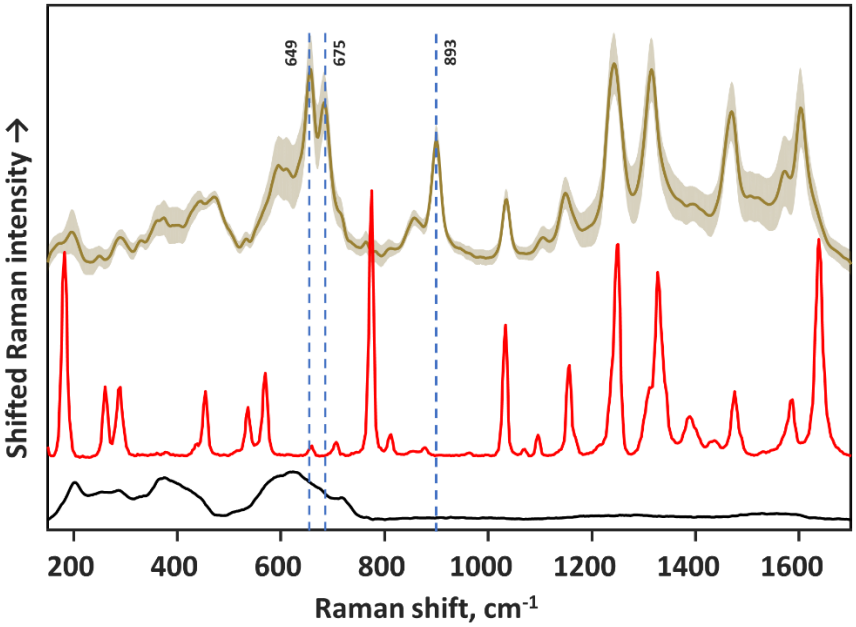

Figure 2.2.4. Raman spectra of MXene film (bottom) and salicylic acid: dried on MXene surface (middle) and on aluminum foil (top). Excitation wavelength – 633 nm.

Table 2.2.2. Vibrational frequencies of crystalline salicylic acid and salicylic acid adsorption upon $Ti_3C_2T_x$ Mxene.

Vibrational frequency, cm^{-1}		Assignment
Crystalline salicylic acid	**Salicylic acid on MXene**	
180	-	δ_{oop}(C-COOH)
258	-	δ_{ip}(C-COOH)
286	-	δ_{ip}(C-OH)
452	-	δ_{ip}(C-COOH)
-	473	δ_{oop}(ring)+ δ_{oop} (OH)
534	-	δ_{oop}(ring)
568	-	δ_{oop}(O-H)[a] + δ_{oop}(ring)
-	595	δ_{ip}(C-C, ring)+ δ_{oop}(OH)
657	654↑	δ_{ip}(-COOH) + δ_{oop}(ring)
705	681↑	δ_{oop}(ring) + δ_{oop}(O-H)[a]
773	-	δ_{ip}(C-H)[a] + 6[c]
850	861	ν(C-OH)[b]+ δ_{ip}(ring)
876	896↑	δ_{oop}(C-H); 17[c]
1031	1031	18[c]
1093		δ(O-H)[b]
1154	1145	δ(O-H)[a]
1164	-	15[c]
1244	1232	δ(O-H)[a] + ν(C-COOH)
1307	-	δ(O-H)[a]
1325	1311	δ(C-O)[b]

Vibrational frequency, cm^{-1}		Assignment
Crystalline salicylic acid	Salicylic acid on MXene	
1386	1397	14[c] + δ(C-O)[b]
1473	1467	19[c]
1583	1567	8[c]
1636	1597↓	ν(C=O)[a]

[a] vibration of atoms in –COOH functional group; [b] vibration of atoms in –OH functional group; ↑ Increased intensity; ↓ Decreased intensity; ν Stretching vibration; δ Deformation vibration. $_{oop}$ Out-of-plane. $_{ip}$ In-plane. [c] The modes derived from benzene.[185]

After drying 2 mM concentration of salicylic acid solution on MXene film, clearly different Raman spectra were measured from the crystalline form (**Figure 2.2.3 B** and **2.2.4**). A distinct enhancement was observed for bands associated to out-of-plane vibrations at 893 cm^{-1} and a band doublet at 681 cm^{-1}, 654 cm^{-1} (**Figure 2.2.4**). For detailed investigation of vibrational modes DFT calculations were performed for monomeric salicylic acid molecule and salicylic acid dimer (as in crystalline salicylic acid form)[186]. Based on calculations these newly emerged bands can be assigned to out-of-plane vibrations of –CH groups and out-of-plane ring deformations, respectively. The increased intensity of out-of-plane vibrational bands was evaluated by calculating enhancement factor. The enhancement factor reached 125, 110 and 220 for the band at 896 cm^{-1} and band doublet at 681 cm^{-1} and 654 cm^{-1}, respectively (532 nm excitation).

When salicylic acid adsorbs onto MXene, it induces redshifts in nearly all spectral bands. Notably, the C=O stretching vibrational band of the carboxylic group experiences the largest shift, moving from 1636 cm^{-1} to 1597 cm^{-1}, a change of 39 cm^{-1}. Other bands also exhibit smaller redshifts, ranging from 12 to 15 cm^{-1}. For instance, the vibrational modes of the benzene ring, initially observed at 1583 cm^{-1} and 1473 cm^{-1}, shift to 1567 cm^{-1} and 1467 cm^{-1}, respectively. The C–O stretching vibration band at 1325 cm^{-1} shifts down to 1311 cm^{-1}, while the spectral band related to the C–O deformation of the hydroxyl group shifts to 1232 cm^{-1}. Interestingly, the benzene ring mode at 1031 cm^{-1} remains unaffected by the adsorption process, as detailed in **Table 2.2.2**.

The enhancement factor for vibrational band at 654 cm^{-1} (associated with carboxyl deformation + out-of-plane C-C bending) varies with the excitation wavelength (**Figure 2.2.5**). The highest enhancement, with a factor of 220, is achieved using 532 nm excitation. Excitation at 785 nm falls within the absorption range of $Ti_3C_2T_x$ MXene, allowing the Raman spectral bands of MXene phonon modes to remain observable. For the 1064 nm excitation profile, a different FT-Raman spectrometer was utilized. In the absence of

salicylic acid, the MXene film absorbs this wavelength, generates heat, and hinders the acquisition of a spectrum. However, when salicylic acid is adsorbed onto MXene, the Raman spectrum can be obtained. This behavior suggests changes in the electron distribution of the MXene layer upon the adsorption of salicylic acid.

Absorption spectra of salicylic acid and $Ti_3C_2T_x$ MXene. Salicylic acid adsorption on MXene is also evident from Vis-NIR spectra (**Figure 2.2.6**). In a water solution of salicylic acid, absorption bands from π-π* and n-π* transitions are visible at approximately 230 nm and 300 nm, respectively.[187] In contrast, salicylic acid adsorbed on a MXene film exhibits a prominent intensity band at 400 nm, with other less distinct bands appearing at 495 nm, 595 nm, and 1080 nm (**Figure 2.2.6 B**). The observed decrease in near-infrared absorption from the MXene film is likely due to the redistribution of conduction band electrons – free charge carriers. These alterations in the absorption spectrum substantiate the formation of a new product from the salicylic acid adsorbed on the $Ti_3C_2T_x$ MXene.

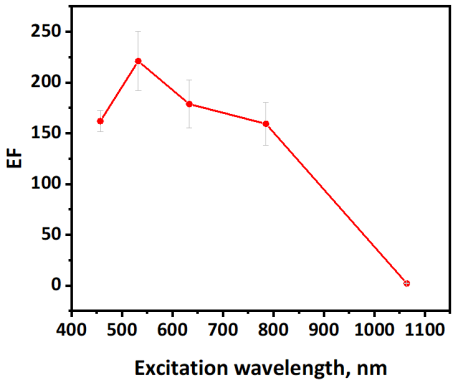

Figure 2.2.5. Calculated SERS enhancement factor (EF) for 2 mM salicylic acid dried on the $Ti_3C_2T_x$ MXene film with different excitation wavelengths.

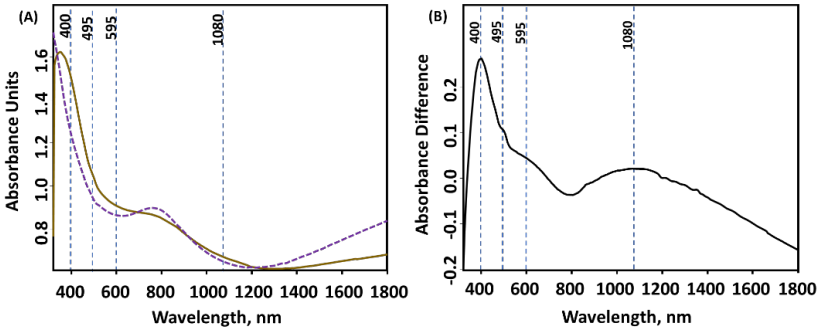

Figure 2.2.6. Vis-NIR absorption spectra of $Ti_3C_2T_x$ MXene film (dotted line) and salicylic acid (straight line) dried on the MXene (**A**); differential spectrum (**B**).

Computational results of salicylic acid and $Ti_3C_2T_x$ MXene interaction. To delve deeper into the interaction between salicylic acid and MXene, DFT based first-principal calculations were conducted using the B3LYP/LanL2DZ level of theory. The study involved constructing and optimizing a $Ti_3C_2(OH)_2$ MXene cluster and its interaction with salicylic acid molecule salicylic acid–MXene structure. The results revealed a propensity for salicylic acid to chemically bond with the titanium atoms in the $Ti_3C_2(OH)_2$ crystal through the oxygen atom of its carboxyl group. The likelihood of this complex formation is firstly confirmed by the geometric parameters of the optimized salicylic acid–MXene structure. Notably, the O–H interatomic bond length in the carboxyl group of salicylic acid expanded from 0.976 Å to 1.536 Å, while the distance between the OH–H group of the $Ti_3C_2(OH)_2$ MXene was 1.034 Å, suggesting a potential proton transfer between the salicylic acid and the MXene cluster. Additionally, the C–O bond length in the carboxyl group increased from 1.232 Å to 1.339 Å. This bond formation is consistent with the observed significant shift of 40 cm^{-1} in the C=O stretching vibrational band of the carboxylic group at 1636 cm^{-1}, and the vanishing of the salicylic acid band at 771 cm^{-1}, which corresponds to benzene ring bending and carboxyl deformation modes. The bond created between salicylic acid and the MXene cluster may facilitate electron density redistribution around both entities. Furthermore, Mulliken population analysis revealed a subtle charge redistribution, shifting from -0.32 in monomeric salicylic acid to -0.98 in the salicylic acid–MXene complex, indicating a change of -0.66.

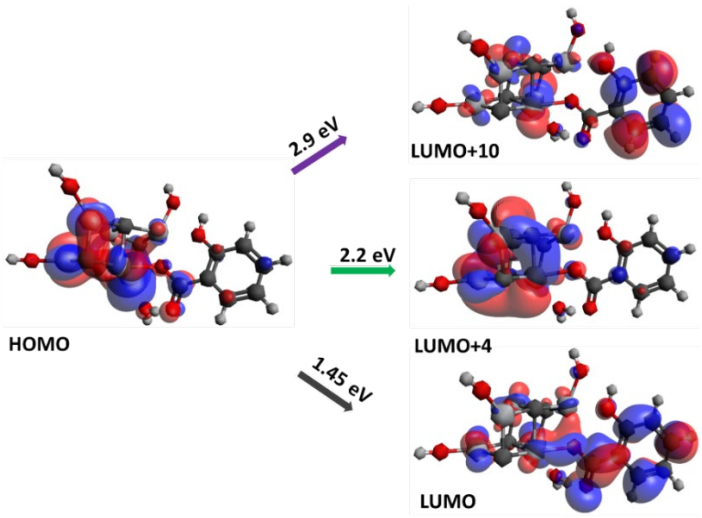

Figure 2.2.7. Calculated (B3LYP/LanL2DZ) molecular orbitals of salicylic acid–MXene complex and required transition energy.

The electron density redistribution within the highest occupied molecular orbital (HOMO) and lowest unoccupied molecular orbital LUMO molecular orbital also indicates the formation of a complex between the carboxyl group of salicylic acid and MXene (**Figure 2.2.7**). In contrast, the LUMO shows a significant electron density transfer from MXene to salicylic acid, with an energy shift of 1.45 eV. Additional charge transfer excitations are evident in the molecular orbitals at LUMO+4 and LUMO+10, with energies of 2.2 eV and 2.9 eV respectively. The calculated excitations of the salicylic acid–MXene complex align with the Vis-NIR absorption spectrum (**Figure 2.2.6**), where the most intense absorption band is at 400 nm (calculated at 428 nm), with lower intensity bands at 495 nm, 595 nm (calculated at 564 nm), and 1080 nm. Compared to the HOMO–LUMO excitation of a solitary salicylic acid molecule, the excitation energy required for the salicylic acid molecule in the complex is reduced from 4.5 eV to 2.9 eV.

Generally, the CT mechanism (and the chemisorption in most cases) is evidenced by several factors. Firstly, asymmetric vibrations are more significantly enhanced than symmetric ones, which is attributed to the B term excitation in resonance Raman spectroscopy. Secondly, the EF is highly dependent on the excitation wavelength. It is worth noting that if the A term is responsible for the resonance Raman signal, then stretching vibrations are amplified, as the totally symmetric vibrations align with the geometry of the excited state of the molecule. Typically, the bond lengths increase when the molecule is in its excited state.

Key points.

- The SERS effect of salicylic acid adsorbed on $Ti_3C_2T_x$ MXene film was observed by a significant enhancement of out-of-plane bending modes of salicylic acid at 896 cm^{-1}, a 681 cm^{-1} and 654 cm^{-1}.
- The adsorption of salicylic acid molecules on MXene is evidenced by spectral markers: the enhancement of bands at 896 cm^{-1}, 681 cm^{-1}, and 654 cm^{-1}, along with a redshift in vibrational frequencies and the disappearance of the carboxyl deformation band at 771 cm^{-1}.
- The experimental enhancement factor (220 for 532 nm wavelength) suggests that chemical mechanism predominantly contribute to the SERS spectra of salicylic acid on MXene.
- The Vis-NIR absorption spectra reveal additional bands at 400 nm, 495 nm, 595 nm, and 1080 nm following salicylic acid adsorption on MXene, consistent with DFT predictions, particularly the 400 nm band (anticipated at 428 nm), and further bands at 495 nm and 595 nm (anticipated at 564 nm) and 1080 nm.

Altogether, the adsorption of salicylic acid on MXene was confirmed experimentally by a) a significant increase in out-of-plane vibrational bands, and b) a significant redshift, c) an enhancement factor value of two orders of magnitude, d) changes in Vis-NIR spectra upon adsorption. The adsorption of salicylic acid on MXene indicates a strong interaction facilitated by the porous surface and high surface area of MXene. These characteristics are indeed advantageous for the development of SERS sensors. However, it is crucial to consider for future research that the MXene lattice may undergo changes due to the use of higher laser power. This factor should be considered when developing SERS sensors.

2.3. Signal Enhancement in Infrared Absorption-Based Remote Sensing: SEIRA Enhancement

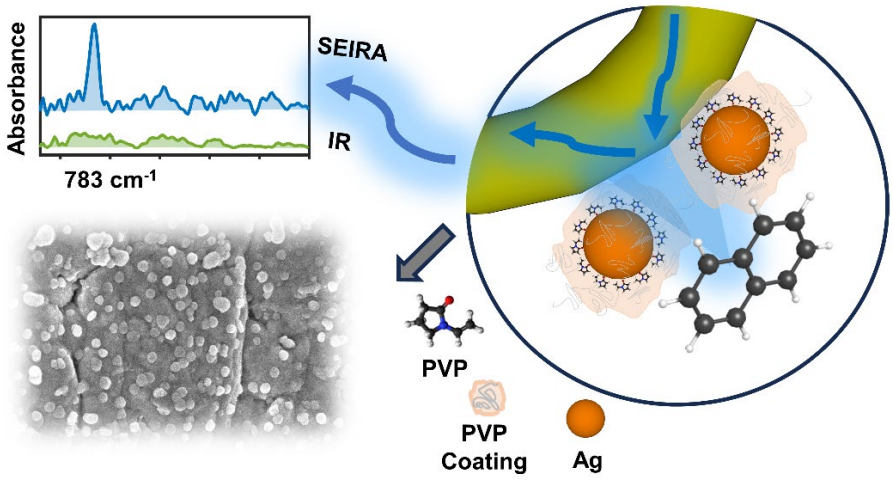

In this subsection results from the **V publication** are presented addressing the third thesis assignment and supporting the third key statement for defense. In this study, the SEIRA effect was implemented, utilizing an infrared fiber probe attachment. This technique employs replaceable silver halide PIR fiber loops, which facilitate low-cost ATR-spectroscopy.

The primary goal of our research is to expand the capabilities of SEIRA spectroscopy for both direct and remote sensing applications. By integrating the SEIRA method with fiber-based technology, we have successfully implemented a system that can operate effectively even in challenging aqueous setups. The ability to identify such a spectral signature in an aqueous environment marks a significant stride in the field of spectroscopic analysis.

2.3.1. Motivation

The motivation for our research is based on the capabilities of fiber-based spectroscopic methods, particularly advantageous for rapid and on-site environmental assessments. These techniques enable the quick acquisition of vibrational spectra, ranging from 2 to 5 minutes, with results ready instantaneously. Fiber-based ATR sensors also facilitate the in-time detection of multiple pollutants, assuming the identification of specific spectral markers are established. Utilizing silver halide fibers, ATR sensors have proven their efficacy in detecting volatile organic compounds (VOCs) down to parts per billion (ppb) in real-world conditions.[188,189] The principle of these ATR sensors is based on generating numerous internal reflections on the active surface, which then interact with the sample molecules. To further refine the process, a hydrophobic polymer layer is applied to the surface, which hinders water molecules from penetrating the active zone, thus allowing only the VOCs of interest to come into proximity to the sensor.

Although SEIRA-based detection of naphthalene is novel to our knowledge, SERS-based detection has been documented in various studies.[190–194] Previous SERS research has shown remarkable sensitivity in detecting naphthalene, with limits as low as 10 ppb using ligand-functionalized mesoporous Au nanoparticles,[190] approximately 6 ppm using colloidal nanoparticles;[192] and 1 ppm (parts per million) employing polystyrene beads coated with gold nanoparticles.[194] However, these studies did not employ fiber-based methods, thus limiting their *in situ* detection capabilities.

Incorporating the SEIRA technique into the fiber-based ATR method has allowed for *in situ* sample analysis, broadening the scope of spectroscopic applications. Our investigation successfully detected naphthalene, a compound with minimal solubility, directly in water at concentrations of 150 and 50 μM using the fiber-based SEIRA approach. This contrasts with prior infrared absorption studies of naphthalene, which were confined to laboratory settings and did not leverage the *in situ* advantages of fiber-based systems.[195,196]

2.3.2. Methods

Silver nanoparticle synthesis. To cover the loop tips with silver nanoparticles, *i.e*. create fiber-based SEIRA tips, silver-polyvinylpyrrolidone capped nanoparticles (Ag-PVP) were produced independently. The method for creating Ag-PVP nanoparticles was derived from the protocol established

by Aherne *et al*.[197] A slight modification was introduced during the seed production stage. The process began with the synthesis of a seed solution, accomplished by reducing a mixture comprising 30 mM PVP and 15 mM silver nitrate ($AgNO_3$) within a 3 ml volume, utilizing a 10 mM sodium borohydride ($NaBH_4$) solution measuring 90 µl. In particular, (I) 40 µl, (II) 50, (III) 80 µl, (IV) 90 µl of the seed solution was employed. This seed solution was combined with 5 ml of distilled water, followed by 1 ml of 10 mM L-ascorbic acid ($C_6H_8O_6$), and ultimately mixed with 0.5 mM of a 3 ml silver nitrate solution; all while being continuously stirred.

Direct nanoparticle synthesis on the loop. The conditions for direct nanoparticle synthesis on the loops were as follows:[198] a 20 ml 1% silver nitrate ($AgNO_3$) solution was initially heated to 60°C. This solution was then mixed with 0.8 ml of 25 % ammonium (NH_3) solution under constant stirring at 60°C. The last step involved adding 1.12 ml of 36 % glucose solution while stirring. The loop was immersed in the solution immediately after mixing, and the reaction lasted for 30 seconds. Afterward, the loop was extracted, washed with deionized water, and allowed to dry.

Production of fiber-based SEIRA loops. The PIR-fiber loops were cleaned with ethanol and acetone. Then, loops were immersed in the Ag-PVP nanoparticle solution for a period of 48 hours. After this duration, the loops were extracted, rinsed with pure deionized water (resistivity of 18.2 MΩ × cm), and allowed to air dry. This procedure led to the successful attachment of Ag-PVP nanoparticles onto the fiber loops.

The characterization of Ag-PVP nanoparticles was carried out using a SEM (Helios Nanolab 650, FEI, Netherlands). SEM images were measured of the Ag-PVP nanoparticles both pre and post application to the PIR-fiber loop tips. The dimensions and distribution of the nanoparticles were quantified using ImageJ software. Concurrently, the Lambda 1050 UV-NIR spectrometer (Perkin Elmer, USA) was utilized to assess the optical characteristics of the Ag-PVP nanoparticle colloidal solution.

Measurements. Standard ATR and ATR-SEIRA spectra of naphthalene solutions were recorded using a FTIR MATRIX-MF spectrometer (Bruker, USA) equipped with a liquid nitrogen-cooled mercury cadmium telluride (MCT) detector. Crystalline naphthalene was analyzed using the Alpha FTIR spectrometer (Bruker Optik GmbH, Germany) with a diamond ATR module and a room-temperature deuterated triglycine sulfate (DTGS) detector. Spectra were measured within a range of 600 – 3500 cm^{-1} at a 4 cm^{-1} resolution, averaging 128 scans. For relevance, spectra are presented within the 700 – 1000 cm^{-1} range. For ATR-SEIRA measurements, the fiber-based SEIRA loop was attached to the probe, and background spectra were obtained

in deionized water (18.2 MΩ × cm). The probe was then submerged in a 150 µM naphthalene solution, and the naphthalene spectra were derived by subtracting the water spectrum. Subtraction coefficients were fine-tuned to reduce water absorption bands in the spectra. Differential spectra of naphthalene, minus water, were generated using Opus 8.2 software (Bruker, Germany) and further refined with the Rubberband/Baseline-correction method. To determine the limit-of-detection (LOD), naphthalene levels were decreased to 50 and 25 µM. The SEIRA signal's consistency was verified by repeatedly immersing the fiber loop tip in a 150 µM naphthalene solution for spectral analysis, followed by rinsing and submerging in deionized water to obtain water spectra. The SNR was calculated by dividing the intensity of the spectral band at approximately 783 cm^{-1} (I_{783}) by the standard deviation ($\sigma_{700-800}$) of the noise within the 700 – 870 cm^{-1} range.

$$SNR = \frac{I_{783}}{\sigma_{700-800}}. \quad (2.3.1)$$

For standard ATR-FTIR analysis of naphthalene solutions, a PIR-fiber loop tip devoid of Ag-PVP nanoparticles was employed, adhering to the same protocol as the ATR-SEIRA measurements. A 90 mM naphthalene solution in ethanol served as a reference for comparison against the ATR-SEIRA spectra.

Enhancement factor calculations. Direct evaluation of the enhancement factor achieved with Ag-PVP nanoparticles in the fiber-based SEIRA setup proved difficult as naphthalene detection was not possible under identical conditions without the nanoparticles. To solve this, we measured the intensity of the naphthalene spectral band, dissolved in ethanol at a concentration of 90 mM, using the same experimental configuration. Ethanol is known for its low absorption around 780 cm^{-1}, which does not interfere with the naphthalene band. Subsequently, the analytical enhancement factor (AEF) was calculated as follows:

$$AEF = \frac{I_{IR\ EtOH} \times c_{IR\ EtOH}}{I_{SEIRA} \times c_{SEIRA}}. \quad (2.3.2)$$

Where $I_{IR\ EtOH}$ and $c_{IR\ EtOH}$ correspond to the intensity and concentration (90 mM) of the 787 cm^{-1} band of naphthalene dissolved in ethanol, respectively; I_{SEIRA} and c_{SEIRA} represent the intensity of the corresponding band and the concentration (150 µM) of naphthalene dissolved in water in the SEIRA approach.

2.3.3. Main results and key points

Fiber Optic Probe and detachable loops. The Fiber Optic ATR Loop Probe together with detachable loops was obtained from (*Art Photonics*, Germany). The ATR Loop Probe is consisted of two PIR fibers (900/1000 µm core/clad diameter) and $AgCl_{0.25}Br_{0.75}/AgCl_{0.5}Br_{0.5}$ core/clad composition. The loop tips consist of 700 µm diameter uncladded PIR fiber with $AgCl_{0.25}Br_{0.75}$ core composition serving as the ATR sensitive element. The principal scheme for changing the loop tips is provided in **Figure 2.3.1**. Proper alignment is ensured by a slot in the shaft, and the loop tip is secured using a fixing cap. The probe can be connected to an FTIR MATRIX-MF spectrometer equipped with a liquid nitrogen-cooled mercury cadmium telluride (MCT) detector for measurements.

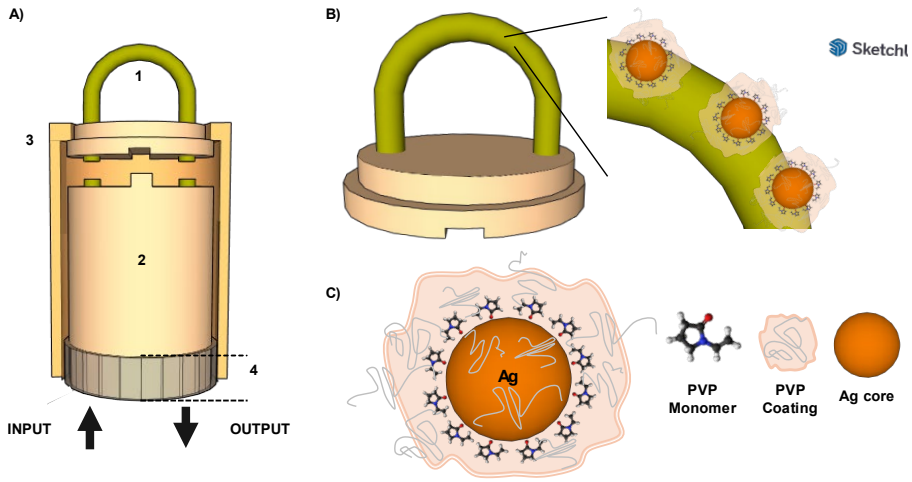

Figure 2.3.1. The principal components of the fiber-based SEIRA experimental setup. (**A**) Principal scheme of the ATR Loop Probe with replaceable PIR-fiber tip: 1 – ATR loop PIR-fiber tip; 2 – ATR probe shaft; 3 – Fixing cap; 4 – Fixing nut. (**B**) Schematic representation of fiber-based SEIRA tip covered with Ag-PVP nanoparticles. (**C**) Structure of Ag-PVP nanoparticle.

Our approach to generating the SEIRA effect involves the application of PVP-coated silver nanoparticles onto a silver halide (specifically, AgCl/AgBr) fiber loop tips from a colloidal solution. The effectiveness of this method is due to the strong binding affinity between the PVP and the surface of AgCl/AgBr fibers. The notable tendency of PVP to adhere to silver halide crystals[199,200] has been demonstrated and is one of the factors why PVP significantly restricts the expansion of the crystals in the silver halide structures.[199–201]

The principal scheme demonstrating the produced Ag-PVP nanoparticles and their assembly on silver halide fiber tip is given in **Figures 2.3.1 B** and **C**. SEM analysis showed the successful assembly of Ag-PVP nanoparticles on the PIR-fiber loop (**Figure 2.3.2**). The nanoparticle size distribution at the tip of the fiber loop mirrors that of the colloidal Ag-PVP nanoparticles (**Figure 2.3.3 A**), averaging 50 ± 10 nm. These nano-sized silver formations on the tip of the loop amplify the infrared absorption signals of nearby target molecules, thereby facilitating the SEIRA effect.

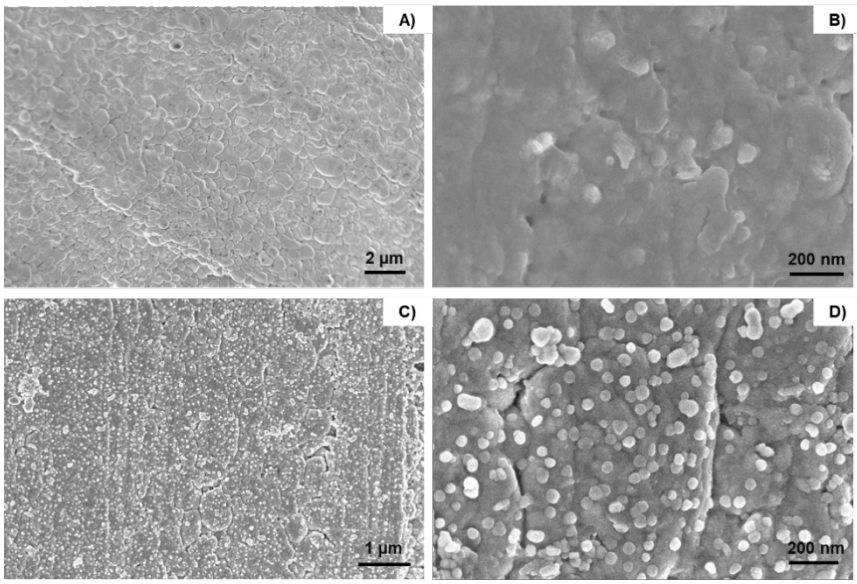

Figure 2.3.2. SEM images of PIR-fiber loops without nanoparticles (**A**, **B**) and with the deposited Ag-PVP nanoparticles (**C**, **D**).

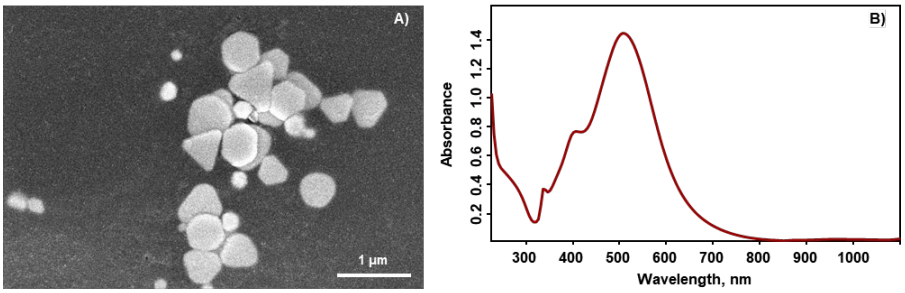

Figure 2.3.3. SEM image (**A**) and UV-Vis-NIR absorption spectrum (**B**) of Ag-PVP nanoparticles.

The optical characteristics of silver nanoparticles are determined by their size and shape, leading to a spectrum with multiple absorption peaks **(Figure 2.3.3 B**). Notably, a peak at 515 nm is linked to the dipole plasmon resonance,

commonly visible at approximately 410 nm for silver nanoparticles,[202] which shifts to higher wavelengths for larger or triangular shapes due to phase retardation effects. The observed FWHM (full width at half maximum) of this band is approximately 190 nm. The broadening of this peak suggests increased radiation damping and decay processes.[197,203] Additionally, a peak at 401 nm indicates in-plane quadrupole resonance,[204] while an out-of-plane quadrupole resonance appears at 335 nm, both associated with non-spherical nanoparticles.[57,197,203,205–208]

SEIRA measurements of naphthalene. Naphthalene, with the molecular formula $C_{10}H_8$, is a volatile member of the polycyclic aromatic hydrocarbons (PAH) featuring a dual-ring structure, as illustrated in **Figure 2.3.4**. Naphthalene was chosen as a model molecule to demonstrate the proficiency of fiber-based SEIRA sensors. Contaminants similar to naphthalene, which possess aromatic rings, are common in numerous pollutants.[209,210] Such sensors could potentially be used for the rapid and *in-situ* detection of organic contaminants in water, a significant challenge for infrared absorption-based sensors. Naphthalene, often found in industrial zones, poses a considerable threat to water bodies due to its widespread use.[211] As a recognized standard industrial chemical, naphthalene is a critical subject for environmental monitoring.[211–214] Tracking its presence is essential for assessing water purity and the effectiveness of purification methods.

To our knowledge, the direct detection of naphthalene in water has not yet been reported. The main challenges include its extremely low water solubility, approximately 200 μM,[215,216] and the strong spectral interference from water.[217–219]. The closest approach to directly detecting naphthalene in water involved using an ATR sensor under extreme pressure and temperature, protected by a thin polymer coating.[196] Additionally, a matrix isolation study in solid matrix utilized infrared absorption to investigate the interactions between naphthalene and water molecules.[195] Other research on naphthalene, involving infrared absorption spectroscopy, was conducted in its gaseous state,[220–222] within solid matrices,[223–225] and in crystalline form using the KBr pellet method.[226,227]

Figure 2.3.4 A shows a solution of 90 mM naphthalene in ethanol;[228] this solvent was chosen due to its high solubility for naphthalene. The detection of naphthalene is evidenced by a distinct spectral peak at 787 cm^{-1}, which signifies the C–H out-of-plane deformational vibration. Additional spectral characteristics at 843 cm^{-1} and 949 cm^{-1} correlate with various C–H deformational vibrations. The peak at 880 cm^{-1} corresponds to the symmetric ν(C–C–O) vibration of ethanol. The conventional fiber ATR absorption

method was unable to detect naphthalene dissolved in water at a concentration close to solubility limit of 150 µM (**Figure 2.3.4 B**).

The fiber-based SEIRA method has facilitated the direct detection of naphthalene in water, allowing the absorption band at 783cm^{-1} to become visible (**Figure 2.3.4 C**). The SNR for naphthalene was assessed using the fiber-based SEIRA method, yielding an SNR of 15. In contrast, the SNR for naphthalene in water with an untreated fiber loop was a mere 1, equivalent to the reference spectrum of water (**Figure 2.3.4 B, D**), indicating inadequate sensitivity of standard fiber ATR method.

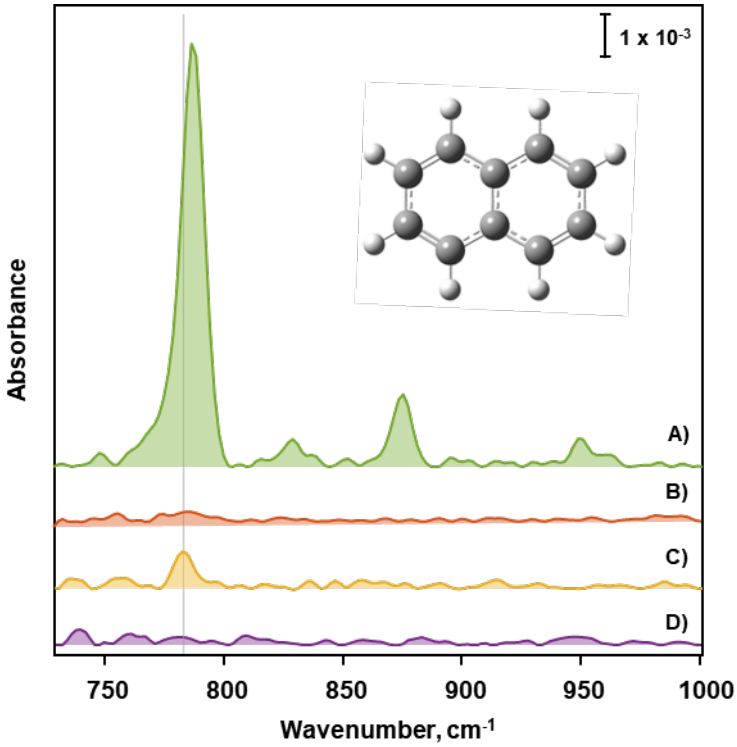

Figure 2.3.4. Standard ATR spectra of 0.09 M naphthalene solution in ethanol (**A**) and of 150 µM naphthalene solution in water (**B**); Fiber-based SEIRA spectrum of 150 µM naphthalene solution in water (**C**) and pure water for comparison (**D**). Inset shows naphthalene molecular structure.

Observations of other spectral bands of naphthalene in water were not made due to their lower intensity. According to literature, the intensity of the band at 783 cm^{-1} is about 15 times greater than that of other bands.[195] Research on naphthalene detection in water under extreme pressures and temperatures identified a spectral band at 782 cm^{-1},[196] consistent with the band position noted in our study. Our findings also show a blueshift of

3 cm^{-1} from the crystalline naphthalene form, aligning with prior research.[195,196] The influence of surrounding molecules on the position of naphthalene's spectral bands was evidenced in a matrix isolation study, which reported shifts up to 8cm^{-1}.[195] The AEF for the absorption band at 783 cm^{-1} was calculated to be 90. This value is expected to be higher when considering the differences in solvent absorption bands in this spectral range.

Utilizing the fiber-optic SEIRA approach, we further decreased the concentration of dissolved naphthalene to ascertain the minimal concentration detectable in water. **Figure 2.3.5** illustrates the corresponding SEIRA spectra for varying concentrations of naphthalene in water. After background correction, a progressive reduction in the intensity of the naphthalene spectral band at 783 cm^{-1} is observed. The minimal concentration of naphthalene that could be reliably detected was established at 50 µM, which corresponds to a SNR of 4. At a reduced concentration of 25 µM, the naphthalene marker becomes imperceptible, indicating that it falls below the LOD.

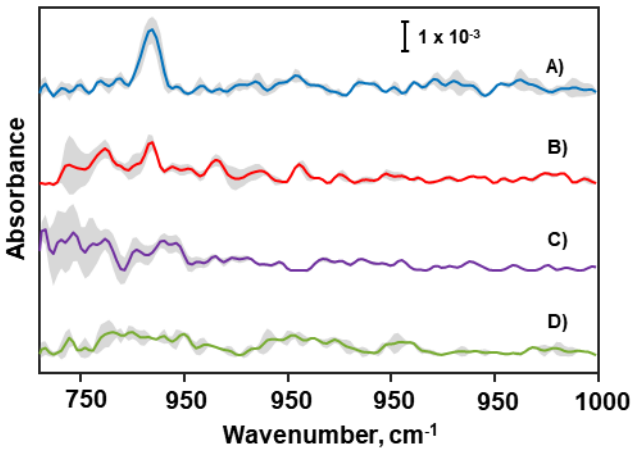

Figure 2.3.5. Fiber-based SEIRA spectra of 150 µM naphthalene (**A**); 50 µM naphthalene (**B**); 25 µM naphthalene (**C**); water (**D**).

The stability and reproducibility of the fiber-based SEIRA signals were evaluated through a series of experiments.

To enhance the reproducibility of the study, the tips of several fiber loops were coated with Ag-PVP nanoparticles. Throughout the growth phase, we utilized different volumes of the seed solution, specifically: (I) 40 µl, (II) 50 µl, (III) 80 µl and (IV) 90 µl. This led to varying ascorbic acid to silver ratios. Despite anticipating that these modifications would impact the concentration and size of nanoparticles in the colloidal solution, we observed

no notable differences in either SEIRA intensity or SNR, as illustrated in **Figure 2.3.6 A** and **Table 2.3.1**.

An alternative nanoparticle deposition method on fiber loops was explored, synthesizing nanoparticles on PIR fibers directly, similar to mirror coating techniques.[198] This yielded a comparable SNR for naphthalene and was not pursued further. Notably, nanoparticles coated with PVP are recognized for their biocompatibility and their unique non-spherical geometry, which offers considerable promise for future applications.[96–100]

Table 2.3.1. Comparative analysis of signal-to-noise ratios (SNR) achieved with SEIRA tips produced under varied nanoparticle synthesis conditions.

SEIRA tip configuration	Seed volume, µl	Ascorbic acid (AA) volume, ml	AA to Ag molar ratio	SNR
(I)	40	1	0.06	12.7
(II)	50	1	0.075	14.7
(III)	80	1	0.12	9.6
(IV)	90	1	0.135	8.4
Direct	-	-	-	12.2

Specifically, ten sequential tests of naphthalene in aqueous solution were performed using an identical fiber loop for the determination of the Ag-PVP nanoparticle stability on the fiber tips. Following each test, the loop was cleansed with extra pure deionized water, after which a spectrum of the pure water was acquired. As depicted in **Figures 2.3.6 B** and **C**, the fiber-based SEIRA spectra of naphthalene for each consecutive test are displayed, with the assay count ascending from the top. Notably, there was an observed increment in noise levels and a decrement in the naphthalene band intensity with successive tests. This phenomenon is likely due to the progressive removal of Ag-PVP nanoparticles during the rinsing process with deionized water. Although PVP interacts with the silver halide surface, the absence of electrostatic forces in deionized water could exclude Ag-PVP nanoparticles from the fiber surface. Furthermore, the lack of naphthalene detection post-rinsing and in the pure water spectra suggests that naphthalene molecules do not strongly adhere to the Ag-PVP nanoparticles on the fiber surface. It is considered that naphthalene adheres to metal surfaces *via* electrostatic forces, as evidenced by the SERS studies.[190–194] Our study supports this theory, as we observed that naphthalene could be washed off from the SEIRA loops with ease, suggesting a non-permanent chemical bond.

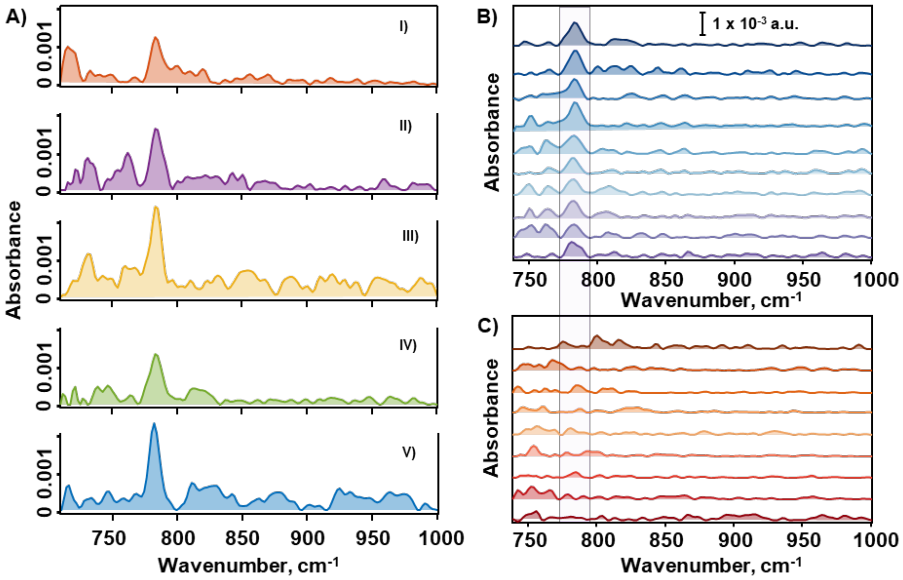

Figure 2.3.6. Fiber-based SEIRA spectra of naphthalene solution in water obtained with SEIRA loop tips deposited with Ag-PVP nanoparticles obtained using different seed solution concentrations: (**I**) 40 µl, (**II**) 50 µl, (**III**) 80 µl, (**IV**) 90 µl and (**V**) direct synthesis approach (**A**). Signal reproducibility during 10 successive measurements: of 150 µM naphthalene fiber-based SEIRA spectra (**B**); the corresponding water spectra (**C**). The number of measurements increases from the top to bottom.

Key points.

- The fiber-based SEIRA approach yielded a significant enhancement factor of 90 in the spectral signal of naphthalene molecules, with the characteristic band at 783 cm^{-1}.
- The LOD for naphthalene in water was determined to be 50 µM, or 0.9 ppm.
- The adsorption detected is predominantly attributed to electrostatic interactions, which is supported by the ease of rinsing naphthalene from the SEIRA loop tips, indicating a non-covalent nature of the molecule-surface interaction.

Our research verifies that the fiber-based SEIRA method, employing silver halide polycrystalline fiber loops and PVP-coated silver nanoparticles, can detect naphthalene in water, when deploying this method for *in situ* measurements in aqueous environments. Nevertheless, our data indicate that single-use fiber-based SEIRA loops, replaced after each measurement, provide consistent outcomes. The simple loop replacement ensures precise measurements with silver halide fiber loops. Our study achieved a detection

limit, LOD, of 50 μM, roughly equivalent to 0.9 ppm, which is competitive with previous findings. Optimizing factors such as nanoparticle concentration, shape, and the capping agent on the fiber loop tips could further improve this LOD. It is noteworthy that the SNR in our study was 15, which can be enhanced by extending acquisition times and averaging the spectra.

Theoretical calculations (refer to the **V publication**) support the physical nature of naphthalene adsorption, with a minimum C–Ag bond length of 2.62 Å, exceeding known C –Ag lengths, suggesting the absence of a covalent bond between Ag and C atoms.[229,230] Additionally, no significant spectral band shifts of naphthalene were observed.

2.4. Signal Enhancement in Infrared Absorption-Based Remote Sensing: Reduction of Fresnel Losses

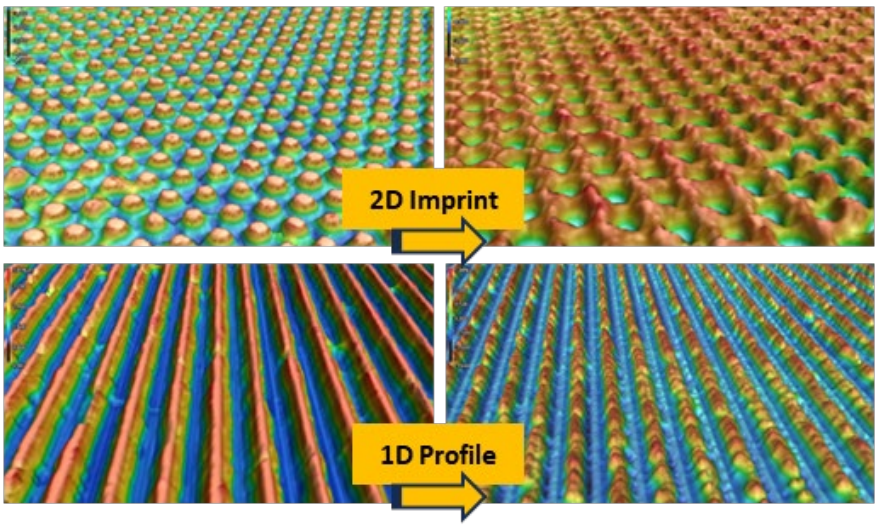

In this subsection results from the **IV publication** are presented addressing the fourth thesis assignment and supporting the fourth key statement for defense. In this study, the optical fiber surface was engineered, specifically targeting the transmission enhancement of PIR silver halide fiber end faces. Methods such as direct imprinting of two-dimensional microstructures and profiling of one-dimensional microstructures were utilized to modify the fiber end faces. An important aspect of this investigation is the formation of ARMs at ambient conditions, a process typically constrained by temperature requirements. The core objective of this study is to demonstrate the feasibility of ARM formation at room temperature, and to substantiate this with spectral and profile characterizations.

The implications of the results demonstrated in this study are broad, offering simple yet effective strategies to improve optical fiber performance, which could enhance applications in spectroscopy fields for both scientific and technological usage.

2.4.1. Motivation

Silver halide ($AgCl_{1-x}Br_x$), PIR fibers exhibit superior transmission in the 3 to 17 μm spectral range (corresponding to 600 – 3300 cm^{-1}).[231] These fibers are utilized in various applications, such as flexible power delivery systems for CO, CO_2, and quantum cascade lasers,[232–234] mid-infrared spectroscopy,[235,236] flexible infrared imaging,[237] and pyrometry.[238,239]

Despite their low inherent losses in the mid-infrared spectrum, PIR fibers suffer from significant Fresnel reflection losses at the fiber ends. This is due to the high refractive index contrast between the fiber material (with an index of approximately $n_{PIR} \approx 2.15$) and air ($n_{air} \approx 1$). This leads to Fresnel reflection losses of about 13 % per surface for 3 – 17 μm wavelengths. Consequently, a PIR fiber segment with two surfaces experiences roughly 25 % loss (at best), significantly hindering the delivery of signal. In systems incorporating multiple PIR fibers, the loss is even greater and can be estimated using the formula:

$$1 - (1 - R)^k, \tag{2.4.1}$$

where R represents the Fresnel reflection coefficient and k the number of interfaces. For instance, PIR fibers are crucial in ATR probes used across various industries for real-time reaction monitoring.[235,236] These probes typically include at least two fibers, resulting in four interfaces and 43 % power loss due to Fresnel reflection. Reducing these losses would greatly enhance the SNR and the sensitivity of both the probe and the entire spectroscopic system, making it a critical area for improvement, particularly for spectroscopic applications.

Several surface modification techniques exist to reduce Fresnel reflection losses, with thin film coating being the most prevalent.[240,241] However, this method has limitations, one of them being a narrow spectral range for spectroscopy.[242] The high refractive index of $AgCl_{1-x}Br_x$ fibers complicates the selection of suitable coating materials. The material sensitivity to heat (above 140 °C) and ultraviolet exposure further narrows the choice of applicable coating techniques. The softness of $AgCl_{1-x}Br_x$ precludes polishing, and its plasticity hinders perfect cleavage. Even slicing techniques used for surface preparation result in suboptimal flatness, leading to poor coating quality. Despite these challenges, there are instances of successful anti-reflection coating applications on silver halide fibers.[243–245]

An alternative strategy for reducing Fresnel reflection involves creating ARMs.[246] Unlike coatings, ARMs achieve an effective refractive index at the

fiber surface through sub-wavelength profiled structures.[246–248] The most notable example is the "moth's eye" structure, which mimics natural designs to trap light,[249–252] theoretically reducing reflection to as low as 0.1 %. This effect is also present in the short wavelength spectrum when the structure period exceeds the wavelength. Profiled structures offer advantages such as being composed of substrate material, and they can also be tailored for a wide spectral and angular range.

Various techniques exist for creating ARMs,[248] including lithography,[247,253] laser ablation,[253–255] and molding.[252,256–258] However, not all are suitable for PIR fiber end faces due to previously mentioned constraints. The most straightforward methods are direct imprinting (also known as embossing or stamping) and profiling with a microstructured knife (referred to as Special Microstructure Anti-Reflection Treatment or SMART).[231] Direct imprinting fabricates two-dimensional ARMs on a fiber tip through contact with a master plate, while profiling creates one-dimensional grooves. These techniques gradually adjust the fiber surface refractive index, improving optical matching.

2.4.2. Methods

Materials. PIR fibers, 0.9 m long, with core/clad diameters of 900/1000 μm and $AgCl_{0.25}Br_{0.75}/AgCl_{0.5}Br_{0.5}$ composition (*Art Photonics*, Germany) were used. A diamond mold plate with an anti-reflective Moth-eye structure (*Telaztec*, USA) served as the master plate for creating two-dimensional patterns (2D-imprinting). Prior to usage, the master plate underwent cleaning to remove any previous $AgCl_{1-x}Br_x$ fiber residues. This cleaning process involved 15 minutes of sonication in concentrated hydrochloric acid solution, followed by rinsing with ethanol and drying under a nitrogen flow.

The knife, used for one-dimensional profiling (1D-profiling) of the fiber surface was crafted from a cleaved silicon substrate etched with grooves. The surface microstructures of the knife were shaped using grayscale photolithography, resulting in an approximate trapezoidal geometry.

The geometry of the micro-grooved one-dimensional silicon knife and the two-dimensional Moth-eye microstructures was optimized for high anti-reflectance performance in the 8 – 12 μm range.

Profile Measurements. To assess the modified fiber end faces, the laser confocal optical profilometer VK-X1100 (*KEYENCE*, USA) was employed. A 100× objective lens (NA = 0.8) with a working distance of 2 mm and resolution of 12 nm (height) and 40 nm (lateral) was used. Profiles of both the original ARMs and those created on the fibers were measured at three

randomly chosen spots in different directions. At least three data points were obtained in each direction, resulting in a total of at least 27 data points. The collected data were averaged, and the standard deviation was calculated.

Transmittance Measurements. To evaluate the performance of the fiber, we utilized setup employed a FTIR spectrometer ReactIR 1000 with a MCT detector to observe transmission changes across a wide wavelength spectrum. We conducted measurements on the original fiber and then on the same fiber after applying ARMs to its ends. The measurement approach is detailed in **Figure 2.4.1**. Since percentages represent fiber transmittance, we express the transmittance improvement as a relative enhancement, calculating the ratio of transmittance between the treated and untreated fiber, also in percentages.

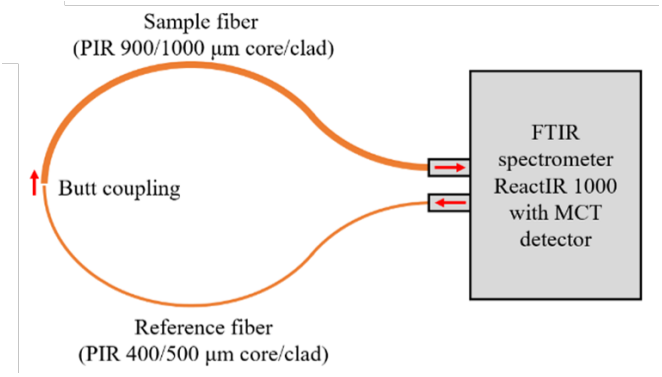

Figure 2.4.1. Scheme of the transmission measurements using a FTIR spectrometer for broad wavelength range.

2.4.3. Main results and key points

The process of creating anti-reflective microstructures. A setup for 2D-imprinting Moth-eye ARMs onto the fiber end was assembled (**Figure 2.4.2 A**). The fiber was secured within plastic tubing, with its ends tightly held in a ferrule using a squeeze connector. This connector effectively immobilized the fiber during the imprinting procedure. Within the setup, the ferrule was secured in a specialized holder, allowing precise adjustments of the relative position of the fiber to the master plate in the x, y, and z directions using micrometer drives. The master plate was then pressed onto the fiber, and the imprinting process was carried out at room temperature (approximately 22 °C).

1D-profiling involves fabricating one-dimensional microstructures, specifically grooves and ridges, through a shaving process using a profiled knife (**Figure 2.4.2 B**). The profiling process was conducted by cutting the fiber tip surface with the structured edge of the knife, at room temperature.

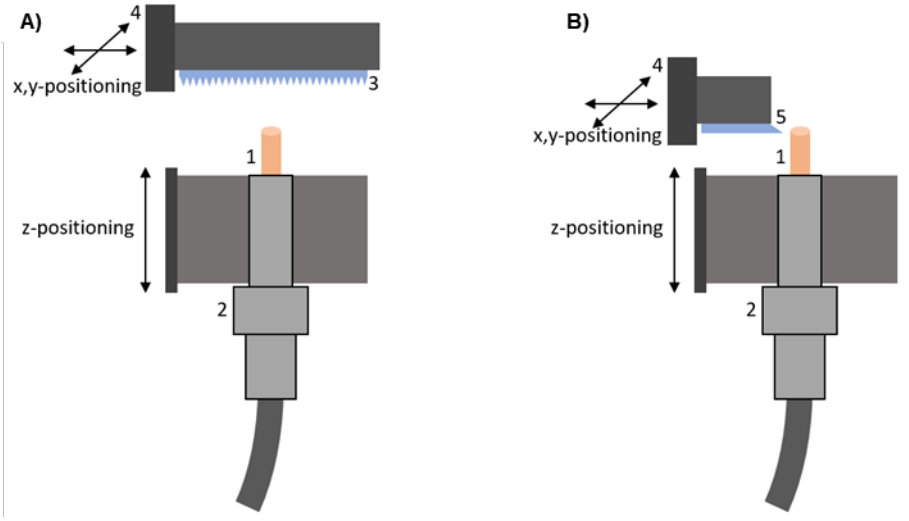

Figure 2.4.2. General scheme of the setup for (**A**) imprinting of ARMs to the fiber end and (**B**) profiling using silicon knife. Setup parts are indicated by numbers: 1 – fiber; 2 – squeeze connector; 3 – master plate; 4 – holder for a master plate.

Obtained structures. The optimal replication of the Moth-eye microstructure, which involves imprinting the entire end surface of the fiber with ARMs, was accomplished after refining the imprinting technique. The master plate, designed to mimic the Moth-eye's hexagonally arrayed truncated cone structure, is known for its anti-reflective properties.[249,250] The anti-reflective efficacy of these structures can be tuned across the visible to mid-infrared spectrum by adjusting parameters such as height, period, and the dimensions at the top and bottom of the structure, as shown in **Figure2.4.3.**[255,259,260] These structures are effective because they produce a gradual refractive index for incident wavelengths that are significantly longer than the dimensions of the structure. The ARMs were imprinted onto $AgCl_{1-x}Br_x$ fibers using Moth-eye cone-shaped microstructures crafted on a diamond plate (**Figure 2.4.3**). Measurements from three-dimensional optical profilometer images of the master plate are presented in **Table 2.4.1** together with the measurements from acquired imprinted structure on the fiber end face. After imprinting, the fiber end face exhibits a negative replica of the master structure. However, deviations from the anticipated inverse form are observed, attributable to the mechanical characteristics of the material such as stiffness, strength, viscoelasticity, toughness, and viscosity.[261] They influence the elastic behavior of the material and the time allowed for the material to flow completely.[262,263]

Table 2.4.1. Profilometer data for fiber ends obtained using 2D-imprinting and 1D-profiling techniques, and the corresponding structures on the master plate and the microstructured knife.

	Period, µm	Top, µm	Bottom, µm	Height, µm
Master plate	3.06±0.18	1.05±0.26	0.6±0.4	1.22±0.3
2D-imprinting	3±0.09	0.89±0.14	0.78±0.16	1.29±0.2
Knife profile	3.74±0.12	0.58±0.18	0.78±0.17	2.15±0.14
1D-profiling	3.8±0.25	0.83±0.21	-	1.75±0.17

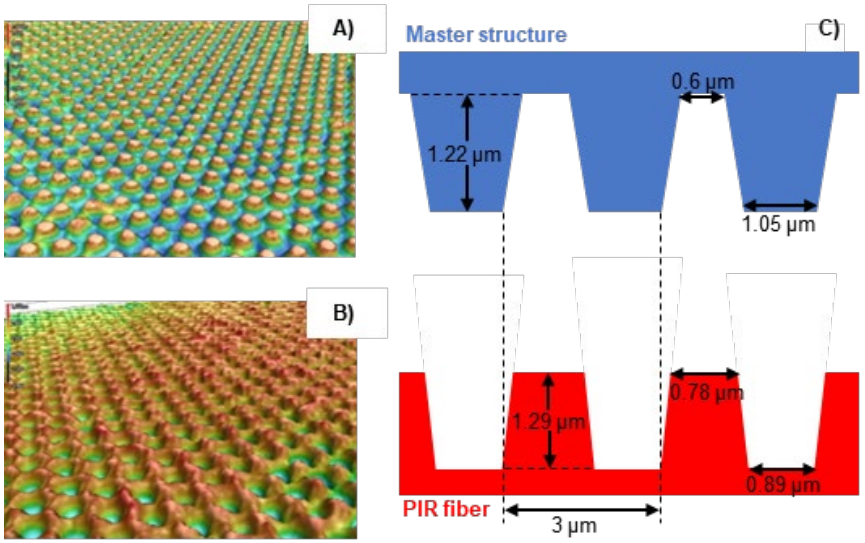

Figure 2.4.3. The profilometer images of the master plate (**A**) and imprinted fiber surface (**B**); geometrical parameters of the master plate profile and imprinted fiber end (**C**).

The bottom dimension of the Moth-eye ARMs shifted from 1.05 ± 0.26 µm to 0.89 ± 0.14 µm upon imprinting. This reduction in size may be attributed to elastic deformation and the incomplete imprinting process. Taking all factors into account, a decrease in the structure height was initially expected due to partial embossing. The time needed for the fiber material to adequately fill the cavities is influenced by the limited plasticity of the material and the dimensions of the master structure.[261] Contrary to expectations, a minor increase in structure height was observed in practice. Variations in size between individual protrusions and cavities may have been exacerbated by uneven pressure applied across the fiber surface, with certain areas experiencing greater pressure than others. Nonetheless, three-dimensional profilometer data clearly show the imprinted microstructures across the entire fiber surface, as illustrated in **Figure 2.4.3 B**.

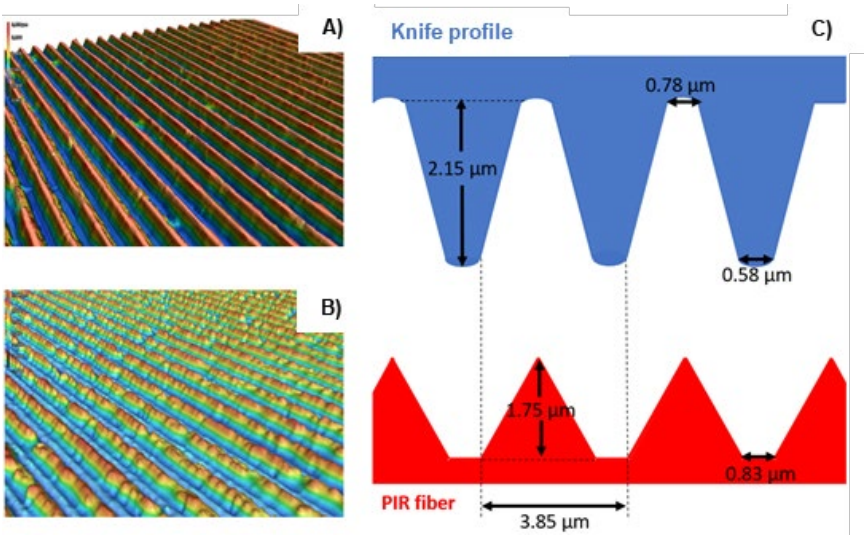

Figure 2.4.4. The profilometer images of grating on the knife edge (**A**) and microstructured fiber surface after slicing (**B**); geometrical parameters of the knife profile and fiber end structure after treating (**C**).

Figure 2.4.4 displays the one-dimensional profile of the microstructured knife alongside the corresponding pattern on the fiber surface. The fiber surface then mirrored the structure geometry of knife edge in an inverted form. The height of the microstructures on the fiber surface profile was approximately 1.75 µm, which is lower than that of the knife 2.15 µm. It was also observed that the top corners on the fiber edge became more pronounced, and the groove bottom width (the distance between ridges) was slightly greater than that on the knife. This discrepancy can be attributed to the incomplete profiling, meaning that the full height of the grooves of the knife was not utilized in the process.

Transmittance measurements. Following the ARM creation, we assessed the transmission properties of the fibers over a broad spectral range using a FTIR spectrometer. The fiber exhibited an increase in transmittance within the 5 – 17 µm spectral range (corresponding to 600 – 2000 cm^{-1}) after Moth-eye 2D-imprinting **(Figure 2.4.5 A)**. Conversely, transmittance diminished in the shorter wavelength range of 2 – 5 µm due to diffraction effects. Notably, Moth-eye imprinting efforts yielded a transmission boost of up to 25.1 %, achieving 75.7 % at the 10.6 µm wavelength when both fiber ends were micro-structured from initial 60.5 %. A notable visual change was observed for the fiber end after imprinting, which turned nearly black, as illustrated in the inset of **Figure 2.4.5**. The 1D-profiling led to transmission increase in the 7.5 – 17 µm spectral range (corresponding to 600 – 1300 cm^{-1}),

with the cut-off wavelength around 7.5 μm, (**Figure 2.4.5 B**). Specifically, the 10.6 μm (corresponding to 1000 cm^{-1}) transmission rose by 22.3 %, rising from 62.7 % to 76.7 % after treating both fiber end surfaces. The impact of diffraction on short-wavelength transmittance was evident for both ARMs. The cut-off wavelengths for this phenomenon varied, attributable to the differing geometrical dimensions of the one-dimensional profile and two-dimensional Moth-eye structures.

At the 10.6 μm wavelength, the transmission ratio of the treated fiber to the initial flat surface stood at 1.25 for 2D-imprinting and 1.22 for 1D-profiling (**Figure 2.4.5 C**). The most favorable outcomes were associated with a single-surface reflectance of 3 % for the 2D-imprinted Moth-eye ARM and 4 % for 1D-profiling at the 10.6 μm wavelength, compared to 13 % for an untreated surface. The collected data on FTIR measurements at the 10.6 μm wavelength from various samples are provided in **Table 2.4.2**.

Table 2.4.2. Results of ARMs treated fiber transmission at 10.6 μm wavelength measured with FTIR spectrometer.

Sample no.	Treatment type	Achieved transmission	Achieved enhancement
1	Non-treated	60.5	-
2	2D-imprinting	75.7	25.1
3	2D-imprinting	73.5	21.4
4	2D-imprinting	74.4	23
5	2D-imprinting	70.1	15.9
6	2D-imprinting	68.8	13.7
7	2D-imprinting	68.9	13.9
8	Non-treated	62.7	-
9	1D-profiling	76.7	22.3
10	1D-profiling	75.2	19.9

Both 1D-profiling and Moth-eye ARM treatments enhance the transmittance of polycrystalline optical fibers within the 7.5 – 17 μm spectral range. The primary distinction lies in the onset of transmission improvement: approximately 5 μm (2000 cm^{-1}) for Moth-eye ARMs and 7.5 μm (1330 cm^{-1}) for 1D-profiling. The relationship between the size and spacing of microstructures affects the cut-off wavelength and the amount of reflected radiation.[264,265] In case of Moth-eye microstructures, the height is an important factor that determines how much reflection is reduced. However, the cut-off wavelength is independent of the height and determined by the period.

Generally, decreasing the period shifts the cut-off wavelength towards shorter wavelengths.[255,265] It is worth noting that the required force for 2D-imprinting was demonstrated to be reduced by half, from 90 N to 45 N, when the fiber surface was heated (150 – 200 °C), thus making it more suitable for further 2D-imprinting optimization.

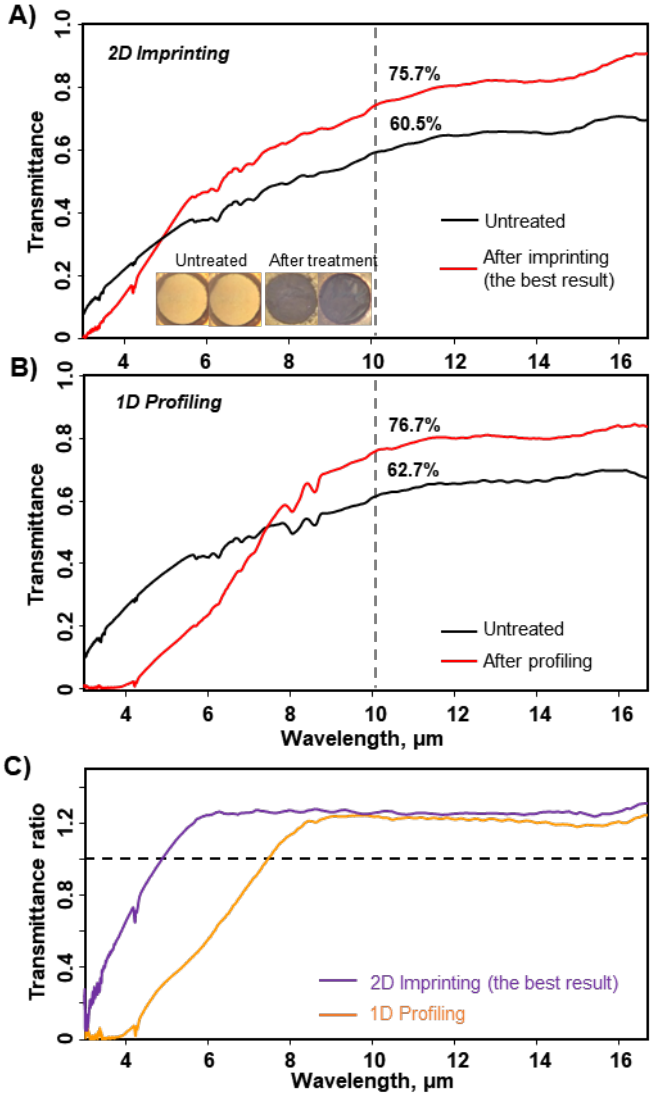

Figure 2.4.5. The measured transmission before and after the 2D Moth-eye imprinting (**A**), 1D-profiling (**B**) and comparison of the increase in fiber transmittance ratio (**C**). The legend inlay shows optical microscope pictures of both fiber ends before and after treatment.

Key points:

- A significant enhancement in the transmittance of PIR silver halide ($AgCl_{1-x}Br_x$) fibers was achieved due to the successful imprinting and profiling of PIR fiber ends at room temperature.
- Transmittance enhancement of PIR fibers was achieved at room temperature by reducing Fresnel reflection up to 22 – 25 % for a 10.6 μm wavelength (corresponding to 1000 cm^{-1}).
- One-dimensional microstructuring achieved transmission enhancement in the 7.5 – 7 μm (corresponding to 600 – 1300 cm^{-1}) range using a simple and cost-effective technique.
- Two-dimensional Moth-eye patterned structure achieved transmission enhancement in the 5 – 17 μm (corresponding to 600 – 2000 cm^{-1}) range technically more challenging technique thus leading to microstructure discrepancies.
- Profilometric measurements reveal that the fiber surface geometrical dimensions differ from those of the master structures, attributable to the low plasticity and polycrystalline nature of the fiber material.

CONCLUSIONS

1. The probe molecules, adenine, adsorb on the magnetite site rather than on gold, as suggested by SERS spectroscopy and theoretical calculations.

2. Significant SERS enhancement of adsorbed adenine (EF = 4×10^4) demonstrated that the magnetic shell does not diminish the electromagnetic enhancement effect provided by the plasmonic core, while the magnetic shell can serve for the manipulation and arrangement of the nanoparticles on a selected surface, as visible from TEM images.

3. Lattice deterioration of $Ti_3C_2T_x$ MXene begins at laser excitation power of 160 kW/cm^2 resulting in the formation of amorphous carbon and hydrocarbons, while the formation of TiO_2 nanoparticles (initially the anatase phase, followed by the rutile phase) is observed at a power density of 550 kW/cm^2 with a 633 nm excitation wavelength.

4. The enhancement of the salicylic acid molecule Raman spectra was observed from $Ti_3C_2T_x$-based MXene, with substantial enhancement of out-of-plane bending modes at 896 cm^{-1}, 681 cm^{-1} and 654 cm^{-1} and a calculated enhancement factor of 220.

5. The redshift of vibrational frequencies and the changes in the UV-Vis spectrum along with DFT calculations indicate that chemical enhancement mechanisms are dominant in the SERS spectra of salicylic acid adsorbed on the MXene surface.

6. Due to the deposition of silver nanoparticles onto the polycrystalline fiber loop tip, the detection of naphthalene dissolved in water by the spectral band at 783 cm^{-1} became possible, with the spectral signal enhanced by a factor of 90.

7. The fibers with micro-structured ends show improved transmission, particularly in the 5 – 17 μm range (corresponding to 600–2000 cm^{-1}), with a significant increase in transmission of 22 – 25% for a 10.6 μm wavelength (1000 cm^{-1}).

LIST OF REFERENCES

(1) Shimizu, M.; Koya, T.; Nakahigashi, A.; Urakami, N.; Yamakami, T.; Arai, S. Kinetics Study and Degradation Analysis through Raman Spectroscopy of Graphite as a Negative-Electrode Material for Potassium-Ion Batteries. *The Journal of Physical Chemistry C* **2020**, *124* (24), 13008–13016. https://doi.org/10.1021/acs.jpcc.0c03020.

(2) Alsaffar, F.; Alodan, S.; Alrasheed, A.; Alhussain, A.; Alrubaiq, N.; Abbas, A.; Amer, Moh. R. Raman Sensitive Degradation and Etching Dynamics of Exfoliated Black Phosphorus. *Sci Rep* **2017**, *7* (1), 44540. https://doi.org/10.1038/srep44540.

(3) Li, Z.; Deen, M.; Kumar, S.; Selvaganapathy, P. Raman Spectroscopy for In-Line Water Quality Monitoring—Instrumentation and Potential. *Sensors* **2014**, *14* (9), 17275–17303. https://doi.org/10.3390/s140917275.

(4) Shepherd, K. D.; Walsh, M. G. Infrared Spectroscopy—Enabling an Evidence-Based Diagnostic Surveillance Approach to Agricultural and Environmental Management in Developing Countries. *J Near Infrared Spectrosc* **2007**, *15* (1), 1–19. https://doi.org/10.1255/jnirs.716.

(5) Dubois, J.; Shaw, R. A. Peer Reviewed: IR Spectroscopy in Clinical and Diagnostic Applications. *Anal Chem* **2004**, *76* (19), 360 A-367 A. https://doi.org/10.1021/ac041647v.

(6) das Chagas e Silva de Carvalho, L. F.; de Lima Morais, T. M.; Nogueira, M. S. Providing Potential Solutions by Using FT-IR Spectroscopy for Biofluid Analysis: Clinical Impact of Optical Screening and Diagnostic Tests. *Photodiagnosis Photodyn Ther* **2023**, *44*, 103753. https://doi.org/10.1016/j.pdpdt.2023.103753.

(7) Freitag, S.; Sulyok, M.; Logan, N.; Elliott, C. T.; Krska, R. The Potential and Applicability of Infrared Spectroscopic Methods for the Rapid Screening and Routine Analysis of Mycotoxins in Food Crops. *Compr Rev Food Sci Food Saf* **2022**, *21* (6), 5199–5224. https://doi.org/10.1111/1541-4337.13054.

(8) Brandily, M. L.; Monbet, V.; Bureau, B.; Boussard-Plédel, C.; Loréal, O.; Adam, J. L.; Sire, O. Identification of Foodborne Pathogens within Food Matrices by IR Spectroscopy. *Sens Actuators B Chem* **2011**, *160* (1), 202–206. https://doi.org/10.1016/j.snb.2011.07.034.

(9) Das, R. S.; Agrawal, Y. K. Raman Spectroscopy: Recent Advancements, Techniques and Applications. *Vibrational Spectroscopy*. 2011. https://doi.org/10.1016/j.vibspec.2011.08.003.

(10) Xue, W.; Yan, H.; He, Y.; Wu, L.; Zhang, X.; Wu, Y.; Xu, J.; He, J.; Yan, C.; Meng, H. Identifying the Molecular Origins of Green BN-TADF Material Degradation and Device Stability via in Situ Raman Spectroscopy. *Chemistry – A European Journal* **2022**, *28* (36). https://doi.org/10.1002/chem.202201006.

(11) Mohammadi, N.; Ganesan, A.; Chantler, C. T.; Wang, F. Differentiation of Ferrocene D5d and D5h Conformers Using IR Spectroscopy. *J Organomet Chem* **2012**, *713*, 51–59. https://doi.org/10.1016/j.jorganchem.2012.04.009.

(12) Fischer, J. L.; Blodgett, K. N.; Harrilal, C. P.; Walsh, P. S.; Davis, Z. S.; Choi, S.; Choi, S. H.; Zwier, T. S. Conformer-Specific Spectroscopy and IR-Induced Isomerization of a Model γ-Peptide: Ac-γ ^{4} -Phe-NHMe. *J Phys Chem A* **2022**, *126* (11), 1837–1847. https://doi.org/10.1021/acs.jpca.2c00112.

(13) Park, S. M.; Kwon, C. H. Development and Verification of Conformer-Specific Vibrational Spectroscopy. *J Phys Chem A* **2021**, *125* (41), 9251–9258. https://doi.org/10.1021/acs.jpca.1c07162.

(14) Lin, X.; Sun, D.-W. Recent Developments in Vibrational Spectroscopic Techniques for Tea Quality and Safety Analyses. *Trends Food Sci Technol* **2020**, *104*, 163–176. https://doi.org/10.1016/j.tifs.2020.06.009.

(15) Pezzotti, G.; Boschetto, F.; Ohgitani, E.; Fujita, Y.; Shin-Ya, M.; Adachi, T.; Yamamoto, T.; Kanamura, N.; Marin, E.; Zhu, W.; Nishimura, I.; Mazda, O. Raman Molecular Fingerprints of SARS-CoV-2 British Variant and the Concept of *Raman Barcode*. *Advanced Science* **2022**, *9* (3). https://doi.org/10.1002/advs.202103287.

(16) Cialla, D.; Deckert-Gaudig, T.; Budich, C.; Laue, M.; Möller, R.; Naumann, D.; Deckert, V.; Popp, J. Raman to the Limit: Tip-enhanced Raman Spectroscopic Investigations of a Single Tobacco Mosaic Virus. *Journal of Raman Spectroscopy* **2009**, *40* (3), 240–243. https://doi.org/10.1002/jrs.2123.

(17) Santos, M. C. D.; Morais, C. L. M.; Lima, K. M. G.; Martin, F. L. Vibrational Spectroscopy in Protein Research toward Virus Identification: Challenges, New Research, and Future Perspectives. In *Vibrational Spectroscopy in Protein Research*; Elsevier, 2020; pp 315–335. https://doi.org/10.1016/B978-0-12-818610-7.00011-6.

(18) Krafft, C.; Popp, J. Diagnosis and Screening of Cancer Tissues by Vibrational Spectroscopy. *Advances in Biomedical Spectroscopy* **2012**, *6*. https://doi.org/10.3233/978-1-61499-059-8-212.

(19) Mohamed, H. T.; Untereiner, V.; Proult, I.; Ibrahim, S. A.; Götte, M.; El-Shinawi, M.; Mohamed, M. M.; Sockalingum, G. D.; Brézillon, S. Characterization of Inflammatory Breast Cancer: A Vibrational Microspectroscopy and Imaging Approach at the Cellular and Tissue Level. *Analyst* **2018**, *143* (24), 6103–6112. https://doi.org/10.1039/C8AN01292J.

(20) Wang, H.; Lee, D.; Wei, L. Toward the Next Frontiers of Vibrational Bioimaging. *Chemical & Biomedical Imaging* **2023**, *1* (1), 3–17. https://doi.org/10.1021/cbmi.3c00004.

(21) Campanella, B.; Palleschi, V.; Legnaioli, S. Introduction to Vibrational Spectroscopies. *ChemTexts* **2021**, *7* (1), 5. https://doi.org/10.1007/s40828-020-00129-4.

(22) Sanghera, J. S.; Aggarwal, I. D. Active and Passive Chalcogenide Glass Optical Fibers for IR Applications: A Review. *J Non Cryst Solids* **1999**, *256–257*, 6–16. https://doi.org/10.1016/S0022-3093(99)00484-6.

(23) Lindad. Crystalline Fiber Optics. In *Infrared Fibers and Their Applications*; SPIE: 1000 20th Street, Bellingham, WA 98227-0010 USA; pp 105–137. https://doi.org/10.1117/3.540899.ch6.

(24) Zhang, J.; Zhang, L. Nanostructures for Surface Plasmons. *Adv Opt Photonics* **2012**, *4* (2), 157. https://doi.org/10.1364/aop.4.000157.

(25) Barnes, W. L.; Dereux, A.; Ebbesen, T. W. Surface Plasmon Subwavelength Optics`. *Nature* **2003**, 824–830.

(26) Aroca, Ricardo. *Surface Enhanced Vibrational Spectroscopy*; Wiley, 2006.

(27) Amer, M. S. *Raman Spectroscopy for Soft Matter Applications*; Wiley, 2009.

(28) Albrecht, M. G.; Creighton, J. A. Anomalously Intense Raman Spectra of Pyridine at a Silver Electrode. *J Am Chem Soc* **1977**, *99* (15). https://doi.org/10.1021/ja00457a071.

(29) Fleischmann, M.; Hendra, P. J.; McQuillan, A. J. Raman Spectra of Pyridine Adsorbed at a Silver Electrode. *Chem Phys Lett* **1974**, *26* (2), 163–166. https://doi.org/10.1016/0009-2614(74)85388-1.

(30) Jeanmaire, D. L.; Van Duyne, R. P. Surface Raman Spectroelectrochemistry: Part I. Heterocyclic, Aromatic, and Aliphatic Amines Adsorbed on the Anodized Silver Electrode. *J Electroanal Chem Interfacial Electrochem* **1977**, *84* (1), 1–20. https://doi.org/10.1016/S0022-0728(77)80224-6.

(31) Wang, H. L.; You, E. M.; Panneerselvam, R.; Ding, S. Y.; Tian, Z. Q. Advances of Surface-Enhanced Raman and IR Spectroscopies: From

Nano/Microstructures to Macro-Optical Design. *Light Sci Appl.* **2021**, *10* (1), 161. https://doi.org/10.1038/s41377-021-00599-2.

(32) Stiles, P. L.; Dieringer, J. A.; Shah, N. C.; Van Duyne, R. P. Surface-Enhanced Raman Spectroscopy. *Annual Review of Analytical Chemistry* **2008**, *1* (1), 601–626. https://doi.org/10.1146/annurev.anchem.1.031207.112814.

(33) Chang, X.; Vijay, S.; Zhao, Y.; Oliveira, N. J.; Chan, K.; Xu, B. Understanding the Complementarities of Surface-Enhanced Infrared and Raman Spectroscopies in CO Adsorption and Electrochemical Reduction. *Nat Commun* **2022**, *13* (1), 2656. https://doi.org/10.1038/s41467-022-30262-2.

(34) Zhumaev, U. E.; Domke, K. F. *Surface-Enhanced Infrared Absorption Spectroscopy*; 2018.

(35) Osawa, M. Surface-Enhanced Infrared Absorption. In *Near-Field Optics and Surface Plasmon Polaritons*; Springer Berlin Heidelberg: Berlin, Heidelberg, 2001; Vol. 81, pp 163–187. https://doi.org/10.1007/3-540-44552-8_9.

(36) Aroca, R.; Rodriguez-Llorente, S. *Surface-Enhanced Vibrational Spectroscopy*; 1997; Vol. 4081409.

(37) Hartstein, A.; Kirtley, J. R.; Tsang, J. C. Enhancement of the Infrared Absorption from Molecular Monolayers with Thin Metal Overlayers. **1980**, *45* (3).

(38) Oksenberg, E.; Shlesinger, I.; Tek, G.; Koenderink, A. F.; Garnett, E. C. Complementary Surface-Enhanced Raman Scattering (SERS) and IR Absorption Spectroscopy (SEIRAS) with Nanorods-on-a-Mirror. *Adv Funct Mater* **2023**, *33* (8). https://doi.org/10.1002/adfm.202211154.

(39) Li, S.; Li, Y.; Yi, R.; Liu, L.; Qu, J. Coherent Anti-Stokes Raman Scattering Microscopy and Its Applications. *Front Phys* **2020**, *8*. https://doi.org/10.3389/fphy.2020.598420.

(40) Bazhenov, A. V; Kveder, V. V; Maksimov, A. A.; Tartakovski, I. I.; Oganyan, R. A.; Ossipyan, Y. A.; Shalynin, A. I. Raman Scattering of Light and IR Absorption in Carbon Nanotubes. *Journal of Experimental and Theoretical Physics* **1998**, *86*, 1030–1034.

(41) Chang, X.; Vijay, S.; Zhao, Y.; Oliveira, N. J.; Chan, K.; Xu, B. Understanding the Complementarities of Surface-Enhanced Infrared and Raman Spectroscopies in CO Adsorption and Electrochemical Reduction. *Nat Commun* **2022**, *13* (1). https://doi.org/10.1038/s41467-022-30262-2.

(42) Li, D.; Xu, C.; Xie, J.; Lee, C. Research Progress in Surface-Enhanced Infrared Absorption Spectroscopy: From Performance Optimization, Sensing Applications, to System Integration. *Nanomaterials*. Multidisciplinary Digital Publishing Institute (MDPI) August 1, 2023. https://doi.org/10.3390/nano13162377.

(43) Zong, C.; Xu, M.; Xu, L.-J.; Wei, T.; Ma, X.; Zheng, X.-S.; Hu, R.; Ren, B. Surface-Enhanced Raman Spectroscopy for Bioanalysis: Reliability and Challenges. *Chem Rev* **2018**, *118* (10), 4946–4980. https://doi.org/10.1021/acs.chemrev.7b00668.

(44) Lu, Y.; Lin, L.; Ye, J. Human Metabolite Detection by Surface-Enhanced Raman Spectroscopy. *Mater Today Bio* **2022**, *13*, 100205. https://doi.org/10.1016/j.mtbio.2022.100205.

(45) Lin, C.; Li, Y.; Peng, Y.; Zhao, S.; Xu, M.; Zhang, L.; Huang, Z.; Shi, J.; Yang, Y. Recent Development of Surface-Enhanced Raman Scattering for Biosensing. *Journal of Nanobiotechnology*. BioMed Central Ltd December 1, 2023. https://doi.org/10.1186/s12951-023-01890-7.

(46) Ouyang, L.; Ren, W.; Zhu, L.; Irudayaraj, J. Prosperity to Challenges: Recent Approaches in SERS Substrate Fabrication. *Rev Anal Chem* **2017**, *36* (1). https://doi.org/10.1515/revac-2016-0027.

(47) Li, C.; Huang, Y.; Li, X.; Zhang, Y.; Chen, Q.; Ye, Z.; Alqarni, Z.; Bell, S. E. J.; Xu, Y. Towards Practical and Sustainable SERS: A Review of Recent Developments in the Construction of Multifunctional Enhancing Substrates. *J Mater Chem C Mater* **2021**, *9* (35), 11517–11552. https://doi.org/10.1039/D1TC02134F.

(48) Smeliková, V.; Kopal, I.; Člupek, M.; Dendisová, M.; Švecová, M. Unveiling the Crucial Role of Chemical Enhancement in the SERS Analysis of Amphetamine–Metal Interactions on Gold and Silver Surfaces: Importance of Selective Amplification of the Narrow Interval of Vibrational Modes. *Anal Chem* **2024**, *96* (14), 5416–5427. https://doi.org/10.1021/acs.analchem.3c05189.

(49) Pérez-Jiménez, A. I.; Lyu, D.; Lu, Z.; Liu, G.; Ren, B. Surface-Enhanced Raman Spectroscopy: Benefits, Trade-Offs and Future Developments. *Chem Sci* **2020**, *11* (18), 4563–4577. https://doi.org/10.1039/D0SC00809E.

(50) Chen, Y.; Hu, Y.; Li, G. A Review on Non-Noble Metal Substrates for Surface-Enhanced Raman Scattering Detection. *Chemosensors*. Multidisciplinary Digital Publishing Institute (MDPI) August 1, 2023. https://doi.org/10.3390/chemosensors11080427.

(51) Dong, L.; Yang, X.; Zhang, C.; Cerjan, B.; Zhou, L.; Tseng, M. L.; Zhang, Y.; Alabastri, A.; Nordlander, P.; Halas, N. J. Nanogapped Au Antennas for Ultrasensitive Surface-Enhanced Infrared Absorption Spectroscopy. *Nano Lett* **2017**, *17* (9), 5768–5774. https://doi.org/10.1021/acs.nanolett.7b02736.

(52) Neubrech, F.; Pucci, A.; Cornelius, T. W.; Karim, S.; García-Etxarri, A.; Aizpurua, J. Resonant Plasmonic and Vibrational Coupling in a Tailored Nanoantenna for Infrared Detection. *Phys Rev Lett* **2008**, *101* (15), 157403. https://doi.org/10.1103/PhysRevLett.101.157403.

(53) Wang, J.; Xie, Z.; Zhu, Y.; Zeng, P.; He, S.; Wang, J.; Wei, H.; Yu, C. Surface-Enhanced Infrared Absorption Spectroscopy (SEIRAS) for Biochemical Analysis: Progress and Perspective. *Trends in Environmental Analytical Chemistry* **2024**, *41*, e00226. https://doi.org/10.1016/j.teac.2024.e00226.

(54) Le Ru, E. C.; Etchegoin, P. G. *Principles of Surface-Enhanced Raman Spectroscopy*; Elsevier, 2009. https://doi.org/10.1016/B978-0-444-52779-0.X0001-3.

(55) Horvath, H. Gustav Mie and the Scattering and Absorption of Light by Particles: Historic Developments and Basics. *J Quant Spectrosc Radiat Transf* **2009**, *110* (11), 787–799. https://doi.org/10.1016/j.jqsrt.2009.02.022.

(56) Johnson, P. B.; Christy, R. W. Optical Constants of the Noble Metals. *Phys Rev B* **1972**, *6* (12), 4370–4379. https://doi.org/10.1103/PhysRevB.6.4370.

(57) Kelly, K. L.; Coronado, E.; Zhao, L. L.; Schatz, G. C. The Optical Properties of Metal Nanoparticles: The Influence of Size, Shape, and Dielectric Environment. *Journal of Physical Chemistry B* **2003**, *107* (3), 668–677. https://doi.org/10.1021/jp026731y.

(58) Cialla, D.; Pollok, S.; Steinbrücker, C.; Weber, K.; Popp, J. SERS-Based Detection of Biomolecules. *Nanophotonics* **2014**, *3* (6). https://doi.org/10.1515/nanoph-2013-0024.

(59) Fazio, B.; D'Andrea, C.; Foti, A.; Messina, E.; Irrera, A.; Donato, M. G.; Villari, V.; Micali, N.; Maragò, O. M.; Gucciardi, P. G. SERS Detection of Biomolecules at Physiological PH via Aggregation of Gold Nanorods Mediated by Optical Forces and Plasmonic Heating. *Sci Rep* **2016**, *6*. https://doi.org/10.1038/srep26952.

(60) Liu, G. L.; Lu, Y.; Kim, J.; Doll, J. C.; Lee, L. P. Magnetic Nanocrescents as Controllable Surface-Enhanced Raman Scattering Nanoprobes for Biomolecular Imaging. *Advanced Materials* **2005**, *17* (22), 2683–2688. https://doi.org/10.1002/adma.200501064.

(61) Adomavičiūtė, S.; Velička, M.; Šablinskas, V. Detection of Aspirin Traces in Blood by Means of Surface-Enhanced Raman Scattering Spectroscopy. *Journal of Raman Spectroscopy* **2020**, *51* (6). https://doi.org/10.1002/jrs.5853.

(62) Kearns, H.; Goodacre, R.; Jamieson, L. E.; Graham, D.; Faulds, K. SERS Detection of Multiple Antimicrobial-Resistant Pathogens Using Nanosensors. *Anal Chem* **2017**, *89* (23). https://doi.org/10.1021/acs.analchem.7b02653.

(63) Li, L.; Liao, M.; Chen, Y.; Shan, B.; Li, M. Surface-Enhanced Raman Spectroscopy (SERS) Nanoprobes for Ratiometric Detection of Cancer Cells. *J Mater Chem B* **2019**, *7* (5). https://doi.org/10.1039/c8tb02828a.

(64) Lee, S.; Chon, H.; Lee, J.; Ko, J.; Chung, B. H.; Lim, D. W.; Choo, J. Rapid and Sensitive Phenotypic Marker Detection on Breast Cancer Cells Using Surface-Enhanced Raman Scattering (SERS) Imaging. *Biosens Bioelectron* **2014**, *51*. https://doi.org/10.1016/j.bios.2013.07.063.

(65) Moore, T. J.; Moody, A. S.; Payne, T. D.; Sarabia, G. M.; Daniel, A. R.; Sharma, B. In Vitro and in Vivo Sers Biosensing for Disease Diagnosis. *Biosensors*. 2018. https://doi.org/10.3390/bios8020046.

(66) Du, Z.; Qi, Y.; He, J.; Zhong, D.; Zhou, M. Recent Advances in Applications of Nanoparticles in SERS in Vivo Imaging. *Wiley Interdisciplinary Reviews: Nanomedicine and Nanobiotechnology*. 2021. https://doi.org/10.1002/wnan.1672.

(67) Bonifacio, A.; Dalla Marta, S.; Spizzo, R.; Cervo, S.; Steffan, A.; Colombatti, A.; Sergo, V. Surface-Enhanced Raman Spectroscopy of Blood Plasma and Serum Using Ag and Au Nanoparticles: A Systematic Study. *Anal Bioanal Chem* **2014**, *406* (9–10). https://doi.org/10.1007/s00216-014-7622-1.

(68) Premasiri, W. R.; Lee, J. C.; Ziegler, L. D. Surface-Enhanced Raman Scattering of Whole Human Blood, Blood Plasma, and Red Blood Cells: Cellular Processes and Bioanalytical Sensing. *Journal of Physical Chemistry B* **2012**, *116* (31). https://doi.org/10.1021/jp304932g.

(69) Premasiri, W. R.; Chen, Y.; Fore, J.; Brodeur, A.; Ziegler, L. D. SERS Biomedical Applications: Diagnostics, Forensics, and Metabolomics. In *Frontiers and Advances in Molecular Spectroscopy*; 2017. https://doi.org/10.1016/B978-0-12-811220-5.00010-1.

(70) Boyd, S.; Bertino, M. F.; Ye, D.; White, L. S.; Seashols, S. J. Highly Sensitive Detection of Blood by Surface Enhanced Raman Scattering. *J Forensic Sci* **2013**, *58* (3). https://doi.org/10.1111/1556-4029.12120.

(71) Psychogios, N.; Hau, D. D.; Peng, J.; Guo, A. C.; Mandal, R.; Bouatra, S.; Sinelnikov, I.; Krishnamurthy, R.; Eisner, R.; Gautam, B.; Young, N.; Xia, J.; Knox, C.; Dong, E.; Huang, P.; Hollander, Z.; Pedersen, T. L.; Smith, S. R.; Bamforth, F.; Greiner, R.; McManus, B.; Newman, J. W.; Goodfriend, T.; Wishart, D. S. The Human Serum Metabolome. *PLoS One* **2011**, *6* (2). https://doi.org/10.1371/journal.pone.0016957.

(72) Shen, Y.; Jacobs, J. M.; Camp, D. G.; Fang, R.; Moore, R. J.; Smith, R. D.; Xiao, W.; Davis, R. W.; Tompkins, R. G. Ultra-High-Efficiency Strong Cation Exchange LC/RPLC/MS/MS for High Dynamic Range Characterization of the Human Plasma Proteome. *Anal Chem* **2004**, *76* (4). https://doi.org/10.1021/ac034869m.

(73) Barbosa, S.; Taboada, P.; Mosquera, V. Fibrillation and Polymorphism of Human Serum Albumin. In *Bio-nanoimaging: Protein Misfolding and Aggregation*; 2013. https://doi.org/10.1016/B978-0-12-394431-3.00032-8.

(74) Xu, W.; Xiao, J.; Chen, Y.; Chen, Y.; Ling, X.; Zhang, J. Graphene-Veiled Gold Substrate for Surface-Enhanced Raman Spectroscopy. *Advanced Materials* **2013**, *25* (6), 928–933. https://doi.org/10.1002/adma.201204355.

(75) Xie, W.; Herrmann, C.; Kömpe, K.; Haase, M.; Schlücker, S. Synthesis of Bifunctional Au/Pt/Au Core/Shell Nanoraspberries for in Situ SERS Monitoring of Platinum-Catalyzed Reactions. *J Am Chem Soc* **2011**, *133* (48), 19302–19305. https://doi.org/10.1021/ja208298q.

(76) Serafinelli, C.; Fantoni, A.; Alegria, E. C. B. A.; Vieira, M. Plasmonic Metal Nanoparticles Hybridized with 2D Nanomaterials for SERS Detection: A Review. *Biosensors*. MDPI April 1, 2022. https://doi.org/10.3390/bios12040225.

(77) Xu, H.; Aizpurua, J.; Käll, M.; Apell, P. Electromagnetic Contributions to Single-Molecule Sensitivity in Surface-Enhanced Raman Scattering. *Phys Rev E* **2000**, *62* (3), 4318–4324. https://doi.org/10.1103/PhysRevE.62.4318.

(78) Yu, J.; Lin, J.; Chen, M.; Meng, X.; Qiu, L.; Wu, J.; Xi, G.; Wang, X. Amorphous Ni(OH)2 Nanocages as Efficient SERS Substrates for Selective Recognition in Mixtures. *Colloids Surf A Physicochem Eng Asp* **2021**, *631*, 127652. https://doi.org/10.1016/J.COLSURFA.2021.127652.

(79) Wang, X.; She, G.; Xu, H.; Mu, L.; Shi, W. The Surface-Enhanced Raman Scattering from ZnO Nanorod Arrays and Its Application for Chemosensors. *Sens Actuators B Chem* **2014**, *193*, 745–751. https://doi.org/10.1016/J.SNB.2013.11.097.

(80) Le Ru, E. C.; Etchegoin, P. G. SERS Enhancement Factors and Related Topics. *Principles of Surface-Enhanced Raman Spectroscopy* **2009**, 185–264. https://doi.org/10.1016/B978-0-444-52779-0.00010-6.

(81) Hugall, J. T.; Baumberg, J. J.; Mahajan, S. Surface-Enhanced Raman Spectroscopy of CdSe Quantum Dots on Nanostructured Plasmonic Surfaces. *Appl Phys Lett* **2009**, *95* (14). https://doi.org/10.1063/1.3243982.

(82) Yang, L.; Yang, Y.; Lombardi, J. R.; Peng, Y.; Huang, Z. Charge Transfer Enhancement in the Surface-Enhanced Raman Scattering of Ta2O5 Superstructures. *Appl Surf Sci* **2020**, *520*, 146325. https://doi.org/10.1016/J.APSUSC.2020.146325.

(83) Peng, Y.; Lin, C.; Long, L.; Masaki, T.; Tang, M.; Yang, L.; Liu, J.; Huang, Z.; Li, Z.; Luo, X.; Lombardi, J. R.; Yang, Y. Charge-Transfer Resonance and Electromagnetic Enhancement Synergistically Enabling MXenes with Excellent SERS Sensitivity for SARS-CoV-2 S Protein Detection. *Nanomicro Lett* **2021**, *13* (1). https://doi.org/10.1007/s40820-020-00565-4.

(84) Ling, X.; Fang, W.; Lee, Y. H.; Araujo, P. T.; Zhang, X.; Rodriguez-Nieva, J. F.; Lin, Y.; Zhang, J.; Kong, J.; Dresselhaus, M. S. Raman Enhancement Effect on Two-Dimensional Layered Materials: Graphene, h-BN and MoS2. *Nano Lett* **2014**, *14* (6), 3033–3040. https://doi.org/10.1021/nl404610c.

(85) Wang, J.; Ma, F.; Sun, M. Graphene, Hexagonal Boron Nitride, and Their Heterostructures: Properties and Applications. *RSC Advances*. Royal Society of Chemistry 2017, pp 16801–16822. https://doi.org/10.1039/c7ra00260b.

(86) Adomavičiūtė-Grabusovė, S.; Ramanavičius, S.; Popov, A.; Šablinskas, V.; Gogotsi, O.; Ramanavičius, A. Selective Enhancement of Sers Spectral Bands of Salicylic Acid Adsorbate on 2d Ti3 C2 Tx-Based Mxene Film. *Chemosensors* **2021**, *9* (8). https://doi.org/10.3390/chemosensors9080223.

(87) Li, J. F.; Huang, Y. F.; Ding, Y.; Yang, Z. L.; Li, S. B.; Zhou, X. S.; Fan, F. R.; Zhang, W.; Zhou, Z. Y.; Wu, D. Y.; Ren, B.; Wang, Z. L.; Tian, Z. Q. Shell-Isolated Nanoparticle-Enhanced Raman Spectroscopy. *Nature* **2010**, *464* (7287). https://doi.org/10.1038/nature08907.

(88) Song, Z. L.; Chen, Z.; Bian, X.; Zhou, L. Y.; Ding, D.; Liang, H.; Zou, Y. X.; Wang, S. S.; Chen, L.; Yang, C.; Zhang, X. B.; Tan, W. Alkyne-Functionalized Superstable Graphitic Silver Nanoparticles for Raman Imaging. *J Am Chem Soc* **2014**, *136* (39). https://doi.org/10.1021/ja507368z.

(89) Yu, X.; Cai, H.; Zhang, W.; Li, X.; Pan, N.; Luo, Y.; Wang, X.; Hou, J. G. Tuning Chemical Enhancement of SERS by Controlling the Chemical Reduction of Graphene Oxide Nanosheets. *ACS Nano* **2011**, *5* (2). https://doi.org/10.1021/nn102291j.

(90) Pan, X.; Li, L.; Lin, H.; Tan, J.; Wang, H.; Liao, M.; Chen, C.; Shan, B.; Chen, Y.; Li, M. A Graphene Oxide-Gold Nanostar Hybrid Based-Paper Biosensor for Label-Free SERS Detection of Serum Bilirubin for Diagnosis of Jaundice. *Biosens Bioelectron* **2019**, *145*. https://doi.org/10.1016/j.bios.2019.111713.

(91) Huang, J.; Guo, M.; Ke, H.; Zong, C.; Ren, B.; Liu, G.; Shen, H.; Ma, Y.; Wang, X.; Zhang, H.; Deng, Z.; Chen, H.; Zhang, Z. Rational Design and Synthesis of Γfe2O3@Au Magnetic Gold Nanoflowers for Efficient Cancer Theranostics. *Advanced Materials* **2015**, *27* (34). https://doi.org/10.1002/adma.201501942.

(92) Song, J.; Duan, B.; Wang, C.; Zhou, J.; Pu, L.; Fang, Z.; Wang, P.; Lim, T. T.; Duan, H. SERS-Encoded Nanogapped Plasmonic Nanoparticles: Growth of Metallic Nanoshell by Templating Redox-Active Polymer Brushes. *J Am Chem Soc* **2014**, *136* (19). https://doi.org/10.1021/ja502024d.

(93) Satheeshkumar, E.; Makaryan, T.; Melikyan, A.; Minassian, H.; Gogotsi, Y.; Yoshimura, M. One-Step Solution Processing of Ag, Au and Pd@MXene Hybrids for SERS. *Sci Rep* **2016**, *6*. https://doi.org/10.1038/srep32049.

(94) Chugh, D.; Jagadish, C.; Tan, H. Large-Area Hexagonal Boron Nitride for Surface Enhanced Raman Spectroscopy. *Adv Mater Technol* **2019**, *4* (8). https://doi.org/10.1002/admt.201900220.

(95) Welford, K. Surface Plasmon-Polaritons and Their Uses. *Optical and Quantum Electronics*. 1991. https://doi.org/10.1007/BF00619516.

(96) Neubrech, F.; Huck, C.; Weber, K.; Pucci, A.; Giessen, H. Surface-Enhanced Infrared Spectroscopy Using Resonant Nanoantennas. *Chem Rev* **2017**, *117* (7), 5110–5145. https://doi.org/10.1021/acs.chemrev.6b00743.

(97) Neuman, T.; Alonso-González, P.; Garcia-Etxarri, A.; Schnell, M.; Hillenbrand, R.; Aizpurua, J. Mapping the near Fields of Plasmonic Nanoantennas by Scattering-Type Scanning near-Field Optical

Microscopy. *Laser Photon Rev* **2015**, *9* (6), 637–649. https://doi.org/10.1002/lpor.201500031.

(98) Olmon, R. L.; Krenz, P. M.; Jones, A. C.; Boreman, G. D.; Raschke, M. B. Near-Field Imaging of Optical Antenna Modes in the Mid-Infrared. *Opt Express* **2008**, *16* (25), 20295–20305. https://doi.org/10.1364/OE.16.020295.

(99) Alonso-González, P.; Albella, P.; Neubrech, F.; Huck, C.; Chen, J.; Golmar, F.; Casanova, F.; Hueso, L. E.; Pucci, A.; Aizpurua, J.; Hillenbrand, R. Experimental Verification of the Spectral Shift between Near- and Far-Field Peak Intensities of Plasmonic Infrared Nanoantennas. *Phys Rev Lett* **2013**, *110* (20). https://doi.org/10.1103/PhysRevLett.110.203902.

(100) Neubrech, F.; Weber, D.; Lovrincic, R.; Pucci, A.; Lopes, M.; Toury, T.; De La Chapelle, M. L. Resonances of Individual Lithographic Gold Nanowires in the Infrared. *Appl Phys Lett* **2008**, *93* (16). https://doi.org/10.1063/1.3003870.

(101) Adato, R.; Yanik, A. A.; Amsden, J. J.; Kaplan, D. L.; Omenetto, F. G.; Hong, M. K.; Erramilli, S.; Altug, H. Ultra-Sensitive Vibrational Spectroscopy of Protein Monolayers with Plasmonic Nanoantenna Arrays. *Proceedings of the National Academy of Sciences* **2009**, *106* (46), 19227–19232. https://doi.org/10.1073/pnas.0907459106.

(102) Le, F.; Brandl, D. W.; Urzhumov, Y. A.; Wang, H.; Kundu, J.; Halas, N. J.; Aizpurua, J.; Nordlander, P. Metallic Nanoparticle Arrays: A Common Substrate for Both Surface-Enhanced Raman Scattering and Surface-Enhanced Infrared Absorption. *ACS Nano* **2008**, *2* (4), 707–718. https://doi.org/10.1021/nn800047e.

(103) Zhong, Y.; Malagari, S. D.; Hamilton, T.; Wasserman, D.; Malagari, D. Review of Mid-Infrared Plasmonic Materials. *J Nanophotonics* **2015**, *9* (1). https://doi.org/10.1117/1.JNP.9.093791.

(104) De Abajo, F. J. G. Graphene Plasmonics: Challenges and Opportunities. *ACS Photonics* **2014**, *1* (3), 133–152. https://doi.org/10.1021/ph400147y.

(105) Autore, M.; Li, P.; Dolado, I.; Alfaro-Mozaz, F. J.; Esteban, R.; Atxabal, A.; Casanova, F.; Hueso, L. E.; Alonso-González, P.; Aizpurua, J.; Nikitin, A. Y.; Vélez, S.; Hillenbrand, R. Boron Nitride Nanoresonators for Phonon-Enhanced Molecular Vibrational Spectroscopy at the Strong Coupling Limit. *Light Sci Appl* **2018**, *7* (4). https://doi.org/10.1038/lsa.2017.172.

(106) Wang, C.; Meloni, M. M.; Wu, X.; Zhuo, M.; He, T.; Wang, J.; Wang, C.; Dong, P. Magnetic Plasmonic Particles for SERS-Based Bacteria

Sensing: A Review. *AIP Advances*. American Institute of Physics Inc. January 1, 2019. https://doi.org/10.1063/1.5050858.

(107) Majetich, S. A.; Lim, J. K.; Tilton, R. D. Plasmonic Magnetic Nanoparticles for Biomedicine. In *Proceedings of the 31st Annual International Conference of the IEEE Engineering in Medicine and Biology Society: Engineering the Future of Biomedicine, EMBC 2009*; IEEE Computer Society, 2009; pp 4477–4478. https://doi.org/10.1109/IEMBS.2009.5333676.

(108) Stafford, S.; Garcia, R. S.; Gun'ko, Y. K. Multimodal Magnetic-Plasmonic Nanoparticles for Biomedical Applications. *Applied Sciences (Switzerland)*. MDPI AG January 11, 2018. https://doi.org/10.3390/app8010097.

(109) Multari, C.; Miola, M.; Laviano, F.; Gerbaldo, R.; Pezzotti, G.; Debellis, D.; Verné, E. Magnetoplasmonic Nanoparticles for Photothermal Therapy. *Nanotechnology* **2019**, *30* (25). https://doi.org/10.1088/1361-6528/ab08f7.

(110) Wu, C. H.; Cook, J.; Emelianov, S.; Sokolov, K. Multimodal Magneto-Plasmonic Nanoclusters for Biomedical Applications. *Adv Funct Mater* **2014**, *24* (43), 6862–6871. https://doi.org/10.1002/adfm.201401806.

(111) Tomitaka, A.; Arami, H.; Raymond, A.; Yndart, A.; Kaushik, A.; Jayant, R. D.; Takemura, Y.; Cai, Y.; Toborek, M.; Nair, M. Development of Magneto-Plasmonic Nanoparticles for Multimodal Image-Guided Therapy to the Brain. *Nanoscale* **2017**, *9* (2), 764–773. https://doi.org/10.1039/c6nr07520g.

(112) Chen, W.; Xu, N.; Xu, L.; Wang, L.; Li, Z.; Ma, W.; Zhu, Y.; Xu, C.; Kotov, N. A. Multifunctional Magnetoplasmonic Nanoparticle Assemblies for Cancer Therapy and Diagnostics (Theranostics). *Macromol Rapid Commun* **2010**, *31* (2), 228–236. https://doi.org/10.1002/marc.200900793.

(113) Mikoliunaite, L.; Talaikis, M.; Michalowska, A.; Dobilas, J.; Stankevic, V.; Kudelski, A.; Niaura, G. Thermally Stable Magneto-Plasmonic Nanoparticles for SERS with Tunable Plasmon Resonance. *Nanomaterials* **2022**, *12* (16). https://doi.org/10.3390/nano12162860.

(114) Fazio, E.; Gökce, B.; De Giacomo, A.; Meneghetti, M.; Compagnini, G.; Tommasini, M.; Waag, F.; Lucotti, A.; Zanchi, C. G.; Ossi, P. M.; Dell'aglio, M.; D'urso, L.; Condorelli, M.; Scardaci, V.; Biscaglia, F.; Litti, L.; Gobbo, M.; Gallo, G.; Santoro, M.; Trusso, S.; Neri, F. Nanoparticles Engineering by Pulsed Laser Ablation in Liquids:

Concepts and Applications. *Nanomaterials*. MDPI AG November 1, 2020, pp 1–50. https://doi.org/10.3390/nano10112317.

(115) Wheeler, D. A.; Adams, S. A.; López-Luke, T.; Torres-Castro, A.; Zhang, J. Z. Magnetic Fe3O4-Au Core-Shell Nanostructures for Surface Enhanced Raman Scattering. *Ann Phys* **2012**, *524* (11), 670–679. https://doi.org/10.1002/andp.201200161.

(116) Guo, Q. H.; Zhang, C. J.; Wei, C.; Xu, M. M.; Yuan, Y. X.; Gu, R. A.; Yao, J. L. Controlling Dynamic SERS Hot Spots on a Monolayer Film of Fe3O4@Au Nanoparticles by a Magnetic Field. *Spectrochim Acta A Mol Biomol Spectrosc* **2016**, *152*, 336–342. https://doi.org/10.1016/j.saa.2015.07.092.

(117) Kim, M.; Osone, S.; Kim, T.; Higashi, H.; Seto, T. Synthesis of Nanoparticles by Laser Ablation: A Review. *KONA Powder and Particle Journal*. Hosokawa Powder Technology Foundation 2017, pp 80–90. https://doi.org/10.14356/kona.2017009.

(118) Tymoczko, A.; Kamp, M.; Rehbock, C.; Kienle, L.; Cattaruzza, E.; Barcikowski, S.; Amendola, V. One-Step Synthesis of Fe-Au Core-Shell Magnetic-Plasmonic Nanoparticles Driven by Interface Energy Minimization. *Nanoscale Horiz* **2019**, *4* (6), 1326–1332. https://doi.org/10.1039/c9nh00332k.

(119) Yan, Z.; Chrisey, D. B. Pulsed Laser Ablation in Liquid for Micro-/Nanostructure Generation. *Journal of Photochemistry and Photobiology C: Photochemistry Reviews* **2012**, *13* (3), 204–223. https://doi.org/10.1016/J.JPHOTOCHEMREV.2012.04.004.

(120) Zhu, X. P.; Suzuki, T.; Nakayama, T.; Suematsu, H.; Jiang, W.; Niihara, K. Underwater Laser Ablation Approach to Fabricating Monodisperse Metallic Nanoparticles. *Chem Phys Lett* **2006**, *427* (1–3), 127–131. https://doi.org/10.1016/j.cplett.2006.05.119.

(121) Amendola, V.; Scaramuzza, S.; Litti, L.; Meneghetti, M.; Zuccolotto, G.; Rosato, A.; Nicolato, E.; Marzola, P.; Fracasso, G.; Anselmi, C.; Pinto, M.; Colombatti, M. Magneto-Plasmonic Au-Fe Alloy Nanoparticles Designed for Multimodal SERS-MRI-CT Imaging. *Small* **2014**, *10* (12), 2476–2486. https://doi.org/10.1002/smll.201303372.

(122) Tymoczko, A.; Kamp, M.; Prymak, O.; Rehbock, C.; Jakobi, J.; Schürmann, U.; Kienle, L.; Barcikowski, S. How the Crystal Structure and Phase Segregation of Au-Fe Alloy Nanoparticles Are Ruled by the Molar Fraction and Size. *Nanoscale* **2018**, *10* (35), 16434–16437. https://doi.org/10.1039/c8nr03962c.

(123) Wagener, P.; Jakobi, J.; Rehbock, C.; Chakravadhanula, V. S. K.; Thede, C.; Wiedwald, U.; Bartsch, M.; Kienle, L.; Barcikowski, S. Solvent-Surface Interactions Control the Phase Structure in Laser-Generated Iron-Gold Core-Shell Nanoparticles. *Sci Rep* **2016**, *6*. https://doi.org/10.1038/srep23352.

(124) Scaramuzza, S.; Polizzi, S.; Amendola, V. Magnetic Tuning of SERS Hot Spots in Polymer-Coated Magnetic-Plasmonic Iron-Silver Nanoparticles. *Nanoscale Adv* **2019**, *1* (7), 2681–2689. https://doi.org/10.1039/c9na00143c.

(125) Šablinskas, V.; Zdaniauskiene, A.; Adomaviciutė-Grabusove, S.; Stankevičius, E.; Petrikaite, V.; Charkova, T.; Mikoliunaite, L.; Trusovas, R.; Selskis, A.; Niaura, G. Magneto-Plasmonic Nanoparticles for SERS; SPIE-Intl Soc Optical Eng, 2021; p 84. https://doi.org/10.1117/12.2597199.

(126) Amendola, V.; Riello, P.; Meneghetti, M. Magnetic Nanoparticles of Iron Carbide, Iron Oxide, Iron@Iron Oxide, and Metal Iron Synthesized by Laser Ablation in Organic Solvents. *The Journal of Physical Chemistry C* **2010**, *115* (12), 5140–5146. https://doi.org/10.1021/jp109371m.

(127) Testa-Anta, M.; Ramos-Docampo, M. A.; Comesaña-Hermo, M.; Rivas-Murias, B.; Salgueiriño, V. Raman Spectroscopy to Unravel the Magnetic Properties of Iron Oxide Nanocrystals for Bio-Related Applications. *Nanoscale Advances*. Royal Society of Chemistry 2019, pp 2086–2103. https://doi.org/10.1039/c9na00064j.

(128) Vasquez, A.; Samolis, P.; Zeng, J.; Sander, M. Y.; Sander, M. Y. Micro-Structuring, Ablation, and Defect Generation in Graphene with Femtosecond Pulses. *OSA Contin* **2019**, *2* (10), 2925. https://doi.org/10.1364/OSAC.2.002925.

(129) Ferrari, A. C.; Robertson, J. Interpretation of Raman Spectra of Disordered and Amorphous Carbon. *Phys Rev B* **2000**, *61* (20), 14095–14107. https://doi.org/10.1103/PhysRevB.61.14095.

(130) Naguib, M.; Kurtoglu, M.; Presser, V.; Lu, J.; Niu, J.; Heon, M.; Hultman, L.; Gogotsi, Y.; Barsoum, M. W. Two-Dimensional Nanocrystals Produced by Exfoliation of Ti 3AlC 2. *Advanced Materials* **2011**, *23* (37), 4248–4253. https://doi.org/10.1002/adma.201102306.

(131) Bhat, A.; Anwer, S.; Bhat, K. S.; Mohideen, M. I. H.; Liao, K.; Qurashi, A. Prospects Challenges and Stability of 2D MXenes for Clean Energy Conversion and Storage Applications. *npj 2D Materials*

and Applications. Nature Research December 1, 2021. https://doi.org/10.1038/s41699-021-00239-8.

(132) Papadopoulou, K. A.; Chroneos, A.; Parfitt, D.; Christopoulos, S. R. G. A Perspective on MXenes: Their Synthesis, Properties, and Recent Applications. *Journal of Applied Physics*. American Institute of Physics Inc. November 7, 2020. https://doi.org/10.1063/5.0021485.

(133) Anasori, B.; Lukatskaya, M. R.; Gogotsi, Y. 2D Metal Carbides and Nitrides (MXenes) for Energy Storage. *Nature Reviews Materials*. Nature Publishing Group January 17, 2017. https://doi.org/10.1038/natrevmats.2016.98.

(134) Gogotsi, Y.; Anasori, B. The Rise of MXenes. *ACS Nano*. American Chemical Society August 27, 2019, pp 8491–8494. https://doi.org/10.1021/acsnano.9b06394.

(135) Xie, Y.; Naguib, M.; Mochalin, V. N.; Barsoum, M. W.; Gogotsi, Y.; Yu, X.; Nam, K. W.; Yang, X. Q.; Kolesnikov, A. I.; Kent, P. R. C. Role of Surface Structure on Li-Ion Energy Storage Capacity of Two-Dimensional Transition-Metal Carbides. *J Am Chem Soc* **2014**, *136* (17), 6385–6394. https://doi.org/10.1021/ja501520b.

(136) Bai, W.; Xiao, C.; Xie, Y. Bulk Superlattice Analogues for Energy Conversion. *Journal of the American Chemical Society*. 2022. https://doi.org/10.1021/jacs.1c09235.

(137) Yadav, P.; Cao, Z.; Barati Farimani, A. DNA Detection with Single-Layer Ti3C2MXene Nanopore. *ACS Nano* **2021**, *15* (3), 4861–4869. https://doi.org/10.1021/acsnano.0c09595.

(138) Wang, Y.; Yue, Y.; Cheng, F.; Cheng, Y.; Ge, B.; Liu, N.; Gao, Y. Ti3C2Tx MXene-Based Flexible Piezoresistive Physical Sensors. *ACS Nano*. American Chemical Society February 22, 2022, pp 1734–1758. https://doi.org/10.1021/acsnano.1c09925.

(139) Wu, Z.; Wei, L.; Tang, S.; Xiong, Y.; Qin, X.; Luo, J.; Fang, J.; Wang, X. Recent Progress in Ti3C2TxMXene-Based Flexible Pressure Sensors. *ACS Nano*. American Chemical Society December 28, 2021, pp 18880–18894. https://doi.org/10.1021/acsnano.1c08239.

(140) Jing, H.; Zhao, P.; Liu, C.; Wu, Z.; Yu, J.; Liu, B.; Su, C.; Lei, W.; Hao, Q. Surface-Enhanced Raman Spectroscopy for Boosting Electrochemical CO2 Reduction on Amorphous-Surfaced Tin Oxide Supported by MXene. *ACS Appl Mater Interfaces* **2023**, *15* (51), 59524–59533. https://doi.org/10.1021/acsami.3c14682.

(141) Ratzker, B.; Messer, O.; Favelukis, B.; Kalabukhov, S.; Maman, N.; Ezersky, V.; Sokol, M. MXene-Based Ceramic Nanocomposites

Enabled by Pressure-Assisted Sintering. *ACS Nano* **2023**, *17* (1), 157–167. https://doi.org/10.1021/acsnano.2c05774.

(142) Yue, Y.; Liu, N.; Ma, Y.; Wang, S.; Liu, W.; Luo, C.; Zhang, H.; Cheng, F.; Rao, J.; Hu, X.; Su, J.; Gao, Y. Highly Self-Healable 3D Microsupercapacitor with MXene-Graphene Composite Aerogel. *ACS Nano* **2018**, *12* (5), 4224–4232. https://doi.org/10.1021/acsnano.7b07528.

(143) Lee, J.; Hong, S.; Sun, Y.; Lee, S. K.; Hwang, U.; Nam, J. do; Suhr, J. Parasitic Reaction Driven Facile Preparation of Segregated-MXene/Polycarbonate Nanocomposites for Efficient Electromagnetic Interference Shielding. *Surfaces and Interfaces* **2023**, *40*. https://doi.org/10.1016/j.surfin.2023.103101.

(144) Hantanasirisakul, K.; Zhao, M. Q.; Urbankowski, P.; Halim, J.; Anasori, B.; Kota, S.; Ren, C. E.; Barsoum, M. W.; Gogotsi, Y. Fabrication of Ti3C2Tx MXene Transparent Thin Films with Tunable Optoelectronic Properties. *Adv Electron Mater* **2016**, *2* (6). https://doi.org/10.1002/aelm.201600050.

(145) Zhang, D.; Wang, R. (John); Wang, X.; Gogotsi, Y. In Situ Monitoring Redox Processes in Energy Storage Using UV–Vis Spectroscopy. *Nat Energy* **2023**, *8* (6). https://doi.org/10.1038/s41560-023-01240-9.

(146) Li, H.; Chen, S.; Boukhvalov, D. W.; Yu, Z.; Humphrey, M. G.; Huang, Z.; Zhang, C. Switching the Nonlinear Optical Absorption of Titanium Carbide MXene by Modulation of the Surface Terminations. *ACS Nano* **2022**, *16* (1). https://doi.org/10.1021/acsnano.1c07060.

(147) Maleski, K.; Ren, C. E.; Zhao, M. Q.; Anasori, B.; Gogotsi, Y. Size-Dependent Physical and Electrochemical Properties of Two-Dimensional MXene Flakes. *ACS Appl Mater Interfaces* **2018**, *10* (29). https://doi.org/10.1021/acsami.8b04662.

(148) Chertopalov, S.; Mochalin, V. N. Environment-Sensitive Photoresponse of Spontaneously Partially Oxidized Ti3C2 MXene Thin Films. *ACS Nano* **2018**, *12* (6). https://doi.org/10.1021/acsnano.8b02379.

(149) Ghassemi, H.; Harlow, W.; Mashtalir, O.; Beidaghi, M.; Lukatskaya, M. R.; Gogotsi, Y.; Taheri, M. L. In Situ Environmental Transmission Electron Microscopy Study of Oxidation of Two-Dimensional Ti3C2 and Formation of Carbon-Supported TiO2. *J Mater Chem A Mater* **2014**, *2* (35). https://doi.org/10.1039/c4ta02583k.

(150) Hong, J.; Paeng, C.; Park, S.; In, I.; Lee, H.; Velhal, N. B.; Yun, T. H.; Jo, C.; Yim, C. Flashlight Treatment for Instantaneous Structuring of Dense MXene Film into Porous MXene/TiO2 Nanocomposite for

Lithium-Ion Battery Anodes. *Chemical Engineering Journal* **2024**, *484*. https://doi.org/10.1016/j.cej.2024.149598.

(151) Kumar, S.; Aftab, S.; Singh, T.; Kumar, M.; Kumar, S.; Seo, Y. Charge Storage Improvement in Uniformly Grown TiO2 on Ti3C2Tx MXene Surface. *J Alloys Compd* **2023**, *968*. https://doi.org/10.1016/j.jallcom.2023.172181.

(152) Sinha, A.; Dhanjai; Zhao, H.; Huang, Y.; Lu, X.; Chen, J.; Jain, R. MXene: An Emerging Material for Sensing and Biosensing. *TrAC - Trends in Analytical Chemistry*. 2018. https://doi.org/10.1016/j.trac.2018.05.021.

(153) Lorencova, L.; Bertok, T.; Dosekova, E.; Holazova, A.; Paprckova, D.; Vikartovska, A.; Sasinkova, V.; Filip, J.; Kasak, P.; Jerigova, M.; Velic, D.; Mahmoud, K. A.; Tkac, J. Electrochemical Performance of Ti3C2Tx MXene in Aqueous Media: Towards Ultrasensitive H2O2 Sensing. *Electrochim Acta* **2017**, *235*. https://doi.org/10.1016/j.electacta.2017.03.073.

(154) An, H.; Habib, T.; Shah, S.; Gao, H.; Patel, A.; Echols, I.; Zhao, X.; Radovic, M.; Green, M. J.; Lutkenhaus, J. L. Water Sorption in MXene/Polyelectrolyte Multilayers for Ultrafast Humidity Sensing. *ACS Appl Nano Mater* **2019**, *2* (2). https://doi.org/10.1021/acsanm.8b02265.

(155) Echols, I. J.; An, H.; Zhao, X.; Prehn, E. M.; Tan, Z.; Radovic, M.; Green, M. J.; Lutkenhaus, J. L. PH-Response of Polycation/Ti3C2TX MXene Layer-by-Layer Assemblies for Use as Resistive Sensors. *Mol Syst Des Eng* **2020**, *5* (1). https://doi.org/10.1039/c9me00142e.

(156) Song, D.; Jiang, X.; Li, Y.; Lu, X.; Luan, S.; Wang, Y.; Li, Y.; Gao, F. Metal−organic Frameworks-Derived MnO2/Mn3O4 Microcuboids with Hierarchically Ordered Nanosheets and Ti3C2 MXene/Au NPs Composites for Electrochemical Pesticide Detection. *J Hazard Mater* **2019**, *373*. https://doi.org/10.1016/j.jhazmat.2019.03.083.

(157) Kim, H.; Wang, Z.; Alshareef, H. N. MXetronics: Electronic and Photonic Applications of MXenes. *Nano Energy*. 2019. https://doi.org/10.1016/j.nanoen.2019.03.020.

(158) Song, Q.; Ye, F.; Kong, L.; Shen, Q.; Han, L.; Feng, L.; Yu, G.; Pan, Y.; Li, H. Graphene and MXene Nanomaterials: Toward High-Performance Electromagnetic Wave Absorption in Gigahertz Band Range. *Advanced Functional Materials*. 2020. https://doi.org/10.1002/adfm.202000475.

(159) Yin, Y.; Cheng, Z.; Wang, L.; Jin, K.; Wang, W. Graphene, a Material for High Temperature Devices - Intrinsic Carrier Density, Carrier Drift

Velocity, and Lattice Energy. *Sci Rep* **2014**, *4*. https://doi.org/10.1038/srep05758.

(160) Xie, H.; Li, P.; Shao, J.; Huang, H.; Chen, Y.; Jiang, Z.; Chu, P. K.; Yu, X. F. Electrostatic Self-Assembly of Ti3C2Tx MXene and Gold Nanorods as an Efficient Surface-Enhanced Raman Scattering Platform for Reliable and High-Sensitivity Determination of Organic Pollutants. *ACS Sens* **2019**, *4* (9), 2303–2310. https://doi.org/10.1021/acssensors.9b00778.

(161) Limbu, T. B.; Chitara, B.; Garcia Cervantes, M. Y.; Zhou, Y.; Huang, S.; Tang, Y.; Yan, F. Unravelling the Thickness Dependence and Mechanism of Surface-Enhanced Raman Scattering on Ti3C2TXMXene Nanosheets. *Journal of Physical Chemistry C* **2020**, *124* (32), 17772–17782. https://doi.org/10.1021/acs.jpcc.0c05143.

(162) Soundiraraju, B.; George, B. K. Two-Dimensional Titanium Nitride (Ti2N) MXene: Synthesis, Characterization, and Potential Application as Surface-Enhanced Raman Scattering Substrate. *ACS Nano* **2017**, *11* (9), 8892–8900. https://doi.org/10.1021/acsnano.7b03129.

(163) Zhu, X.; Liu, P.; Xue, T.; Ge, Y.; Ai, S.; Sheng, Y.; Wu, R.; Xu, L.; Tang, K.; Wen, Y. A Novel Graphene-like Titanium Carbide MXene/Au–Ag Nanoshuttles Bifunctional Nanosensor for Electrochemical and SERS Intelligent Analysis of Ultra-Trace Carbendazim Coupled with Machine Learning. *Ceram Int* **2021**, *47* (1). https://doi.org/10.1016/j.ceramint.2020.08.121.

(164) Liu, R.; Jiang, L.; Lu, C.; Yu, Z.; Li, F.; Jing, X.; Xu, R.; Zhou, W.; Jin, S. Large-Scale Two-Dimensional Titanium Carbide MXene as SERS-Active Substrate for Reliable and Sensitive Detection of Organic Pollutants. *Spectrochim Acta A Mol Biomol Spectrosc* **2020**, *236*. https://doi.org/10.1016/j.saa.2020.118336.

(165) Elumalai, S.; Lombardi, J. R.; Yoshimura, M. The Surface-Enhanced Resonance Raman Scattering of Dye Molecules Adsorbed on Two-Dimensional Titanium Carbide Ti3C2T: X(MXene) Film. *Mater Adv* **2020**, *1* (2). https://doi.org/10.1039/d0ma00091d.

(166) Salles, P.; Pinto, D.; Hantanasirisakul, K.; Maleski, K.; Shuck, C. E.; Gogotsi, Y. Electrochromic Effect in Titanium Carbide MXene Thin Films Produced by Dip-Coating. *Adv Funct Mater* **2019**, *29* (17). https://doi.org/10.1002/adfm.201809223.

(167) Kumar, S.; Park, H. M.; Singh, T.; Kumar, M.; Seo, Y. Long-Term Stability Studies and Applications of Ti3C2Tx MXene. *Int J Energy Res* **2023**, *2023*. https://doi.org/10.1155/2023/5275439.

(168) Lipatov, A.; Alhabeb, M.; Lukatskaya, M. R.; Boson, A.; Gogotsi, Y.; Sinitskii, A. Effect of Synthesis on Quality, Electronic Properties and Environmental Stability of Individual Monolayer Ti3C2 MXene Flakes. *Adv Electron Mater* **2016**, *2* (12). https://doi.org/10.1002/aelm.201600255.

(169) Alhabeb, M.; Maleski, K.; Anasori, B.; Lelyukh, P.; Clark, L.; Sin, S.; Gogotsi, Y. Guidelines for Synthesis and Processing of Two-Dimensional Titanium Carbide (Ti3C2Tx MXene). *Chemistry of Materials* **2017**, *29* (18). https://doi.org/10.1021/acs.chemmater.7b02847.

(170) Mauchamp, V.; Bugnet, M.; Bellido, E. P.; Botton, G. A.; Moreau, P.; Magne, D.; Naguib, M.; Cabioc'H, T.; Barsoum, M. W. Enhanced and Tunable Surface Plasmons in Two-Dimensional Ti3 C2 Stacks: Electronic Structure versus Boundary Effects. *Phys Rev B Condens Matter Mater Phys* **2014**, *89* (23). https://doi.org/10.1103/PhysRevB.89.235428.

(171) Kang, Z.; Ma, Y.; Tan, X.; Zhu, M.; Zheng, Z.; Liu, N.; Li, L.; Zou, Z.; Jiang, X.; Zhai, T.; Gao, Y. MXene–Silicon Van Der Waals Heterostructures for High-Speed Self-Driven Photodetectors. *Adv Electron Mater* **2017**, *3* (9). https://doi.org/10.1002/aelm.201700165.

(172) Dillon, A. D.; Ghidiu, M. J.; Krick, A. L.; Griggs, J.; May, S. J.; Gogotsi, Y.; Barsoum, M. W.; Fafarman, A. T. Highly Conductive Optical Quality Solution-Processed Films of 2D Titanium Carbide. *Adv Funct Mater* **2016**, *26* (23). https://doi.org/10.1002/adfm.201600357.

(173) Gonçalves, M.; Melikyan, A.; Minassian, H.; Makaryan, T.; Petrosyan, P.; Sargsian, T. Interband, Surface Plasmon and Fano Resonances in Titanium Carbide (Mxene) Nanoparticles in the Visible to Infrared Range. *Photonics* **2021**, *8* (2). https://doi.org/10.3390/photonics8020036.

(174) Schlücker, S. *Surface Enhanced Raman Spectroscopy: Analytical, Biophysical and Life Science Applications*; 2010. https://doi.org/10.1002/9783527632756.

(175) Hu, T.; Hu, M.; Gao, B.; Li, W.; Wang, X. Screening Surface Structure of MXenes by High-Throughput Computation and Vibrational Spectroscopic Confirmation. *Journal of Physical Chemistry C* **2018**, *122* (32). https://doi.org/10.1021/acs.jpcc.8b04427.

(176) Sarycheva, A.; Gogotsi, Y. Raman Spectroscopy Analysis of the Structure and Surface Chemistry of Ti3C2T XMXene. *Chemistry of*

Materials **2020**, *32* (8). https://doi.org/10.1021/acs.chemmater.0c00359.

(177) Benchakar, M.; Loupias, L.; Garnero, C.; Bilyk, T.; Morais, C.; Canaff, C.; Guignard, N.; Morisset, S.; Pazniak, H.; Hurand, S.; Chartier, P.; Pacaud, J.; Mauchamp, V.; Barsoum, M. W.; Habrioux, A.; Célérier, S. One MAX Phase, Different MXenes: A Guideline to Understand the Crucial Role of Etching Conditions on Ti3C2Tx Surface Chemistry. *Appl Surf Sci* **2020**, *530*. https://doi.org/10.1016/j.apsusc.2020.147209.

(178) Naguib, M.; Mashtalir, O.; Lukatskaya, M. R.; Dyatkin, B.; Zhang, C.; Presser, V.; Gogotsi, Y.; Barsoum, M. W. One-Step Synthesis of Nanocrystalline Transition Metal Oxides on Thin Sheets of Disordered Graphitic Carbon by Oxidation of MXenes. *Chemical Communications* **2014**, *50* (56). https://doi.org/10.1039/c4cc01646g.

(179) Hu, T.; Wang, J.; Zhang, H.; Li, Z.; Hu, M.; Wang, X. Vibrational Properties of Ti3C2 and Ti3C2T2 (T = O, F, OH) Monosheets by First-Principles Calculations: A Comparative Study. *Physical Chemistry Chemical Physics* **2015**, *17* (15). https://doi.org/10.1039/c4cp05666c.

(180) Berger, E.; Lv, Z. P.; Komsa, H. P. Raman Spectra of 2D Titanium Carbide MXene from Machine-Learning Force Field Molecular Dynamics. *J Mater Chem C Mater* **2022**, *11* (4). https://doi.org/10.1039/d2tc04374b.

(181) Smith, M. W.; Dallmeyer, I.; Johnson, T. J.; Brauer, C. S.; McEwen, J. S.; Espinal, J. F.; Garcia-Perez, M. Structural Analysis of Char by Raman Spectroscopy: Improving Band Assignments through Computational Calculations from First Principles. *Carbon N Y* **2016**, *100*, 678–692. https://doi.org/10.1016/J.CARBON.2016.01.031.

(182) Ma, J.; Li, W.; Morgan, B. J.; Światowska, J.; Baddour-Hadjean, R.; Body, M.; Legein, C.; Borkiewicz, O. J.; Leclerc, S.; Groult, H.; Lantelme, F.; Laberty-Robert, C.; Dambournet, D. Lithium Intercalation in Anatase Titanium Vacancies and the Role of Local Anionic Environment. *Chem Mater* **2018**, *30* (9), 3078–3089. https://doi.org/10.1021/acs.chemmater.8b00925.

(183) Hou, C.; Xie, J.; Yang, H.; Chen, S.; Liu, H. Preparation of Cu_2O@$TiOF_2$/TiO_2 and Its Photocatalytic Degradation of Tetracycline Hydrochloride Wastewater. *RSC Adv* **2019**, *9* (65), 37911–37918. https://doi.org/10.1039/C9RA07999H.

(184) Liu, S.; Yu, J.; Wang, W. Effects of Annealing on the Microstructures and Photoactivity of Fluorinated N-Doped TiO_2. *Phys Chem Chem*

Phys **2010**, *12* (38), 12308–12315. https://doi.org/10.1039/C0CP00036A.

(185) Wilson, E. B. The Normal Modes and Frequencies of Vibration of the Regular Plane Hexagon Model of the Benzene Molecule. *Physical Review* **1934**, *45* (10). https://doi.org/10.1103/PhysRev.45.706.

(186) Volovšek, V.; Colombo, L.; Furić, K. Vibrational Spectrum and Normal Coordinate Calculations of the Salicylic Acid Molecule. *Journal of Raman Spectroscopy* **1983**, *14* (5), 347–352. https://doi.org/10.1002/jrs.1250140511.

(187) Trivedi, M. K.; Dahryn Trivedi, A. B.; Khemraj Bairwa, H. S. Fourier Transform Infrared and Ultraviolet-Visible Spectroscopic Characterization of Biofield Treated Salicylic Acid and Sparfloxacin. *Nat Prod Chem Res* **2015**, *03* (05). https://doi.org/10.4172/2329-6836.1000186.

(188) Walsh, J. E.; MacCraith, B. D.; Meaney, M.; Vos, J. G.; Regan, F.; Lancia, A.; Artjushenko, S. Sensing of Chlorinated Hydrocarbons and Pesticides in Water Using Polymer Coated Mid-Infrared Optical Fibres. *Analyst* **1996**, *121* (6), 789. https://doi.org/10.1039/an9962100789.

(189) Lu, R.; Li, W.-W.; Mizaikoff, B.; Katzir, A.; Raichlin, Y.; Sheng, G.-P.; Yu, H.-Q. High-Sensitivity Infrared Attenuated Total Reflectance Sensors for in Situ Multicomponent Detection of Volatile Organic Compounds in Water. *Nat Protoc* **2016**, *11* (2), 377–386. https://doi.org/10.1038/nprot.2016.013.

(190) Zhang, D.; Hao, R.; Zhang, L.; You, H.; Fang, J. Ratiometric Sensing of Polycyclic Aromatic Hydrocarbons Using Capturing Ligand Functionalized Mesoporous Au Nanoparticles as a Surface-Enhanced Raman Scattering Substrate. *Langmuir* **2020**, *36* (38), 11366–11373. https://doi.org/10.1021/acs.langmuir.0c02271.

(191) Li, C.; Zhang, Y.; Ye, Z.; Bell, S. E. J.; Xu, Y. Combining Surface-Accessible Ag and Au Colloidal Nanomaterials with SERS for in Situ Analysis of Molecule–Metal Interactions in Complex Solution Environments. *Nat Protoc* **2023**, *18* (9), 2717–2744. https://doi.org/10.1038/s41596-023-00851-6.

(192) Li, C.; Chen, Z.; Huang, Y.; Zhang, Y.; Li, X.; Ye, Z.; Xu, X.; Bell, S. E. J.; Xu, Y. Uncovering Strong π-Metal Interactions on Ag and Au Nanosurfaces under Ambient Conditions via in-Situ Surface-Enhanced Raman Spectroscopy. *Chem* **2022**, *8* (9), 2514–2528. https://doi.org/10.1016/j.chempr.2022.06.008.

(193) Naqvi, S. M. Z. A.; Awais, M.; Wei, Z.; Wu, J.; Raghavan, V.; Hu, J.; Khan, M. I. Chemical Processing and Waste Management Using SERS: A Nanovative Gateway for Sustainable and Robust Bioremediation for Agricultural Lands. *Biomass Convers Biorefin* **2024**. https://doi.org/10.1007/s13399-024-05433-4.

(194) Péron, O.; Rinnert, E.; Toury, T.; Lamy De La Chapelle, M.; Compère, C. Quantitative SERS Sensors for Environmental Analysis of Naphthalene. *Analyst* **2011**, *136* (5), 1018–1022. https://doi.org/10.1039/c0an00797h.

(195) Sandford, S. A.; Bernstein, M. P.; Allamandola, L. J. The Mid-Infrared Laboratory Spectra of Naphthalene ($C_{10}H_8$) in Solid H_2O. *Astrophys J* **2004**, *607* (1), 346–360. https://doi.org/10.1086/383461.

(196) Heath, C.; Myers, M.; Pejcic, B. The Effect of Pressure and Temperature on Mid-Infrared Sensing of Dissolved Hydrocarbons in Water. *Anal Chem* **2017**, *89* (24), 13391–13397. https://doi.org/10.1021/acs.analchem.7b03623.

(197) Aherne, D.; Ledwith, D. M.; Gara, M.; Kelly, J. M. Optical Properties and Growth Aspects of Silver Nanoprisms Produced by a Highly Reproducible and Rapid Synthesis at Room Temperature. *Adv Funct Mater* **2008**, *18* (14), 2005–2016. https://doi.org/10.1002/adfm.200800233.

(198) Jiang, B.; Li, M.; Bai, F.; Yu, H.; Mwenya, T.; Li, Y.; Song, D. Morphology-Controlled Synthesis of Silver Nanoparticles on the Silicon Substrate by a Facile Silver Mirror Reaction. *AIP Adv* **2013**, *3* (3). https://doi.org/10.1063/1.4794956.

(199) Jukić, M.; Sviben, I.; Zorić, Z.; Milardović, S. Effect of Polyvinylpyrrolidone on the Formation AgBr Grains in Gelatine Media. *Croatica Chemica Acta* **2012**, *85* (3), 269–276. https://doi.org/10.5562/cca1919.

(200) Chen, D.; Chen, Q.; Zhang, W.; Ge, L.; Shao, G.; Fan, B.; Lu, H.; Zhang, R.; Yang, D.; Shao, G. Freeze-Dried PVP-Ag+ Precursors to Novel AgBr/AgCl-Ag Hybrid Nanocrystals for Visible-Light-Driven Photodegradation of Organic Pollutants. *Superlattices Microstruct* **2015**, *80*, 136–150. https://doi.org/10.1016/j.spmi.2015.01.004.

(201) Pueskuelev, G.; Zarnorechki, O.; Kabaivanov, Vi. On the Influence of Polyvinylpyrrolidone (PVP) during the Synthesis of Ultrafine Emulsions. *The Journal of Photographic Science* **1974**, *22* (5), 235–238. https://doi.org/10.1080/00223638.1974.11737785.

(202) Zhang, Q.; Li, N.; Goebl, J.; Lu, Z.; Yin, Y. A Systematic Study of the Synthesis of Silver Nanoplates: Is Citrate a “Magic” Reagent? *J Am*

Chem Soc **2011**, *133* (46), 18931–18939. https://doi.org/10.1021/ja2080345.

(203) Munechika, K.; Smith, J. M.; Chen, Y.; Ginger, D. S. Plasmon Line Widths of Single Silver Nanoprisms as a Function of Particle Size and Plasmon Peak Position. *Journal of Physical Chemistry C* **2007**, *111* (51), 18906–18911. https://doi.org/10.1021/jp076099e.

(204) Zhang, Q.; Li, N.; Goebl, J.; Lu, Z.; Yin, Y. A Systematic Study of the Synthesis of Silver Nanoplates: Is Citrate a "Magic" Reagent? *J Am Chem Soc* **2011**, *133* (46), 18931–18939. https://doi.org/10.1021/ja2080345.

(205) Jin, R.; Cao, Y.; Mirkin, C. A.; Kelly, K. L.; Schatz, G. C.; Zheng, J. G. Photoinduced Conversion of Silver Nanospheres to Nanoprisms. *Science (1979)* **2001**, *294* (5548), 1901–1903. https://doi.org/10.1126/science.1066541.

(206) Sun, Y.; Xia, Y. Triangular Nanoplates of Silver: Synthesis, Characterization, and Use as Sacrificial Templates For Generating Triangular Nanorings of Gold. *Advanced Materials* **2003**, *15* (9), 695–699. https://doi.org/10.1002/adma.200304652.

(207) Samanta, S.; Sarkar, P.; Pyne, S.; Sahoo, G. P.; Misra, A. Synthesis of Silver Nanodiscs and Triangular Nanoplates in PVP Matrix: Photophysical Study and Simulation of UV–Vis Extinction Spectra Using DDA Method. *J Mol Liq* **2012**, *165*, 21–26. https://doi.org/10.1016/j.molliq.2011.10.002.

(208) Sherry, L. J.; Jin, R.; Mirkin, C. A.; Schatz, G. C.; Van Duyne, R. P. Localized Surface Plasmon Resonance Spectroscopy of Single Silver Triangular Nanoprisms. *Nano Lett* **2006**, *6* (9), 2060–2065. https://doi.org/10.1021/nl061286u.

(209) Pereira, L.; Mondal, P. K.; Alves, M. Aromatic Amines Sources, Environmental Impact and Remediation. In *Pollutants in Buildings, Water and Living Organisms*; 2015. https://doi.org/10.1007/978-3-319-19276-5_7.

(210) Kirkok, S. K.; Kibet, J. K.; Kinyanjui, T. K.; Okanga, F. I. A Review of Persistent Organic Pollutants: Dioxins, Furans, and Their Associated Nitrogenated Analogues. *SN Appl Sci* **2020**, *2* (10). https://doi.org/10.1007/s42452-020-03551-y.

(211) Jia, C.; Batterman, S. A Critical Review of Naphthalene Sources and Exposures Relevant to Indoor and Outdoor Air. *Int J Environ Res Public Health* **2010**, *7* (7). https://doi.org/10.3390/ijerph7072903.

(212) Howard, P. H. *Handbook of Environmental Fate and Exposure Data for Organic Chemicals*; 1991. https://doi.org/10.1201/9780203719305.
(213) Buckpitt, A.; Boland, B.; Isbell, M.; Morin, D.; Shultz, M.; Baldwin, R.; Chan, K.; Karlsson, A.; Lin, C.; Taff, A.; West, J.; Fanucchi, M.; Van Winkle, L.; Plopper, C. Naphthalene-Induced Respiratory Tract Toxicity: Metabolic Mechanisms of Toxicity. *Drug Metab Rev* **2002**, *34* (4). https://doi.org/10.1081/DMR-120015694.
(214) Lee, B.-D.; Hosomi, M. Ethanol Washing of PAH-Contaminated Soil and Fenton Oxidation of Washing Solution. *Journal of Material Cycles and Waste Management* **2000**, *2*, 24–30. https://doi.org/10.1007/s10163-999-0012-7.
(215) Shiu, W. Y.; Bobra, M.; Bobra, A. M.; Maijanen, A.; Suntio, L.; Mackay, D. The Water Solubility of Crude Oils and Petroleum Products. *Oil and Chemical Pollution* **1990**, *7* (1), 57–84. https://doi.org/10.1016/S0269-8579(05)80034-6.
(216) Page, C. A.; Bonner, J. S.; Sumner, P. L.; Autenrieth, R. L. Solubility of Petroleum Hydrocarbons in Oil/Water Systems. *Mar Chem* **2000**, *70* (1–3), 79–87. https://doi.org/10.1016/S0304-4203(00)00016-5.
(217) Perakis, F.; De Marco, L.; Shalit, A.; Tang, F.; Kann, Z. R.; Kühne, T. D.; Torre, R.; Bonn, M.; Nagata, Y. Vibrational Spectroscopy and Dynamics of Water. *Chem Rev* **2016**, *116* (13), 7590–7607. https://doi.org/10.1021/acs.chemrev.5b00640.
(218) Verma, P. K.; Kundu, A.; Puretz, M. S.; Dhoonmoon, C.; Chegwidden, O. S.; Londergan, C. H.; Cho, M. The Bend+Libration Combination Band Is an Intrinsic, Collective, and Strongly Solute-Dependent Reporter on the Hydrogen Bonding Network of Liquid Water. *J Phys Chem B* **2018**, *122* (9), 2587–2599. https://doi.org/10.1021/acs.jpcb.7b09641.
(219) Ramasesha, K.; De Marco, L.; Mandal, A.; Tokmakoff, A. Water Vibrations Have Strongly Mixed Intra- and Intermolecular Character. *Nat Chem* **2013**, *5* (11), 935–940. https://doi.org/10.1038/nchem.1757.
(220) Constantinidis, P.; Schmitt, H. C.; Fischer, I.; Yan, B.; Rijs, A. M. Formation of Polycyclic Aromatic Hydrocarbons from Bimolecular Reactions of Phenyl Radicals at High Temperatures. *Physical Chemistry Chemical Physics* **2015**, *17* (43), 29064–29071. https://doi.org/10.1039/c5cp05354d.
(221) Scharko, N. K.; Oeck, A. M.; Tonkyn, R. G.; Baker, S. P.; Lincoln, E. N.; Chong, J.; Corcoran, B. M.; Burke, G. M.; Weise, D. R.; Myers, T. L.; Banach, C. A.; Griffith, D. W. T.; Johnson, T. J. Identification of

Gas-Phase Pyrolysis Products in a Prescribed Fire: First Detections Using Infrared Spectroscopy for Naphthalene, Methyl Nitrite, Allene, Acrolein and Acetaldehyde. *Atmos Meas Tech* **2019**, *12* (1), 763–776. https://doi.org/10.5194/amt-12-763-2019.

(222) Lemmens, A. K.; Ferrari, P.; Loru, D.; Batra, G.; Steber, A. L.; Redlich, B.; Schnell, M.; Martinez-Haya, B. Wetting of a Hydrophobic Surface: Far-IR Action Spectroscopy and Dynamics of Microhydrated Naphthalene. *Journal of Physical Chemistry Letters* **2023**, *14* (48), 10794–10802. https://doi.org/10.1021/acs.jpclett.3c02854.

(223) Hudgins, D. M.; Sandford, S. A.; Allamandola, L. J. Infrared Spectroscopy of Polycyclic Aromatic Hydrocarbon Cations. 1. Matrix-Isolated Naphthalene and Perdeuterated Naphthalene. *J Phys Chem* **1994**, *98* (16), 4243–4253. https://doi.org/10.1021/j100067a008.

(224) Hudgins, D. M.; Sandford, S. A. Infrared Spectroscopy of Matrix Isolated Polycyclic Aromatic Hydrocarbons. 1. PAHs Containing Two to Four Rings. *J Phys Chem A* **1998**, *102* (2), 329–343. https://doi.org/10.1021/jp9834816.

(225) Szczepanski, J.; Roser, D.; Personette, W.; Eyring, M.; Pellow, R.; Vala, M. Infrared Spectrum of Matrix-Isolated Naphthalene Radical Cation. *J Phys Chem* **1992**, *96* (20), 7876–7881. https://doi.org/10.1021/j100199a010.

(226) Suthan, T.; Rajesh, N. P.; Dhanaraj, P. V.; Mahadevan, C. K. Growth and Characterization of Naphthalene Single Crystals Grown by Modified Vertical Bridgman Method. *Spectrochim Acta A Mol Biomol Spectrosc* **2010**, *75* (1), 69–73. https://doi.org/10.1016/j.saa.2009.09.041.

(227) Gurusamy, S.; Krishnaveni, K.; Sankarganesh, M.; Sathish, V.; Thanasekaran, P.; Mathavan, A. Multiple Target Detection and Binding Properties of Naphthalene-Derived Schiff-Base Chemosensor. *J Mol Liq* **2021**, *325*. https://doi.org/10.1016/j.molliq.2020.115190.

(228) Berryman, P. J.; Faux, D. A.; Dunstan, D. J. Solvation Pressure in Ethanol by Molecular Dynamics Simulations. *Phys Rev B Condens Matter Mater Phys* **2007**, *76* (10). https://doi.org/10.1103/PhysRevB.76.104303.

(229) Boukhvalov, D. W.; Zhidkov, I. S.; Kurmaev, E. Z.; Fazio, E.; Cholakh, S. O.; D'Urso, L. Atomic and Electronic Structures of Stable Linear Carbon Chains on Ag-Nanoparticles. *Carbon N Y* **2018**, *128*, 296–301. https://doi.org/10.1016/j.carbon.2017.11.044.

(230) Hibble, S. J.; Cheyne, S. M.; Hannon, A. C.; Eversfield, S. G. Beyond Bragg Scattering: The Structure of AgCN Determined from Total Neutron Diffraction. *Inorg Chem* **2002**, *41* (5), 1042–1044. https://doi.org/10.1021/ic015610u.

(231) Artyushenko, V.; Bocharnikov, A.; Sakharova, T.; Usenov, I. Mid-infrared Fiber Optics for 1 — 18 Mm Range. *Optik & Photonik* **2014**, *9* (4), 35–39. https://doi.org/10.1002/opph.201400062.

(232) Butvina, L. N.; Okhrimchuk, A. G.; Butvina, A. L.; Dianov, E. M.; Lichkova, N. V.; Zagorodnev, V. N. Low Loss Micro and Nano Structured Single Mode Crystalline Fibers for 5-15 Mm. In *Advances in Optical Materials*; OSA: Washington, D.C., 2011; p AIThD4. https://doi.org/10.1364/AIOM.2011.AIThD4.

(233) Israeli, S.; Katzir, A. Optical Losses of AgClBr Crystals and Fibers in the Middle Infrared. *Opt Mater (Amst)* **2011**, *33* (11), 1825–1828. https://doi.org/10.1016/j.optmat.2011.07.002.

(234) Butvina, L. N.; Dianov, E. M.; Lichkova, N. V.; Zavgorodnev, V. N.; Kuepper, L. Crystalline Silver Halide Fibers with Optical Losses Lower than 50 DB/Km in Broad IR Region and Their Applications. In *Advances in Fiber Optics*; Dianov, E. M., Ed.; 2000; Vol. 4083, p 238. https://doi.org/10.1117/12.385651.

(235) Bogomolov, A.; Heßling, M.; Wenzel, U.; Princz, S.; Hellmuth, T.; Bernal, M. J. B.; Sakharova, T.; Usenov, I.; Artyushenko, V.; Meyer, H. Development and Testing of Mid-Infrared Sensors for in-Line Process Monitoring in Biotechnology. *Sens Actuators B Chem* **2015**, *221*, 1601–1610. https://doi.org/10.1016/j.snb.2015.07.118.

(236) Bogomolov, A. Developing Multisensory Approach to the Optical Spectral Analysis. *Sensors* **2021**, *21* (10), 3541. https://doi.org/10.3390/s21103541.

(237) Korsakova, E.; Markham, S.; Mani, A.; Silien, C.; Bauer, J.; Tofail, S. A. M.; Zhukova, L.; Korsakov, A. MIR Imaging Bundles of Ordered Silver Halide Polycrystalline Fibres for Thermal Transmission and Imaging. *J Therm Anal Calorim* **2020**, *142* (1), 245–253. https://doi.org/10.1007/s10973-020-09811-8.

(238) Sade, S.; Eyal, O.; Scharf, V.; Katzir, A. Fiber-Optic Infrared Radiometer for Accurate Temperature Measurements. *Appl Opt* **2002**, *41* (10), 1908. https://doi.org/10.1364/AO.41.001908.

(239) Lee, B.; Yoo, W. J.; Cho, D. H.; Jang, K. W.; Chung, S.-C.; Tack, G.-R. Low-Temperature Radiometric Measurements Using a Silver Halide Optical Fiber and Infrared Optical Devices. *Opt Rev* **2007**, *14* (5), 355–357. https://doi.org/10.1007/s10043-007-0355-z.

(240) Raut, H. K.; Ganesh, V. A.; Nair, A. S.; Ramakrishna, S. Anti-Reflective Coatings: A Critical, in-Depth Review. *Energy Environ Sci* **2011**, *4* (10), 3779. https://doi.org/10.1039/c1ee01297e.

(241) Krogman, K. C.; Druffel, T.; Sunkara, M. K. Anti-Reflective Optical Coatings Incorporating Nanoparticles. *Nanotechnology* **2005**, *16* (7), S338–S343. https://doi.org/10.1088/0957-4484/16/7/005.

(242) Sun, J.; Cui, X.; Zhang, C.; Zhang, C.; Ding, R.; Xu, Y. A Broadband Antireflective Coating Based on a Double-Layer System Containing Mesoporous Silica and Nanoporous Silica. *J Mater Chem C Mater* **2015**, *3* (27), 7187–7194. https://doi.org/10.1039/C5TC00986C.

(243) Nagli, L.; German, A.; Katzir, A.; Tschepe, J.; Prapavat, V.; Eberle, H.-G.; Mueller, G. J. Optical Catheters Based on Silver Halide Infrared Fibers. In *Medical and Fiber Optic Sensors and Delivery Systems*; Croitoru, N. I., Miyagi, M., Orellana, G., Verga Scheggi, A., Sterenborg, H. J. C. M., Eds.; 1995; Vol. 2631, pp 208–215. https://doi.org/10.1117/12.229184.

(244) Glebov, V. N.; Leonov, P. G.; Malyutin, A. M.; Yakunin, V. P. Protective Antireflection Coatings for Optical IR Fibers Based on Silver Halogenides. In *Seventh International Conference on Laser and Laser-Information Technologies*; Panchenko, V. Y., Golubev, V. S., Eds.; 2002; Vol. 4644, p 363. https://doi.org/10.1117/12.464165.

(245) Wallner, O.; Artjuschenko, V. G.; Flatscher, R. Development of Silver-Halide Single-Mode Fibers for Modal Filtering in the Mid-Infrared. In *New Frontiers in Stellar Interferometry*; Traub, W. A., Ed.; 2004; Vol. 5491, p 636. https://doi.org/10.1117/12.551609.

(246) Han, Z. W.; Wang, Z.; Feng, X. M.; Li, B.; Mu, Z. Z.; Zhang, J. Q.; Niu, S. C.; Ren, L. Q. Antireflective Surface Inspired from Biology: A Review. *Biosurf Biotribol* **2016**, *2* (4), 137–150. https://doi.org/10.1016/j.bsbt.2016.11.002.

(247) Hobbs, D. S.; McLeod, B. D.; Kelsey, A. F.; Leclerc, M. A.; Sabatino III, E. Automated-Interference-Lithography-Based Systems for Generation of Submicron-Feature Size Patterns. In *Micromachine Technology for Diffractive and Holographic Optics*; Lee, S. H., Cox, J. A., Eds.; 1999; Vol. 3879, pp 124–135. https://doi.org/10.1117/12.360517.

(248) Bushunov, A. A.; Tarabrin, M. K.; Lazarev, V. A. Review of Surface Modification Technologies for Mid-Infrared Antireflection Microstructures Fabrication. *Laser and Photonics Reviews*. 2021. https://doi.org/10.1002/lpor.202000202.

(249) Parker, A. R.; Townley, H. E. Biomimetics of Photonic Nanostructures. *Nat Nanotechnol* **2007**, *2* (6), 347–353. https://doi.org/10.1038/nnano.2007.152.

(250) Wilson, S. J.; Hutley, M. C. The Optical Properties of "Moth Eye" Antireflection Surfaces. *Optica Acta: International Journal of Optics* **1982**, *29* (7), 993–1009. https://doi.org/10.1080/713820946.

(251) Ducros, C.; Brodu, A.; Lorin, G.; Emieux, F.; Pereira, A. Optical Performances of Antireflective Moth-Eye Structures. Comparison with Standard Vacuum Antireflection Coatings for Application to Outdoor Lighting LEDs. *Surf Coat Technol* **2019**, *379*, 125044. https://doi.org/10.1016/j.surfcoat.2019.125044.

(252) Jacobo-Martín, A.; Rueda, M.; Hernández, J. J.; Navarro-Baena, I.; Monclús, M. A.; Molina-Aldareguia, J. M.; Rodríguez, I. Bioinspired Antireflective Flexible Films with Optimized Mechanical Resistance Fabricated by Roll to Roll Thermal Nanoimprint. *Sci Rep* **2021**, *11* (1), 2419. https://doi.org/10.1038/s41598-021-81560-6.

(253) Fu, Y.; Soldera, M.; Wang, W.; Voisiat, B.; Lasagni, A. F. Picosecond Laser Interference Patterning of Periodical Micro-Architectures on Metallic Molds for Hot Embossing. *Materials* **2019**, *12* (20), 3409. https://doi.org/10.3390/ma12203409.

(254) Tarabrin, M. K.; Bushunov, A. A.; Teslenko, A. A.; Sakharova, T.; Hinkel, J.; Usenov, I.; Döhler, T.; Geißler, U.; Artyushenko, V.; Lazarev, V. A. Fabrication of an Antireflection Microstructure on AgClBr Polycrystalline Fiber by Single Pulse Femtosecond Laser Ablation. *Opt Mater Express* **2021**, *11* (2), 487. https://doi.org/10.1364/OME.413971.

(255) Bushunov, A. A.; Tarabrin, M. K.; Lazarev, V. A.; Karasik, V. E.; Korostelin, Y. V.; Frolov, M. P.; Skasyrsky, Y. K.; Kozlovsky, V. I. Fabrication of Anti-Reflective Microstructures on Chalcogenide Crystals by Femtosecond Laser Ablation. *Opt Mater Express* **2019**, *9* (4), 1689. https://doi.org/10.1364/OME.9.001689.

(256) Rank, A.; Lang, V.; Lasagni, A. F. High-Speed Roll-to-Roll Hot Embossing of Micrometer and Sub Micrometer Structures Using Seamless Direct Laser Interference Patterning Treated Sleeves . *Adv Eng Mater* **2017**, *19* (11). https://doi.org/10.1002/adem.201700201.

(257) Yamada, K.; Umetani, M.; Tamura, T.; Tanaka, Y.; Nishii, J. Formation of Antireflective Structure on the Surface of Optical Glass by Molding. In *Advanced Fabrication Technologies for Micro/Nano Optics and Photonics*; Suleski, T. J., Schoenfeld, W. V., Wang, J. J., Eds.; 2008; Vol. 6883, p 688303. https://doi.org/10.1117/12.762408.

(258) Du, G.; Yang, Q.; Chen, F.; Liu, H.; Deng, Z.; Bian, H.; He, S.; Si, J.; Meng, X.; Hou, X. Direct Fabrication of Seamless Roller Molds with Gapless and Shaped-Controlled Concave Microlens Arrays. *Opt Lett* **2012**, *37* (21), 4404. https://doi.org/10.1364/OL.37.004404.

(259) Hobbs, D. S. Laser Damage Threshold Measurements of Anti-Reflection Microstructures Operating in the near UV and Mid-Infrared. In *Laser-Induced Damage in Optical Materials: 2010*; Exarhos, G. J., Gruzdev, V. E., Menapace, J. A., Ristau, D., Soileau, M. J., Eds.; 2010; Vol. 7842, p 78421Z. https://doi.org/10.1117/12.867411.

(260) MacLeod, B. D.; Hobbs, D. S. Long Life, High Performance Anti-Reflection Treatment for HgCdTe Infrared Focal Plane Arrays. In *Infrared Technology and Applications XXXIV*; Andresen, B. F., Fulop, G. F., Norton, P. R., Eds.; 2008; Vol. 6940, p 69400Y. https://doi.org/10.1117/12.778736.

(261) Guo, L. J. Nanoimprint Lithography: Methods and Material Requirements. *Advanced Materials* **2007**, *19* (4), 495–513. https://doi.org/10.1002/adma.200600882.

(262) Bogdanski, N.; Wissen, M.; Möllenbeck, S.; Scheer, H.-C. Structure Size Dependent Recovery of Thin Polystyrene Layers in Thermal Imprint Lithography. *Microelectron Eng* **2007**, *84* (5–8), 860–863. https://doi.org/10.1016/j.mee.2007.01.093.

(263) Heyderman, L. J.; Schift, H.; David, C.; Gobrecht, J.; Schweizer, T. Flow Behaviour of Thin Polymer Films Used for Hot Embossing Lithography. *Microelectron Eng* **2000**, *54* (3–4), 229–245. https://doi.org/10.1016/S0167-9317(00)00414-7.

(264) Han, K.; Chang, C.-H. Numerical Modeling of Sub-Wavelength Anti-Reflective Structures for Solar Module Applications. *Nanomaterials* **2014**, *4* (1), 87–128. https://doi.org/10.3390/nano4010087.

(265) Weiblen, R. J.; Menyuk, C. R.; Busse, L. E.; Shaw, L. B.; Sanghera, J. S.; Aggarwal, I. D. Optimized Moth-Eye Anti-Reflective Structures for As_2S_3 Chalcogenide Optical Fibers. *Opt Express* **2016**, *24* (10), 10172. https://doi.org/10.1364/OE.24.010172.

SANTRAUKA

ĮVADAS

Virpesinė spektroskopija yra universalus analitinis įrankis, dažnai naudojamas medžiagų analizei[1,2] tokiose srityse kaip aplinkos mokslai,[3,4] klinikinė diagnostika,[5,6] maisto sauga,[7] patogenų nustatymas[8] ir kt.[9] Virpesinės spektroskopijos universalumas slypi gebėjime atskirti cheminius junginius,[10] net labai panašius vienas į kitą, pavyzdžiui, izomerus arba konformerus.[11–13] Ji laikoma vienu pagrindinių įrankiu, turinčiu didelį potencialą biologinėje analizėje dėl savo neinvazinio pobūdžio ir tikslumo, kas yra labai svarbu jautriems biologiniams mėginiams. Virpesinė spektroskopija leidžia nustatyti pesticidų likučius,[14] identifikuoti virusus,[15–17] atpažinti vėžinius audinius.[18,19] Ji gali būti taikoma analizuojant kietas medžiagas, skysčius ir dujas.[21]

Virpesinė spektroskopija susideda iš dviejų pagrindinių šakų: Ramano sklaidos ir infraraudonosios sugerties spektroskopijų. Abi šios šakos susijusios su molekulinių ryšių pokyčiais. Nors gauta informacija apie molekulinius virpesius yra panaši ir paprastai papildo viena kitą, skirtumas matomas abiejų spektroskopijų technologijose ir metoduose. Tai yra naudojamos spinduliuotės šaltiniai, optiniai komponentai, detektoriai, kaip ir pagrindiniai fizikiniai mechanizmai, skiriasi.[21]

Signalo stiprinimas virpesinėje spektroskopijoje gali būti pasiektas mažinant spektrinio signalo nuostolius, kurie yra susiję su naudojamomis technologijomis ir metodikomis. Pavyzdžiui, nuotolinėje spektroskopijoje naudojami šviesolaidžiai sukelia papildomus signalo nuostolius dėl (i) sugerties ir sklaidos šviesolaidžio medžiagoje arba (ii) dėl atspindžio signalui keliaujant per kelias terpių ribas.[22,23] Signalo stiprinimas taip pat gali būti pasiektas stiprinant pačių molekulių generuojamą spektrinį signalą. Signalo stiprinimas dėl žymiai intensyvesnio elektrinio lauko aplink plazmoninį paviršių, naudojant metalo nanostruktūras, žinomas kaip paviršiaus sustiprintos Ramano sklaidos (SERS) arba paviršiaus sustiprintos infraraudonųjų spindulių sugerties (SEIRA) spektroskopijos. SERS efektui gauti dažniausiai naudojamos plazmoninės metalo nanodalelės arba nanostruktūrizuoti substratai.[24–27] Šis metodas itin sparčiai vystėsi nuo pat atradimo 1970-aisiais.[28–30] Toks susidomėjimas SERS spektroskopija gali būti priskirtas keliems veiksniams. Pirma, SERS signalo stiprinimas tiesiogiai proporcingas elektrinio lauko stipriui, pakeltam ketvirtuoju laipsniu.[27,31,32] Antra, metalo nanodalelės yra svarbios SERS efektui pasiekti dėl jų

lokalizuoto paviršiaus plazmonų rezonanso (LSPR). Kai nanodalelių LSPR dažnis sutampa su Ramano žadinimo dažniu, tai lemia itin didelį Ramano signalo sustiprėjimą $10^3 – 10^9$ karto.[46] Galiausiai, abi šios sąlygos lemia, kad SERS pasiekia išskirtinai didelį stiprinimo faktorių.[31,33–36]

Analogiškas stiprinimas buvo pastebėtas SEIRA spektroskopijoje 1980-aisiais[37] naudojant metalo nanodaleles. Nors infraraudonosios sugerties skerspjūvis yra žymiai didesnis nei Ramano sklaidos,[38–40] SEIRA efekte stebimas stiprinimas yra palyginti nedidelis, sustiprinantis elektrinį lauką tik dviem eilėmis.[31] Nepaisant to, šis efektas, nors ir ne toks ženklus kaip Ramano spektroskopijoje, gali labai praplėsti infraraudonosios spektroskopijos taikymo galimybes. Pagrindiniai stiprinimo mechanizmai yra panašūs tiek SERS, tiek SEIRA spektroskopijose.[41] Paprastai stiprinimas atsiranda dėl kur kas intensyvesnio elektrinio lauko esančio šalia molekulių, kuris yra laisvųjų krūvių svyravimo plazmoninėje medžiagoje rezultatas. Infraraudonosios sugerties spektroskopijoje šios plazmoninės medžiagos ir plazmonų žadinimo mechanizmai skiriasi lyginant su Ramano sklaidos spektroskopija.

Nepaisant to, SEIRA ir SERS spektroskopijos vis dar susiduria su problemomis, susijusiomis su medžiagomis, naudojamomis stiprinimui išgauti. Norint efektyviau panaudoti šiuos stiprinimo efektus, reikia įveikti šias kliūtis. Viena pagrindinių SERS kliūčių yra signalo neatsikartojamumas, kuris stabdo automatinį SERS taikymą biomedicinoje. Todėl daug pastangų dedama kuriant SERS substratus, kurie generuoja labiau atsikartojantį spektrinį signalą, išlaikant aukštą stiprinimo faktorių. Tokia pažanga palengvintų SERS taikymą moksliniuose tyrimuose ir medicininėje diagnostikoje.

SEIRA spektroskopija susiduria su keliais kitokiais iššūkiais. Pagrindiniai iššūkiai yra žymiai mažesnis stiprinimo faktorius, todėl būtina sukurti tinkamas medžiagas, kurios gali sužadinti plazmoninius rezonansus infraraudonųjų spindulių diapazone ir yra ekonomiškos.[42] Kitas svarbus aspektas yra tai, kad SEIRA metodas turėtų būti labiau pritaikytas platesniam panaudojimui realiomis sąlygomis. Tai reikalauja kruopštaus nanostruktūrų projektavimo ir sudėtingų gamybos technologijų.

Disertacijoje bus naudojami abu virpesinės spektroskopijos tipai, siekiant sustiprinti signalą, gaunamą iš biologinių molekulių. Tai apima SERS substratų signalo atsikartojamumo ir specifiškumo gerinimą. Taip pat apima SEIRA technikos taikymo išplėtimą nuotoliniam aptikimui ir *in situ* tyrimams naudojant infraraudonosios srities šviesolaidžio sistemą.

DISERTACIJOS TIKSLAS

Šios disertacijos tikslas – patobulinti virpesinės spektroskopijos sritis, tiriant naujas substratines medžiagas, skirtas paviršiaus sustiprintai virpesinei spektroskopijai ir siekiant pagerinti biologiškai svarbių molekulių aptikimo efektyvumą.

DISERTACIJOS UŽDAVINIAI

Norint pasiekti disertacijos tikslą, buvo išsikelti šie uždaviniai:

- Ištirti hibridinių nanodalelių magnetinių ir plazmoninių savybių įtaką siekiant pagerinti substratų SERS signalo stiprinimo charakteristikas adenino biomolekulėms.
- Patikrinti $Ti_3C_2T_x$ MXene galimybes panaudojimui SERS spektroskopijoje, tiriant MXene ir salicilo rūgšties sąveiką.
- Kambario temperatūroje suformuoti atspindį mažinančias mikrostruktūras ant šviesolaidžio optinių paviršių, siekiant sustiprinti signalo pralaidumą plačiame bangų ilgių diapazone taikymui infraraudonojoje spektroskopijoje.
- Išplėsti SEIRA spektroskopijos galimybes *in situ* taikymui modifikuojant šviesolaidinio zondo sistemą sidabro nanodalelėmis naftaleno priemaišoms vandenyje aptikti.

DARBO NAUJUMAS IR AKTUALUMAS

Šioje disertacijoje atskleidžiamas svarbus SERS ir SEIRA metodų vaidmuo praplečiant virpesinės spektroskopijos galimybių ribas. Kaip atsakas į daugelį nuolatinių iššūkių, kylančių tobulinant šiuos metodus, disertacijoje pagrindinis dėmesys skiriamas medžiagų manipuliavimui, siekiant pagerinti esamus arba atrasti naujus substratus, kurie galėtų būti panaudoti stiprinimo efektyvumui padidinti. Šiame darbe naudojami SEIRA ir SERS spektroskopijų metodai, siekiant pagerinti biologiškai svarbių molekulių aptikimą.

Aktuali SERS spektroskopijos problema, kurią vis dar reikia išspręsti, yra signalo intensyvumo neatsikartojamumas, kuris šiuo metu riboja automatizuotą SERS taikymą biomedicininėje analizėje.[43–45] Siekiant

sumažinti šią problemą, moksliniai tyrimai aktyviai sutelkiami į substratų, kurie ne tik išlaiko didelį signalo stiprinimą, bet ir signalo atsikartojamumą, paiešką ir tobulinimą.[46] Tai leistų išplėsti SERS taikymo galimybes tiek mokslinių tyrimų, tiek medicininės diagnostikos srityse. Kitos problemos, su kuriomis susiduria SERS spektroskopija apima cheminį substratų užterštumą ir menką specifiškumą tam tikroms molekulėms.

Šiame darbe nagrinėjamas hibridinių metalinių magnetoplazmoninių nanodalelių, pagamintų impulsinės lazerinės ablacijos būdu skysčiuose (PLAL), panaudojimas SERS stiprinimo charakteristikoms gerinti. Šios nanodalelės sprendžia dvi pagrindines SERS substratų problemas: signalo atsikartojamumo trūkumą ir cheminį užterštumą, dėl kurio dažnai atsiranda pašalinių medžiagų spektriniai signalai.[47–49] Integruojant magnetines ir plazmonines savybes, šias nanodaleles galima valdyti, taip sustiprinant SERS signalą ir atsikartojamumą. Šiame darbe pateiktais tyrimais siekiama patvirtinti nanodalelių magnetines ir plazmonines savybes biomolekulių tyrimams, kas įgalintų sukurti patikimesnius SERS pagrindu veikiančius jutiklius, ypač vertingus biochemijoje ir medicininėje diagnostikoje.

Disertacijoje dėmesys skiriamas $Ti_3C_2T_x$ MXene pritaikymui SERS spektroskopijoje. MXene ir salicilo rūgšties sąveika atskleidė spektrinių juostų intensyvumo sustiprėjimą. Ypač sustiprėjo tos juostos, kurios atitinka neplokštuminius, antisimetrinius virpesius, kas būdinga cheminio stiprinimo mechanizmui. Tai indikuoja, kad $Ti_3C_2T_x$ MXene galėtų veikti kaip jutiklis, pasižymintis cheminėmis signalo stiprinimo savybėmis, padidinantis tikslinių molekulių selektyvumą ir labiau atsikartojančius SERS signalus.[50]

SEIRA spektroskopija susiduria su kitokiais iššūkiais, pavyzdžiui, mažesniu stiprinimo faktoriumi. Norint pasiekti didelį stiprinimo faktorių reikia naudoti medžiagas, galinčias sužadinti plazmoninius rezonansus plačiame infraraudonųjų bangų diapazone.[42] Tam paprastai reikia sudėtingų nanostruktūrų gamybos technologijų, tokių kaip elektronų pluošto litografija.[51,52] Dauguma tyrimų, atliekamų SEIRA srityje, yra orientuoti į substrato formavimą ir aukšto stiprinimo faktoriaus gavimą, mažai tyrinėjama SEIRA integracija į realius taikymus.[53]

Šioje disertacijoje siūlomas metodas, susiejantis SEIRA efektą su infraraudonosios srities šviesolaidiniu zondu. Naudojami polikristalinio šviesolaidžio zondo antgaliai, pasižymintys pažeistu visiškuoju vidaus atspindžiu (ATR), kas įgalina ATR-SEIRA spektroskopiją. Tyrimų tikslas buvo išplėsti SEIRA taikymą tiesioginiam ir nuotoliniam panaudojimui ten, kur tradiciniai metodai yra netinkami, pavyzdžiui, mažai tirpių junginių nustatymui vandeninėje aplinkoje. Šiame darbe pademonstruotas naftaleno

aptikimas vandenyje, negalimas standartiniu infraraudonosios sugerties metodu.

Darbe taip pat gilinamasi į infraraudonosios srities šviesolaidžio paviršių struktūrizavimą siekiant padidinti šviesolaidžio pralaidumą. Šviesolaidžio galams modifikuoti buvo naudojami tokie metodai kaip mikrostruktūrų įspaudimas ir profiliavimas. Pagrindinis šio tyrimo aspektas yra atspindį mažinančių mikrostruktūrų suformavimas kambario temperatūroje. Rezultatai demonstruoja paprastas strategijas, skirtas pagerinti infraraudonosios srities šviesolaidžio pralaidumo našumą, o tai gali būti naudinga įvairiems technologiniams ir moksliniams taikymams.

DISERTACIJOS GINAMIEJI TEIGINIAI:

1. Ramano signalo stiprinimas adenino molekulėms gali būti sėkmingai realizuotas panaudojant hibridines nanodaleles, turinčias magnetinių ir plazmoninių savybių, kurios leidžia suformuoti tvarkingą nanodalelių substratą.
2. Salicilo rūgšties molekulių Ramano signalas yra sustiprinamas ant $Ti_3C_2T_x$ MXene substrato, šis stiprinimas priskiriamas cheminiam mechanizmui.
3. Naftaleno molekulių infraraudonosios sugerties signalo stiprinimas gali būti pasiektas naudojant sidabro nanodaleles nusodintas ant šviesolaidinio zondo paviršiaus, įgalinančio pažeistą visiškąjį vidaus atspindį.
4. Infraraudonosios srities šviesolaidyje signalas gali būti sustiprinamas mikrostruktūrizuojant šviesolaidžio optinius galus, kas pagerina signalo pralaidumą.

PAGRINDINIAI REZULTATAI

Signalo stiprinimas panaudojant magnetoplazmonines nanodaleles

- Hibridinės magnetoplazmoninės nanodalelės, turinčios išorinį geležies apvalkalą ir vidinį aukso branduolį buvo sėkmingai pagamintos PLAL metodu, apimančiu lazerinę taikinio abliaciją acetone, todėl gaunamas platus nanodalelių dydžio ir sudėties pasiskirstymas.

- Hibridinės magnetoplazmoninės nanodalelės pasižymi silpnomis magnetinėmis savybėmis, o išliekamasis įmagnetėjimas yra apie 1 emu/g, tai siejama su dideliu aukso kiekiu nanodalelėse.
- Magnetoplazmoninių nanodalelių Ramano spektrai pasižymi plačiomis D ir G juostomis atitinkamai ties 1586–1591 cm^{-1} ir 1328–1360 cm^{-1} ir magnetito spektrine juosta ties 667–674 cm^{-1}.
- Apskaičiuota, kad SERS stiprinimo faktorius naudojant šias nanodaleles yra 5,8 (± 2,8) × 10^4 4-merkaptobenzoinės rūgšties molekulėms, žadinant 633 nm bangos ilgio lazeriu.
- Remiantis SERS spektrais ir teoriniais skaičiavimais, adeninas adsorbuojasi ant magnetoplazmoninių nanodalelių magnetito apvalkalo; tai galima atskirti nuo adsorbcijos aukso paviršiuje pagal spektrinius žymenis: žemadažnes juostas ties 295 cm^{-1} ir 218 cm^{-1}; 1483 cm^{-1} juostos žemadažnį poslinkį į 1464 cm^{-1}.

Mikoliunaite, L.; Stankevičius, E.; **Adomavičiūtė-Grabusovė, S**.; Petrikaitė, V.; Trusovas, R.; Talaikis, M.; Skapas, M.; Zdaniauskienė, A.; Selskis, A.; Šablinskas, V.; Niaura, G. *Magneto-Plasmonic Nanoparticles Generated by Laser Ablation of Layered Fe/Au and Fe/Au/Fe Composite Films for SERS Application.* Coatings, 2023, 13, 1523. DOI: 10.3390/coatings13091523

Signalo stiprinimas panaudojant dvidimensį MXene substratą taikymui sers spektroskopijoje

- Salicilo rūgšties molekulių SERS stiprinimas buvo pastebėtas ant $Ti_3C_2T_x$ MXene substrato žymiai suintensyvėjus neplokštuminiams deformaciniams salicilo rūgšties virpesiams ties 896 cm^{-1}, 681 cm^{-1} ir 654 cm^{-1}.
- Salicilo rūgšties molekulių adsorbciją ant MXene liudija spektriniai žymenys: juostų intensyvumo padidėjimas ties 896 cm^{-1}, 681 cm^{-1} ir 654 cm^{-1}, kartu su žemadažniu virpesių poslinkiu ir karboksilo deformacinio virpesio, kurį atitinka spektrinė juosta ties 771 cm^{-1}, susilpnėjimu.
- Eksperimentinis stiprinimo faktorius (lygus 220, kai žadinančios bangos ilgis yra 532 nm) rodo, kad prie salicilo rūgšties spektrinio stiprinimo daugiausia prisideda cheminis mechanizmas.
- Po salicilo rūgšties adsorbcijos ant MXene substrato elektroninės sugerties spektrai atskleidžia atsirandančias papildomas juostas, atitinkančias teorinių skaičiavimų prognozes: 400 nm juosta

(apskaičiuota ties 428 nm), juostos ties 495 nm ir 595 nm (apskaičiuota ties 564 nm) ir 1080 nm.

Salicilo rūgšties adsorbcija ant MXene substrato buvo eksperimentiškai patvirtinta a) reikšmingu neplokštuminių virpesinių juostų suintensyvėjimu ir b) žemadažniu poslinkio, c) stiprinimo koeficiento reikšme (šimtų eilės), d) elektroninės sugerties spektrų pokyčiu po adsorbcijos. Salicilo rūgšties adsorbcija ant MXene substrato indikuoja sąveiką, kurią palengvina didelis MXene paviršiaus plotas ir akytas paviršius. Šios MXene substrato savybės yra naudingos kuriant SERS jutiklius. Tačiau būsimiems tyrimams labai svarbu atsižvelgti į tai, kad MXene struktūra gali pasikeisti dėl pernelyg didelės lazerio galios. Į šį veiksnį derėtų atsižvelgti kuriant SERS jutiklius.

Adomavičiūtė-Grabusovė, S.; Ramanavičius, S.; Popov, A.; Šablinskas, V.; Gogotsi, O.; Ramanavičius, A. *Selective Enhancement of SERS Spectral Bands of Salicylic Acid Adsorbate on 2D Ti3C2Tx-Based MXene Film*. Chemosensors, 2021, 9, 223. DOI: 10.3390/chemosensors9080223

Adomaviciute-Grabusove, **S.;** Popov, A.; Ramanavicius, S.; Sablinskas, V.; Shevchuk, K.; Gogotsi, O.; Baginskiy, I.; Gogotsi, Y.; Ramanavicius, A. *Monitoring $Ti_3C_2T_x$ MXene Degradation Pathways Using Raman Spectroscopy.* ACS Nano, 2024. DOI: 10.1021/acsnano.4c02150

Signalo stiprinimas nuotolinėje infraraudonosios sugerties spektroskopijoje: seira stiprinimas

- Šviesolaidinis SEIRA pademonstravo naftaleno molekulių spektrinio signalo stiprinimo koeficientą, lygų 90, juostai ties 783 cm^{-1}.
- Nustatyta, naftaleno vandenyje aptikimo riba yra 50 µM arba 0.9 ppm.
- Naftaleno adsorbcija siejama su elektrostatinėmis sąveikomis, kurias patvirtina lengvas naftaleno nuplovimas nuo SEIRA zondo paviršiaus, o tai rodo nekovalentinį molekulės ir paviršiaus sąveikos pobūdį.

Tyrimai patvirtina, kad šviesolaidinis SEIRA metodas, naudojant sidabro halogenido polikristalinio šviesolaidžio zondą ir polimeru dengtas sidabro nanodaleles, gali aptikti naftaleną vandenyje. Taikant šį metodą *in situ* eksperimentams vandeninėje terpėje buvo pasiekta 50 µM naftaleno koncentracijos aptikimo riba, panaši su literatūroje pateikiamais rezultatais ir maždaug atitinkanti 0.9 ppm. Optimizuojant tokius veiksnius kaip nanodalelių

koncentracija, forma ir šviesolaidžio zondo antgalio padengimas gali sumažinti šią aptikimo ribą. Mūsų tyrimo metu užregistruotas spektrų signalo-triukšmo santykis buvo 15, tai gali būti padidinta prailginant spektrų kaupimo laiką.

Teoriniai skaičiavimai (žr. publikaciją nr. 4) patvirtina fizinį naftaleno adsorbcijos pobūdį. Apskaičiuotas minimalus C – Ag jungties ilgis yra 2,62 Å, ir viršija žinomus C – Ag ilgius, o tai rodo, kad tarp Ag ir C atomų nėra kovalentinio ryšio. Be to, reikšmingų naftaleno spektrinių juostų poslinkių nepastebėtas.

Adomaviciute-Grabusove, S.; Bibikova, O.; Sakharova, T.; Artyushenko, V.; Sablinskas, V. *Development of Silver Halide Fiber-Based SEIRA Approach for Detection of Pollutants in Aqueous Environment.* ACS Applied Nano Materials (submitted 2024, May 25)

Signalo stiprinimas nuotolinėje infraraudonosios sugerties spektroskopijoje: Frenelio atspindžio mažinimas

- Polikristalinio infraraudonosios srities šviesolaidžio pralaidumas buvo padidintas iki 22 – 25 % 10,6 μm bangos ilgiui (atitinka 1000 cm^{-1}) kambario temperatūroje sumažinus Frenelio atspindžius.
- Naudojant paprastą ir ekonomišką metodą, vienmatė mikrostruktūra (grioveliai) padidino pralaidumą 7,5 – 7 μm bangos ilgių diapazone.
- Dvidimensė „kandies akių“ rašto struktūra padidino pralaidumą 5 – 17 μm bangos ilgių diapazone (atitinka 600 – 2000 cm^{-1}), naudojant techniškai sudėtingesnę metodiką.
- Profilometriniai matavimai atskleidė, kad šviesolaidžio optinio paviršiaus geometriniai matmenys po mikrostruktūrizavimo skiriasi nuo motininių mikrostruktūrų matmenų, tikėtina dėl šviesolaidžio medžiagos plastiškumo ir polikristališkumo.

Adomavičiūtė-Grabusovė, S.; Hinkel, J.; Usenov, I.; Novikov, A.S.; Sakharova, T.; Döhler, T.; Geißler, U.; Feliksberger, E.; Artyushenko, V. *Microstructuring of the end-surface for silver halide polycrystalline fibers to suppress Fresnel reflection,* Opt. Mater. Express, 2022, 12, 34-48. DOI: 10.1364/OME.439904

IŠVADOS

1. Tiriamoji molekulė, adeninas, adsorbuojasi ant magnetito paviršiaus, o ne aukso, kaip rodo adenino SERS spektroskopija ir teoriniai skaičiavimai.

2. Adsorbuoto adenino SERS stiprinimo faktorius (EF = 5×10^4) parodė, kad magnetinis apvalkalas nesumažina plazmoninės šerdies sukuriamo elektromagnetinio stiprinimo efekto, be to magnetinis apvalkalas gali būti naudojamas manipuliuoti ir išdėstyti nanodaleles pasirinktame paviršiuje, kaip galima matyti iš elektroninės mikroskopijos atvaizdų.
3. $Ti_3C_2T_x$ MXene gardelės irimas prasideda esant 160 kW/cm^2 lazerio galios tankiui, todėl susidaro amorfinė anglis ir angliavandeniliai, o TiO_2 nanodalelių susidarymas (iš pradžių anatazės fazės, po to rutilo fazės) stebimas esant 550 kW/cm^2 galios tankiui.
4. Salicilo rūgšties molekulės SERS signalo stiprinimas buvo pastebėtas naudojant $Ti_3C_2T_x$ pagrindu pagamintą MXene substratą, žymiai suintensyvėjus neplokštuminiams deformaciniams virpesiams ties 896 cm^{-1}, 681 cm^{-1} ir 654 cm^{-1}, apskaičiuotas stiprinimo koeficientas lygus 220.
5. Salicilo rūgšties, adsorbuotos ant MXene substrato paviršiaus virpesinių juostų žemadažnis poslinkis, elektroninės sugerties spektro pokyčiai ir teorinių skaičiavimų rezultatai indikuoja, kad dominuoja cheminis SERS stiprinimo mechanizmas.
6. Dėl infraraudonosios srities šviesolaidinio zondo antgalio padengimo sidabro nanodalelėmis tapo įmanoma aptikti vandenyje ištirpusį naftaleną, identifikuojamą spektrine juosta ties 783 cm^{-1}, o spektrinis signalas buvo padidintas 90 kartų.
7. Infraraudonosios srities šviesolaidžių pralaidumas padidėjo 5 – 17 μm diapazone (atitinka 600 – 2000 cm^{-1}), mikrostruktūrizavus optinius galus; o 10,6 μm bangos ilgiui (kas atitinka 1000 cm^{-1}) pralaidumas padidėjo 22 – 25 %.

CURRICULUM VITAE

Sonata Adomavičiūtė-Grabusovė

Date of birth	23rd of June, 1994
Scientific degree, academic title	**Lecturer, junior researcher; doctoral student**
ORCID iD	0000-0003-2923-0347
Email	sonata.adomaviciute@ff.vu.lt
Competencies	**Vibrational spectroscopy, teaching, preparation of scientific publications, data analysis, planning and conducting experiments**

Scientific interests

Raman spectroscopy and Surface Enhanced Raman Spectroscopy (SERS) for analysis of biological fluids, traces of analyte.
Chemical synthesis of plasmonic nanoparticles (Ag and Au) for SERS and its analysis.
functionalization of nanoparticles.
Fiber-based IR absorption and Raman spectroscopy. Improvement of spectral signal obtained through fiber.
Fiber-based SERS spectroscopy.
Research of novel plasmonic materials for enhancement of spectral signal.

Doctoral studies

University	Title of the thesis	Date	Scientific degree
Vilnius University	Enhancing Vibrational Spectra of Biomolecules Using Non-standard Substrates and Materials	2024	PhD (Physical sciences)

Education

Vilnius University, 2019	MSc (Laser physics)
Vilnius University, 2017	BSc (Physics)

Professional experience

Years	Institution	Position
2015	Biomedical Physics Laboratory, National Cancer Institute	Professional practice
2017-2019	Chemical Physics Institute, VU	Engineer

2019	Chemical Physics Institute, VU	Laboratory technician
2019-now	Chemical Physics Institute, VU	Lecturer
2020-2023	Chemical Physics Institute, VU	Junior researcher
2023-now	Department of Organic Chemistry, FTMC	Junior researcher
2024-now	Ltd "Art21"	Researcher

Teaching activities

Laboratory works for undergraduate students "Vibrational spectroscopy" (in English and Lithuanian)
Laboratory works for students "Physics"
Laboratory works for graduate students "Biosensors" (in English and Lithuanian)
Laboratory works "Optics" for undergraduate students (in English and Lithuanian)

Scientific internships

Place	Duration	Years
Art Photonics GmbH, Germany	3 months	2018
Art Photonics GmbH, Germany	6 months	2020

Research projects, grants and contracts

1. High-level R&D (SMART). Project funded under measure 01.2.2-LMT-K-718 by European Regional Development Fund "Magneto-plasmonic nanoparticles for SERS analysis of biological surfaces (SM-ARTSERS)" 2020 – 2024. **Junior Researcher**
2. Researcher Groups Project funded by Research Council of Lithuania titled "Magneto-plasmonic nanoparticles for UV-SERRS detection of low-molecular-weight biomarkers (MAG-UV-SERRS)". **Junior researcher**
3. International European Institute of Innovation and Technology (EIT) project: Universities For Deep Tech And Entrepreneurship (UNITeD) No. 1620. 2023 – 2024. **Junior Researcher**

Other activities

Organiser of International Conference for Students of Physics and Natural Sciences „Open Readings" – 2015, 2017-2018.
Science Promotion Activities:
Conducting laboratory tours for students, pupils in the laboratories of the Institute of Chemical Physics.
Participation in conference „Presentation of Lithuanian Universities" Karaganda State Medical University, Karaganda, Kazakhstan, September 23-27, 2019.

ACKNOWLEDGEMENT

First and foremost, I would like to express my deepest gratitude to my whole family for support and the invaluable lessons they have imparted from the very beginning. I am heartily thankful for my husband, who has been with me throughout my entire journey as a PhD student. He has been the first editor of my publications (his name should probably be added as a co-author to the majority of them) and my best discussion opponent. While I did not always agree with his ideas, our debates often led to a deeper understanding of physical concepts and phenomena. Indeed, I am fortunate to have a partner with whom I can share a passion for understanding this world.

I am profoundly grateful to my supervisor, Prof. Valdas Šablinskas, for his guidance, insightful feedback, and the vast opportunities to learn. His expertise has been instrumental in shaping my research and bringing this thesis to fruition.

I would also like to extend my heartfelt thanks to my colleagues and lab mates at the Chemical Physics Institute: Martynas, Rasa, Dovilė, Rimantė, Jogilė, and Gerda. Your support, motivation, and collaboration have made this journey both productive and truly enjoyable. The time spent among friends will be unforgettable and especially cherished as I continue my journey in life.

Special thanks to Prof. Justinas Čeponkus for his guidance and the knowledge he generously shared with me.

I would also like to express my gratitude for the opportunity to participate in fascinating and groundbreaking projects with Prof. Gediminas Niaura's scientific group. I am deeply thankful for being welcomed into this forward-thinking research team.

Lastly, I would like to thank everyone who has contributed to this thesis, directly or indirectly. Your support and encouragement have been invaluable, and I am truly grateful.

COPIES OF INCLUDED PUBLICATIONS

coatings

MDPI

Article

Magneto-Plasmonic Nanoparticles Generated by Laser Ablation of Layered Fe/Au and Fe/Au/Fe Composite Films for SERS Application

Lina Mikoliunaite [1,2,*], Evaldas Stankevičius [3], Sonata Adomavičiūtė-Grabusovė [4], Vita Petrikaitė [3], Romualdas Trusovas [3], Martynas Talaikis [1], Martynas Skapas [5], Agnė Zdaniauskienė [1], Algirdas Selskis [5], Valdas Šablinskas [4] and Gediminas Niaura [1,*]

[1] Department of Organic Chemistry, Center for Physical Sciences and Technology (FTMC), Sauletekio Av. 3, LT-10257 Vilnius, Lithuania; martynas.talaikis@ftmc.lt (M.T.); agne.zdaniauskiene@ftmc.lt (A.Z.)
[2] Department of Physical Chemistry, Faculty of Chemistry and Geosciences, Vilnius University, Naugarduko Str. 24, LT-03225 Vilnius, Lithuania
[3] Department of Laser Technologies, Center for Physical Sciences and Technology (FTMC), Savanoriu Av. 231, LT-02300 Vilnius, Lithuania; estankevicius@ftmc.lt (E.S.); vita.petrikaite@ftmc.lt (V.P.); romualdas.trusovas@ftmc.lt (R.T.)
[4] Institute of Chemical Physics, Faculty of Physics, Vilnius University, Sauletekio Av. 3, LT-10257 Vilnius, Lithuania; sonata.adomaviciute@ff.vu.lt (S.A.-G.); valdas.sablinskas@ff.vu.lt (V.Š.)
[5] Department of Characterization of Materials, Center for Physical Sciences and Technology (FTMC), Sauletekio Av. 3, LT-10257 Vilnius, Lithuania; martynas.skapas@ftmc.lt (M.S.); algirdas.selskis@ftmc.lt (A.S.)
* Correspondence: lina.mikoliunaite@ftmc.lt (L.M.); gediminas.niaura@ftmc.lt (G.N.)

Abstract: Magneto-plasmonic nanoparticles were fabricated using a 1064 nm picosecond-pulsed laser for ablation of Fe/Au and Fe/Au/Fe composite thin films in acetone. Nanoparticles were characterized by electron microscopy, ultraviolet-visible (UV-VIS) absorption, and Raman spectroscopy. Hybrid nanoparticles were arranged on an aluminum substrate by a magnetic field for application in surface-enhanced Raman spectroscopy (SERS). Transmission electron microscopy and energy dispersive spectroscopy analysis revealed the spherical core-shell (Au-Fe) structure of nanoparticles. Raman spectroscopy of bare magneto-plasmonic nanoparticles confirmed the presence of magnetite (Fe_3O_4) without any impurities from maghemite or hematite. In addition, resonantly enhanced carbon-based bands were detected in Raman spectra. Plasmonic properties of hybrid nanoparticles were probed by SERS using the adsorbed biomolecule adenine. Based on analysis of experimental spectra and density functional theory modeling, the difference in SERS spectra of adsorbed adenine on laser-ablated Au and magneto-plasmonic nanoparticles was explained by the binding of adenine to the Fe_3O_4 structure at hybrid nanoparticles. The hybrid nanoparticles are free from organic stabilizers, and because of the biocompatibility of the magnetic shell and SERS activity of the plasmonic gold core, they can be widely applied in the construction of biosensors and biomedicine applications.

Keywords: magneto-plasmonic nanoparticles; laser ablation; SERS; thin film; magnetite; gold; core-shell nanoparticles

Citation: Mikoliunaite, L.; Stankevičius, E.; Adomavičiūtė-Grabusovė, S.; Petrikaitė, V.; Trusovas, R.; Talaikis, M.; Skapas, M.; Zdaniauskienė, A.; Selskis, A.; Šablinskas, V.; et al. Magneto-Plasmonic Nanoparticles Generated by Laser Ablation of Layered Fe/Au and Fe/Au/Fe Composite Films for SERS Application. *Coatings* **2023**, *13*, 1523. https://doi.org/10.3390/coatings13091523

Academic Editor: Roberto Teghil

Received: 11 July 2023
Revised: 19 August 2023
Accepted: 25 August 2023
Published: 30 August 2023

1. Introduction

Magneto-plasmonic nanoparticles are composites that combine magnetic and plasmonic materials in a confined nanoscale area and simultaneously exhibit magnetic and plasmonic properties [1–4]. They typically use Fe, Co, or Ni-based magnetic materials. The most popular among them are iron and magnetite. Fe_3O_4 is known to be nontoxic, biocompatible, and possesses an inducible magnetic moment; thus, it can be used for hyperthermia, targeted drug delivery, extraction of biomolecules, lab-on-a-chip construction, and other biomedical applications [5–8]. A noble metal (Au, Ag, or Pt) that separately could be used for resonance energy processes such as nanometal surface energy transfer

(NSET), fluorescence resonance energy transfer (FRET), cascade energy transfer (CET), metal-enhanced fluorescence (MEF), plasmon-induced resonance energy transfer (PIRET), and surface-enhanced Raman scattering (SERS) [9,10], adds to the system plasmonic components that could expand the application field of these nanostructures to stable molecule detection using SERS [11]. Such nanoparticles may consist of a noble metal layer/magnetic core or form an inverse structure [1]. Magneto-plasmonic nanoparticles are one of the new multifunctional materials for medical applications [3,4]. Nanocomposites of various combinations are used for phototherapy [12], as contrast agents in magnetic resonance imaging [13], brain disease treatment [14], cancer therapy and diagnostics [15], drug delivery, and hyperthermia applications [16]. For applications in diagnostics and even therapeutic fields, the plasmonic properties of these nanoparticles are of the utmost importance. The plasmonic nature of these nanoparticles leads to high molecular sensitivity in cases of application in SERS or high photothermal efficiency, while magnetic properties ensure control of the spatial position of nanoparticles.

Laser irradiation has proven to be a versatile tool for nanoparticle synthesis [17]. Laser ablation is a method for producing nanoparticles, nanowires, quantum dots, and core-shell nanoparticles [18–21]. Laser can be used to form nanoparticles by melting thin metal coatings or targets [19,20,22], ablation of metal granules [23], forming noble metal surfaces [24], or Si substrates that could later be covered with SERS active metal [25,26]. During the ablation process in gas, nanoparticles are created by the nucleation and growth of laser-evaporated species in a background gas. The ultra-fast vapor quenching is helpful for the production of high-purity nanoparticles in the quantum size range (<10 nm) [18]. One of the most commonly used methods for generating laser nanoparticles is pulsed laser ablation in liquids [27,28]. In this method, a pulsed laser beam is focused onto a solid target placed in a liquid medium that could be acetone, water, methyl methacrylate, or others [29]. Pulsed laser ablation in liquids is an attractive technique as it is chemically clean and requires no additional chemicals that, in some cases, may even be toxic [30,31]. This method is also attractive as the available target and fluid materials are extensive, including various metals and their alloys, semiconductors, oxides, alloys, and carbon allotropes.

Magneto-plasmonic Fe/Au alloy nanoparticles can be successfully ablated using solid Au-Fe targets in ethanol [32] and acetone [33]. Laser-induced generation of alloy and core-shell nanoparticles by ablation of multilayer films was previously investigated by Amendola et al. [34,35]. Alternatively, alloys of plasmonic/magnetic or plasmonic/plasmonic metals could also be used [25,29,36]. Nanosecond laser ablation yields higher relative concentrations of core-shell nanoparticles than picosecond ablation due to differences in laser radiation-plasma plume interaction time frames [35]. In the reference [34], nanoparticles were formed using a nanosecond laser of 1064 nm wavelength. Experiments were carried out with water and ethanol. Alloy nanoparticles were synthesized by ablation of Fe/Au layers of different thicknesses and compositions. Using ethanol as an ablation medium, alloy nanoparticles were formed with sizes of 7–8 nm with a standard deviation of 4–6 nm, whereas core-shell nanoparticles with a Fe core were achieved using water. Their results proved successful in the synthesis of alloy nanoparticles from films of 100–200 nm order thickness. Recently, authors demonstrated the formation of Fe/Au nanoparticles using laser ablation of bulk alloy targets [32]. Ablated nanoparticles or surface structures could later be decorated with chemically synthesized structures [24,37,38] or could be used as reductors of metal salts [22,39]. The produced nanoparticles were applied for rat blood analysis [23], detection of explosives [22,24,40], pyrromethene [41], antibiotics [26], pesticides [24,36,39], and many other molecules [38].

In our work, picosecond-laser ablation experiments for nanoparticle generation were carried out in acetone. It acts as a medium for the growth and stabilization of the nanoparticles. Acetone has been widely used in nanomaterial synthesis due to its ability to solubilize various metal precursors and provide a controlled environment for nanoparticle formation. The targets for ablation were created as composite coatings of varying thicknesses and layers of Fe/Au and Fe/Au/Fe. Various parameters were altered and optimized for the

synthesis of stable, plasmonic nanoparticles that also possess magnetic properties. These nanoparticles were applied for SERS analysis of the adenine molecule. The obtained results were compared to DFT-calculated spectra and showed that biological molecules preferably adsorb on magnetite surfaces.

2. Materials and Methods

2.1. Materials

Iron and gold targets for laser ablation were obtained from Micro-to-Nano (Haarlem, The Netherlands). Acetone (≥99.9%), used for the ablation procedure, was purchased from Honeywell (Charlotte, NC, USA). Adenine (≥99%), D_2O (99.9 atom% D), and ethanol (99.5%) were purchased from Sigma-Aldrich (St. Louis, MO, USA), and deionized water (18.2 MΩ·cm) was obtained from the Direct-Q 3UV purification system (St. Louis, MO, USA). 4-mercaptobenzoic acid (4-MBA) for SERS was from Thermo Scientific (Loughborough, UK).

2.2. Target Preparation

Gold and iron coatings (Fe/Au and Fe/Au/Fe) were prepared on a soda-lime glass substrate with a thickness of 1 mm using magnetron sputtering machine Q150T ES (Quorum, Laughton, UK) at room temperature in an Ar atmosphere of 10^{-3} bar with a deposition rate of 0.27 and 0.22 nm/s for gold and iron films, respectively. Gold and iron targets with a purity of 99.99% (Au) and 99.95% (Fe) were used. The thickness of thin metal films was controlled by varying the sputtering time. During deposition, the sample holder was rotating at 8 rpm. Before deposition, the soda-lime glass substrates were cleaned by washing with deionized water and holding for 2 h in concentrated H_2SO_4. After that, substrates were washed with water and sonicated two times in ethanol for 20 min. Finally, substrates were dried under nitrogen flow. The coating types and layer thicknesses are presented in Table 1.

Table 1. Composition of tested Fe/Au and Fe/Au/Fe layered coatings used in laser ablation experiments.

Denotation	1st Layer Fe Layer Thickness (nm)	2nd Layer Au Layer Thickness (nm)	3rd Layer Fe Layer Thickness (nm)
Fe50/Au150	50	150	-
Fe100/Au150	100	150	-
Fe50/Au150/Fe25	50	150	25
Fe50/Au150/Fe50	50	150	50

2.3. Laser Ablation Procedure

A picosecond laser Atlantic (Ekspla, Vilnius, Lithuania) was used to generate magnetoplasmonic nanoparticles. A Galvoscanner hurrySCAN (ScanLab, Puchheim, Germany) with a 160 mm focal distance focusing objective was used for beam control. The pulse duration was 10 ps, the laser irradiation wavelength was 1064 nm, and the pulse repetition rate was 100 kHz. The laser beam was focused on a sample target inside the chamber, filled with acetone. The whole coated sample area was scanned with a laser beam using a hatch pattern. The distance between adjacent lines was 50 μm, scanning speed was 500 mm/s. The average laser irradiation power was 5 W, and the laser fluence was ~1.3 J/cm^2. The chosen fluence was similar to other authors' works: 1 J/cm^2 [42], 0.8 J/cm^2 [43], and 2.5 J/cm^2 [44]. The setup for laser ablation experiments is shown in Figure 1.

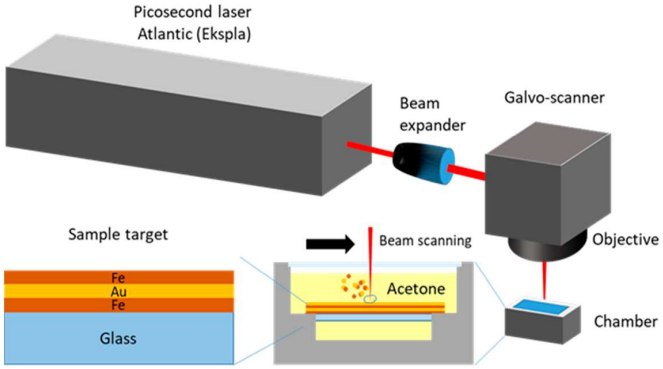

Figure 1. Experimental setup for the generation of magneto-plasmonic nanoparticles by laser ablation procedure.

Pure gold nanoparticles for comparison were also obtained using laser ablation. Gold targets were placed in a chamber filled with deionized water with 0.024 mM KCl. The final volume of the liquid was 19 mL. Ablation was conducted for 5 min, using 5 W of laser power.

2.4. Sample Characterization and Preparation for SERS Measurements

Ablated nanoparticles were characterized using UV-VIS-NIR, TEM, and SEM equipment. For extinction spectra measurements, a UV-VIS-NIR Lambda 1050 spectrometer (Perkin Elmer, Waltham, MA, USA) was employed (in the range 300–800 nm). Nanoparticles were imaged using scanning electron microscopy (SEM) using a dual-beam system, Helios Nanolab 650 (Thermo Scientific, Eindhoven, The Netherlands), and a transmission electron microscope, FEI Tecnai G2 F20 X-TWIN (Thermo Scientific, Eindhoven, The Netherlands).

The preparation of SERS substrates was performed as follows: The Nd magnet was wrapped in aluminum foil, cleaned with ethanol, dried, and immersed in a colloid of generated Fe/Au or Fe/Au/Fe nanoparticles for 60 s. The extracted magnet was washed with deionized water and dried. For comparison, pure gold nanoparticles were prepared by simply dropping a few drops of generated solution on aluminum foil and drying. The plasmonic properties of the generated nanoparticles were verified by measuring the SERS spectra of the test molecules (adenine and 4-mercaptobenzoic acid). The enhancement factor (*EF*) was calculated using 4-mercaptobenzoic acid. A 0.1 mM adenine solution in water was selected to evaluate the SERS performance for the analysis of biomolecules. One drop (25 µL) of a 0.1 mM adenine solution was dripped on the previously prepared SERS substrate. Spectra were measured by focusing a laser beam on the substrate with magneto-plasmonic nanoparticles in the presence of a water solution containing adenine.

The SERS spectra were measured using a MonoVista CRS+ spectrometer (S&I, Warstein, Germany) with an integrated optical microscope with a 100×/0.80 NA objective. An excitation wavelength of 632.8 nm was used, and the laser beam was focused on an area of approximately 1 μm^2 on the sample. The Raman spectra of the magneto-plasmonic nanoparticle substrate were recorded at a power of 0.8 mW. SERS spectra of the adsorbed adenine were acquired with a power of 2.5 mW. Raman spectra of adenine in solid state and 7.0 mM H_2O and D_2O solutions were recorded with the Raman spectrometer HyperFlux PRO Plus (Tornado Spectral Systems, Mississauga, ON, Canada), equipped with a thermoelectrically cooled fiber-optic cable and a 785 nm wavelength laser source. The powder sample was probed using 30 mW power and 10 s accumulation, while the adenine solutions were probed with 495 mW and 600 s. SERS enhancement factors at excitation

wavelengths 632.8, 785, and 830 nm were evaluated by using an inVia Raman spectrometer (Renishaw, Wotton-under-Edge, Gloucestershire, UK).

2.5. Density Functional Theory Modelling

Optimized geometry and numerical frequencies of adenine and adenine complexes in a vacuum were calculated using Orca 5.0.1 software [45] at the B3LYP theory level using the def2-TZVPP basis set. No imaginary frequencies were obtained.

3. Results

Laser ablation procedures for layered structures were conducted in deionized water, acetone, and isopropanol. In deionized water, the obtained nanoparticles aggregated in a few minutes after laser ablation and were not suitable for further investigation. Nanoparticle stability in isopropanol was moderate; however, the best results were obtained using acetone, so this solvent was chosen.

3.1. Structural and Magnetic Characterization of Magneto-Plasmonic Nanoparticles

The magneto-plasmonic nanoparticles ablated in acetone possessed magnetic properties, which can be confirmed by SEM images (Figure 2) of nanoparticles on aluminum foil substrates, oriented according to the magnetic field lines. From the images, different-sized nanoparticles are seen up to a few hundred nanometers.

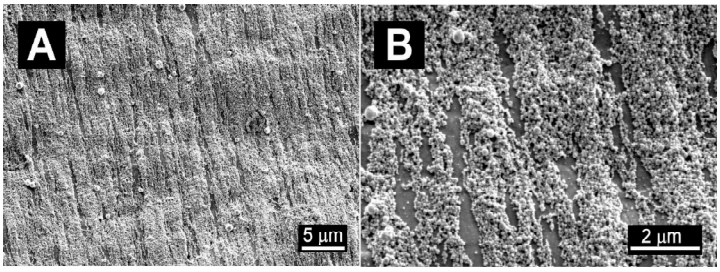

Figure 2. SEM image of magneto-plasmonic nanoparticles (Fe50/Au150/Fe25) concentrated by a magnetic field on an aluminum foil substrate. Two magnifications are presented: a scale bar of 5 µm (**A**) and 2 µm (**B**).

Figure 3 displays TEM measurements of the magneto-plasmonic nanoparticles generated from the Fe50/Au150/Fe25 and Fe50/Au150 targets. TEM imaging revealed the formation of spherical core-shells and homogeneous nanoparticles with a wide size distribution. The ImageJ program was used to calculate the size distribution of nanoparticles. The nanoparticles' diameter in samples Fe50/Au150/Fe25 was 46 $\pm$ 12 nm, while samples Fe50/Au150 showed 59 $\pm$ 28 nm. The energy dispersive spectroscopy (EDS) analysis (Figure 4B) confirmed that the core is composed of Au and is covered with a shell containing Fe and O. The high overall amount of oxygen in the sample is due to its abundance in the atmosphere and on the sample; however, a slightly higher percentage of O on the nanoparticles, especially at the sides of them, indicates the formation of magnetite. Thus, from the TEM images, the darker nanoparticles are composed of gold, while the lighter ones are iron oxide. The separately distributed homogeneous gold and iron nanoparticles are also registered. The amount of carbon in the sample is high due to the sample preparation for TEM; a copper mesh with a carbon layer was used for visualization, so detection of carbon in the ablated sample is hardly possible.

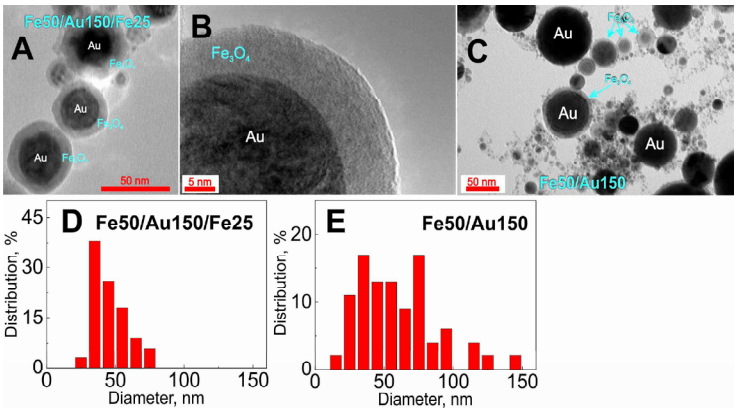

Figure 3. TEM images of magneto-plasmonic nanoparticles generated from Fe50/Au150/Fe25 targets at different magnifications: 50 nm scale bar (**A**) and 5 nm scale bar (**B**) and nanoparticles from Fe50/Au150 target (**C**). The size distribution of nanoparticles is presented below: for Fe50/Au150/Fe25 (**D**) and for Fe50/Au150 (**E**).

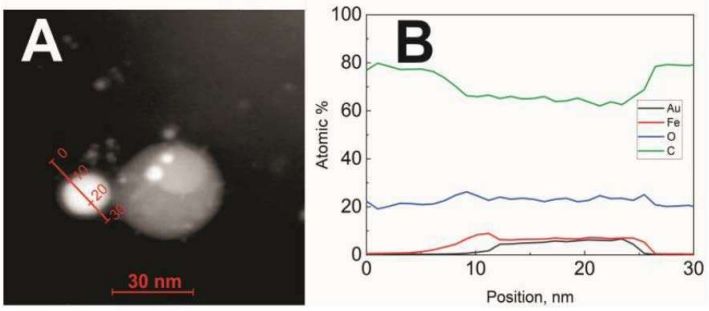

Figure 4. TEM image of the analyzed nanoparticle (**A**); EDS analysis of the composition of magneto-plasmonic core-shell nanoparticles generated from Fe50/Au150/Fe25 targets (**B**).

The magnetization of the sample was tested with an external magnet attached to the side of the bottle with the laser-ablated sample. The result is presented in Figure S1. In part B, the majority of nanoparticles are attracted to the side of the bottle. However, some nanoparticles remain in solution. These might be separate gold nanoparticles or very small iron oxide nanoparticles that are not affected by an external magnetic field. The magnetization of the sample was measured as described in our previous work [46]. The experimental results and Brillouin function approximation are presented in Figure S2. It revealed that the sample is weakly magnetic. Obtained parameters: coercivity ~26 mT; saturations of mass magnetization ~2.7 emu/g; remanent magnetization ~1 emu/g. The magnetization is divided by the mass of the sample, which includes the gold part as well, resulting in weak residual magnetization. High coercivity is obtained due to larger (200–300 nm) nanoparticles.

3.2. UV-VIS Spectroscopic Analysis

The extinction spectra of the nanoparticle solution obtained from two-layered (Figure 5A) or three-layered (Figure 5B) systems show a distinct plasmon resonance band characteristic for gold nanoparticles, with the maximum at a 509–528 nm interval. The optical extinction spectrum corresponds to the absorption of spherical Au nanoparticles

of size 10–60 nm [47,48]. In addition to this, the general rise of the background going to the shorter wavelengths is visible. It can be attributed to the scattering effect of the nonplasmonic iron nanoparticles. This rise was also clearly observed in our previous work related to the synthesis and analysis of magneto-plasmonic nanoparticles [46]. The plasmonic peaks in a two-layer system are more distinguished from the background in comparison to a three-layered system (Figure 5). This could be due to a larger amount of Fe nanoparticles produced from a three-layer target that creates a higher background and hides part of the plasmonic band. The slight shift of the plasmonic resonance band to a lower wavelength in the case of nanoparticles prepared from three-layered coatings might be related to the smaller diameter of the nanoparticles and/or, to some extent, the formation of AuFe nanoalloys [34].

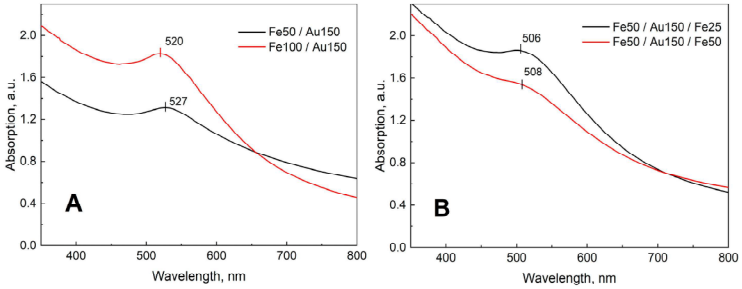

Figure 5. UV-VIS extinction spectra of magneto-plasmonic nanoparticles obtained by ablation of two-layer (**A**) and three-layer (**B**) metal films in acetone in the wavelength range 350−800 nm.

3.3. SERS of Magneto-Plasmonic Nanoparticles

Prior to the analysis of the adsorbed probe biomolecule adenine, we recorded SERS spectra of bare magneto-plasmonic nanoparticles (Figure 6). The SERS spectra show broad spectral features in the vicinity of 1586–1591 and 1328–1360 cm^{-1} which are characteristic of carbon material G and D vibrational bands, respectively [49–52]. The intensity of these bands is resonantly enhanced; therefore, even a small amount of carbon material may result in relatively intense Raman features. This carbon material was most likely created during the laser-ablation process in acetone. Similar bands were previously observed in the Raman spectra of magneto-plasmonic nanoparticles prepared by laser ablation in organic solvents [53]. We found that the relative intensity of these bands varied from sample to sample. We were not able to connect the relative intensity of carbon bands with the composition of films used for laser ablation. The clearly defined band at 667–674 cm^{-1} signifies the presence of magnetite (Fe_3O_4) at the surface of hybrid nanoparticles [54,55]. This band was assigned to the A_{1g} symmetry mode associated with the symmetric stretching vibration of Fe-O bonds [32]. Importantly, no bands characteristic of maghemite (γ-Fe_2O_3, broad peaks at 350, 500, and 700 cm^{-1}) or hematite (α-Fe_2O_3, strong and narrow bands at 412 and 290 cm^{-1}) structures are visible in the spectrum, indicating the presence of the pure magnetite phase [56]. One can see that the relative intensity of the magnetite band compared with carbon features is slightly higher in the case of a sample prepared with a higher amount of Fe in the initial coating (a three-layer film) (Figure 6). The discussed spectral features are distinct for all synthesized nanoparticles, irrelevant to the ablation target used. Only subtle variations appear in the parameters of carbon compounds and magnetite bands.

The enhancement factor (*EF*) for these nanoparticles was calculated using the SERS reporter molecule 4-MBA [57,58]. The obtained value for the 632.8 nm excitation wavelength is 5.8 ($\pm$2.8) $\times$ 10^4; the calculation procedure is presented in Supporting Information. More than ten times lower *EF* was obtained for the 785 and 830 nm excitation wavelengths (Figure S3). Shumskaya et al. indicated that an *EF* of the order of 10^4 is sufficient for SERS

applications in the construction of chemo- and biosensors [59]. Such an *EF* was estimated for Ni/Au core-shell magneto-plasmonic nanoparticles by using Methylene Blue dye as a test analyte [59]. Li et al. reported an *EF* of 1.1 × 10^5 for Fe_3O_4/Au nanostructures by analysis of SERS spectra from malachite green dye [60]. The magneto-plasmonic Fe_3O_4/Au composites prepared by the solvent-thermal method exhibited SERS analytical *EF* exceeding 2 × 10^5 for the analysis of 4-nitrothiophenol [61]. Ye et al. developed silicon-based substrates with microarrays where magneto-plasmonic Fe_3O_4/Au nanoparticles were assembled for SERS analysis of rhodamine 6G dye [62]. Such structures gave SERS EFs higher than 10^6. Hu et al. reported on the possibility of tuning SERS *EF* from 10^4 to 10^7 by using liquid substrates containing suspensions of Fe_3O_4 /Au nanoparticles [63]. It was found that magneto-plasmonic Fe_2O_3/Au nanoparticles are able to provide SERS *EF* around 10^5 by using 2-naphthalenethiol as a probe molecule [64].

The structure of magneto-plasmonic nanoparticles obtained in this work is different compared with laser-ablation synthesized nanoparticles in acetone from bulk Fe-Au tar-get [29]. Wagener et al. demonstrated the solvent-controlled phase structure of nanoparticles; an iron-gold core-shell structure was obtained in acetone [29]. The mechanism of the laser ablation process in liquids is very complex and still under extensive development [65,66]. The difference might be associated with the laser treatment of thin coatings in our study and the application of a picosecond-pulsed laser instead of the femtosecond-pulsed radiation employed in our work [65]. TEM images (Figure 4) clearly show lower electronic contrast for the shell of nanoparticles compared with the core, which has a lower electronic density typical for iron oxides [53].

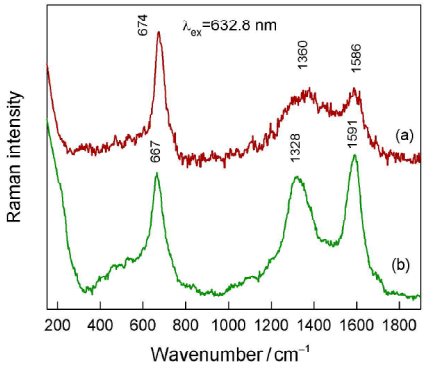

Figure 6. SERS spectra of bare magneto-plasmonic nanoparticles prepared by laser-ablation from (a) Fe50/Au150/Fe25 and (b) Fe50/Au150 films. Intensities are normalized to the intensity of the Fe_3O_4 band near 674/666 cm^{-1}. The excitation wavelength is 632.8 nm (0.8 mW).

3.4. SERS of Adenine Adsorbed at Magneto-Plasmonic Nanoparticles

Plasmonic properties of nanoparticles were verified by employing SERS spectroscopy of adsorbed adenine (Ade) as a probe biomolecule [67]. For this, SERS spectra of adenine adsorbed from a 0.1 mM water solution on a magneto-plasmonic nanoparticle substrate were measured. Further detailed SERS studies using adenine solution revealed that the highest SERS signal was obtained using the SERS substrate prepared with laser ablation synthesized from Fe100/Au150 and Fe50/Au150 coatings. This might be due to the composition of the obtained nanoparticles. In both of these samples, the amount of gold was relatively higher than that of iron. Figure 7 shows the SERS spectra of adsorbed Ade on magneto-plasmonic nanoparticles with the SERS spectra of this probe ligand on laser-ablated Au nanoparticles. For comparison, Raman spectra of the solid-state form and aqueous solutions of Ade prepared with H_2O and D_2O solvents as well as an acidic water solution are demonstrated in Figure 8. Two bands marked by the star at 981 and

1051 cm^{-1} are associated with stretching vibrations of solution SO_4^{2-} and HSO_4^- ions, respectively [68]. The positions of vibrational bands and assignments are listed in Table 2. The clearly resolved band at 683 cm^{-1} visible in SERS spectra (Figure 7) belongs to Fe_3O_4. The presence of this band confirms the preservation of magnetite structure upon adsorption of the probe biomolecule. Adenine possesses multiple adsorption sites (ring π system, ring nitrogens, and NH_2 group) (Figure 9) and can be positively or negatively charged depending on protonation at the N1 site (pK_1 = 4.1) or ring deprotonation (pKa = 9.8) [69,70]. The most intense band in the SERS spectra at 736 cm^{-1} corresponds to adenine ring breathing vibration [71–76]. The corresponding band in the Raman spectrum of adenine powder appears at a considerably lower frequency (723 cm^{-1}). Such a shift is characteristic of adsorbed adenine on the Au surface [69,71]. This mode downshifts to 707 cm^{-1} upon labile hydrogens' exchange to deuterons in D_2O solution (Figure 8). Comparison of Ade solution spectra at pH 6.2 and 1.5 reveals a shift of the 1486 cm^{-1} band to 1408 cm^{-1}, the 1332 cm^{-1} band to 1312 cm^{-1}, the absence of the 1251 cm^{-1} band, and a shift of the 623 cm^{-1} band to 617 cm^{-1} (Figure 8). In SERS spectra, the bands at 1454–1464 cm^{-1} (which corresponds to the Ade solution band at 1486 cm^{-1}), 1342–1348 cm^{-1} (the solution band at 1332 cm^{-1}), 1236–1240 cm^{-1} (the solution band at 1251 cm^{-1}), and 627–629 cm^{-1} (the solution band at 622 cm^{-1}) are visible, indicating a neutral form of the adsorbed Ade ring. DFT modeling suggested an increase in the frequency of ring breathing mode from 725 to 743 cm^{-1} upon bonding of the N3 site with the Au^+ ion, while an upshift of only 2 cm^{-1} was demonstrated upon metal binding to the N7 site [69]. Thus, our experimental SERS data are consistent with the strong interaction of the Ade ring with the surface through the N3 atom. However, the involvement of the N9 atom with surface bonding is also possible, as was suggested previously [71].

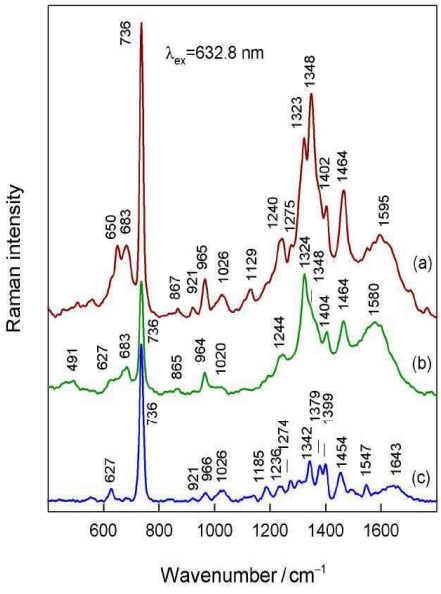

Figure 7. SERS spectra of adenine adsorbed from 0.1 mM aqueous solution on magneto-plasmonic nanoparticle substrate and on gold nanoparticle substrate produced by laser ablation of (a) Fe100/Au150, (b) Fe50/Au150, and (c) bulk Au target. The excitation wavelength is 632.8 nm (2.5 mW).

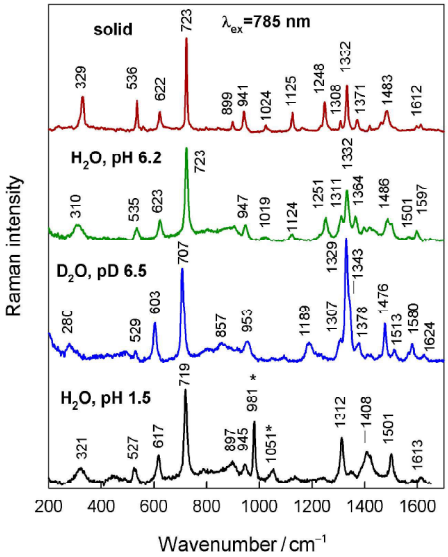

Figure 8. Raman spectra of solid adenine and solutions (7 mM) prepared with H_2O (pH 6.2), D_2O (pD 6.5), and acidic (pH 1.5) H_2O solution. The excitation wavelength is 785 nm. The stars denote the bands that originated from SO_4^{2-} (981 cm^{-1}) and HSO_4^- (1051 cm^{-1}) species.

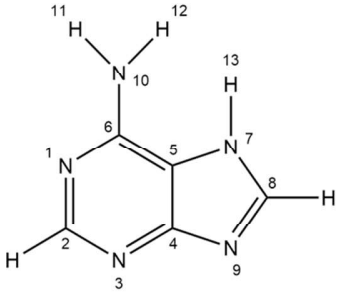

Figure 9. Molecular structure and atom labeling of adenine tautomer N7H.

A comparison of SERS spectra from adsorbed Ade on laser-ablated Au and magneto-plasmonic nanoparticles reveals considerable differences in the relative intensities and frequencies of prominent bands (Figure 7). The higher relative intensity of ring breathing mode near 736 cm^{-1} is consistent with a more perpendicular orientation of the ring plane with respect to the surface for Ade adsorbed on laser-ablated Au nanoparticles. The band at 964–966 cm^{-1} was assigned to the rocking NH_2 vibrational mode coupled with stretching of the N1-C6 bond and deformation of the N7-C8-N9 group (r(NH_2) + ν(N1-C6) + δ(N7-C8-N9)) (Table 2). An increase in the relative intensity of this band indicates an increase in the angle between the Ade ring plane and the surface normal. The clearly defined SERS band 1454–1464 cm^{-1} was assigned to the ν(N1-C6) + β(C2H) + ν(C2-N3) + δ(NH_2) vibrational mode (Table 2). In the Ade solid-state spectrum, this band appears at 1483 cm^{-1} and shifts to 1476 cm^{-1} in D_2O solutions (Figure 8). The frequency of this band differs considerably when comparing SERS spectra on Au (1454 cm^{-1}) and magneto-plasmonic (1464 cm^{-1}) nanoparticles. Such a frequency shift suggests the involvement of the NH_2 group in the interaction of Ade with a surface of magneto-plasmonic nanoparticles. Similar

intensification of high-frequency bands in the vicinity of 1300–1400 cm^{-1} compared with ring breathing mode at 735 cm^{-1} was observed in the SERS spectra of Ade adsorbed on Ni and Ni-Ag nanoparticles [77]. Based on density functional theory (DFT) analysis and the similarity of spectra observed at Ni and Ni-Ag surfaces, it was suggested that Ade primarily interacts with Ni adsorption sites [77].

Table 2. Experimental and calculated vibrational frequencies of adenine and model surface complexes and assignments of the bands.

Solid State	Solution H_2O (D_2O)	SERS Au	SERS Au-Fe_3O_4	Calc. Ade (N7H)	Calc. Au_3-Ade(N7H)	Calc. Fe_3O_4-Ade(N7H) A	Calc. Fe_3O_4-Ade(N7H) B	Assignments
1483 m	1486 m (1476 m)	1454 m	1464 s	1509	1488	1495	1503	β(C2H), ν(N1-C6), ν(C2-N3), δ(NH_2)
1371 w	1364 m (1378 w)	1399 w	1402 w	1405	1383	1396	1390	ν(C4-C5), β(CH_2)
1332 s	1332 s (1329 vs)	1342 m	1348	1365	1337	1342	1334	ν(C2-N3), ν(C8-N9), β(C2H)
1248 m	1251 m (1189 m)	1236	1240	1226	1226	1228	1240	ν(C2-N3), β(C8H), ν(C8-N9)
941 m	947 m (953 m)	966 w	965 m	948	979	985	981	δ(N7-C8-N9), ν(N1-C6), r(NH_2)
723 vs	723 vs (707 vs)	736 vs	736 vs	726	732	725, 736	715	ring breathing, ν(Fe-O)
622 m	623 m (603 m)	627 sh	629 sh	618	621	627	686	ν(C5-C6), β(R1), β(R2)
							371	ν(Fe-N10)
			295 m, br			243, 263		ν(Fe-N3), ν(Fe-N9), ν(Fe-O)
			218 w, br			151, 208, 216		ν(Fe-N3), ν(Fe-N9)
		200 m, br			187			ν(Au-N3), ν(Au-N9)

Abbreviations: ν, stretching; δ, deformation; β, in-plane bending; R1, six-membered ring; R2, five-membered ring; vs, very strong; m, middle, w, weak; br, broad; sh, shoulder.

Analysis of low-frequency SERS spectra reveals insights into the bonding of Ade to laser-ablated Au and magneto-plasmonic nanoparticles (Figure 10). Spectrum from bare magneto-plasmonic nanoparticles before adsorption of Ade does not show any clear low-frequency vibrational mode. However, the broad low-frequency band at 200 cm^{-1} is visible in the spectrum of Ade adsorbed on laser-ablated Au nanoparticles (Figure 10a). A different SERS spectrum was observed for Ade adsorbed on a substrate prepared from magneto-plasmonic nanoparticles; a broad band centered at 295 cm^{-1} became clearly visible along with another lower intensity feature near 218 cm^{-1}. We suggest these low-frequency modes are related to the bonding of Ade nitrogens with Fe_3O_4 structures.

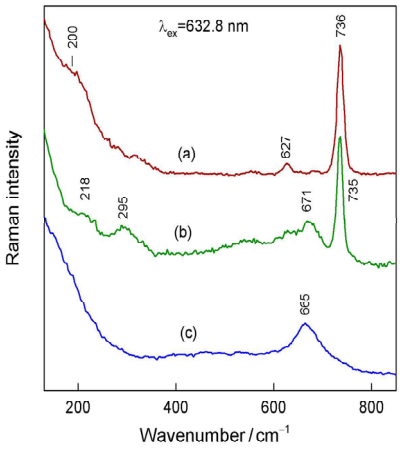

Figure 10. SERS spectra in the low-frequency region (130–850 cm^{-1}). (a) adenine adsorbed at Au NPs prepared by laser ablation, (b) adenine adsorbed at Fe-Au nanoparticles prepared by laser ablation of Fe50/Au150/Fe25 film, and (c) SERS spectrum of bare Fe-Au nanoparticles prepared by laser ablation of Fe50/Au150/Fe25 film. The excitation wavelength is 632.8 nm.

3.5. DFT Modelling of SERS Spectra

To gain more insights into the interaction of adenine with magneto-plasmonic nanoparticles, DFT modeling of the Raman spectra of adsorption complexes was conducted. Figure 11 shows optimized structures of Ade (tautomer N7H) and adsorption complexes of Ade with the Au_3 cluster and Fe_3O_4. Two adsorption sites, through N3/N9 atoms and N10/N7H, were modeled for interaction with the magnetite surface. The calculated Raman spectra are shown in Figure 12. In the case of the Au_3-adenine complex, the prominent ring breathing mode shifts to higher wavenumbers, from 726 cm^{-1} (free Ade) to 732 cm^{-1}. Such a frequency upshift agrees very well with the experimental SERS spectrum (Figure 7). A similar increase in frequency of the ring breathing mode was predicted by the Fe_3O_4-adenine (A) complex. In this case, two bands associated with ring breathing mode coupled with Fe-O stretching are visible at 725/736 cm^{-1}. However, ring breathing mode was found at considerably lower wavenumbers (715 cm^{-1}) in the case of the Fe_3O_4-adenine (B) complex. Thus, the bonding of Ade with N10/N7H sites does not predict the experimentally observed shift of this mode, suggesting that the major interaction site of Ade with Fe_3O_4 corresponds to the bonding of Fe with N3/N9 atoms. DFT calculations predict a considerably stronger interaction of Fe_3O_4 with the N3 site compared with N9 because of the noticeably shorter Fe-N3 bond length (201.3 pm) compared with Fe-N9 (208.1 pm) (Figure 11).

The DFT calculations predict the downshift of the high-frequency band at 1509 cm^{-1} (free Ade) to 1488 and 1495 cm^{-1} upon bonding adenine with the Au_3 cluster or Fe_3O_4 through the N3/N9 sites, respectively (Table 2), while only a small shift (6 cm^{-1}) is predicted for the Fe_3O_4-Ade (B) complex. In experimental spectra, a significant decrease (19–29 cm^{-1}) in frequency was detected (Table 2). The band at 941 cm^{-1} (solid-state Ade spectrum) was found to be sensitive to the interaction between the Ade rings. The frequency of this band increased by 6 cm^{-1} in the solution spectrum (Figure 8, Table 2). A high upshift (24–25 cm^{-1}) frequency of this band was detected in SERS spectra (Table 2). In agreement with experimental data, DFT modeling predicts an upshift frequency of this mode of 31–37 cm^{-1} upon the formation of surface complexes.

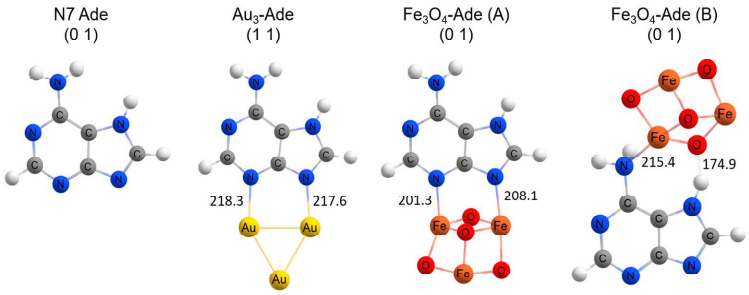

Figure 11. Optimized structures of N7H adenine tautomer, Au_3-adenine complex, and Fe_3O_4-adenine complexes formed at N3-/N9- and N10-/N7H- interaction sites, Fe_3O_4-Ade (A) and Fe_3O_4-Ade (B), respectively. Numbers in brackets indicate charge and multiplicity. The lengths of chemical bonds are indicated in pm.

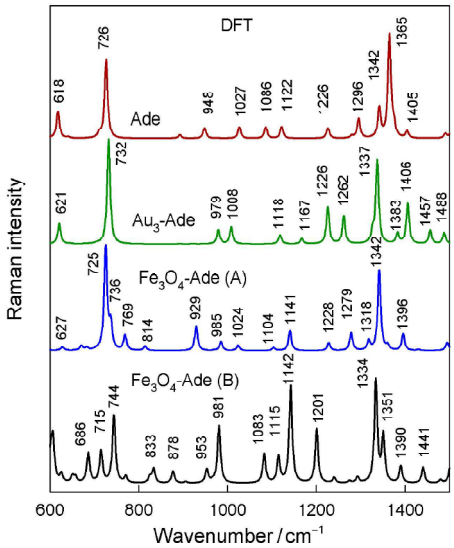

Figure 12. Calculated Raman spectra of N7H adenine tautomer, Au_3-adenine complex, and Fe_3O_4-adenine complexes formed at N3-/N9- and N10-/N7H- interaction sites, Fe_3O_4-Ade (A) and Fe_3O_4-Ade (B), respectively.

DFT analysis of low-frequency vibrational modes predicts the position of the metal-adsorbate Au-N3 vibrational mode at 187 cm^{-1} (Table 2). This confirms the origin of the experimentally observed broad SERS band near 200 cm^{-1} from adenine adsorbed on laser-ablated Au nanoparticles as associated with Au-N stretching vibration (Figure 10). Peak position coincides well with previously reported DFT analysis of stretching vibration of the Au-N3 bond (196 cm^{-1}) for the adsorption complex Ade-Au^+ [69]. In the case of hybrid magneto-plasmonic nanoparticles, the broad low-frequency bands were observed at different wavenumbers, i.e., 218 and 295 cm^{-1}. DFT modeling suggests that these bands originate from Fe-N stretching vibrations associated with N3 and N9 atoms (Table 2).

4. Conclusions

In this work, we have obtained chemically clean magneto-plasmonic nanoparticles from layered Fe/Au and Fe/Au/Fe thin film coatings by applying 1064 nm picosecond laser

ablation in acetone. The magnetic properties of nanoparticles were used to extract them from acetone and arrange them on an aluminum substrate for SERS applications. Based on TEM, EDS, and Raman spectroscopy data, we demonstrated that hybrid nanoparticles consisted of a plasmonic (Au) core and a magnetic (Fe_3O_4) shell. Hybrid magneto-plasmonic nanoparticles exhibited distinct plasmon resonance bands characteristic of spherical gold colloids, with a maximum at 509–528 nm. SERS spectra revealed that the probe molecule-adenine, adsorbs on the magnetite site instead of gold, suggesting that the magnetic shell is sufficiently compact to prevent penetration of adenine into the gold core. The interaction of adenine with magnetite was also confirmed by DFT calculations. A strong SERS signal from adsorbed adenine demonstrated that the magnetic shell does not markedly diminish the electromagnetic enhancement provided by the plasmonic core. A magnetic shell can serve for manipulation and arrangement of nanoparticles at a chosen surface, while a plasmonic core can ensure vibrational spectroscopy sensing of nucleic acid bases and other biomolecules. Because the magnetic shell (magnetite, Fe_3O_4) is biocompatible, hybrid nanoparticles can be employed in biomedicine applications [78].

Supplementary Materials: The following supporting information can be downloaded at https://www.mdpi.com/article/10.3390/coatings13091523/s1. Figure S1: Solution of ablated magneto-plasmonic nanoparticles in acetone (A) just prepared and (B) in 15 min after exposure to a permanent magnet; Figure S2: Hysteresis loop of the laser ablated magneto-plasmonic nanoparticles (Fe50/Au150/Fe25) (black) and approximation with the Brillouin function (red); description of enhancement factor calculations; Figure S3: (A) SERS spectra of a 4-MBA molecule obtained using magneto-plasmonic nanoparticles at 633, 785, and 830 nm laser radiations. Shaded areas represent the standard deviation from nine measurements. (B) SERS enhancement factors calculated for different laser excitations.

Author Contributions: L.M.: investigation, methodology, writing–original preparation, writing–review, and editing; E.S.: methodology, conceptualization, formal analysis; S.A.-G.: investigation, methodology, visualization; V.P.: investigation, visualization, formal analysis; R.T.: visualization, formal analysis, methodology; M.T.: investigation, methodology, formal analysis, DFT calculation; M.S.: investigation, methodology, formal analysis; A.Z.: methodology, formal analysis, visualization; A.S.: investigation, methodology, formal analysis; V.Š.: methodology, conceptualization, supervision; G.N.: conceptualization, supervision, writing—original draft preparation, writing—review, and editing. All authors have read and agreed to the published version of the manuscript.

Funding: This work has received funding from the European Regional Development Fund (Project No. 01.2.2-LMT-K-718-03-0078) under a grant agreement with the Research Council of Lithuania (LMTLT).

Institutional Review Board Statement: Not applicable.

Informed Consent Statement: Not applicable.

Data Availability Statement: Not applicable.

Acknowledgments: The authors gratefully acknowledge the Center of Spectroscopic Characterization of Materials and Electronic/Molecular Processes (SPECTROVERSUM Infrastructure) for the use of Raman spectrometers. Authors thank Voitech Stankevic and PhD student Jorunas Dobilas for magnetization measurements.

Conflicts of Interest: The authors declare no conflict of interest.

References

1. Tran, V.T.; Kim, J.; Tufa, L.T.; Oh, S.; Kwon, J.; Lee, J. Magnetoplasmonic Nanomaterials for Biosensing/Imaging and in Vitro/in Vivo Biousability. *Anal. Chem.* **2018**, *90*, 225–239. [CrossRef] [PubMed]
2. Lai, H.; Xu, F.; Wang, L. A review of the preparation and application of magnetic nanoparticles for surface-enhanced Raman scattering. *J. Mater. Sci.* **2018**, *53*, 8677–8698. [CrossRef]
3. Lim, J.; Majetich, S.A. Composite magnetic-plasmonic nanoparticles for biomedicine: Manipulation and imaging. *Nano Today* **2013**, *8*, 98–113. [CrossRef]

4. Wang, C.; Meloni, M.M.; Wu, X.; Zhuo, M.; He, T.; Wang, J.; Wang, C.; Dong, P. Magnetic-plasmonic particles for SERS-based bacteria sensing: A review. *AIP Adv.* **2019**, *9*, 010701. [CrossRef]
5. Anik, M.I.; Hossain, M.K.; Hossain, I.; Mahfuz, A.M.U.B.; Rahman, M.T.; Ahmed, I. Recent progress of magnetic nanoparticles in biomedical applications: A review. *Nano Sel.* **2021**, *2*, 1146–1186. [CrossRef]
6. Materon, E.M.; Miyazaki, C.M.; Carr, O.; Joshi, N.; Picciani, P.H.S.; Dalmaschio, C.J.; Davis, F.; Shimizu, F.M. Magnetic nanoparticles in biomedical applications: A review. *Appl. Surf. Sci.* **2012**, *6*, 100163. [CrossRef]
7. Yew, Y.P.; Shameli, K.; Miyake, M.; Khairudin, N.B.B.A.; Mohamad, S.E.B.; Naiki, T.; Lee, K.X. Green biosynthesis of superparamagnetic magnetite Fe_3O_4 nanoparticles and biomedical applications in targeted anticancer drug delivery system: A review. *Arab. J. Chem.* **2020**, *13*, 2287–2308. [CrossRef]
8. Ganapathe, L.S.; Mohamed, M.A.; Yunus, R.M.; Berhanuddin, D.D. Magnetite (Fe_3O_4) Nanoparticles in Biomedical Application: From Synthesis to Surface Functionalisation. *Magnetochemistry* **2020**, *6*, 68. [CrossRef]
9. He, Z.; Li, F.; Zuo, P.; Tian, H. Principles and Applications of Resonance Energy Transfer Involving Noble Metallic Nanoparticles. *Materials* **2023**, *16*, 3083. [CrossRef]
10. Muntean, C.M.; Cuibus, D.; Boca, S.; Falamas, A.; Tosa, N.; Brezestean, I.A.; Bende, A.; Barbu-Tudoran, L.; Moldovan, R.; Bodoki, E.; et al. Gold vs. Silver Colloidal Nanoparticle Films for Optimized SERS Detection of Propranolol and Electrochemical-SERS Analyses. *Biosensors* **2023**, *13*, 530. [CrossRef]
11. Miyazaki, C.M.; Martin, C.S.; Constantino, C.J.L. Gold conjugated-magnetite nanoparticles for magnetic concentration towards reproducibility and repeatability of SERS measurements. *Colloids Surf. A Physicochem. Eng.* **2023**, *671*, 131661. [CrossRef]
12. Multari, C.; Miola, M.; Laviano, F.; Gerbaldo, R.; Pezzotti, G.; Debellis, D.; Verné, E. Magnetoplasmonic Nanoparticles for Photothermal Therapy. *Nanotechnology* **2019**, *30*, 255705. [CrossRef] [PubMed]
13. Stafford, S.; Serrano Garcia, R.; Gun'ko, Y.K. Multimodal Magnetic-Plasmonic Nanoparticles for Biomedical Applications. *Appl. Sci.* **2018**, *8*, 97. [CrossRef]
14. Tomitaka, A.; Arami, H.; Raymond, A.; Yndart, A.; Kaushik, A.; Jayant, R.D.; Takemura, Y.; Cai, Y.; Toborek, M.; Nair, M. Development of Magneto-Plasmonic Nanoparticles for Multimodal Image-Guided Therapy to the Brain. *Nanoscale* **2017**, *9*, 764–773. [CrossRef] [PubMed]
15. Chen, W.; Xu, N.; Xu, L.; Wang, L.; Li, Z.; Ma, W.; Zhu, Y.; Xu, C.; Kotov, N.A. Multifunctional Magnetoplasmonic Nanoparticle Assemblies for Cancer Therapy and Diagnostics (Theranostics). *Macromol. Rapid Commun.* **2010**, *31*, 228–236. [CrossRef] [PubMed]
16. Urries, I.; Muñoz, C.; Gomez, L.; Marquina, C.; Sebastian, V.; Arruebo, M.; Santamaria, J. Magneto-Plasmonic Nanoparticles as Theranostic Platforms for Magnetic Resonance Imaging, Drug Delivery and NIR Hyperthermia Applications. *Nanoscale* **2014**, *6*, 9230–9240. [CrossRef] [PubMed]
17. Feng, Y.; Liang, M.; You, R.; Li, T.; Zhu, L. Femtosecond Laser Fabrication of Noble Metal Plasma Nanostructures and Its Application-A Mini Review. *Front. Phys.* **2022**, *10*, 918372. [CrossRef]
18. Kim, M.; Osone, S.; Kim, T.; Higashi, H.; Seto, T. Synthesis of Nanoparticles by Laser Ablation: A Review. *KONA Powder Part. J.* **2017**, *34*, 80–90. [CrossRef]
19. Stankevičius, E.; Garliauskas, M.; Laurinavičius, L.; Trusovas, R.; Tarasenko, N.; Pauliukaitė, R. Engineering Electrochemical Sensors Using Nanosecond Laser Treatment of Thin Gold Film on ITO Glass. *Electrochim. Acta* **2019**, *297*, 511–522. [CrossRef]
20. Stankevičius, E.; Ignatjev, I.; Petrikaitė, V.; Selskis, A.; Niaura, G. Gold Nanoparticles Generated Using the Nanosecond Laser Treatment of Multilayer Films and Their Use for SERS Applications. *ACS Omega* **2021**, *6*, 33889–33898. [CrossRef]
21. Petrikaitė, V.; Skapas, M.; Stankevičius, E. Generation of gold and silver nanoparticles using laser ablation of thin bimetallic films and bulk targets in water. *Opt. Mater.* **2023**, *137*, 113535. [CrossRef]
22. Verma, A.K.; Soni, R.K. Laser ablation synthesis of bimetallic gold-palladium core@shell nanoparticles for trace detection of explosives. *Opt. Laser Technol.* **2023**, *163*, 109429. [CrossRef]
23. Ondieki, A.M.; Birech, Z.; Kaduki, K.A.; Mwangi, P.W.; Mwenze, N.M.; Juma, M.; Jeptoo, C.; Dlamini, M.S.; Maaza, M. Fabrication of surface-enhanced Raman spectroscopy substrates using silver nanoparticles produced by laser ablation in liquids. *Spectrochim. Acta A Mol. Biomol. Spectrosc.* **2023**, *296*, 122694. [CrossRef] [PubMed]
24. Rathod, J.; Byram, C.; Kanaka, R.K.; Bharati, M.S.S.; Banerjee, D.; Akkanaboina, M.; Soma, V.R. Hybrid Surface-Enhanced Raman Scattering Substrates for the Trace Detection of Ammonium Nitrate, Thiram, and Nile Blue. *ACS Omega* **2022**, *7*, 15969–15981. [CrossRef] [PubMed]
25. Szymborski, T.; Stepanenko, Y.; Nicinski, K.; Piecyk, P.; Berus, S.M.; Adamczyk-Poplawska, M.; Kaminska, A. Ultrasensitive SERS platform made via femtosecond laser micromachining for biomedical applications. *J. Mater. Res. Technol.* **2021**, *12*, 1496–1507. [CrossRef]
26. Tran, T.D.; Nguyen, T.H.; Nguyen, T.B. Silver nanostructure on ablated silicon wafer prepared via pulsed laser ablation for surface enhanced Raman spectroscopy. *J. Raman Spectrosc.* **2022**, *53*, 1039–1047. [CrossRef]
27. Yan, Z.; Chrisey, D.B. Pulsed Laser Ablation in Liquid for Micro-/Nanostructure Generation. *J. Photochem. Photobiol. C Photochem. Rev.* **2012**, *13*, 204–223. [CrossRef]
28. Fazio, E.; Gökce, B.; De Giacomo, A.; Meneghetti, M.; Compagnini, G.; Tommasini, M.; Waag, F.; Lucotti, A.; Zanchi, C.G.; Ossi, P.M.; et al. Nanoparticles Engineering by Pulsed Laser Ablation in Liquids: Concepts and Applications. *Nanomaterials* **2020**, *10*, 2317. [CrossRef]

29. Wagener, P.; Jakobi, J.; Rehbock, C.; Chakravadhanula, V.S.K.; Thede, C.; Wiedwald, U.; Bartsch, M.; Kienle, L.; Barcikowski, S. Solvent-surface interactions control the phase structure in lasergenerated iron-gold core-shell nanoparticles. *Sci. Rep.* **2016**, *6*, 23352. [CrossRef]
30. Itina, T.E. On Nanoparticle Formation by Laser Ablation in Liquids. *J. Phys. Chem. C* **2011**, *115*, 5044–5048. [CrossRef]
31. Zhu, X.P.; Suzuki, T.; Nakayama, T.; Suematsu, H.; Jiang, W.; Niihara, K. Underwater Laser Ablation Approach to Fabricating Monodisperse Metallic Nanoparticles. *Chem. Phys. Lett.* **2006**, *427*, 127–131. [CrossRef]
32. Amendola, V.; Scaramuzza, S.; Litti, L.; Meneghetti, M.; Zuccolotto, G.; Rosato, A.; Nicolato, E.; Marzola, P.; Fracasso, G.; Anselmi, C.; et al. Magneto-Plasmonic Au-Fe Alloy Nanoparticles Designed for Multimodal SERS-MRI-CT Imaging. *Small* **2014**, *10*, 2476–2486. [CrossRef] [PubMed]
33. Tymoczko, A.; Kamp, M.; Prymak, O.; Rehbock, C.; Jakobi, J.; Schürmann, U.; Kienle, L.; Barcikowski, S. How the Crystal Structure and Phase Segregation of Au–Fe Alloy Nanoparticles Are Ruled by the Molar Fraction and Size. *Nanoscale* **2018**, *10*, 16434–16437. [CrossRef]
34. Amendola, V.; Scaramuzza, S.; Carraro, F.; Cattaruzza, E. Formation of Alloy Nanoparticles by Laser Ablation of Au/Fe Multilayer Films in Liquid Environment. *J. Colloid Interface Sci.* **2017**, *489*, 18–27. [CrossRef] [PubMed]
35. Tymoczko, A.; Kamp, M.; Rehbock, C.; Kienle, L.; Cattaruzza, E.; Barcikowski, S.; Amendola, V. One-step synthesis of Fe-Au core-shell magnetic-plasmonic nanoparticles driven by interface energy minimization. *Nanoscale Horiz.* **2019**, *4*, 1326–1332. [CrossRef]
36. Byram, C.; Rathod, J.; Moram, S.S.B.; Mangababu, A.; Soma, V.R. Picosecond Laser-Ablated Nanoparticles Loaded Filter Paper for SERS-Based Trace Detection of Thiram, 1,3,5-Trinitroperhydro-1,3,5-triazine (RDX), and Nile Blue. *Nanomaterials* **2022**, *12*, 2150. [CrossRef] [PubMed]
37. Zuo, P.; Jiang, L.; Li, X.; Tian, M.Y.; Yuan, Y.J.; Han, W.N.; Ma, L.; Hu, L.F.; He, Z.H.; Li, F. MoS_2 core-shell nanoparticles prepared through liquid-phase ablation and light exfoliation of femtosecond laser for chemical sensing. *Sci. China Technol. Sci.* **2023**, *66*, 853–862. [CrossRef]
38. Vendamani, V.S.; Beeram, R.; Soma, V.R. MoS_2 nanosheets decorated plasmonic silicon nanowires as SERS substrates for ultra-sensitive multiple analyte detection. *J. Alloys Compd.* **2023**, *959*, 170573. [CrossRef]
39. Mohammed, M.S.; Hadi, I.H.; Jawad, M.F.; Alwan, A.M. Accurate Synthesis and Performance of SERS Sensing of Au/Ag Nanocomposites Site-Deposited on Apple Surfaces. *Plasmonics* **2023**. [CrossRef]
40. Qayyum, H.; Amin, S.; Ahmed, W.; Mohamed, T.; Rehman, Z.U.; Hussain, S. Laser-based two-step synthesis of Au-Ag alloy nanoparticles and their application for surface-enhanced Raman spectroscopy (SERS) based detection of rhodamine 6G and urea nitrate. *J. Mol. Liq.* **2022**, *365*, 120120. [CrossRef]
41. Hammad, Q.K.; Ayyash, A.N.; Mutlak, F.A.H. Improving SERS substrates with Au/Ag-coated Si nanostructures generated by laser ablation synthesis in PVA. *J. Opt.* **2022**, *52*, 1528–1536. [CrossRef]
42. Zhang, D.; Liu, J.; Li, P.; Tian, Z.; Liang, C. Recent Advances in Surfactant-Free, Surface-Charged, and Defect-Rich Catalysts Developed by Laser Ablation and Processing in Liquids. *ChemNanoMat* **2017**, *3*, 512–533. [CrossRef]
43. Nasiri, H.; Dorranian, D.; Sari, A.H. Green laser assisted gold-iron oxide nanocomposite production, Radiation Effects and Defects in Solids. *Radiat. Eff. Defects Solids* **2022**, *177*, 277–293. [CrossRef]
44. Muniz-Miranda, M.; Muniz-Miranda, F.; Giorgetti, E. Spectroscopic and Microscopic Analyses of Fe_3O_4/Au Nanoparticles Obtained by Laser Ablation in Water. *Nanomaterials* **2020**, *10*, 132. [CrossRef] [PubMed]
45. Neese, F. The ORCA program system. *Wiley Interdiscip. Rev. Comput. Mol. Sci.* **2012**, *2*, 73–78. [CrossRef]
46. Mikoliunaite, L.; Talaikis, M.; Michalowska, A.; Dobilas, J.; Stankevic, V.; Kudelski, A.; Niaura, G. Thermally stable magneto-plasmonic nanoparticles for SERS with tunable plasmon resonance. *Nanomaterials* **2022**, *12*, 2860. [CrossRef] [PubMed]
47. Haiss, W.; Thanh, N.T.K.; Aveyard, J.; Fernig, D.G. Determination of size and concentration of gold nanoparticles from UV-Vis spectra. *Anal. Chem.* **2007**, *79*, 4215–4221. [CrossRef] [PubMed]
48. Khlebtsov, N.G. Determination of size and concentration of gold nanoparticles from extinction spectra. *Anal. Chem.* **2008**, *80*, 6620–6625. [CrossRef]
49. Ferrari, A.C.; Robertson, J. Interpretation of Raman spectra of disordered and amorphous carbon. *Phys. Rev. B* **2000**, *61*, 14095–14107. [CrossRef]
50. Trusovas, R.; Račiukaitis, G.; Niaura, G.; Barkauskas, J.; Valušis, G.; Pauliukaite, R. Recent Advances in Laser Utilization in the Chemical Modification of Graphene Oxide and Its Applications. *Adv. Opt. Mater.* **2016**, *4*, 37–65. [CrossRef]
51. Smith, M.W.; Dallmeyer, I.; Johnson, T.J.; Brauer, C.S.; McEwen, J.S.; Espinal, J.F.; Garcia-Perez, M. Structural Analysis of Char by Raman Spectroscopy: Improving Band Assignments through Computational Calculations from First Principles. *Carbon* **2016**, *100*, 678–692. [CrossRef]
52. Vasquez, A.; Samolis, P.; Zeng, J.; Sander, M.Y. Micro-Structuring, Ablation, and Defect Generation in Graphene with Femtosecond Pulses. *OSA Contin.* **2019**, *2*, 2925. [CrossRef]
53. Amendola, V.; Riello, P.; Meneghetti, M. Magnetic nanoparticles of iron carbide, iron oxide, iron@iron oxide, and metal iron synthesized by laser ablation in organic solvents. *J. Phys. Chem. C* **2011**, *115*, 5140–5146. [CrossRef]
54. Shebanova, O.N.; Lazor, P. Raman Spectroscopic Study of Magnetite ($FeFe_2O_4$): A New Assignment for the Vibrational Spectrum. *J. Solid State Chem.* **2003**, *174*, 424–430. [CrossRef]

55. Bersani, D.; Lottici, P.P.; Montenero, A. Micro-Raman investigation of iron oxide films produced by sol-gel synthesis. *J. Raman Spectrosc.* **1999**, *30*, 355–360. [CrossRef]
56. Testa-Anta, M.; Ramos-Docampo, M.A.; Comesaña-Hermo, M.; Rivas-Murias, B.; Salgueiriño, V. Raman spectroscopy to unravel the magnetic properties of iron oxide nanocrystals for bio-related applications. *Nanoscale Adv.* **2019**, *1*, 2086–2103. [CrossRef]
57. Orendorff, C.J.; Gole, A.; Sau, T.K.; Murphy, C. Surface-enhanced Raman spectroscopy of self-assembled monolayers: Sandwich architecture and nanoparticle shape dependence. *Anal. Chem.* **2005**, *77*, 3236–3266. [CrossRef]
58. Smith, E.; Dent, G. *Modern Raman Spectroscopy: A Practical Approach*; John Wiley & Sons: Chichester, UK, 2005.
59. Shumskaya, A.; Korolkov, I.; Rogachev, A.; Ignatovich, Z.; Kozlovskiy, A.; Zdorovets, M.; Anisovich, M.; Bashouti, M.; Shalabny, A.; Busool, R.; et al. Synthesis of Ni@Au core-shell magnetic nanotubes for bioapplication and SERS detection. *Colloids Surf. A.* **2021**, *626*, 127077. [CrossRef]
60. Li, Z.H.; Bai, J.H.; Zhang, X.; Lv, J.M.; Fan, C.S.; Zhao, Y.M.; Wu, Z.L.; Xu, H.J. Facile synthesis of Au nanoparticle-coated Fe_3O_4 magnetic composite nanospheres and their application in SERS detection of malachite green. *Spectrochim. Acta A* **2020**, *241*, 118532. [CrossRef]
61. Wang, L.-P.; Huang, Y.-B.; Lai, Y.-H. Surface enhanced Raman scattering activity of dual-functional Fe_3O_4/Au composites. *Appl. Surf. Sci.* **2018**, *435*, 290–296. [CrossRef]
62. Ye, M.; Wei, Z.; Hu, F.; Wang, J.; Ge, G.; Hu, Z.; Shao, M.; Lee, S.-T.; Liu, J. Fast assembling microarrays of superparamagnetic Fe_3O_4@Au nanoparticle clusters as reproducible substrates for surface-enhanced Raman scattering. *Nanoscale* **2015**, *7*, 13427–13437. [CrossRef] [PubMed]
63. Hu, F.; Lin, H.; Zhang, Z.; Liao, F.; Shao, M.; Lifshitz, Y.; Lee, S.-T. Smart liquid SERS substrates based on Fe_3O_4/Au nanoparticles with reversibly tunable enhancement factor for practical quantitative detection. *Sci. Rep.* **2014**, *4*, 7204. [CrossRef] [PubMed]
64. Kumar, G.V.P.; Rangarajan, N.; Sonia, B.; Deepika, P.; Rohman, N.; Narayana, C. Metal-coated magnetic nanoparticles for surface enhanced Raman scattering studies. *Bull. Mater. Sci.* **2011**, *34*, 207–216. [CrossRef]
65. Kanitz, A.; Hoppius, J.S.; Sanz, M.M.; Maicas, M.; Ostendorf, A.; Gurevich, E.L. Synthesis of magnetic nanoparticles by ultrashot pulsed laser ablation of iron in different liquids. *ChemPhysChem* **2017**, *18*, 1155–1164. [CrossRef] [PubMed]
66. Kanitz, A.; Kalus, M.-R.; Gurevich, E.L.; Ostendorf, A. Review on experimental and theoretical investigations of the early stage, femtoseconds to microseconds processes during laser ablation in liquid-phase for the synthesis of colloidal nanoparticles. *Plasma Sources Sci. Technol.* **2019**, *28*, 103001. [CrossRef]
67. Bell, S.E.J.; Charron, G.; Cortés, E.; Kneipp, J.; de la Chapelle, M.L.; Langer, J.; Procházka, M.; Tran, V.; Schlücker, S. Towards reliable and quantitative surface-enhanced Raman scattering (SERS): From key parameters to good analytical practice. *Angew. Chem. Int. Ed.* **2020**, *59*, 5454–5462. [CrossRef] [PubMed]
68. Niaura, G.; Malinauskas, A. Surface-enhanced Raman spectroscopy of ClO_4^- and SO_4^{2-} anions adsorbed at a Cu electrode. *J. Chem. Soc. Faraday Trans.* **1998**, *94*, 2205–2211. [CrossRef]
69. Kundu, J.; Neumann, O.; Janesko, B.G.; Zhang, D.; Lal, S.; Barhoumi, A.; Scuseria, G.E.; Halas, N.J. Adenine- and adenosine monophosphate (AMP)-gold binding interactions studied by surface-enhanced Raman and infrared spectroscopies. *J. Phys. Chem. C* **2009**, *113*, 14390–14397. [CrossRef]
70. Russo, N.; Toscano, M.; Grand, A.; Jolibois, F. Protonation of thymine, cytosine, adenine, and guanine DNA nucleic acid bases: Theoretical investigation into the framework of density functional theory. *J. Comput. Chem.* **1998**, *19*, 989–1000. [CrossRef]
71. Yao, G.; Zhai, Z.; Zhong, J.; Huang, Q. DFT and SERS Study of 15N Full-Labeled Adenine Adsorption on Silver and Gold Surfaces. *J. Phys. Chem. C* **2017**, *121*, 9869–9878. [CrossRef]
72. Pagliai, M.; Caporali, S.; Muniz-Miranda, M.; Pratesi, G.; Schettino, V. SERS, XPS, and DFT study of adenine adsorption on silver and gold surfaces. *J. Phys. Chem. Lett.* **2012**, *3*, 242–245. [CrossRef] [PubMed]
73. Huang, R.; Yang, H.-T.; Cui, L.; Wu, D.-Y.; Ren, B.; Tian, Z.-Q. Structural and charge sensitivity of surface-enhanced Raman spectroscopy of adenine on silver surface: A quantum chemical study. *J. Phys. Chem. C* **2013**, *117*, 23730–23737. [CrossRef]
74. Alula, M.T.; Yang, J. Photochemical decoration of silver nanoparticles on magnetic microspheres as substrates for the detection of adenine by surface-enhanced Raman scattering. *Anal. Chim. Acta* **2014**, *812*, 114–120. [CrossRef] [PubMed]
75. Giese, B.; McNaughton, D. Surface-enhanced Raman spectroscopic and density functional theory study of adenine adsorption to silver surfaces. *J. Phys. Chem. B* **2002**, *106*, 101–112. [CrossRef]
76. Lang, X.-F.; Yin, P.-G.; You, T.-T.; Jiang, L.; Guo, L. A DFT investigation of surface-enhanced Raman scattering of adenine and 2′-deoxyadenosine 5′-monophosphate on Ag20 nanoclusters. *ChemPhysChem* **2011**, *12*, 2468–2475. [CrossRef] [PubMed]
77. Gellini, C.; Deepak, F.L.; Muniz-Miranda, M.; Caporali, S.; Muniz-Miranda, F.; Pedone, A.; Innocenti, C.; Sangregorio, C. Magneto-plasmonic colloidal nanoparticles obtained by laser ablation of nickel and silver targets in water. *J. Phys. Chem. C* **2017**, *121*, 3597–3606. [CrossRef]
78. Pang, Y.; Wang, C.; Wang, J.; Sun, Z.; Xiao, R.; Wang, S. Fe_3O_4@Ag magnetic nanoparticles for microRNA capture and duplex-specific nuclease signal amplification-based SERS detection in cancer cells. *Biosens. Bioelectron.* **2016**, *79*, 574–580. [CrossRef]

chemosensors

MDPI

Article

Selective Enhancement of SERS Spectral Bands of Salicylic Acid Adsorbate on 2D $Ti_3C_2T_x$-Based MXene Film

Sonata Adomavičiūtė-Grabusovė [1,*], Simonas Ramanavičius [2,3], Anton Popov [4], Valdas Šablinskas [1], Oleksiy Gogotsi [5] and Arūnas Ramanavičius [2,*]

[1] Institute of Chemical Physics, Vilnius University, Sauletekio Av. 3, LT-10257 Vilnius, Lithuania; valdas.sablinskas@ff.vu.lt
[2] Department of Physical Chemistry, Faculty of Chemistry and Geosciences, Institute of Chemistry, Vilnius University, Naugarduko 24, LT-03225 Vilnius, Lithuania; simonas.ramanavicius@ftmc.lt
[3] Center for Physical Sciences and Technology, Sauletekio Av. 3, LT-10257 Vilnius, Lithuania
[4] NanoTechnas—Center of Nanotechnology and Materials Science, Faculty of Chemistry and Geosciences, Institute of Chemistry, Vilnius University, Naugarduko St. 24, LT-03225 Vilnius, Lithuania; anton.popov@chgf.vu.lt
[5] Materials Research Center Ltd., Krzhyzhanovskogo Str. 3, 01001 Kiev, Ukraine; agogotsi@mrc.org.ua
* Correspondence: sonata.adomaviciute@ff.vu.lt (S.A.-G.); Arunas.Ramanavicius@chf.vu.lt (A.R.)

Abstract: In this research, we have demonstrated that 2D $Ti_3C_2X_n$-based MXene (MXene) films are suitable for the design of surface-enhanced Raman spectroscopy (SERS)-based sensors. The enhanced SERS signal was observed for a salicylic acid molecule on $Ti_3C_2T_x$-based MXene film. Confirmation of the adsorption of the salicylic acid molecule and the formation of a salicylic acid–MXene complex were determined by experimental SERS-based spectral observations such as greatly enhanced out-of-plane bending modes of salicylic acid at 896 cm^{-1} and a band doublet at 681 cm^{-1} and 654 cm^{-1}. Additionally, some other spectral features indicate the adsorption of salicylic acid on the MXene surface, namely, a redshift of vibrational modes and the disappearance of the carboxyl deformation spectral band at 771 cm^{-1}. The determined enhancement factor indicates the value that can be expected for the chemical enhancement mechanism in SERS of 220 for out-of-plane vibrational modes. Theoretical modeling based on density functional theory (DFT) calculations using B3LYP/6311G++ functional were performed to assess the formation of the salicylic acid/MXene complex. Based on the calculations, salicylic acid displays affinity of forming a chemical bond with titanium atom of $Ti_3C_2(OH)_2$ crystal via oxygen atom in hydroxyl group of salicylic acid. The electron density redistribution of the salicylic acid–MXene complex leads to a charge transfer effect with 2.2 eV (428 nm) and 2.9 eV (564 nm) excitations. The experimentally evaluated enhancement factor can vary from 220 to 60 when different excitation wavelengths are applied.

Keywords: MXenes; SERS sensor; 2D materials; Ti_2C_3; salicylic acid; density functional theory (DFT)

check for updates

Citation: Adomavičiūtė-Grabusovė, S.; Ramanavičius, S.; Popov, A.; Šablinskas, V.; Gogotsi, O.; Ramanavičius, A. Selective Enhancement of SERS Spectral Bands of Salicylic Acid Adsorbate on 2D $Ti_3C_2T_x$-Based MXene Film. *Chemosensors* **2021**, *9*, 223. https://doi.org/10.3390/chemosensors9080223

Academic Editor: Santiago Sanchez-Cortés

Received: 7 July 2021
Accepted: 9 August 2021
Published: 13 August 2021

1. Introduction

A recently discovered class of specific two-dimensional (2D) materials—MXenes—promises a variety of applications with encouraging improvement in plasmonics, conductivity and catalysis compared to these properties of conventional non-metallic substances such as graphene. Due to the high concentration of free charges, the conductivity of these substances is metallic-like and higher than that of graphene [1,2]. Nevertheless, these materials are quite new, and the most relevant publications considering the optical and electric properties of MXenes have appeared just in the last decade.

MXenes were synthesized from MAX ($M_{n+1}AX_n$, where n = 1, 2 or 3) phase for the first time in 2011 [3]. Here, M represents a III–VI group transition metal, A is typically an element from IIIA or IVA group (e.g., Al, Si, Cd, Ga, etc.) and X usually depicts carbides, nitrides or carbonitrides, though over 30 different types of MXenes have been reported so far and even more are predicted to exist [4]. Henceforth, MXenes are generally produced

by selectively etching the middle element of the MAX three-dimensional lattice A, thus obtaining layers of MAX phase that ought to be further separated by various intercalant agents or sonication yielding 2D MXenes. Recently, research of this material class expanded rapidly. This is especially obvious for the $Ti_3C_2T_x$ MXene compounds (T_x here denotes the terminal functional group, usually -O, -OH or -F) formed from Ti_3AlC_2 (MAX phase). These MXenes are studied most extensively since their synthesis is widely established, and they exhibit higher metallic conductivity in comparison to that of molybdenum and nitride-based MXenes [5–8]. Nevertheless, further investigations are directed towards the efficient synthesis of other MXene types that can yield more defect-less 2D MXene layers [4,6].

Due to unique morphology and composition, these materials have the potential to be used in sensor design [9,10] as catalysts [11–13]. High conductivity, transparency and tunable work function enable the application of these materials in the design of optoelectronic devices, including solar cells. $Ti_3C_2T_x$ MXene has the potential to be used as an additive in a charge transport layer or as an electrode in perovskite and organic solar cells [14]. In addition, intriguing metal-like properties (e.g., the decrease of conductivity by the increase of temperature) and high conductivity determined by a high density of charge carriers were observed for MXenes [15–17]. The reported concentration of free charge carriers for $Ti_3C_2T_x$ MXene is 2×10^{21} cm^{-3} [18], while in noble metal nanoparticles, it is approximately 6×10^{22} cm^{-3} [19] and for graphene, 3×10^{13} cm^{-2} [1,2]. The conductivity of MXenes can be altered by their surface termination groups [20], leading to a possible application as supercapacitors [21,22], resistive sensors [23–25] and other applications in electrochemistry [26], electronics [27]. As a result of the relatively high concentration of free electrons, the plasmonic effect of MXenes reclassifies these materials into a class of metals because the plasmon frequency depends on the density of free electrons [19]. For this reason, MXenes might be used as a substitute for metallic nanostructures with the ability to enhance internal vibrations of molecules at near proximity as is in surface-enhanced Raman spectroscopy (SERS) [28–30].

It is widely accepted that two mechanisms can cause the SERS effect: (i) electromagnetic mechanism occurring due to localized plasmon resonance of noble metal nanostructures (such as silver, gold, platinum), which enhances the intensity of Raman spectral bands up to six orders of magnitude and (ii) chemical mechanism, which occurs because of interacting electronic energy levels between the substrate and the adsorbed molecule that causes a shift in electronic energy levels of the molecule. The enhancement due to chemical mechanism is lower and usually does not exceed two orders of magnitude [31]. However, until now, only enhanced resonance Raman spectra of dye molecules (such as rhodamine 6G, crystal violet, methylene blue, malachite green) adsorbed on the MXene surface were observed, and the enhancement was explained by the chemical mechanism [28–30]. The chemical enhancement between the MXene materials and the adsorbed dye molecules occurs because of the coupling between the dye and MXene energy levels. This coupling can be considered as a chemical mechanism of SERS [30,32,33]. Nevertheless, the electromagnetic mechanism of enhancing the SERS signal due to the free electron oscillations in MXene layers cannot be neglected as well [34,35].

The application of MXenes as SERS substrates is desirable in such cases when non-metal SERS substrates with a different chemical affinity towards molecules are needed. Moreover, the enhancement from 2D thin materials is beneficial in comparison to three-dimensional surfaces due to the larger specific surface area of 2D materials. Additionally, the localized plasmon resonance frequency in the metal nanoparticles depends on the shape and size of these nanoparticles which are determined during the synthesis of the nanoparticles, whereas for 2D materials such as graphene and MXenes, the surface plasmon resonance frequency can be influenced by different functional groups and/or controlled by an external electric field [20,36]. The possibility to use MXenes as a SERS substrate not only for sensing molecules with electron-level energy similar to that of MXenes would provide a wider field of application and, therefore, is highly desirable. SERS-based sensing

is used for the detection of various molecules (or ions), usually at much lower limits of detection than by conventional spectroscopic methods. The high sensitivity of the method is directly related to the adsorption of the analyte molecules on the nanoparticles. Thus, the adsorption of the molecules leads to enhanced intensity of the Raman spectrum.

Salicylic acid can act as a model molecule for studies of SERS enhancement on MXene film. This molecule consists of a benzene ring and carboxyl group. The Carboxyl group is involved in the adsorption of salicylic acid on the customary SERS substrates—silver or gold nanoparticles. Salicylic acid is known to be SERS-active when silver and gold nanoparticles are used, but this molecule does not exhibit electronic absorption in the visible spectral range.

In this research, the adsorption of salicylic acid molecules and the formation of salicylic acid–MXene complex were confirmed by experimental SERS-based spectral observations. The enhanced SERS signal was observed for salicylic acid molecules on $Ti_3C_2T_x$-based MXene film. The goal of this work is to study the enhancement of Raman spectral bands of salicylic acid when it is adsorbed on MXene film and to elucidate the enhancement features of MXenes when they are used as SERS substrates.

2. Materials and Methods

2.1. Synthesis of $Ti_3C_2T_x$ MXene Substrates

In this study, MXenes were prepared by etching 0.1 g of Ti_2AlC_3 MAX phase in 10 mL of 5 wt.% hydrofluoric acid solution. Solution was stirred for 24 h at 25 °C temperature. After this step, the solution was centrifuged in order to remove residue of hydrofluoric acid. Centrifugation proceeded until the pH of solution became neutral. Finally, the MXene films on a microscope glass slide were prepared. For this purpose, the glass slides were covered with 0.5 mL of aqueous MXene solution (0.01 g/mL) and dried under nitrogen atmosphere.

2.2. Characterization of MXene Film and Its Interaction with Adsorbate

Sample images and elemental analysis were performed by scanning electron microscope *Helios Nanolab 650* (FEI, Eindhoven, Netherlands) equipped with an EDX spectrometer X-Max (Oxford Instruments, Abingdon, UK). X-ray diffraction (XRD) analysis was performed using Ni-filtered Cu Kα radiation on *MiniFlex II* diffractometer (Rigaku, Tokyo, Japan) working in Bragg–Brentano (θ/2θ) geometry. The diffractograms were recorded within 2θ angle range from 5° to 60° at a step width of 0.02° and speed of 2/min. Resistivity measurements were performed on a thin-film gold interdigitated electrode *ED-IDE3-Au* (Micrux Technologies, Oviedo, Spain).

Characteristic spectroscopic range of interband transition and plasmonic response of MXenes were determined by ultraviolet, visible and near-infrared range (UV-Vis-NIR) absorption spectroscopy. UV-Vis-NIR electronic absorption spectra were acquired with dual-channel *Lambda-1050* spectrometer (PerkinElmer, Boston, MA, USA). The spectra were obtained in the range 350–2300 nm with 5 nm resolution.

$Ti_3C_2T_x$-based MXene film and its interaction with salicylic acid (SA) were investigated by means of Raman spectroscopy. *MonoVista CRS+* Raman microscope system (S & I GmbH, Warstein, Germany) equipped with four excitation lasers (457 nm, 532 nm, 633 nm and 785 nm) and a liquid-nitrogen-cooled CCD detector were used for acquiring the spectra. Diameter of the focused laser beam on the sample was ≈ 1 μm, and its power density on the sample was ≈ 20 kW/cm^2 (for 633 nm excitation) and ≈ 45 kW/cm^2 (for 785 nm excitation). Before the measurements, the spectrometer was calibrated to a fundamental vibrational band at 520.7 cm^{-1} of silicon wafer. Fourier transform *MultiRAM* spectrometer (Bruker, Mannheim, Germany) equipped with liquid-nitrogen-cooled Ge diode detector was used for the calculations of enhancement factor for salicylic acid–MXene complex with 1064 nm excitation wavelength.

Solution of salicylic acid in water with concentration equal to 2 mM was prepared. Two drops (5 μL each) of the solution were dried on the glass substrate covered by the MXene film. To ensure the most homogenous distribution of salicylic acid molecules, the

drying was performed in a confined space when the saturated vapor diminishes the surface tension in air–water interface and more uniform distribution can be achieved. The same volume of salicylic acid solution was dried on the aluminum foil as a reference. Salicylic acid solution spread to form a 2 mm spot on the film. After drying out, no crystallization occurred on the MXene film, while on the reference glass substrate, crystals of salicylic acid were formed. Presented SERS spectra of salicylic acid were recorded on 20 randomly chosen positions on the MXene surface and averaged. The standard deviation for the spectral intensity of salicylic acid on MXene substrate was calculated while applying 3 s acquisition time.

2.3. Computational Methods

In order to make more detailed analysis of the interaction between salicylic acid and MXene, theoretical calculations of structure and vibrational spectra of monomeric salicylic acid and salicylic acid dimer were performed by means of quantum chemistry calculations implemented in Gaussian 09W software package [37]. The salicylic acid dimer was chosen to resemble the crystalline structure of solid-state salicylic acid. The density functional theory (DFT) calculations using B3LYP/6311G^{++} functional were performed. For the investigation of the salicylic acid–MXene complex, the 2 × 2 × 1 supercell expansion of $Ti_3C_2(OH)_2$ MXene crystal structure (of 20 atoms) was built and optimized. Initially, geometry optimization was performed separately for salicylic acid (B3LYP/6311G^{++}) and $Ti_3C_2(OH)_2$ cluster (B3LYP/LanL2DZ) and for their complex afterward (B3LYP/LanL2DZ). No virtual frequencies were present after the complex optimization. The excited-state calculations were performed to assess the redistribution of the electronic energy levels.

3. Results

3.1. Characterization of MXene Films

The structure and morphology of the MAX phase and synthesized MXene-based materials were evaluated using the scanning electron microscopy (SEM) imaging technique (Figure 1). The compact and layered morphology, which is typical for ternary carbide [38], was obtained in the case of the MAX phase. Etching with 5 wt.% HF solution allows preparing $Ti_3C_2T_x$, for which the structure is quite similar to that of the MAX phase. However, MXene layers were slightly opened. The 'accordion-like' structure was not observed. A possible explanation may be found in low hydrofluoric acid concentration, which is insufficient for the formation of a sufficient amount of H_2 evolving during the exothermic reaction of hydrofluoric acid with aluminum atoms. Successful etching of aluminum atoms was confirmed by energy-dispersive X-ray spectroscopy (EDX) analysis (Table 1). It was revealed that the number of aluminum atoms in MXenes decreased by five times in comparison with the initial amount of these atoms in the MAX phase.

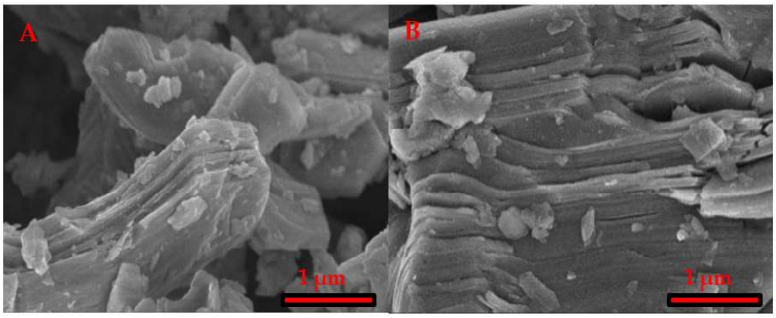

Figure 1. SEM images of (**A**) MAX phase (Ti_3AlC_2) and (**B**) MXenes ($Ti_3C_2T_x$).

Table 1. EDX analysis results for aluminum (Al) and titanium (Ti) atomic ratio in MAX phase and MXene samples.

Sample	Atomic Ratio, %	
	Aluminum (Al)	Titanium (Ti)
MAX phase (Ti_3AlC_2)	39.39 ± 0.96	60.61 ± 0.96
MXenes ($Ti_3C_2T_x$)	6.33 ± 1.97	93.67 ± 1.97

Comparing resistivity of MAX phase and MXenes etched in 5 wt.% HF, it was measured that the resistivity of samples at room temperature decreased from 36 Ω to 20.5 Ω. A decrease in sample resistivity might be explained by a reduced amount of aluminum by etching and the formation of semi-metallic Ti_3C_2 MXene structures.

The synthesis of MXenes was confirmed using XRD analysis (Figure 2). A shift of the (002) peak of Ti_3AlC_2 at 9.5° to 7.3° for the $Ti_3C_2T_x$ was observed. Such sufficiently large shift is typical for wet multilayered MXene samples [39], whereas an intense and sharp (002) peak is characteristic for MXenes etched by hydrofluoric acid [40]. Such results, together with the absence of other MAX phase characteristic peaks in MXene spectra, coincide with EDX analysis results and confirm successful etching of Al out of Ti_3AlC_2.

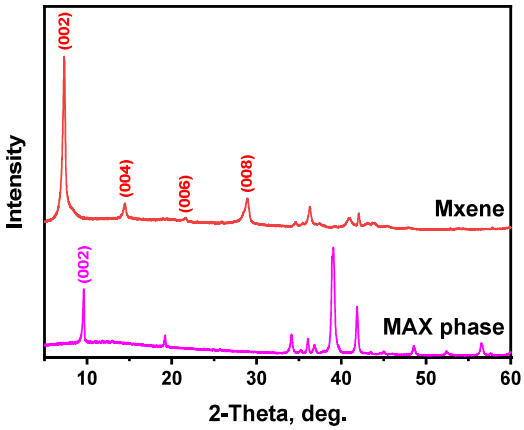

Figure 2. XRD patterns of MAX phase (Ti_3AlC_2) and MXene ($Ti_3C_2T_x$) powders.

Usually, MXene films are composed of various sizes of $Ti_3C_2T_x$ flakes (lateral sizes vary from 0.1 to ~5 µm). In contrast, the thickness of monolayered MXene is supposed to be about 0.95 nm [41]

Due to weak interaction between neighboring individual MXene flakes, the electric and plasmonic properties of the film do not significantly depend on the thickness of MXene structures, though the correlation between metallic behavior and the origin of the terminal chemical groups of MXenes is well expressed [17,21,34,42]. MXenes terminated with -F and -OH feature higher conductivity and plasmonic response to incident radiation in comparison to the oxidized MXenes.

The plasmonic response and other optical properties of the MXene substrate were assessed by the mean of UV-Vis-NIR absorption spectroscopy (Figure 3). Relying on the correlation between the optical density and the thickness of the film [17,21,43], we estimated the thickness to be approximately 70 nm.

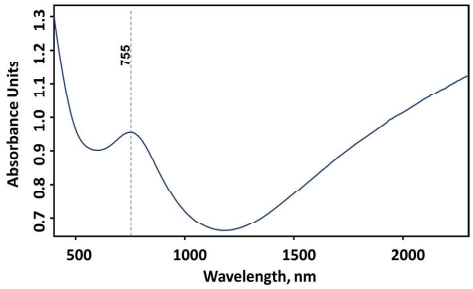

Figure 3. UV-Vis-NIR absorption spectrum of dried 70 nm thick $Ti_3C_2T_x$ MXene film on the glass slide.

The UV-Vis-NIR absorption spectrum of 70 nm thick $Ti_3C_2T_x$-based MXene film contains a broad spectral band (full width at half maximum—195 nm) characteristic for delaminated MXenes. The center of this band is located at 750 nm (1.65 eV). The origin of the spectral band is attributed to the interband transition. The plasmonic nature of this band is controversial. Some researchers assign bands in this spectral range to transversal plasmon resonance [42,44], while other studies suggest that the plasmonic activity of MXenes occurs as a consequence of the real part of the dielectric function, becoming negative only in the near-infrared spectral range, implying that the plasma frequency of MXenes is also in this range and excitation of surface plasmons can be expected at longer wavelengths. During this research, we adhere to the assignment of this absorption band to the interband transition because: (i) no plasmonic activities were observed in this spectral range and (ii) the characteristics of enhanced SERS spectra of salicylic acid indicate a chemical enhancement mechanism. It is important to note that the thickness of the MXene film or the size and shape of the individual $Ti_3C_2T_x$ flakes have no influence on the interband gap. The position of the spectral band can only be shifted by changing the concentration of free charge carriers that can be altered with different terminal groups of $Ti_3C_2T_x$ MXene lattice [17,21,34,42]. Therefore, we did not observe a shift in the interband transition energy when a thicker (120 nm thick) MXene film was deposited.

Considering the origin of the absorption band, transversal and longitudinal plasmon resonances are predicted to be closer to the middle infrared spectral range. It is notable that the maximum of the spectral band related to the plasmon resonance is located at $\lambda > 2200$ nm (see Figure 2). According to the calculations, the width of the plasmon band might be influenced by the high size dispersion of MXene flakes [45]. It should be noted that in order to increase the contribution of the electromagnetic enhancement mechanism into the amplification of the SERS spectrum together with the chemical enhancement mechanism, the plasmon resonance should be observed in the visible region of the spectrum. Fortunately, the plasmon resonance wavelength can be tailored by changing the flake dimensions [45,46].

3.2. Raman Spectra of MXene Films

Further assessment of MXene film composition can be performed using Raman spectroscopy data. The positions of Raman spectral bands of the MXene by itself are mostly caused by various vibrations of $Ti_3C_2T_x$ lattice and the terminal groups. Consequently, the presence of different terminal groups and even interactions with the target molecules can be distinguished by examining the spectral changes.

The Raman spectra of an MXene film on a glass plate obtained with 532 nm, 633 nm and 785 nm excitation are presented in Figure 4. The spectral bands of $Ti_3C_2T_x$ lattice vibrations that interest us occur in the range of 100–850 cm^{-1}. Excitation with a 532 nm laser yields a Raman spectrum with a relatively low signal-to-noise ratio ($S/N \approx 52$), whereas it is higher in the case of 633 nm and 785 nm excitations ($S/N > 100$).

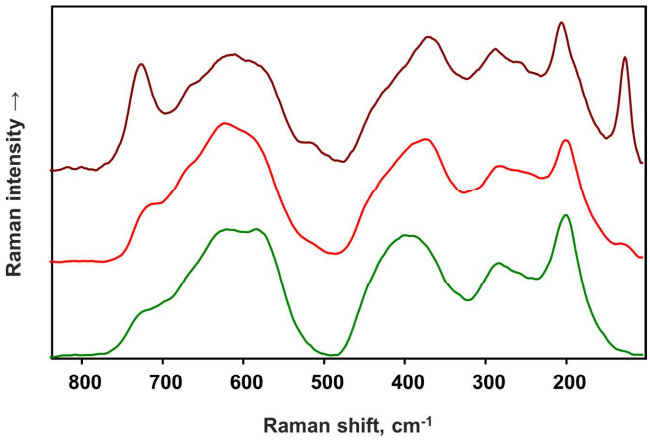

Figure 4. Raman spectra of MXene film with 532 nm (bottom), 633 nm (middle) and 785 nm (top) excitation.

It is worth mentioning that only a rather low power of 532 nm laser excitation could be used for acquiring the spectra. Structural and chemical changes of MXene film have been observed due to rapid oxidation when laser power exceeded 5 mW. In this case, the power density on the sample exceeded 1.5 MW/cm^2. Some degradation of the film was noticeable starting from 17 kW/cm^2 excitation beam power density. In the case of rapid oxidation, the intense G and D spectral bands arising from allotropic forms of carbon (formed from $Ti_3C_2T_x$ lattice) emerge along with the Raman spectrum of TiO_2 in anatase form, exhibiting the most intense spectral band at 143 cm^{-1}. Rapid oxidation is known to disrupt the structure of the MXene film [47]. Due to the disruption, Ti is oxidized into TiO_2 by the formation of anatase nanoparticles and graphitic or amorphous carbon [48]. Raman spectra acquired with 532 nm and 633 nm excitation fit very well with the literature data [22,48]. The lattice phonon modes of $Ti_3C_2T_x$ MXene terminated with different chemical groups are observed as a combination of the broader spectral bands at 129 cm^{-1} (ω_1), 198 cm^{-1} (ω_2), 709 cm^{-1} (ω_3), 667 cm^{-1} (ω_4), 281 cm^{-1} (ω_5) and 371 cm^{-1} (ω_7) [49]. Higher energy vibrational spectral bands presumably occur from non-uniform, defected MXene films and the presence of free carbon materials [24,48,50]. G and D spectral bands distinctive for the carbon materials are also present in the MXene spectra. The G band in MXene samples was observed at 1581 cm^{-1}, and the D band was almost imperceptible. Generally, the G band in carbon materials occurs because of sp^2 hybridization caused by C-C stretching being observed in both chain and ring structures, whereas the D band is observable only in the defected ring structures [51]. In our observations, the appearance of graphene bands indicates the disruption in MXene lattice structure and oxidation of MXenes. We will further address this issue in our forthcoming research.

The spectrum obtained with 785 nm excitation is somewhat different from other spectra. As can be seen in the UV-Vis-NIR absorption spectrum (Figure 3). MXenes in this spectral region have a spectral band arising due to IBT (the corresponding absorption band center, in our case, is at 750 nm). Thus, resonance effects are expected in the Raman spectrum with a 785 nm excitation laser. As a consequence of resonant lattice vibrations, the new spectral bands become observable. The new band at 120 cm^{-1} arises from the in-plane vibration mode of Ti and C atoms of the MXene lattice. In addition, the new out-of-plane breathing mode (ω_6) band at 513 cm^{-1} becomes discernible. During this vibration, terminal atoms are mainly moving in a transversal direction to the lattice plane. The intensity increase for the band at 722 cm^{-1} is observed as well. The spectral band at 722 cm^{-1} represents out-of-plane vibrations of C atoms perpendicular to the 2D plane

of MXene film. The gradual increase in the intensity of these bands is observed when excitation wavelength changes from 532 nm, 633 nm to 785 nm.

The appearance of new spectral bands can be explained by the resonant condition of excitation [44,45,49]. The enhancement of certain vibrational modes occurs when the exciting frequency comes into resonance with the lowest excited state. Usually, total symmetric modes experience the greatest enhancement (through A term). In this case, the symmetric normal modes, in which vibrations involve bonds that are affected by the change in the electronic state of excited molecules, are enhanced. Nevertheless, the enhancement of non-symmetric normal modes is possible when two excited states are coupled by the normal mode vibration (B term). Hence, in both cases, the enhanced modes correspond to the interaction between the molecule ground and excited states [52,53].

Furthermore, the lower energy vibrational spectral bands of $Ti_3C_2T_x$ MXenes can be used for the determination of the changes in surface terminal groups (=O, –OH or –F) [49,54,55]. The most stable MXene film is the one with carbonyl (=O) terminal group, e.g., $Ti_3C_2O_2$ [56] whilst, during the first step of synthesis of MXene—etching of Al—they are terminated with the -F group. Usually, it is considered that MXenes are terminated with all these functional groups to some degree [57]. Very promising spectral bands for the determination of terminal groups are the out-of-plane mode of C vibrations (ω_3), which is calculated to be located at 694 cm^{-1} in $Ti_3C_2(OH)_2$ MXene and at 730 cm^{-1} in $Ti_3C_2O_2$ and the out-of-plane mode of mainly Ti and terminal atoms vibrations (ω_2). It was experimentally proved that ω_3 mode becomes red-shifted when the =O terminal group is reduced into the –OH group [30], while ω_2 redshifts from 218 cm^{-1} to 208 cm^{-1} [49]. Other distinct Raman spectral bands of $Ti_3C_2O_2$ are the out-of-plane mode of =O at 371 cm^{-1} and Ti and the =O in-plane vibrational mode at 589 cm^{-1}. The bands at 281 cm^{-1} –OH in-plane and 667 cm^{-1}—C atom out-of-plane vibrational modes arise from $Ti_3C_2(OH)_2$. Raman vibrational frequencies observed for MXene films and assignments of the spectral bands are presented in Table 2.

Table 2. Vibrational frequencies of $Ti_3C_2T_x$-based MXene films.

Vibrational Freq., cm^{-1}			Calculated Freq., cm^{-1} [49]	Assignments [49]
532 nm	**633 nm**	**785 nm**		
W	129	120	128	$(Ti,C)^{ip}$, $Ti_3C_2F_2$; ω_1
198	198	199	190	$(Ti,F)^{oop}$, $Ti_3C_2F_2$; ω_2
257	W	258	231	$(F)^{ip}$, $Ti_3C_2F_2$; ω_5
287	281	280	278	$(OH)^{ip}$, $Ti_3C_2(OH)_2$; ω_5
390	371	366	347	$(O)^{ip}$, $Ti_3C_2O_2$; ω_5
W	511 [a]	513 [b]	514	$(OH)^{oop}$, $Ti_3C_2(OH)_2$; ω_6
590 [a]	589 [a]	584 [a]	586	$(O)^{oop}$, $Ti_3C_2O_2$; ω_6
621	620	615	622	$(C)^{ip}$, $Ti_3C_2(OH)_2$; ω_4
673 [a]	667 [a]	655	684	$(C)_{oop}$, $Ti_3C_2(OH)_2$; ω_3
715	709 [a]	722 [b]	730	$(C)^{oop}$, $Ti_3C_2O_2$; ω_3
W	W	W		D band
1550	1581	1520 [a]		G band

[a] Decreased intensity in spectral band compared to 785 nm excitation. [b] Increased intensity in spectral band compared to 785 nm excitation. [W] Not prominent or weak band. [ip] In-plane phonon mode. [oop] Out-of-plane phonon mode.

3.3. Interaction between Salicylic Acid and MXenes

An interesting effect was observed when salicylic acid (SA) solution was dried on the MXene film. The measured Raman spectrum of salicylic acid on MXene film clearly differs from that of crystalline salicylic acid (Figure 5). The redshifts of the vibrational bands are evident and indicate an interaction between salicylic acid molecules and the $Ti_3C_2T_x$-based MXene film. The appearance of prominent Raman spectral bands at 896 cm^{-1} and a band doublet at 681 cm^{-1} and 654 cm^{-1} confirms the interaction between salicylic acid and the MXene. Based on our DFT calculations performed for monomeric salicylic acid molecule and salicylic acid dimer (as in crystalline salicylic acid form), these newly emerged bands

can be assigned to out-of-plane vibrations of CH groups and out-of-plane ring deformation, respectively. The latter usually displays a low Raman signal intensity of the crystalline form of SA. The increased intensity of out-of-plane vibrational bands was evaluated by calculating enhancement factor for intensified bands as:

$$Enhancement\ factor = (I_{SERS} \times N_{Raman})/(I_{Raman} \times N_{SERS}) \quad (1)$$

where I_{SERS} and I_{Raman} are SERS and Raman spectral band intensities, N_{Raman} and N_{SERS}—number of excited molecules for Raman and SERS experiments.

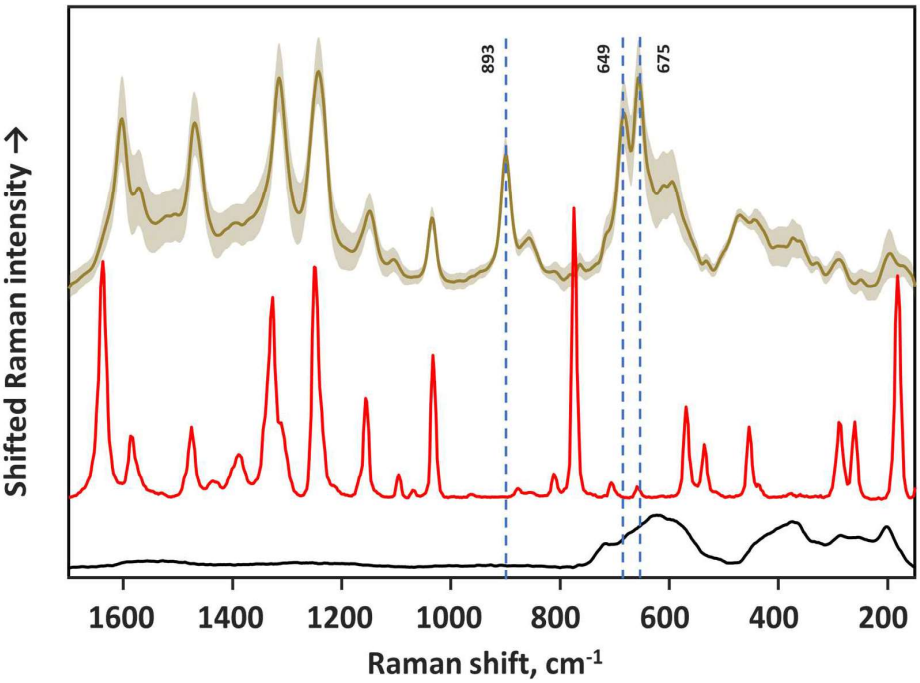

Figure 5. Raman spectra of MXene film (bottom) and salicylic acid: dried on MXene surface (middle) and on aluminum foil (top). Excitation wavelength—633 nm.

Comparing salicylic acid deposited directly on aluminum surface and on the MXene film, enhancement factor reached 125, 110 and 220 for the band at 896 cm^{-1} and band doublet at 681 cm^{-1} and 654 cm^{-1}, respectively (532 nm excitation).

Additionally, an increase in intensities and redshifts were observed for the other salicylic acid spectral bands. The largest shift occurred for the C=O stretching vibrational band of the carboxylic group at 1636 cm^{-1} which shifted by 39 cm^{-1} to 1597 cm^{-1}; the other bands experienced smaller redshifts—from 12 to 15 cm^{-1}. For example, the vibrational modes of the benzene ring observed at 1583 cm^{-1} and 1473 cm^{-1} were shifted to 1567 cm^{-1} and 1467 cm^{-1}, respectively. The C–O stretching band at 1325 cm^{-1} is shifted down to 1311 cm^{-1}; the spectral band of the C–O deformation of the hydroxyl group at 1244 cm^{-1} is shifted to 1232 cm^{-1}. Indeed, the only spectral band that did not experience observable shift is the benzene ring mode at 1031 cm^{-1}. The assignments of the experimental spectral bands for (i) salicylic acid crystals formed on the pure aluminum surface and (ii) vibrational shifts for salicylic acid on MXene film are provided in Table 3.

Table 3. Vibrational frequencies of crystalline salicylic acid and SA–MXene complex.

Crystalline Salicylic Acid, Freq. cm^{-1}	Salicylic Acid on MXenes, Freq. cm^{-1}	Assignments
180	-	δ_{oop}(C-COOH)
258	-	δ_{ip}(C-COOH)
286	-	δ_{ip}(C-OH)
452	-	δ_{ip}(C-COOH)
-	473	δ_{oop}(ring) + δ_{oop} (OH)
534	-	δ_{oop}(ring)
568	-	δ_{oop}(O-H) [a] + δ_{oop}(ring)
-	595	δ_{ip}(C-C, ring)+ δ_{oop}(OH)
657	654 ↑	δ_{ip}(-COOH) + δ_{oop}(ring)
705	681 ↑	δ_{oop}(ring) + δ_{oop}(O-H) [a]
773	-	δ_{ip}(C-H) [a] + 6 [c]
850	861	ν(C-OH) [b]+ δ_{ip}(ring)
876	896 ↑	δ_{oop}(C-H); 17 [c]
1031	1031	18 [c]?
1093		δ(O-H) [b]
1154	1145	δ(O-H) [a]
1164	-	15 [c]
1244	1232	δ(O-H) [a] + ν(C-COOH)
1307	-	δ(O-H) [a]
1325	1311	δ(C-O) [b]
1386	1397	14 [c] + δ(C-O) [b]
1473	1467	19 [c]
1583	1567	8 [c]
1636	1597 ↓	ν(C=O) [a]

[a] Vibration of atoms in –COOH functional group. [b] Vibration of atoms in –OH functional group. ↑ Increased intensity. ↓ Decreased intensity. Stretching vibration. δ Deformation vibration. $_{oop}$ Out-of-plane. $_{ip}$ In-plane. [c] Modes derived from benzene [58].

Partly due to the porous MXene surface and high surface area, salicylic acid molecules can spread easily and interact with the MXenes. Indication of such interaction is the change in color from purple to yellowish when salicylic acid is dried on the MXene film (Figure 6 inset). Salicylic acid molecules are prone to form crystals when drying, though: after drying on the MXene film, no crystals are visible.

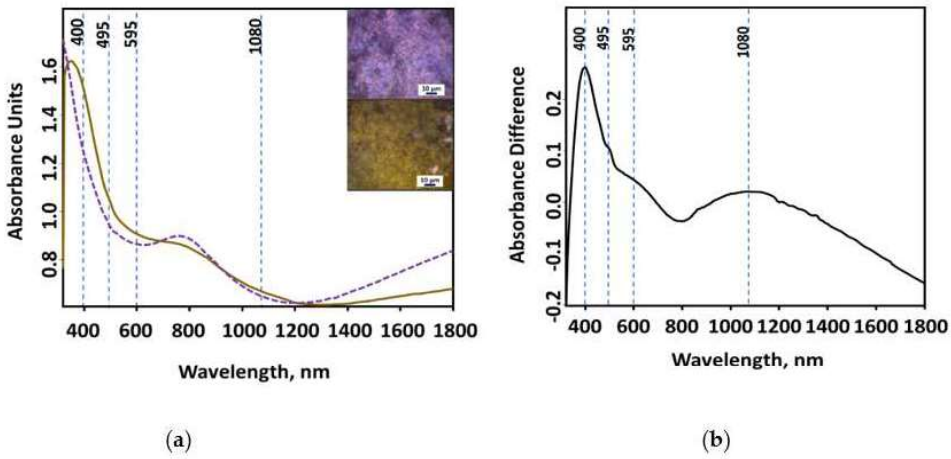

Figure 6. UV-Vis-NIR absorption spectra of the $Ti_3C_2T_x$-based MXene film (dotted line) and salicylic acid (straight line) dried on the MXene (**a**); differential spectrum (**b**). Inset—optical microscope images of MXene film (left) and salicylic acid dried on the MXene film (right).

Detailed investigation of the interaction between salicylic acid molecules and $Ti_3C_2T_x$ MXene can be completed by analyzing UV-Vis-NIR spectra. The change in UV-Vis-NIR absorption spectrum of salicylic acid–MXene film is clearly seen in the differential spectrum where the MXene spectrum is subtracted from salicylic acid on the MXene spectrum (Figure 6b). Salicylic acid water solution features absorption bands from π to π^* and n to π^* transitions at $\approx$ 230 nm and $\approx$ 300 nm, whereas salicylic acid–MXene film possesses the highest intensity band at 400 nm. Other, less distinct bands are at 495 nm, 595 nm and 1080 nm. The decrease in near-infrared absorption range from MXene film is probably caused by redistribution of conduction band electrons—free charge carriers. These changes in the absorption spectrum confirm that salicylic acid and MXene are forming complex structures.

These spectral changes can be explained by the formation of the salicylic acid–MXene complex and the charge-transfer effect. It is already known that certain molecules form complexes with $Ti_3C_2T_x$ MXenes and, therefore, can undergo charge transfer [30,32,33]. For that matter, the SERS enhancement derived from the MXene films is explained using this charge transfer mechanism and, naturally, by the chemical enhancement mechanism. Briefly, the chemical enhancement is thought to be active because of one of these factors: (i) the charge transfer mechanism between the adsorbed molecule and the substrate and (ii) the influence of the substrate on the molecular polarizability tensor elements that changes the efficiency of Raman scattering. In the case of charge transfer, the Raman signal is enhanced because of the pre-resonance or resonance condition of the excitation to the adsorbate–substrate complex. Thus, the charge transfer mechanism can be traced by: (i) the greater enhancement of the antisymmetric vibrations compared to symmetric ones (due to the B term excitation of resonance Raman); (ii) enhancement of the stretching vibrations (in the resonant condition of excitation, the totally symmetric vibrations in accordance with the excited state geometry of the molecule are enhanced (due to A term mechanism). The bond length between atoms usually increases in the excited molecule state); (iii) high dependence of the EF on the excitation wavelength.

The first indication of the charge transfer effect in the salicylic acid–MXene complex is the greater enhancement of asymmetric vibrational modes. Since the salicylic acid molecule is in the C_s point symmetry group, the vibrational modes of salicylic acid can only be classified as in-plane (A′) or out-of-plane (A″) vibrations. The latter is less symmetric and, as seen in Figure 5, was enhanced via salicylic acid–MXene interaction. The dependence of salicylic acid–MXene Raman spectra on the excitation wavelength is presented in Figure 7.

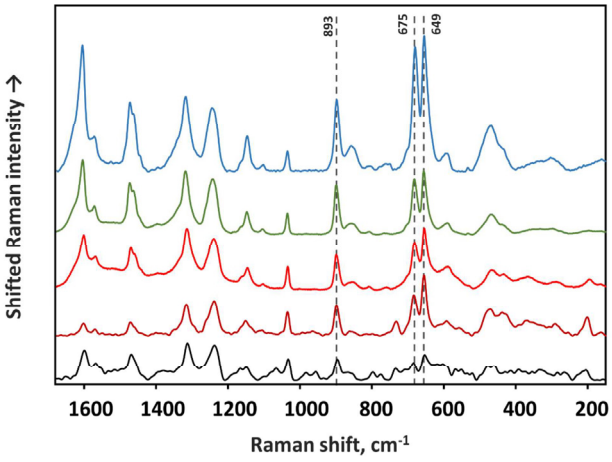

Figure 7. Raman spectra of salicylic acid–MXene complex with different excitations. Excitations from top to bottom: 457 nm; 532 nm; 633 nm; 785 nm; 1064 nm.

Based on the spectra acquired at different excitations, the enhancement factor dependence on the excitation can be evaluated (Figure 8). To minimize the influence of spectrometer response to different wavelength, the crystalline salicylic acid was acquired with each excitation, and the salicylic acid–MXene complex spectrum was compared to crystalline salicylic acid spectrum acquired at the same conditions.

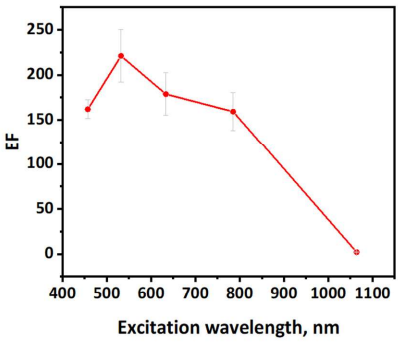

Figure 8. Calculated SERS enhancement factor (EF) for 2 mM salicylic acid dried on the MXene film with different excitation wavelengths.

Indeed, the SERS enhancement factor for out-of-plane vibrations is as expected for the chemical enhancement mechanism. The enhancement factor for the substrate covered by the salicylic acid–MXene complex was calculated for the most enhanced vibrational band at 654 cm^{-1} (carboxyl deformation + out-of-plane C-C bending). As the enhancement factor value dependency on the excitation wavelength indicates, the highest enhancement of 220 is achieved with a 532 nm laser (Figure 8). Nevertheless, 457 nm and 633 nm excitations also yield comparable enhancement of 165 and 178, respectively. The 785 nm excitation fell into the absorption of MXenes; for this reason, the Raman spectral bands of MXene phonon modes are still observable in the spectrum, and the enhancement factor reaches 150. For the excitation profile of 1064 nm, an entirely different Fourier Transform-Raman spectrometer was used. It was observed that MXene film without salicylic acid highly absorbs this wavelength, generates heat and makes the registration of spectrum with this excitation impossible. Nevertheless, when the salicylic acid–MXene complex is excited, the characteristic spectrum is observed, which is indicating changes in the electron distribution of the MXene layer.

It is worth mentioning that based on our results, the chemical mechanism of enhancement takes place between salicylic acid and MXenes. The observable hot spot effect of SERS substrates arises when the intensity crucially depends on the different spots of the sample, because of the electromagnetic mechanism of enhancement when the analyte molecule is trapped between two nanoparticles [31]. The random distribution of these hot spots varies the absolute intensity of SERS bands. In our case, the chemical enhancement mechanism makes the substrate more uniform in the sense of changes in the intensity of the Raman bands. For the calculations of the enhancement factor, the absolute intensity is important, but for further studies, the normalization to a specific spectral band can be considered (for salicylic acid, it was the only spectral band at 1031 cm^{-1} that did not shift, and for this reason, it is considered to be unaffected by chemical enhancement mechanism).

However, the comparison of the achieved enhancement factor for salicylic acid with that of conventional SERS materials such as silver and gold nanostructures is difficult. Limited literature is available concerning the SERS enhancement factor of salicylic acid. To the best of our knowledge, the evaluation of the analytical enhancement factor for salicylic acid adsorbed on silver and gold nanoparticles with 1064 nm excitation is presented only in one of our previous works [59]. The determined enhancement factors for gold and

silver nanoparticles prepared with different synthesis methods and stabilizing agents are presented in Table 4.

Table 4. Comparison of enhancement factors for salicylic acid achieved with different materials.

Substrate Material	Excitation	Enhancement Factor
Citrate-stabilized AgNPs	1064 nm	2.5×10^4
Polymer-stabilized AgNPs	1064 nm	1.2×10^4
Citrate-stabilized AuNPs	1064 nm	2.5×10^3
Polymer-stabilized AuNPs	1064 nm	3.8×10^3
$Ti_3C_2T_x$ MXene	532 nm	2.2×10^2

AgNPs—silver nanoparticles. AuNPs—gold nanoparticles.

3.4. Computational Results of Salicylic Acid Interaction with MXene

In order to make a more detailed investigation of the salicylic acid and MXene interaction, the first-principle calculations based on DFT were performed. For salicylic acid–MXene complex investigation, the cluster of $Ti_3C_2(OH)_2$ supercell was built and optimized (B3LYP/LanL2DZ). According to the calculations, salicylic acid displays affinity of forming a chemical bond with titanium atom of $Ti_3C_2(OH)_2$ crystal via oxygen atom in carboxyl group of salicylic acid. The likeness of the complex formation is assured based on geometrical parameters of optimized geometry of the salicylic acid–MXene complex. The length of the O-H interatomic bond in the salicylic acid carboxyl group increased from 0.976 to 1.536 Å, whereas the distance between the $Ti_3C_2(OH)_2$ MXene OH-H group was 1.034 Å, indicating the possible proton transfer between SA and the MXene cluster. The C-O bond length in the carboxyl group also increased from 1.232 to 1.339 Å. The bond formation between salicylic acid and $Ti_3C_2(OH)_2$ MXene can explain the drastic experimental shift of 40 cm^{-1} for the C=O stretching vibrational band of the carboxylic group at 1636 cm^{-1} and the disappearance of the salicylic acid band at 771 cm^{-1} (benzene ring bending + carboxyl deformation modes). The formed bond between salicylic acid and the MXene cluster can become a channel for electron density redistribution around the salicylic acid and MXene cluster. Moreover, the charge distribution on the atoms from the performed Mulliken population analysis indicates a slight charge redistribution by −0.66 when from −0.32 (monomeric salicylic acid) to −0.98 (salicylic acid–MXene complex).

As can be expected, the electron density in the highest occupied molecular orbital minus 1 (HOMO-1) and lower molecular orbitals is focused on the donor $Ti_3C_2(OH)_2$ MXene. In the HOMO molecular orbital, the electron density redistribution is already observed, also indicating the formation of a complex bond between the carboxyl group of salicylic acid and MXene, whereas in the lowest unoccupied molecular orbital (LUMO), the high electron density shifts from MXene to salicylic acid (1.45 eV). Based on the electron density in molecular orbitals, other charge transfer excitations are observed at LUMO + 4 (2.2 eV) and LUMO + 10 (2.9 eV) (Figure 9). The calculated salicylic acid–MXene complex excitations are in accordance with the observed UV-Vis absorption spectrum (Figure 6), where the most intense absorption band is observed at 400 nm (calculated—428 nm) and lower bands—at 495 nm and 595 nm (calculated—564 nm) and 1080 nm. By comparing the HOMO-LUMO excitation of the monomeric salicylic acid molecule, the required salicylic acid molecule excitation energy decreased from 4.5 eV to 2.9 eV.

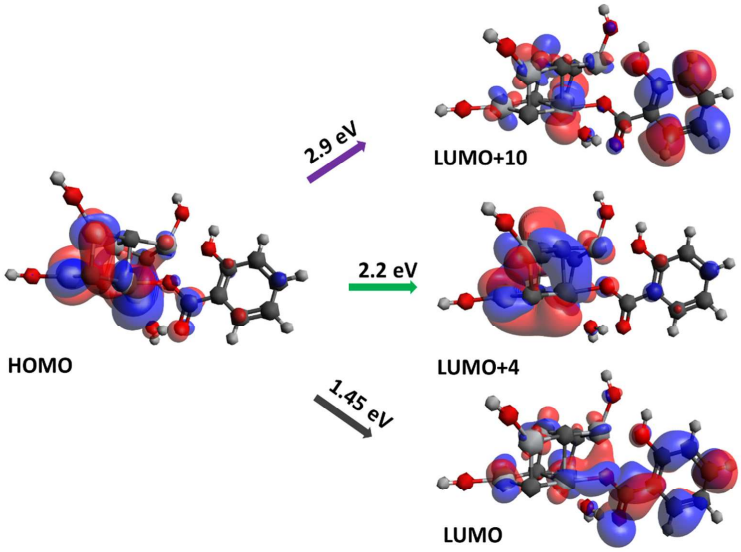

Figure 9. Calculated (B3LYP/LanL2DZ) molecular orbitals of salicylic acid–MXene complex and required transition energy.

4. Discussion

In the search for non-metallic SERS substrates, a very big role is placed on the very high enhancement of vibrations. Briefly, the chemical enhancement mechanism of SERS in widely used metal nanoparticles contributes to the total enhancement effect only on the order of 10–100, whereas the electromagnetic enhancement mechanism is thought to be responsible for spectral enhancement as high as 10^6 times [31]. Thus, the electromagnetic enhancement should enhance the molecular spectra by a huge amount. Nevertheless, the electromagnetic enhancement mechanism depends strongly on the charge carrier concentration in materials and thus their metallic properties.

During the last decade, the metallic properties of MXenes were investigated rather comprehensively. Similar to other 2D semimetals [16], MXenes show plasmonic behavior and the negative real part of the dielectric function in the near-infrared range [17,34,42,46]. Experimental findings for highly oriented MXene films reveal that at wavelengths longer than 1000 nm, the real part of the dielectric function becomes negative, indicating the onset of free-electron plasma oscillations [17,42,46]. The wavelength threshold at which MXene films become metallic depends on the film thickness [34,46], and thus can be slightly shifted. Furthermore, SEM [22] and atomic force microscopy [55] images clearly reveal the structure of MXenes as the flakes are packed in the form of multilayer sheets. After the delamination, these sheets part out. Extended studies of optical properties of the monolayer flake revealed that the free-electron plasma oscillations occur in two spectral regions: (I) at wavelengths longer than 885 nm and (II) in the narrow 615–740 nm region [42]. The surface plasmon in the latter region was assigned to transversal plasmon resonance (1.7 eV). The transversal plasmon resonance is insensitive to the size and shape of the flake, but it depends on the concentration of free charge carriers that can be altered with the different terminal groups [17,34,42,46].

In performed studies, it was reported that some molecules could interact with multilayered MXenes. Intercalated molecules increase the distance between individual $Ti_3C_2T_x$ mono-sheets and, due to mechanical agitation, cause the delamination of multilayered MXene flakes. Usually, such intercalants are dimethyl sulfoxide DMSO, tetraalkylammonium hydroxide, isopropylamine, hydrazine, urea, Li^+ ions [60,61] or even water molecules [62].

As a result of this process, a large surface area of MXene layers becomes available for interaction, which is desirable for the SERS enhancement. In this work, SERS spectra of the salicylic acid–MXene complex was observed for both the multilayered and delaminated MXenes (it should be noted that for the latter, SERS intensity and reproducibility were higher). This supports our prediction that salicylic acid was also responsible for partial delamination of MXene layers.

MXenes have a mixture of oxygen, hydroxyl and fluoride terminal groups that can be protonated/deprotonated at different pHs [23]. At higher hydrogen ion concentration (lower pH), the oxidation of MXenes is slowed down; therefore, a higher surface concentration of hydroxyl terminal groups is favored. Due to pronation at low pH, the hydroxyl terminal groups provide a slightly positive charge on the surface of the MXene layer. This fact should be considered while investigating the mechanism of interaction between MXene and salicylic acid. Moreover, salicylic acid is deprotonated in deionized water (loses hydrogen ions from the carboxylic group); thus, it has a negative charge localized at the carboxylic group that also favors the formation of hydrogen bonds with terminal hydroxyl groups. Therefore, salicylic acid adsorbs well to the hydroxyl-terminated MXene layer.

Out-of-plane vibrations of salicylic acid are enhanced when the molecule interacts with MXene. These spectral changes indicate the molecule of salicylic acid is lying flat on the MXene film. It is known that for dye molecules, charge transfer between the electronic dye level and MXene electronic level takes place, and as a consequence, the dye molecules experience enhancement. Nevertheless, the electromagnetic enhancement mechanism from MXenes, which is expected, was still not observed, neither in our study nor to the best of our knowledge in any other studies.

5. Conclusions

The surface-enhanced effect of spectral Raman bands of salicylic acid adsorbed on $Ti_3C_2T_x$-based MXene film was observed for the first time. The adsorption of the salicylic acid molecule and the formation of a salicylic acid–MXene complex was confirmed by experimental spectral observations such as substantial enhancement of out-of-plane bending modes of salicylic acid at 896 cm^{-1}, 681 cm^{-1} and 654 cm^{-1}. Additionally, other spectral features indicate the adsorption of salicylic acids, such as the redshift of some vibrational frequencies as well as the disappearance of the carboxyl deformation spectral band at 771 cm^{-1}. The values of calculated experimental enhancement factors indicate that chemical enhancement mechanisms are dominant in SERS spectra of salicylic acid adsorbed on the MXene surface. For the deformation out-of-plane vibrational modes, this factor varies from 220 (at λ = 532 nm) to 60 (at λ = 1064 nm).

Author Contributions: Conceptualization: S.A.-G. and A.R.; Methodology: S.A.-G., A.P., S.R. and O.G.; Software: S.A.-G. and V.Š., formal analysis: S.A.-G., A.P., S.R. and O.G.; Writing—original draft preparation: S.A.-G.; Writing—review and editing: V.Š. A.P., S.R. and A.R.; Supervision: V.Š. and A.R. All authors have read and agreed to the published version of the manuscript.

Funding: This project has received funding from H2020 Marie Skłodowska-Curie Actions (CanBioSe 778157, SALSETH 872370).

Institutional Review Board Statement: Not applicable.

Informed Consent Statement: Not applicable.

Data Availability Statement: Not applicable.

Acknowledgments: Computations were performed on resources at the High Performance Computing Center, 'HPC Sauletekis', at the Vilnius University Faculty of Physics.

Conflicts of Interest: The authors declare no conflict of interest.

References

1. Yan, Y.; Cheng, Z.; Li, W.; Jin, K.; Wang, W. Graphene, a material for high temperature devices—Intrinsic carrier density, carrier drift velocity and lattice energy. *Sci. Rep.* **2014**, *4*, 5758. [CrossRef]

2. Song, Q.; Ye, F.; Kong, L.; Shen, Q.; Han, L.; Feng, L.; Yu, G.; Pan, Y.; Li, H. Graphene and MXene Nanomaterials: Toward High-Performance Electromagnetic Wave Absorption in Gigahertz Band Range. *Adv. Funct. Mater.* **2020**, *30*, 2000475. [CrossRef]
3. Naguib, M.; Kurtoglu, M.; Presser, V.; Lu, J.; Niu, J.; Heon, M.; Hultman, L.; Gogotsi, Y.; Barsoum, M.W. Two-dimensional nanocrystals produced by exfoliation of Ti_3AlC_2. *Adv. Mater.* **2011**, *23*, 4248–4253. [CrossRef]
4. Gogotsi, Y.; Anasori, B. The rise of MXenes. *CS Nano* **2019**, *13*, 8491–8494. [CrossRef]
5. Bhat, A.; Anwer, S.; Bhat, K.S.; Mohideen, M.I.H.; Liao, K.; Qurashi, A. Prospects challenges and stability of 2D MXenes for clean energy conversion and storage applications. *NPJ 2D Mater. Appl.* **2021**, *5*, 61. [CrossRef]
6. Papadopoulou, K.A.; Chroneos, A.; Parfitt, D.; Christopoulos, S. A perspective on MXenes: Their synthesis, properties, and recent applications. *J. Appl. Phys.* **2020**, *128*, 17. [CrossRef]
7. Anasori, B.; Luhatskaya, M.R.; Gogotsi, Y. 2D metal carbides and nitrides (MXenes) for energy storage. *Nat. Rev. Mater.* **2017**, *2*, 16098. [CrossRef]
8. Shahzad, F.; Iqbal, A.; Kim, H.; Koo, C.M. 2D Transition Metal Carbides (MXenes): Applications as an Electrically Conducting Material. *Adv. Mater.* **2020**, *32*, 2002159. [CrossRef]
9. Sinha, A.; Zhao, H.; Huang, Y.; Lu, X.; Chen, J.; Jain, R. MXene: An emerging material for sensing and biosensing. *TrAC Trends Anal. Chem.* **2018**, *105*, 424–435. [CrossRef]
10. Ramanavicius, S.; Ramanavicius, A. Progress and Insights in the Application of MXenes as New 2D Nano-Materials Suitable for Biosensors and Biofuel Cell Design. *Int. J. Mol. Sci.* **2020**, *21*, 9224. [CrossRef]
11. Xie, X.; Chen, S.; Ding, W.; Nie, Y.; Wei, Z. An extraordinarily stable catalyst: Pt NPs supported on two-dimensional $Ti_3C_2X_2$ (X= OH, F) nanosheets for oxygen reduction reaction. *Chem. Commun.* **2013**, *49*, 10112–10114. [CrossRef] [PubMed]
12. Zhang, J.; Zhao, Y.; Guo, X.; Chen, C.; Dong, C.L.; Liu, R.S.; Han, C.P.; Li, Y.; Gogotsi, Y.; Wang, G. Single platinum atoms immobilized on an MXene as an efficient catalyst for the hydrogen evolution reaction. *Nat. Catal.* **2018**, *1*, 985–992. [CrossRef]
13. Ran, J.; Gao, G.; Li, F.T.; Ma, T.Y.; Du, A.; Qiao, S.Z. Ti_3C_2 MXene co-catalyst on metal sulfide photo-absorbers for enhanced visible-light photocatalytic hydrogen production. *Nat. Commun.* **2017**, *8*, 13907. [CrossRef]
14. Yin, L.; Li, Y.; Yao, X.; Wang, Y.; Jia, L.; Liu, Q.; Li, J.; Li, Y.; He, D. MXenes for Solar Cells. *Nano-Micro Lett.* **2021**, *13*, 78. [CrossRef]
15. Enyashin, A.N.; Ivanovskii, A.L. Two-dimensional titanium carbonitrides and their hydroxylated derivatives: Structural, electronic properties and stability of MXenes $Ti_3C_{2-x}N_x(OH)_2$ from DFTB calculations. *J. Solid State Chem.* **2013**, *207*, 42–48. [CrossRef]
16. Zhu, Z.; Zou, Y.; Hu, W.; Li, Y.; Gu, Y.; Cao, B.; Guo, N.; Wang, L.; Song, J.; Zhang, S.; et al. Near-Infrared Plasmonic 2D Semimetals for Applications in Communication and Biology. *Adv. Funct. Mater.* **2016**, *26*, 1793–1802. [CrossRef]
17. Dillon, A.D.; Ghidiu, M.J.; Krick, A.L.; Griggs, J.; May, S.J.; Gogotsi, Y.; Barsoum, M.W.; Fafarman, A.T. Highly conductive optical quality solution-processed films of 2D titanium carbide. *Adv. Funct. Mater.* **2016**, *26*, 4162–4168. [CrossRef]
18. Miranda, A.; Halim, J.; Barsoum, M.W.; Lorke, A. Electronic properties of freestanding $Ti_3C_2T_x$ MXene monolayers. *Appl. Phys. Lett.* **2016**, *108*, 033102. [CrossRef]
19. Lee, K.S.; El-Sayed, M.A. Gold and Silver Nanoparticles in Sensing and Imaging: Sensitivity of Plasmon Response to size, shape, and metal composition. *J. Phys. Chem. B* **2016**, *110*, 19220–19225. [CrossRef] [PubMed]
20. Hart, J.L.; Hantanasirisakul, K.; Lang, A.C.; Anasori, B.; Pinto, D.; Pivak, Y.; van Omme, J.T.; May, S.J.; Gogotsi, Y.; Taheri, M.L. Control of MXenes' electronic properties through termination and intercalation. *Nat. Commun.* **2019**, *10*, 522. [CrossRef]
21. Mariano, M.; Mashtalir, O.; Antonio, F.Q.; Ryu, W.H.; Deng, B.; Xia, F.; Gogotsi, Y.; Taylor, A.D. Solution-processed titanium carbide MXene films examined as highly transparent conductors. *Nanosale* **2016**, *8*, 16371–16378. [CrossRef] [PubMed]
22. Melchior, S.A.; Raju, K.; Ike, I.S.; Erasmus, R.M.; Kabongo, G.; Sigalas, I.; Iyuke, S.E.; Ozoemena, K.I. High-voltage symmetric supercapacitor based on 2d titanium carbide (mxene, Ti_2CT_x)/carbon nanosphere composites in a neutral aqueous electrolyte. *J. Electrochem. Soc.* **2018**, *165*, A501–A511. [CrossRef]
23. Echols, I.J.; An, H.; Zhao, X.; Prehn, E.M.; Tan, Z.; Radovic, M.; Green, M.J.; Lutkenhaus, J.L. pH-Response of polycation/$Ti_3C_2T_x$ MXene layer-by-layer assemblies for use as resistive sensors. *Mol. Syst. Des. Eng.* **2020**, *5*, 366–375. [CrossRef]
24. Lorencova, L.; Bertok, T.; Dosekova, E.; Holazova, A.; Paprckova, D.; Vikartovska, A.; Sasinkova, V.; Filip, J.; Kasak, P.; Jerigova, M.; et al. Electrochemical performance of $Ti_3C_2T_x$ MXene in aqueous media: Towards ultrasensitive H_2O_2 sensing. *Electrochim. Acta* **2017**, *235*, 471–479. [CrossRef]
25. An, H.; Habib, T.; Shah, S.; Gao, H.; Patel, A.; Echols, I.; Zhao, X.; Radovic, M.; Green, M.J.; Lutkenhaus, J.L. Water sorption in MXene/polyelectrolyte multilayers for ultrafast humidity sensing. *ACS Appl. Nano Mater.* **2019**, *2*, 948–955. [CrossRef]
26. Song, D.; Jiang, X.; Li, Y.; Lu, X.; Luan, S.; Wang, Y.; Li, Y.; Gao, F. Metal–organic frameworks-derived MnO_2/Mn_3O_4 microcuboids with hierarchically ordered nanosheets and Ti_3C_2 MXene/Au NPs composites for electrochemical pesticide detection. *J. Hazard. Mater.* **2019**, *373*, 367–376. [CrossRef]
27. Kim, H.; Wang, Z.; Alshareef, H.N. MXetronics: Electronic and photonic applications of MXenes. *Nano Energy* **2019**, *60*, 179–197. [CrossRef]
28. Velusamy, D.B.; El-Demellawi, J.K.; El-Zohry, A.M.; Giugni, A.; Lopatin, S.; Hedhili, M.N.; Mansour, A.E.; Fabrizio, E.D.; Mohammed, O.F.; Alshareef, H.N. MXenes for Plasmonic Photodetection. *Adv. Mater.* **2019**, *31*, 1807658. [CrossRef]
29. Zhu, X.; Liu, P.; Xue, T.; Ge, Y.; Ai, S.; Sheng, Y.; Wu, R.; Xu, L.; Tang, K.; Wen, Y. A novel graphene-like titanium carbide MXene/Au–Ag nanoshuttles bifunctional nanosensor for electrochemical and SERS intelligent analysis of ultra-trace carbendazim coupled with machine learning. *Ceram. Int.* **2021**, *47*, 173–184. [CrossRef]

30. Hu, M.; Li, Z.; Hu, T.; Zhu, S.; Zhang, C.; Wang, X. High-Capacitance Mechanism for $Ti_3C_2T_x$ MXene by in Situ Electrochemical Raman Spectroscopy Investigation. *ACS Nano* **2016**, *10*, 11344–11350. [CrossRef]
31. Le Ru, E.; Etchegoin, P. *Principles of Surface-Enhanced Raman Spectroscopy: And Related Plasmonic Effects*; Elsevier: Amsterdam, The Netherlands, 2008.
32. Liu, R.; Jiang, L.; Lu, C.; Yu, Z.; Li, F.; Jing, X.; Xu, R.; Zhou, W.; Jin, S. Large-scale two-dimensional titanium carbide MXene as SERS-active substrate for reliable and sensitive detection of organic pollutants. *Spectrochim. Acta Part A Mol. Biomol. Spectrosc.* **2020**, *236*, 118336. [CrossRef] [PubMed]
33. Elumalai, S.; Lombardi, J.R.; Yoshimura, M. The surface-enhanced resonance Raman scattering of dye molecules adsorbed on two-dimensional titanium carbide $Ti_3C_2T_x$ (MXene) film. *Mater. Adv.* **2020**, *1*, 146–152. [CrossRef]
34. Mauchamp, V.; Bugnet, M.; Bellido, E.P.; Botton, G.A.; Moreau, P.; Magne, D.; Naguib, M.; Cabioc'h, T.; Barsoum, M.W. Enhanced and tunable surface plasmons in two-dimensional Ti_3C_2 stacks:Electronic structure versus boundary effects. *Phys. Rev. B* **2014**, *89*, 235428. [CrossRef]
35. Lashgari, H.; Abolhassani, M.R.; Boochani, A.; Elahi, S.M.; Khodadadi, J. Electronic and optical properties of 2D graphene-like compounds titanium carbides and nitrides: DFT calculations. *Solid State Commun.* **2014**, *195*, 61–69. [CrossRef]
36. Kumada, N.; Tanabe, S.; Hibino, H.; Kamata, H.; Hashisaka, M.; Muraki, K.; Fujisawa, T. Plasmon transport in graphene investigated by time-resolved electrical measurements. *Nat. Commun.* **2013**, *4*, 1363. [CrossRef]
37. Frish, M.J.; Trucks, G.W.; Schlegel, H.B.; Scuseria, G.E.; Robb, M.A.; Cheeseman, J.R.; Scalmani, G.; Barone, V.; Mennucci, B.; Paterson, G.A. *Gaussian 09, Revision A.02*; Gaussian Inc.: Wallingford, CT, USA, 2009.
38. Alhabeb, M.; Maleski, K.; Anasori, B.; Lelyukh, P.; Clark, L.; Sin, S.; Gogotsi, Y. Guidelines for Synthesis and Processing of Two-Dimensional Titanium Carbide ($Ti_3C_2T_x$ MXene). *Chem. Mater.* **2017**, *29*, 7633–7644. [CrossRef]
39. Shekhirev, M.; Shuck, C.E.; Sarycheva, A.; Gogotsi, Y. Characterization of MXenes at every step, from their precursors to single flakes and assembled films. *Prog. Mater. Sci.* **2020**, *120*, 100757. [CrossRef]
40. Rasool, K.; Helal, M.; Ali, A.; Ren, C.; Gogotsi, Y.; Mahmoud, K. Antibacterial Activity of $Ti_3C_2T_x$ MXene. *ACS Nano* **2016**, *10*, 3674–3684. [CrossRef] [PubMed]
41. Xia, Y.; Mathis, T.S.; Zhao, M.Q.; Anasori, B.; Dang, A.; Zhou, Z.; Cho, H.; Gogotsi, Y.; Yang, S. Thickness-independent capacitance of vertically aligned liquid-crystalline MXenes. *Nature* **2018**, *557*, 409–412. [CrossRef]
42. El-Demellawi, J.K.; Lopatin, S.; Yin, J.; Mohammed, O.F.; Alshareef, H.N. Tunable Multipolar Surface Plasmons in 2D $Ti_3C_2T_x$ MXene Flakes. *ACS Nano* **2018**, *12*, 8485–8493. [CrossRef] [PubMed]
43. Halim, J.; Lukatskaya, M.R.; Cook, K.M.; Lu, J.; Smith, C.R.; Näslund, L.Å.; May, S.J.; Hultman, L.; Gogotsi, Y.; Eklund, P.; et al. Transparent Conductive Two-Dimensional Titanium Carbide Epitaxial Thin Films. *Chem. Mater.* **2014**, *26*, 2374–2381. [CrossRef]
44. Lioi, D.B.; Neher, G.; Heckler, J.E.; Back, T.; Mehmood, F.; Nepal, D.; Pachter, R.; Vaia, R.; Kennedy, W.J. Electron-Withdrawing Effect of Native Terminal Groups on the Lattice Structure of $Ti_3C_2T_x$ MXenes Studied by Resonance Raman Scattering: Implications for Embedding MXenes in Electronic Composites. *ACS Appl. Nano Mater.* **2019**, *2*, 6087–6091. [CrossRef]
45. Sarycheva, A.; Makaryan, T.; Maleski, K.; Satheeshkumar, E.; Melikyan, A.; Minassian, H.; Yoshimura, M.; Gogotsi, Y. Two-dimensional titanium carbide (MXene) as surface-enhanced Raman scattering substrate. *J. Phys. Chem. C* **2017**, *121*, 19983–19988. [CrossRef]
46. Chaudhuri, K.; Alhabeb, M.; Wang, Z.; Shalaev, V.M.; Gogotsi, Y.; Boltasseva, A. Highly Broadband Absorber Using Plasmonic Titanium Carbide. *ACS Photonics* **2018**, *5*, 1115–1122. [CrossRef]
47. Lotfi, R.; Naguib, M.; Yilmaz, D.E.; Nanda, J.; Van Duin, A.C. A comparative study on the oxidation of two-dimensional Ti 3 C 2 MXene structures in different environments. *J. Mater. Chem. A* **2018**, *6*, 12733–12743. [CrossRef]
48. Naguib, M.; Mashtalir, O.; Lukatskaya, M.R.; Dyatkin, B.; Zhang, C.; Presser, V.; Gogotsi, Y.; Barsoum, M.W. One-step synthesis of nanocrystalline transition metal oxides on thin sheets of disordered graphitic carbon by oxidation of MXenes. *Chem. Commun.* **2014**, *50*, 7420–7423. [CrossRef]
49. Hu, T.; Wang, J.; Zhang, H.; Li, Z.; Hu, M.; Wang, X. Vibrational properties of Ti_3C_2 and $Ti_3C_2T_2$ (T = O, F, OH) monosheets by first-principles calculations: A comparative study. *Phys. Chem. Chem. Phys.* **2015**, *17*, 9997–10003. [CrossRef]
50. Sang, X.; Xie, Y.; Lin, M.W.; Alhabeb, M.; Van Aken, K.L.; Gogotsi, Y.; Kent, P.R.; Xiao, K.; Unocic, R.R. Atomic Defects in Monolayer Titanium Carbide ($Ti_3C_2T_x$) MXene. *ACS Nano* **2016**, *10*, 9193–9200. [CrossRef] [PubMed]
51. Childres, I.; Jauregui, L.A.; Park, W.; Cao, H.; Chen, Y.P. Raman spectroscopy of graphene and related materials. *New Dev. Photon Mater. Res.* **2013**, *1*, 1–20.
52. Albrecht, A.C. On the theory of Raman intensities. *J. Chem. Phys.* **1961**, *34*, 1476–1484. [CrossRef]
53. Hirakawa, A.Y.; Tsuboi, M. Molecular geometry in an excited electronic state and a preresonance Raman effect. *Science* **1975**, *188*, 359–361. [CrossRef]
54. Hu, M.; Hu, T.; Li, Z.; Yang, Y.; Cheng, R.; Yang, J.; Cui, C.; Wang, X. Surface functional groups and interlayer water determine the electrochemical capacitance of $Ti_3C_2T_x$ MXene. *ACS Nano* **2018**, *12*, 3578–3586. [CrossRef] [PubMed]
55. Sarycheva, A.; Gogotsi, Y. Raman Spectroscopy Analysis of the Structure and Surface Chemistry of $Ti_3C_2T_x$ MXene. *Chem. Mater.* **2020**, *32*, 3480–3488. [CrossRef]
56. Wang, H.W.; Naguib, M.; Page, K.; Wesolowski, D.J.; Gogotsi, Y. Resolving the structure of $Ti_3C_2T_x$ mxenes through multilevel structural modeling of the atomic pair distribution function. *Chem. Mater.* **2016**, *28*, 349–359. [CrossRef]

57. Ibragimova, R.; Puska, M.J.; Komsa, H.P. pH-dependent distribution of functional groups on titanium-based MXenes. *ACS Nano* **2019**, *13*, 9171–9181. [CrossRef]
58. Wilson, E.B. The Normal Modes and Frequencies of Vibration of the Regular Plane Hexagon Model of the Benzene Molecule. *Phys. Rev.* **1934**, *45*, 706–714. [CrossRef]
59. Adomavičiūtė, S.; Velička, M.; Šablinskas, V. Detection of aspirin traces in blood by means of surface-enhanced Raman scattering spectroscopy. *J. Raman Spectrosc.* **2020**, *51*, 919–931. [CrossRef]
60. Mashtalir, O.; Naguib, M.; Mochalin, V.N.; Dall'Agnese, Y.; Heon, M.; Barsoum, M.W.; Gogotsi, Y. Intercalation and delamination of layered carbides and carbonitrides. *Nat. Commun.* **2013**, *4*, 1716. [CrossRef] [PubMed]
61. Naguib, M.; Come, J.; Dyatkin, B.; Presser, V.; Taberna, P.L.; Simon, P.; Barsoum, M.W.; Gogotsi, Y. MXene: A promising transition metal carbide anode for lithium-ion batteries. *Electrochem. Commun.* **2012**, *16*, 61–64. [CrossRef]
62. Ghidiu, M.; Lukatskaya, M.R.; Zhao, M.Q.; Gogotsi, Y.; Barsoum, M.W. Conductive two-dimensional titanium carbide 'clay'with high volumetric capacitance. *Nature* **2014**, *516*, 78–81. [CrossRef] [PubMed]

ACS NANO

www.acsnano.org

ARTICLE

Monitoring $Ti_3C_2T_x$ MXene Degradation Pathways Using Raman Spectroscopy

Sonata Adomaviciute-Grabusove,* Anton Popov, Simonas Ramanavicius,* Valdas Sablinskas, Kateryna Shevchuk, Oleksiy Gogotsi, Ivan Baginskiy, Yury Gogotsi, and Arunas Ramanavicius*

Cite This: https://doi.org/10.1021/acsnano.4c02150

Read Online

ABSTRACT: **Extending applications of $Ti_3C_2T_x$ MXene in nanocomposites and across fields of electronics, energy storage, energy conversion, and sensor technologies necessitates simple and efficient analytical methods. Raman spectroscopy is a critical tool for assessing MXene composites; however, high laser powers and temperatures can lead to the materials' deterioration during the analysis. Therefore, an in-depth understanding of MXene photothermal degradation and changes in its oxidation state is required, but no systematic studies have been reported. The primary aim of this study was to investigate the degradation of the MXene lattice through Raman spectroscopic analysis. Distinct spectral markers were related to structural alterations within the $Ti_3C_2T_x$ material after subjecting it to thermal- and laser-induced degradation. During the degradation processes, spectral markers were revealed for several specific steps: a decrease in the number of interlayer water molecules, a decrease in the number of −OH groups, formation of C−C bonds, oxidation of the lattice, and formation of TiO_2 nanoparticles (first anatase, followed by rutile). By tracking of position shifts and intensity changes for $Ti_3C_2T_x$, the spectral markers that signify the initiation of each step were found. This spectroscopic approach enhances our understanding of the degradation pathways of MXene, and facilitating enhanced and dependable integration of these materials into devices for diverse applications, from energy storage to sensors.**

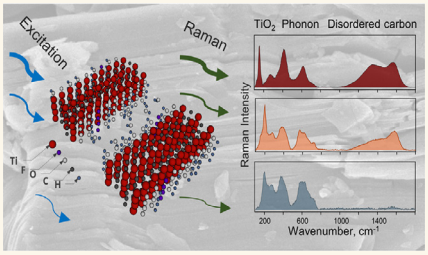

KEYWORDS: *2D materials, MXenes, Raman spectroscopy, TiO_2 nanoparticles, $Ti_3C_2T_x$, MXene degradation, laser-induced disruption*

INTRODUCTION

The rapidly expanding family of two-dimensional (2D) materials, MXenes, emerged with the discovery of 2D $Ti_3C_2T_x$ in 2011.[1,2] MXenes are carbides, nitrides, oxycarbides, and carbonitrides of transition metals with the general formula $M_{n+1}X_nT_x$ (where n = 1, 2, 3, or 4; M depicts a transition metal, *e.g.*, Ti, V, Nb, Mo; X represents C and/or N (O substitution is possible); T_x refers to surface functional groups, *e.g.*, −OH, −F, = O, *etc.*). MXenes are generally produced by selectively etching the middle element A of the parent MAX phase (where A refers to elements from the main groups III−VI, such as Al or Si), thus releasing 2D MX layers. Multiple layers of MXenes are further separated by various intercalants and/or sonication, yielding 2D MXenes. In particular, $Ti_3C_2T_x$ MXene has a long history of research and is notable for inexpensive synthesis from earth-abundant elements and its outstanding properties, such as high conductivity, hydrophilicity, redox-active surfaces, *etc.*[3−5] Further investigations are also directed toward efficiently producing different MXene types that can yield defect-free 2D MXene layers.[4,6]

The increasing attention to MXene can be attributed, in part, to its wide range of applications across various fields, including energy storage[5,7−9] and conversion[3,9,10] (such as supercapacitors and batteries), sensor development,[11−19] electronic components,[7,8,20−23] and the fabrication of nanocomposites for numerous other applications.[5] Many optical,[24] electronic,[9] and chemical properties[25] of MXene depend on structural changes, including variations in material oxidation state,[9,22,24,26] and the presence of amorphous carbon or TiO_2 nanoparticles[27−29] that arise during lattice degradation.[30−33] The sensitivity of MXene to environmental and structural changes makes it an excellent sensor material. MXene can function as a sensor on its own[11−15] or be integrated as a

Received: February 14, 2024
Revised: April 16, 2024
Accepted: April 25, 2024

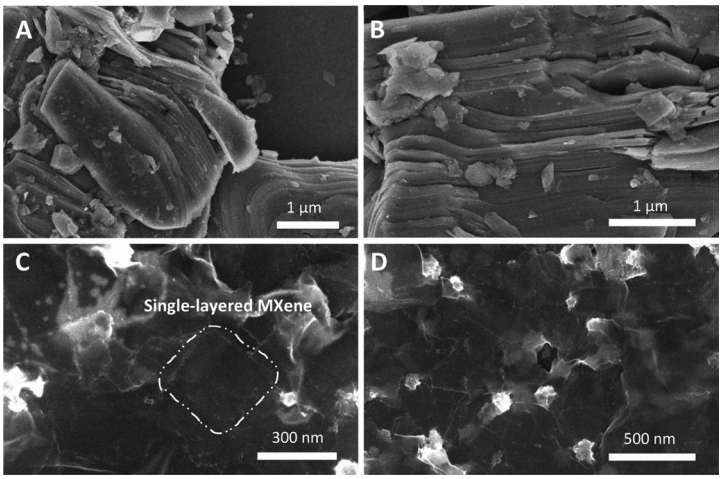

Figure 1. SEM images of multilayered powder (A, B) and delaminated single-layered films of (C, D) $Ti_3C_2T_x$ MXene.

crucial component in nanocomposites for sensor applications.[13,16−19]

Raman spectroscopy is a powerful analytical technique used to study the stability and degradation properties of materials,[34−40] and it is particularly useful for assessing MXene quality during fabrication of devices and sensors. It is sensitive to interactions between chemical species and alterations in lattice structures, making it applicable to detect the presence of amorphous compounds, as well as traces of transition metal oxides commonly found in the structure of MXene. The Raman spectra can reveal detailed information about the structural and surface chemistry of MXenes,[41] detect TiO_2 structures,[42−44] and assess lattice oxidation and degradation,[22,24,45,46] among other valuable applications.[24,42,43,47] Raman spectroscopy-guided sensor development provides enhanced performance, while Raman assessment ensures quality during composite fabrication. Moreover, the application of MXene in sensor technology not only benefits from Raman spectroscopy for analysis but also contributes to the advancement of Raman spectroscopy techniques, enhancing their sensitivity and broadening their applicability.[7,8,20,24,48]

The Raman spectral bands of $Ti_3C_2T_x$ MXene have been assigned to lattice phonon modes based on density functional theory calculations and additional computational methods.[41,42,49] Notably, while most computational predictions were based on homogeneous surface groups (=O, −OH, and −F), MXene terminations appear to be inhomogeneous when synthesized by the wet chemical etching method. The presence of complex surface groups has been confirmed by computational calculations[50−53] in tandem with analytical techniques,[54,55] *e.g.*, pair distribution function (PDF), X-ray photoelectron spectroscopy (XPS), electron energy loss spectroscopy (EELS), and Raman spectroscopy.[24,43,49,51,55] Due to the mixed terminations and defects in the MXene lattice, the deconvolution of Raman spectra can be very complicated. Nevertheless, a recent study utilized machine-learning force field computations to provide further insights into the nature of complex Raman bands by incorporating computational Raman modes for hybrid surface groups along with the concept of symmetry breaking in the lattice.[51] This approach successfully explained the broadening of Raman bands and the appearance of additional in-plane modes when considering hybrid −O(OH) surface groups.

The primary objective of this study is to uncover the spectral changes observed in treated MXene films. It includes tentative assignments of these features to the vibrational modes discussed in the literature.[24,43,49,51] However, it should be emphasized that the observed changes in the Raman spectra are not exclusive to any specific termination type. Instead, they are a result of the overall structural complexity arising from the presence of various terminations in the MXene samples. This study also highlights the effects of film degradation on MXene Raman spectra, which encompass oxygenation and deterioration of the MXene lattice, reduction of interlayer water, and other changes.[9,56−59] In particular, we focused on the Raman spectral markers associated with processes resulting from laser-induced changes, such as oxidation and partial destruction of the lattice. Further investigations of lattice transitions were conducted by using the thermal treatment of MXene films. In general, spectral differences in the Raman spectra of the degraded MXene films were found, which can be attributed to (I) a decrease in the number of molecules trapped between the MXene sheets, (II) the decrease in the number of −OH groups, and (III) oxidation of MXene. Understanding MXene degradation pathways may contribute to the design of energy storage and sensor materials with improved stability. Therefore, the findings presented in this study guide sensor development, enabling precise detection in diverse applications.

RESULTS

Scanning Electron Microscopy (SEM), Energy-Dispersive X-ray (EDX) Analysis, X-ray Diffraction (XRD), and Visible−Near-Infrared (Vis−NIR) Spectroscopy Characterization of Synthesized MXene. The morphology

https://doi.org/10.1021/acsnano.4c02150
ACS Nano XXXX, XXX, XXX−XXX

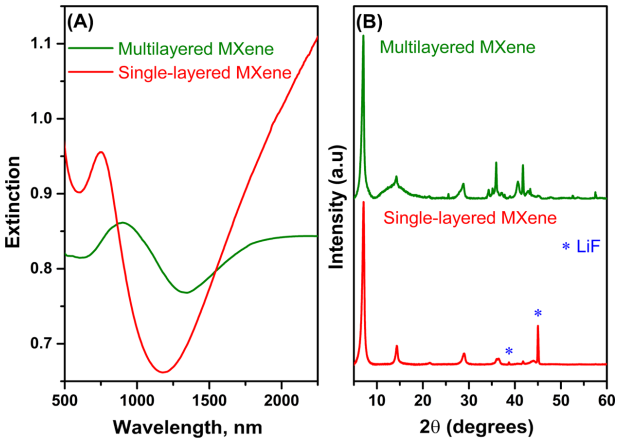

Figure 2. Comparison between the multilayered and single-layered MXene samples. (A) Vis−NIR absorption spectrum and (B) XRD patterns of multilayered and delaminated single-layered MXene.

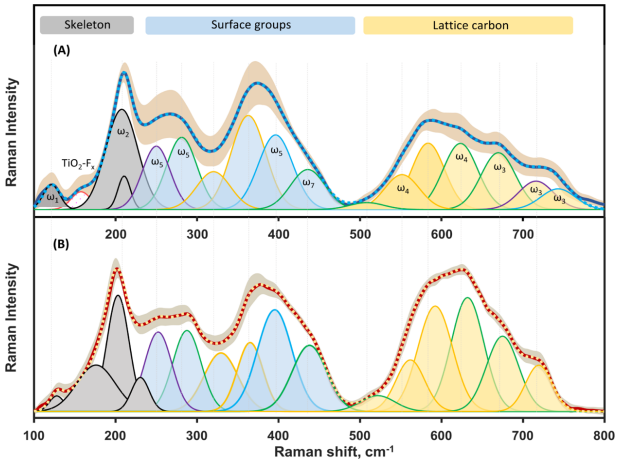

Figure 3. Deconvoluted Raman spectra in low-frequency (100−800 cm^{-1}) spectral region of multilayered (A) and single-layered $Ti_3C_2T_x$ MXene (B). The excitation wavelength was 633 nm. Spectra are separated into spectral regions: skeleton vibrations of all lattice atoms (gray); the surface group region that mainly consists of vibrations associated with the outermost atoms in the material (blue); the lattice carbon region that represents phonon modes of the carbon atoms (yellow). The peak profiles mark our proposed assignment of phonon modes from different homogeneously terminated $Ti_3C_2T_x$. Modes associated with $Ti_3C_2(OH)_2$ are outlined with the green line, $Ti_3C_2O_2$ with the blue line, $Ti_3C_2F_2$ with the violet line, and the complex peak profiles, constituting several MXene types, with the yellow line. The peak profile arising from Ti oxyfluoride is outlined with a pink line.

of synthesized MXene was investigated with SEM imaging (Figure 1). The stacked lamellae were observed in the $Ti_3C_2T_x$ multilayered MXene (Figure 1A,1B). After delamination, single-layered MXene flakes were formed and are shown in Figure 1C,D.

Delamination efficiency was confirmed by EDX analysis (Figure S1), which showed the presence of traces of aluminum, suggesting successful etching of the MAX phase and the formation of multilayered MXene. The aluminum residues were present as relatively uniform amorphous structures on the surface of the MXene sheets and did not affect the parameters investigated in this study. XRD analysis also confirmed the successful etching and delamination of the MXene samples (Figure 2B). The XRD patterns of synthesized MXene are presented in Figure 2B. The results clearly show that the MXene was synthesized, as indicated by the shift of the (002) peak to 7.0 and 7.1° in the case of multilayered and single-layered MXene, respectively.[60] However, the XRD pattern of multilayered MXene (Figure 2B) from 33 to 44° is similar to that of the MAX phase,[11] suggesting incomplete etching and/

https://doi.org/10.1021/acsnano.4c02150
ACS Nano XXXX, XXX, XXX−XXX

or washing. In the case of single-layered MXene, two additional diffraction peaks at 38.7 and 45° are observed, which match the XRD data of LiF (00-004-0857) and indicate the presence of residual LiF after washing the MXene samples.

The differences between the multilayered and single-layered samples are also visible in the vis−NIR extinction spectra (Figure 2A). The spectra match the literature.[48]

The extinction spectrum of MXene, obtained after the delamination step, reveals an extinction band at ≈750 nm originating from interband transition.[20,48,61−63] Additionally, the extinction observed at wavelengths above 1100 nm has been previously assigned to plasmonic oscillations.[48,61] Our previous research reported increased energy losses, resulting from electronic transitions in the near-infrared (NIR) range for $Ti_3C_2T_x$ MXene.[11] Generally, the overlap between the plasmonic frequencies and electronic transitions leads to less pronounced and wide-band plasmon resonances,[64,65] which are observed in our case. The multilayered MXene is expected to have lower extinction in this range due to its lower charge-carrier density than single-layered MXene and different surface functional groups.

To conduct a comprehensive qualitative study of MXene, dried MXene films were separately stored in oxygen and nitrogen gas environments and investigated using both vis−NIR and Raman spectroscopy (Figures S2 and S3). The observed spectral differences between the freshly formed films and those stored in oxygen may be attributed to the partial oxidation of MXene. Previous studies have shown that the extent of oxidation depends on the oxygen content during storage[47,66,67] and temperature.[27]

Raman Spectroscopy Characterization of Single-Layered and Multilayered MXene. A further distinction between the single-layered and multilayered $Ti_3C_2T_x$ MXene can be made by vibrational spectroscopy, *e.g.*, by investigating Raman scattering. Generally, two spectral regions are important for Raman spectroscopic analysis of MXene: the low-frequency (100−800 cm^{-1}) one, which represents lattice vibrations (phonons), and the region from 1000 to 1800 cm^{-1}, which represents C−C stretching vibrations of carbon structures occurring in MXene films.

In the $Ti_3C_2T_x$ fingerprint region, the computational approach was able to provide mode assignments for homogeneously terminated MXene and explain the appearance of additional in-plane modes in MXene with heterogeneous terminations—two at approximately 300−400 cm^{-1} and two at 550−650 cm^{-1}. Our research incorporated these heterogeneous modes in the deconvoluted Raman profile of single-layered and multilayered MXene (Figure 3). Despite the difficulty in interpreting the Raman bands, the fitted Gaussian peak profiles align well with the proposed mode positions in this spectral region. Additionally, previous works suggested several markers for increasing =O content in MXene, such as blue shifts of the bands at approximately 700 and 395 cm^{-1} and a red shift of the band at approximately 620 cm^{-1}.[51] Correspondingly, in the case of voltage-induced oxidation of MXene, a red shift of the 620 cm^{-1} band and blue shift of the 395 cm^{-1} band were observed as well.[22,24,43,45]

Generally, Raman spectra of single-layered and multilayered MXene possess only minor differences. These differences might arise from various factors, including the number of synthesis steps,[42,43,47] variations in the interlayer spacing, and the presence of water and potential intercalants between the layers (Figure 3). The Raman spectra of multilayered MXene exhibit comparably lower intensity bands in the 560−800 cm^{-1} spectral region, which are mainly associated with the vibrations of the lattice carbon atoms. A notable reduction in intensity is observed for the complex band at approximately 620 cm^{-1}, which we mainly attribute to the in-plane vibrations of the carbon atoms. The complexity arises from different ratios of =O, −OH, and −F terminations affecting this and most other bands in MXene spectra. Several studies have shown that the red shift of this band indicates the oxidation of MXene.[22,45,51] Thus, in this research, we assigned the spectral region at approximately 590 cm^{-1} to $Ti_3C_2O_2$ MXene structures, while the region at approximately 667 cm^{-1} was assigned to $Ti_3C_2(OH)_2$ MXene structures (Table 1 and Figure 3).

Table 1. Experimentally Observed Raman Bands of Single-Layered and Multilayered $Ti_3C_2T_x$ MXene[a]

vibrational frequency, cm^{-1}				
single-layered		multilayered		
633 nm	785 nm	633 nm	785 nm	MXene type[49,51]
122	122[b]	122	123[b]	complex[49]
154	154	154	154	
200	201	211	210	complex[49]
256	258	258[c]	258	$Ti_3C_2F_2$[49,51]
283	283	284	283	$Ti_3C_2(OH)_2$[49]
372	372[b]	370	371[b]	complex[51]
450		452		$Ti_3C_2(OH)_2$[49]
511	513[b]	505[c]	512[b]	$Ti_3C_2(OH)_2$[49]
590	584	590	585	$Ti_3C_2O_2$[49,51]
626	617	621	616	complex[51]
667	667	667	668	$Ti_3C_2(OH)_2$[49,51]
712	722[b]	734	737[b]	$Ti_3C_2O_2$[49]
1396	1396			
1582	1582	1562	1561	

[a]Complex—two or more different MXene types. [b]Increased intensity in spectral band compared to 633 nm excitation. [c]Not prominent or weak band.

The most prominent contrast between the single-layered and multilayered MXene becomes evident in the band associated with the ω_2 mode (out-of-plane skeleton vibration of all atoms in the lattice, Table S1). The loosening of the ω_2 mode due to less confined out-of-plane vibrations in single-layered MXene leads to an observed red shift of the band from 211 to 200 cm^{-1} (Table 1). Similarly, a red shift is observed for the other out-of-plane vibrational modes at 734 cm^{-1} in multilayered MXene to 711 cm^{-1} in single-layered MXene. Notably, the latter band also shows sensitivity for the −O or −F content on the surface[51] and further underscores its dependence on the synthesis route.[42]

When comparing the Raman spectra of single-layered MXene collected using different excitation wavelengths, notable changes are observed primarily under preresonance conditions (Figure S4). From vis−NIR extinction spectra, the resonance Raman condition for MXene samples in our study was excitation with a wavelength of 750 nm (Figure 2). Excitation with a 785 nm laser provides photon energy close to the resonance Raman condition. The preresonance excitation yields Raman spectra with high intensity of a few resonant spectral bands (Figure S5). These bands include 122 cm^{-1} ("skeleton vibration"), which is associated with the in-plane vibrational mode of all atomic groups, 513 cm^{-1} (associated

https://doi.org/10.1021/acsnano.4c02150
ACS Nano XXXX, XXX, XXX−XXX

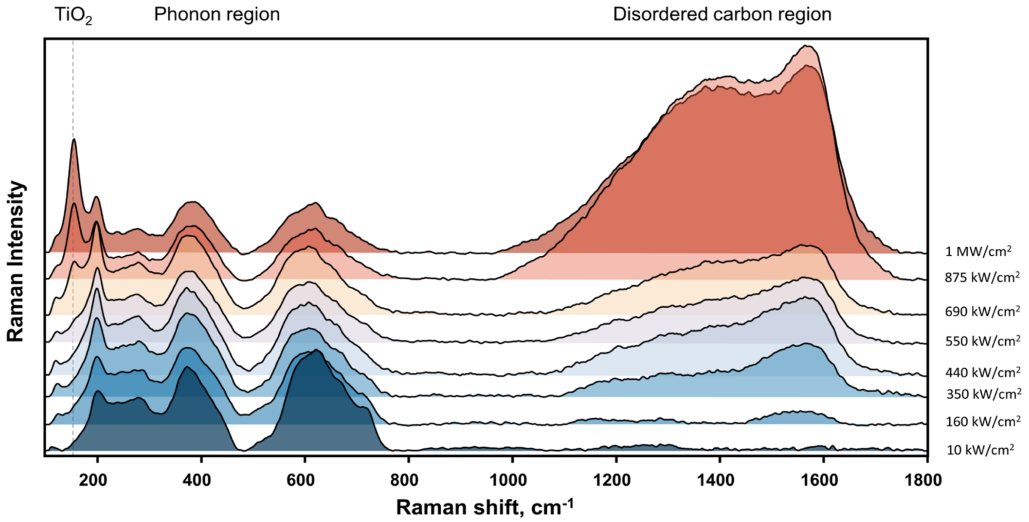

Figure 4. Changes in the Raman spectrum of $Ti_3C_2T_x$ are due to laser radiation. The laser power density varied from 10 kW/cm^2 to 1 MW/cm^2. Three spectral regions are marked as TiO_2 (spectral region of titanium oxide formation), phonon region (lower frequency vibrations), and disordered carbon region (vibrations of C−C bonds). The applied excitation wavelength was 633 nm.

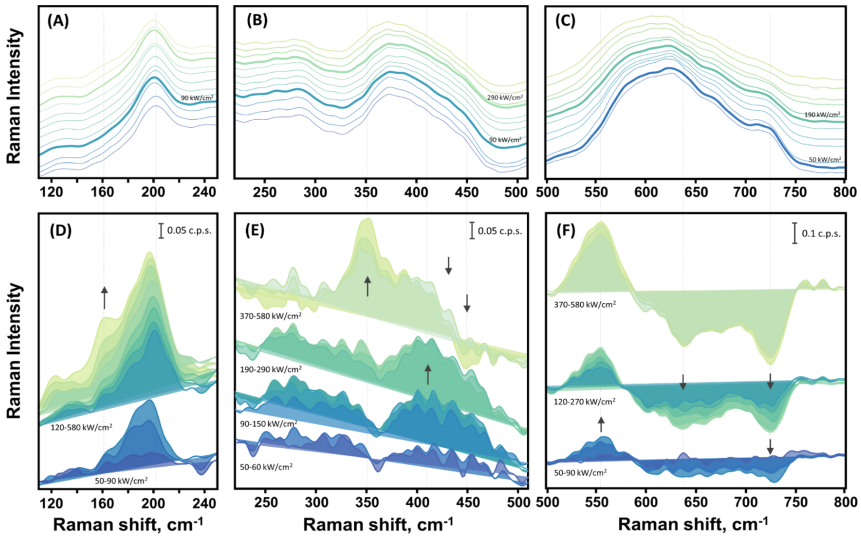

Figure 5. Low-frequency (100−800 cm^{-1}) Raman spectrum of deteriorating $Ti_3C_2T_x$ MXene due to 633 nm laser illumination (A−C) along with the corresponding differential spectra (D−F). The laser power density was changed: from 30, 50, 60; 90, 120, 150, 190, 230, 290, 370; and 470 to 580 kW/cm^2 with the spectra arranged from bottom to top in that order. To enhance clarity, the differential spectra, illustrating newly emerging spectral markers, are presented separately in the bottom panels. The arrows indicate changes in the spectra that emerge with an increasing laser power density. Data were smoothed with a Savitzky−Golay filter, and the unsmoothed spectra are shown in Figure S6.

with the out-of-plane ω_6 mode of $Ti_3C_2(OH)_2$), and 722 cm^{-1} (associated with the out-of-plane ω_3 mode of mainly $Ti_3C_2O_2$) bands.

Laser-Induced Disruption of MXene. The disruption of the MXene lattice was achieved by using different laser wavelengths: 633, 532, and 457 nm. Each laser generates a distinct power density on the sample and induces lattice

https://doi.org/10.1021/acsnano.4c02150
ACS Nano XXXX, XXX, XXX−XXX

defects, which can be traced by Raman spectroscopy. The evolution of phonon bands was first examined using a 633 nm laser in the power density range of 10 kW/cm^2−1 MW/cm^2 (Figure 4). Additionally, samples were analyzed at a higher laser power density, which enables a rapid deterioration of the lattice, using a 532 nm laser (with the power density range of 20 kW/cm^2−26 MW/cm^2) and a 457 nm laser (with the power density range of 240 kW/cm^2−4.9 MW/cm^2) (Figures S7−S10). Comparable spectral patterns were observed for various excitation wavelengths at equivalent power densities. Reasons for MXene deterioration were previously identified and include (i) inner titanium (Ti) atom diffusion to outer layers in the presence of lattice defect; (ii) the formation of C−C bonds between different MXene planes; and (iii) the formation of TiO_2.[68]

The first apparent sign of lattice disruption in MXene can be seen in the disordered carbon spectral region of 1000−1800 cm^{-1} (Figure 4). Amorphous carbon and hydrocarbons begin to form at excitation powers of 160 kW/cm^2. Broad G and D bands can be observed at 1582 cm^{-1} (full width at half-maximum—fwhm of 300 cm^{-1}) and 1396 cm^{-1} (fwhm—120 cm^{-1}), respectively. The G band appears from C−C bond vibration in all sp^2 hybridized carbon systems, while the D band appears in disordered carbon ring systems.[69,70] Under 633 nm excitation, the intensity of the G band of disordered carbon continuously increased with increasing power density, reaching its maximum at 875 kW/cm^2. As the laser power density is further increased, the disordered carbon bands gradually weaken due to the widespread deterioration of C−C bonds, as shown in Figure 4.

The final and most abrupt step of MXene deterioration, namely, the formation of TiO_2 nanoparticles, was observed at a power density of 550 kW/cm^2 with 633 nm excitation. The formation was observed at lower power densities: 330 and 390 kW/cm^2 with 532 and 457 nm excitations, respectively, and advancing until approximately 1.5−1.6 MW/cm^2 (Figures S7−S10). TiO_2 formed from MXene can exist in two crystal structures: anatase and rutile. The anatase phase is the first to appear as it requires less energy to form. The anatase phase was identified by the most intense band at 154 cm^{-1} associated with the E_g mode. In our work, this mode appeared blue-shifted at low laser power densities, which is a sign of defects and oxygen deficiency in the anatase structure.[71−73] A higher content of anatase TiO_2 in the MXene sample is indicated by additional markers−spectral bands at 406 and 633 cm^{-1}, which are associated with B_{1g} and E_g modes, respectively, along with the red shift of E_g mode to 144 cm^{-1}. Further increasing the laser power density initiated the formation of the rutile phase of TiO_2. Spectral markers of the rutile phase start to dominate in the Raman spectra when the laser power density exceeds 2 MW/cm^2 (Figures S8−S10).

Low-Frequency Raman Spectrum of MXene Samples Subjected to Laser-Induced Disruption. Spectral changes of photodisrupted MXene are also observable in the phonon region of 100−800 cm^{-1} (Figure 5A−5C). Lattice vibrations were analyzed using laser excitation at a power density range of 30 to 580 kW/cm^2. More intense laser light severely disrupts the MXene layers. Therefore, the results for such samples are not included in the analysis. No significant differences were found when using various wavelengths for the excitation of Raman scattering (Figure S4). Consequently, we focus on the results obtained with 633 nm excitation (Figure 5).

The analysis of lattice phonon bands was conducted through differential spectra (Figure 5D−F). Initially, the spectrum obtained using the lowest laser power density was subtracted from the presented spectra. As the laser power density increased to 60 kW/cm^2, the 199 cm^{-1} spectral band, associated with the ω_2 mode, and the surface group bands increased in intensity, while the lattice carbon region became less intense. A slight red shift was observed in the 199 cm^{-1} band at 60 kW/cm^2, likely due to the heating of the sample. The upturn in laser power density to 90 kW/cm^2 revealed a pronounced blue shift for the ω_2 mode to 204 cm^{-1} (Figure 5A,D). Indeed, the blue shift is not expected and indicates the stiffening of the mode due to the removal of water molecules trapped between the MXene layers.[57,59] It has been shown that the loss of water and surface functional groups reduces the interlayer spacing, causing individual monolayers to converge,[9,56,58,59] though the loss of surface groups requires a higher temperature to desorb.[59]

In our study, we observed changes linked to increasing =O content in MXene[22,24,43,45] in addition to the reduction of interlayered water. Specifically, a blue shift in the complex band at 372 cm^{-1} was noted (Figure 5C). This blue shift was observed when the excitation power density was between 90 and 290 kW/cm^2, before anatase formation, indicating oxidation of the MXene.[24,42,43] The spectral region at 410 cm^{-1} displayed increased intensity within this power density range, which contributed to the observed blue shift in the 372 cm^{-1} band (Figure 5E). Another indication of oxidation is the red shift of the wide complex band at 626 cm^{-1}.[24] This red shift, peaking at 620 cm^{-1}, is noticeable in the spectra starting from 190 kW/cm^2 (Figure 5C). However, differential spectra reveal that changes in this area appeared much sooner. Furthermore, we observed the gradual increase of the band at 550 cm^{-1}, which is associated with $Ti_3C_2O_2$ structures in this work, together with a decrease of the band at 640 cm^{-1}, which we link to $Ti_3C_2(OH)_2$. These changes were observed even at a low laser power density of 50 kW/cm^2 and persisted as the power density reached 580 kW/cm^2 (Figure 5F). The decrease in the spectral region at 640 cm^{-1} became more pronounced at 190 kW/cm^2. Interestingly, we did not observe a blue shift of the band at 372 cm^{-1} when anatase was formed (when the sample was excited by 370 kW/cm^2 power density). However, we did observe a red shift of the complex band at 620 cm^{-1} in this case.

The bands at 283 and 256 cm^{-1} experience a rapid decrease starting at 370 kW/cm^2 (Figure 5B). The spectral band of anatase TiO_2 at 154 cm^{-1} appears together with the rapid growth of the band observed at 350 cm^{-1} when the sample is excited by a power density of 370 kW/cm^2. Other studies have reported that the band at 350 cm^{-1} is associated with the presence of −F the MXene.[43] However, our results suggest that the band at 350 cm^{-1} might be associated with the formation of TiO_2 structures, since they appear together.

Analyzing the intensity ratios of Raman bands associated with various vibrational modes of MXenes with different terminations can provide valuable insights into structural changes. This approach allows us to clearly distinguish indications of interlayer water reduction, MXene oxidation, and lattice disruptions. However, as previously mentioned, most of the MXene bands are complex; therefore, the assignments for these bands should be made with caution. This study focuses on analyzing the intensity changes of the most prominent MXene Raman bands. To enhance readability,

https://doi.org/10.1021/acsnano.4c02150
ACS Nano XXXX, XXX, XXX−XXX

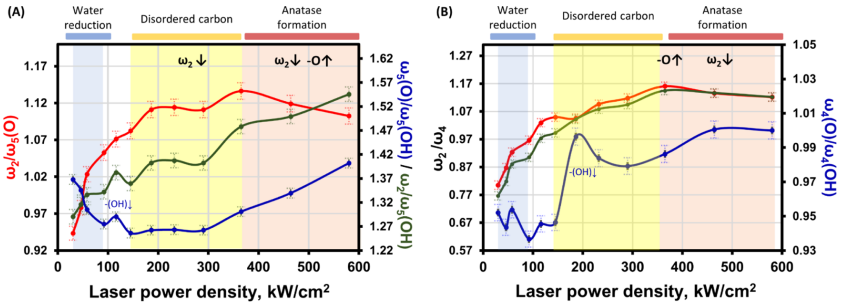

Figure 6. Intensity ratios of MXene Raman bands associated with different vibrational modes of $Ti_3C_2O_2$ and $Ti_3C_2(OH)_2$. The intensity ratios $I_{\omega 2}/I_{\omega 5(O)}$ (red line), $I_{\omega 2}/I_{\omega 5(OH)}$ (green line), and $I_{\omega 5(O)}/I_{\omega 5(OH)}$ (blue line) of ω_2 and ω_5 modes of either = O or −OH-terminated MXene (A). The intensity ratios $I_{\omega 2}/I_{4(O)}$ (red line), $I_{\omega 2}/I_{\omega 4(OH)}$ (green line), and $I_{\omega 4(O)}/I_{\omega 4(OH)}$ (blue line) of ω_2 and ω_4 modes of either ═O or −OH-terminated MXene (B). The main changes in the MXene lattice are noted above the graph: −O↑—increasing oxidation; ω_2↓—reduction of the ω_2 mode intensity. The main processes distinguished by spectral markers appearing in the spectra are noted above the graphs: reduction of interlayered water, formation of disordered carbon bands, and formation of anatase.

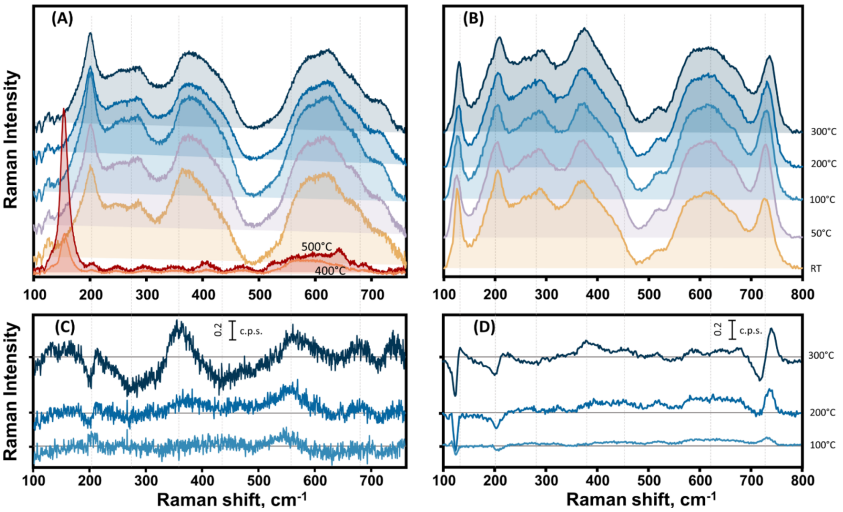

Figure 7. Raman spectra in the phonon spectral region (100−800 cm^{-1}) of $Ti_3C_2T_x$-based MXene deteriorating due to heating. Raman excitation wavelengths were 633 nm (A) and 785 nm (B). Subtracted spectra are presented in (C, D) at excitation wavelengths of 633 and 785 nm, respectively. MXene treatment temperatures of 50, 100, 200, and 300 °C are indicated at the right axis of the figure. Spectra recorded after heating to 400 and 500 °C are shown in (A).

we made tentative assignments of these bands to the lattice modes of $Ti_3C_2O_2$ and $Ti_3C_2(OH)_2$.

Specifically, we calculated the intensity ratios of the ω_2 mode and the peaks at 372 or 283 cm^{-1}, which were related to the ω_5 modes of either ═O-terminated MXene ($I_{\omega 2}/I_{\omega 5(O)}$) or −OH-terminated MXene ($I_{\omega 2}/I_{\omega 5(OH)}$), respectively. Given the complexity of the bands, we also considered other ratios between the ω_2 mode and peaks at 590 or 626 cm^{-1}, assigned to the ω_4 modes of = O-terminated MXene ($I_{\omega 2}/I_{\omega 4(O)}$), or −OH-terminated MXene $I_{\omega 2}/I_{\omega 4(OH)}$ as complementary information. These intensity ratios offered insights into the changes in surface groups.

In general, the intensity of the ω_2 mode increases with an increasing power density at low levels. The $I_{\omega 5(O)}/I_{\omega 5(OH)}$ ratio, on the other hand, decreased from 1.37 to 1.26 (at 150 kW/cm^2) and then began increasing at 370 kW/cm^2, reaching 2.1 (at 1 MW/cm^2) (Figure 6A, blue curve). The decrease in the $I_{\omega 5(O)}/I_{\omega 5(OH)}$ ratios at low laser power densities could be explained by the changes in interlayer spacing from the water in the sample. This correlates to the blue shift of the ω_2 mode at 90 kW/cm^2, indicating the water reduction. After the complete water reduction (at 120 kW/cm^2 laser power density), the amount of −OH surface groups decreases, as was observed in annealing studies.[57] It is marked by a bump in the green and blue curves in Figure 6A at 120 kW/cm^2

https://doi.org/10.1021/acsnano.4c02150
ACS Nano XXXX, XXX, XXX−XXX

together with a rapid increase in the $I_{\omega4(O)}/I_{\omega4(OH)}$ ratio from 0.95 to 1.00 at 190 kW/cm^2 (Figure 6B, blue curve).

Following this process, lattice deterioration becomes evident from 150 kW/cm^2 by the onset of C−C formation, as indicated by the appearance of spectral bands related to disordered carbon (Figure 4). This deterioration is characterized by a decrease in the $I_{\omega2}/I_{\omega5(OH)}$ and $I_{\omega5(O)}/I_{\omega5(OH)}$ ratios. Notably, the $Ti_3C_2(OH)_2$ MXene is supposed to be the least stable.[57] Another sign of $Ti_3C_2(OH)_2$ diminishing is evidenced by the sharp increase in the $I_{\omega4(O)}/I_{\omega4(OH)}$ at 190 kW/cm^2. The decrease in $I_{\omega4(O)}/I_{\omega4(OH)}$ ratio (Figure 6B, blue curve) is observed for the range 190−290 kW/cm^2, which coincides with the increasing intensity of disordered carbon bands and indicates further lattice deterioration.

The sudden rise in $I_{\omega2}/I_{\omega5(O)}$, $I_{\omega2}/I_{\omega5(OH)}$, together with a rise in $I_{\omega5(O)}/I_{\omega5(OH)}$ and $I_{\omega4(O)}/I_{\omega4(OH)}$ ratios at 370 kW/cm^2 indicates the initiation of anatase formation and further oxidation of the $Ti_3C_2T_x$ MXene, presumably signifying the diminishing of surface groups. As oxidation progresses (with increasing laser power density), the most noticeable change is the decreasing $I_{\omega2}/I_{\omega5(O)}$ ratio. Interestingly, the marker for lattice degradation just before the appearance of the anatase band (characterized by a bump at 154 cm^{-1} in the spectra) can be observed from these ratios, as well. The $I_{\omega2}/I_{\omega5(O)}$ and $I_{\omega2}/I_{\omega5(OH)}$ ratios show a slight decrease just before the appearance of the anatase band in the spectra (at 290 kW/cm^2).

Impact of Annealing Temperature on MXene Samples. Temperature-induced changes in the MXene lattice occur at elevated temperatures. As previously mentioned, the thermal effect alters both the surface functional groups and the lattice structure of the MXene while reducing the number of water molecules trapped between the monolayers.[9,56−58,74] To distinguish between reversible and irreversible lattice changes, MXene films were dried on a SiO_2-based substrate and then annealed at various temperatures from 50 to 500 °C. The efficiency of these effects can be investigated using the Raman spectra of annealed MXene samples. To accomplish this, Raman spectra were obtained with preresonance (785 nm) and nonresonance (633 nm) excitations before and after annealing.

Almost no difference was observed when comparing the Raman spectra of the sample before and after heating to 50 °C (Figure 7A,7C). However, a significant increase in the intensities of the wide G and D bands in the carbon spectral region at 1582 and 1396 cm^{-1} is observed as the temperature increases from 200 to 300 °C (Figure S11). When the MXene sample is heated to 400 °C, the intensities of the carbon spectral bands decrease and a new band belonging to the defective TiO_2 anatase phase appears at 154 cm^{-1}. At 500 °C, no carbon bands are detected, and only anatase bands at 154, 406, and 633 cm^{-1} are observed (Figure 7A).

In the phonon spectral region of the MXene sample, almost no spectral changes are observed after heating at 50 °C, except for a slight increase in intensity of the 201 cm^{-1} band, which may indicate the initiation of reduction of interlayered water, as discussed earlier.[56] The shifts in phonon bands, regarded as spectral markers for a reduction in interlayered molecules, were not discernible for 633 nm excitation (Figure 7C). Heating to 300 °C resulted in red shifts of surface termination bands from 372 to 368 cm^{-1} (associated with MXene oxidation) and from 256 to 246 cm^{-1}. The latter shift correlates with an intensity drop at 283 cm^{-1} (Figure 7C). We related this red shift to the decrease in −(OH) surface groups due to several factors: $Ti_3C_2(OH)_2$ is supposed to be less stable and degrade first,[57] and the computational studies of MXene indicate the presence of $Ti_3C_2F_2$ vibrational mode in this spectral range with generally stable mode position.[49,51] It is worth mentioning that contrary to the laser-induced study, no blue shift of the 372 cm^{-1} band or signal increase at 410 or 450 cm^{-1} was observed during annealing.

The excitation at 785 nm provides complementary results (Figure 7B,7D). Annealing at 50 and 200 °C resulted in a coincident blue shift of the ω_2 mode from 201 to 208 cm^{-1}, respectively. Noticeable changes compared with excitation at 633 nm were observed for the resonant bands at 722 and 122 cm^{-1} (Table 1). These bands show gradual blue shifts from 722 to 734 cm^{-1} and from 122 to 127 cm^{-1} as the temperature increases from 50 to 300 °C. The blue shift of the bands at 122 and 202 cm^{-1} may indicate the removal of interlayer water.

Based on the results of the laser-induced study, several irreversible changes in the MXene lattice were observed. First, a reduction in interlayered water was observed from 200 °C, as indicated by the blue shift of the ω_2 mode. Second, the band at approximately 626 cm^{-1} was red-shifted to 550 cm^{-1}, indicating oxidation of the MXene, starting from 100 °C. Third, further oxidation was indicated by a decrease in intensity of the band at approximately 280 cm^{-1}, accompanied by an increase in intensity of the band at 372 cm^{-1} (for MXene heated at 200 °C). Fourthly, progressing oxidation was indicated by a significant decrease in the bands at 283 cm^{-1}, at ∼435 cm^{-1}, and at 626 cm^{-1} (associated with the $Ti_3C_2(OH)_2$ MXene) and an increase in intensity at 550 cm^{-1} (associated with the oxidation of MXene structure). Lastly, a new band at 154 cm^{-1} was observed for MXene heated at 400 °C, indicating the formation of anatase TiO_2.

DISCUSSION

While we observed significant spectral changes following MXene film treatments (both laser-induced and heat-induced degradation), interpretation of these changes is challenging due to the lack of computational validation for heterogeneous surface terminations. However, these spectral changes are consistent with the results of other annealing and MXene treatment studies.[22,45,51,57]

The spectral changes during the MXene film treatment with a laser were observed and can be outlined in several steps. (I) The reduction of interlayered molecules (together with water) was observed from the blue shift of the band at 200 cm^{-1} at low power densities. (II) A further increase in power density resulted in reduction in surface groups. We hypothesize that this reduction can be inferred from the blue shift of the 370 cm^{-1} band coupled with a spike in the $I_{\omega2}/I_{\omega4(OH)}$ ratio, indicating a decrease in −(OH) surface groups.[49] Another indication of oxidation, the red shift of the 620 cm^{-1} band, was noticed at higher power densities but was visible even during the formation of TiO_2 structures. These spectral markers indicate changes in surface groups, allowing us to pinpoint when these changes initiate. The blue shift of the 370 cm^{-1} band is observed first, though it only occurs at lower power densities. Differential spectra unveil subtler changes occurring even at lower laser power densities for the 620 cm^{-1} band. We observed a gradual increase in the band at 550 cm^{-1}, which was accompanied by a decrease in the band at 640 cm^{-1}. These changes were noticeable, even at a low laser power density of 50 kW/cm^2. (III) The formation of the C−C bonds occurred due to defects in the lattice structure. (IV) TiO_2 structures started to form. It was noted that the reduction of surface

https://doi.org/10.1021/acsnano.4c02150
ACS Nano XXXX, XXX, XXX−XXX

groups was intertwined with the formation of C−C bonds and the beginning of the formation of TiO_2 structures.

During the thermal treatment of MXene films, the most pronounced spectral changes occurred for samples heated to 200−300 °C. A red shift of the band at ∼620 cm^{-1} was observed as a sign of oxidation, but no blue shift of the band at ∼370 cm^{-1} was observed. However, a red shift of the latter band was observed for samples heated to 300 °C. It is important to note that in the study of laser-induced deterioration of MXene, the blue shift of the 370 cm^{-1} band was visible only until the formation of anatase began, after which a red shift was observed likewise. Based on the mode assignments of the homogeneous MXene, we can infer that the significant decrease in the bands at approximately 283, 435, and 620 cm^{-1} is associated with the $Ti_3C_2(OH)_2$ MXene. Heating to 400 °C or above destroyed the MXene lattice. It should be noted that heating was conducted in a furnace and not under vacuum conditions. In the case of vacuum annealing, it is expected that carbon bands would still be visible at higher temperatures due to the absence of oxygen.

The differences in MXene degradation observed with laser and thermal treatments could be attributed to more severe temperature changes or different treatment conditions. In the furnace, the temperature is uniformly distributed across the entire sample. However, when heating with a laser, there is a significant temperature difference between the laser spot and the surrounding area. Another important difference to consider is the heating duration of the samples in the furnace, which was 30 min, while the laser treatment was limited to 5−10 min. As a result, the trends for disordered carbon and anatase formation were different.

The previously identified spectral changes induced by MXene lattice deterioration, caused by laser or thermal treatment, can be adapted to determine the MXene film aging. MXene films aged in oxygen and nitrogen environments differ from each other (Figure S3). The film kept in an oxygen environment is supposed to oxidize, increasing the number of =O surface functional groups. Indeed, the blue shift of the complex band at 372 cm^{-1} was only observed for MXene aged in an oxygen environment. However, the formation of TiO_2 was not observed from the Raman spectra.

CONCLUSIONS

This study focused on exploring lattice transitions in $Ti_3C_2T_x$ MXene evoked by thermal and laser treatments using Raman spectroscopy as the primary analytical technique. In the laser-induced degradation study, the out-of-plane mode shifted with reduction in the interlayer water at lower power densities, followed by a blue shift of the band associated with the increasing =O content and diminishing of the bands of −OH-terminated MXenes. Amorphous carbon and hydrocarbons formed at excitation powers of 160 kW/cm^2, while the formation of TiO_2 nanoparticles (first the anatase phase, followed by a rutile phase) was observed at a power density of 550 kW/cm^2 with 633 nm excitation wavelength. In the heating process, exposure to 100 °C led to a red shift of the out-of-plane mode, indicating the initiation of oxidation processes, while more pronounced oxidation and interlayer water reduction markers were observed at 200−300 °C. Finally, at 400 °C, a new band indicated the formation of anatase TiO_2. Unlike laser treatment, no blue shift in certain bands was observed, indicating distinct degradation mechanisms under thermal conditions.

The findings presented here enhance the integration of Raman spectroscopy into MXene analysis by increasing our understanding of degradation pathways *via* related spectral markers. The critical optical and electric properties of MXene depend on structural changes, oxidation state, and the presence of amorphous carbon; thereby, the relation of Raman markers to degradation stages provides an invaluable tool for quickly assessing the structure of MXene. Further use of this knowledge enables the application of MXenes as components in more complex material structures while continuing to employ fast and straightforward Raman spectroscopy for characterization and analysis.

EXPERIMENTAL SECTION

Synthesis of Multilayered $Ti_3C_2T_x$ MXene Colloidal Solutions. MXene used in this study was synthesized by selective etching Al layers from a Ti_3AlC_2 (Materials Research Center Ltd.; ≤40 μm particle size) MAX phase precursor. Detailed synthesis of multilayered $Ti_3C_2T_x$ MXene proceeded as described elsewhere.[11] Briefly, 0.1 g of Ti_3AlC_2 was gradually added to 5 wt % hydrofluoric acid (HF, Honeywell, 40 wt %, ACS, 7664-39-3) solution. The mixture was stirred at 200 rpm/min and kept on a thermostat for 24 h at 25 °C. After etching, the products were washed from the residues of acid with Milli-Q water by centrifugation in plastic centrifuge tubes at 2550 rcf for 10 min until the clear supernatant reached neutral pH. The sediments collected during centrifugation were multilayered $Ti_3C_2T_x$ MXene.

Synthesis of Single-Layered $Ti_3C_2T_x$ MXene. To obtain single-layered MXene using the minimally intensive layer delamination (MILD) method,[60] 0.1 g of Ti_3AlC_2 was gradually added to the 9 M hydrochloric acid (HCl, Roth, 37 wt %, ACS, 7647−01−0) solution with dissolved 1 g of LiF (Roth, >99%, 7789−24−4). The mixture was stirred at 200 rpm/min and kept on a thermostat for 48 h at 35 °C. The products were washed with Milli-Q water by centrifugation in plastic centrifuge tubes 3 times until the supernatant became dark, which indicates delamination. Then, centrifugation was continued, and a dark supernatant with delaminated, single-layered $Ti_3C_2T_x$ MXene was collected. All substrates analyzed in this study were prepared by drop-casting of 0.01 g/mL solution of MXene on microscopic glass.

Characterization of MXene Structures. $Ti_3C_2T_x$ MXene morphology and elemental composition were evaluated by a scanning electron microscope Helios Nanolab 650 (FEI, Eindhoven, Netherlands) equipped with an EDX spectrometer X-Max (Oxford Instruments, Abingdon, U.K.). X-ray diffraction analysis was executed using Ni-filtered Cu Kα radiation on a MiniFlex II diffractometer (Rigaku, Tokyo, Japan) in Bragg−Brentano ($\theta/2\theta$) geometry within 2θ angle ranging from 5 to 60° with a step width of 0.02° and a sweep rate of 1°/min.

Optical characterization of MXene was performed using Vis−NIR and vibrational Raman spectroscopy. Extinction spectra were acquired in the spectral region 450−2300 nm using a Lambda 1050 UV−vis−NIR spectrophotometer (PerkinElmer). A MonoVista CRS+ Raman microscope (Spectroscopy & Imaging GmbH, Germany) equipped with 457, 532, 633, and 785 nm excitation lasers, 100×/0.8 NA objective, and a liquid nitrogen-cooled CCD detector was used for Raman analysis. All Raman spectra were collected using a 300 s exposure time. A 1500 lines/mm grating was employed to collect all spectra except those acquired with 785 nm excitation and for the 633 nm excitation, where a 300 lines/mm grating was used to cover the 100−1800 cm^{-1} spectral range. Before the measurements, the spectrometer was calibrated to the fundamental vibrational band of a silicon wafer at 520.7 cm^{-1}.

For Raman spectroscopic analysis, the laser power was kept at ≈0.4 mW, which ensures a laser power density of ≈60 kW/cm^2. The laser power was adjusted for the laser-induced deterioration study and is specified in the Results Section. The data in the deconvoluted Raman spectra and the low-frequency (100−800 cm^{-1}) Raman spectrum of

https://doi.org/10.1021/acsnano.4c02150
ACS Nano XXXX, XXX, XXX−XXX

deteriorating $Ti_3C_2T_x$ MXene in Figure 5 were smoothed using a Savitzky–Golay filter with a 9-point window. The unsmoothed spectra are provided in the Supporting Information.

For the evaluation of successful MXene synthesis, Raman mapping was conducted across a 10 × 10 μm^2 area of the sample with a 1 μm step and no spectral markers of the MAX phase were observed. Additionally, both EDX and XRD analyses showed no trace of the MAX phase.

Assessment of MXene Stability. The prepared MXene samples were subjected to different treatments: thermal annealing and storage under various conditions. For thermal annealing, the samples were placed in a furnace (Zhermack DM 40, Badia Polesine, Italy) by holding at 50, 100, 200, 300, 400, and 500 °C for 30 min. To study the stability of MXene under different storage conditions, MXene films were placed in a cuvette that was flushed and subsequently filled with dry oxygen or nitrogen gas and stored for 1 week at room temperature.

ASSOCIATED CONTENT

Supporting Information

The Supporting Information is available free of charge at https://pubs.acs.org/doi/10.1021/acsnano.4c02150.

EDX mapping images of single-layered $Ti_3C_2T_x$ MXene flakes; vis–NIR extinction, Raman spectra and corresponding analysis of single-layered MXene flakes separately stored in oxygen and nitrogen gas environments; Raman spectra, analysis, and band assignment table of single-layered MXene obtained with different excitation wavelengths; Raman spectra of multilayered and single-layered MXene excited with 785 nm laser; Raman spectra of deteriorating Mxene due to laser illumination (457, 532, 633 nm) and due to heating (PDF)

AUTHOR INFORMATION

Corresponding Authors

Sonata Adomaviciute-Grabusove – *Institute of Chemical Physics, Vilnius University, LT-10257 Vilnius, Lithuania*; Email: sonata.adomaviciute@ff.vu.lt

Simonas Ramanavicius – *Department of Organic Chemistry, Centre for Physical Sciences and Technology, LT-10257 Vilnius, Lithuania*; Email: simonas.ramanavicius@ftmc.lt

Arunas Ramanavicius – *Department of Physical Chemistry, Institute of Chemistry, Faculty of Chemistry and Geosciences, Vilnius University, LT-03225 Vilnius, Lithuania; Department of Nanotechnology, Centre for Physical Sciences and Technology, LT-10257 Vilnius, Lithuania*; orcid.org/0000-0002-0885-3556; Email: arunas.ramanavicius@chf.vu.lt

Authors

Anton Popov – *NanoTechnas—Center of Nanotechnology and Materials Science, Institute of Chemistry, Faculty of Chemistry and Geosciences, Vilnius University, LT-03225 Vilnius, Lithuania*; orcid.org/0000-0002-9867-1931

Valdas Sablinskas – *Institute of Chemical Physics, Vilnius University, LT-10257 Vilnius, Lithuania*

Kateryna Shevchuk – *A.J. Drexel Nanomaterials Institute and Materials Science & Engineering Department, Drexel University, Philadelphia, Pennsylvania 19104, United States*; orcid.org/0000-0001-7411-3110

Oleksiy Gogotsi – *Materials Research Center, Ltd., 03142 Kyiv, Ukraine*; orcid.org/0000-0002-3173-4432

Ivan Baginskiy – *Materials Research Center, Ltd., 03142 Kyiv, Ukraine*; orcid.org/0000-0002-0092-9018

Yury Gogotsi – *A.J. Drexel Nanomaterials Institute and Materials Science & Engineering Department, Drexel University, Philadelphia, Pennsylvania 19104, United States*

Complete contact information is available at: https://pubs.acs.org/10.1021/acsnano.4c02150

Notes

The authors declare no competing financial interest.

ACKNOWLEDGMENTS

This project has received funding from the Research Council of Lithuania (LMTLT), agreement No S-PD-22-155. Research at Drexel University was supported by a U.S. National Science Foundation grant (DMR-2041050) and EU Horizon Europe research program projects #101131147 "ESCULAPE" and #101086184 "MX-MAP". The authors are grateful to Dr. Arnas Naujokaitis for scanning electron microscopy imaging.

REFERENCES

(1) Naguib, M.; Kurtoglu, M.; Presser, V.; Lu, J.; Niu, J.; Heon, M.; Hultman, L.; Gogotsi, Y.; Barsoum, M. W. Two-Dimensional Nanocrystals Produced by Exfoliation of Ti_3AlC_2. *Adv. Mater.* **2011**, *23* (37), 4248–4253.

(2) Anasori, B.; Gogotsi, Y. *2D Metal Carbides and Nitrides (MXenes)*; Springer: Cham, 2019.

(3) Bhat, A.; Anwer, S.; Bhat, K. S.; Mohideen, M. I. H.; Liao, K.; Qurashi, A. Prospects Challenges and Stability of 2D MXenes for Clean Energy Conversion and Storage Applications. *npj 2D Mater. Appl.* **2021**, *5* (1), No. 61.

(4) Papadopoulou, K. A.; Chroneos, A.; Parfitt, D.; Christopoulos, S.-R. G. A Perspective on MXenes: Their Synthesis, Properties, and Recent Applications. *J. Appl. Phys.* **2020**, *128* (17), No. 170902.

(5) Anasori, B.; Lukatskaya, M. R.; Gogotsi, Y. 2D Metal Carbides and Nitrides (MXenes) for Energy Storage. *Nat. Rev. Mater.* **2017**, *2* (2), No. 16098.

(6) Gogotsi, Y.; Anasori, B. The Rise of MXenes. *ACS Nano* **2019**, *13* (8), 8491–8494.

(7) Li, J.; Levitt, A.; Kurra, N.; Juan, K.; Noriega, N.; Xiao, X.; Wang, X.; Wang, H.; Alshareef, H. N.; Gogotsi, Y. MXene-Conducting Polymer Electrochromic Microsupercapacitors. *Energy Storage Mater.* **2019**, *20*, 455–461.

(8) Zhang, D.; Wang, R.; Wang, X.; Gogotsi, Y. In Situ Monitoring Redox Processes in Energy Storage Using UV–Vis Spectroscopy. *Nat. Energy* **2023**, *8* (6), 567–576.

(9) Xie, Y.; Naguib, M.; Mochalin, V. N.; Barsoum, M. W.; Gogotsi, Y.; Yu, X.; Nam, K.-W.; Yang, X.-Q.; Kolesnikov, A. I.; Kent, P. R. C. Role of Surface Structure on Li-Ion Energy Storage Capacity of Two-Dimensional Transition-Metal Carbides. *J. Am. Chem. Soc.* **2014**, *136* (17), 6385–6394.

(10) Bai, W.; Xiao, C.; Xie, Y. Bulk Superlattice Analogues for Energy Conversion. *J. Am. Chem. Soc.* **2022**, *144* (8), 3298–3313.

(11) Adomavičiūtė-Grabusovė, S.; Ramanavičius, S.; Popov, A.; Šablinskas, V.; Gogotsi, O.; Ramanavičius, A. Selective Enhancement of SERS Spectral Bands of Salicylic Acid Adsorbate on 2D $Ti_3C_2T_x$-Based MXene Film. *Chemosensors* **2021**, *9* (8), No. 223.

(12) Wang, Y.; Yue, Y.; Cheng, F.; Cheng, Y.; Ge, B.; Liu, N.; Gao, Y. $Ti_3C_2T_x$ MXene-Based Flexible Piezoresistive Physical Sensors. *ACS Nano* **2022**, *16* (2), 1734–1758.

(13) Wu, Z.; Wei, L.; Tang, S.; Xiong, Y.; Qin, X.; Luo, J.; Fang, J.; Wang, X. Recent Progress in $Ti_3C_2T_x$ MXene-Based Flexible Pressure Sensors. *ACS Nano* **2021**, *15* (12), 18880–18894.

(14) Yadav, P.; Cao, Z.; Farimani, A. B. DNA Detection with Single-Layer Ti_3C_2 MXene Nanopore. *ACS Nano* **2021**, *15* (3), 4861–4869.

(15) Jing, H.; Zhao, P.; Liu, C.; Wu, Z.; Yu, J.; Liu, B.; Su, C.; Lei, W.; Hao, Q. Surface-Enhanced Raman Spectroscopy for Boosting Electrochemical CO_2 Reduction on Amorphous-Surfaced Tin Oxide Supported by MXene. *ACS Appl. Mater. Interfaces* **2023**, *15* (51), 59524−59533.
(16) Ratzker, B.; Messer, O.; Favelukis, B.; Kalabukhov, S.; Maman, N.; Ezersky, V.; Sokol, M. MXene-Based Ceramic Nanocomposites Enabled by Pressure-Assisted Sintering. *ACS Nano* **2023**, *17* (1), 157−167.
(17) Yue, Y.; Liu, N.; Ma, Y.; Wang, S.; Liu, W.; Luo, C.; Zhang, H.; Cheng, F.; Rao, J.; Hu, X.; Su, J.; Gao, Y. Highly Self-Healable 3D Microsupercapacitor with MXene−Graphene Composite Aerogel. *ACS Nano* **2018**, *12* (5), 4224−4232.
(18) Lee, J.; Hong, S.; Sun, Y.; Lee, S. K.; Hwang, U.; Nam, J.-d.; Suhr, J. Parasitic Reaction Driven Facile Preparation of Segregated-MXene/Polycarbonate Nanocomposites for Efficient Electromagnetic Interference Shielding. *Surf. Interfaces* **2023**, *40*, No. 103101.
(19) Weng, X.; Weng, Z.; Qin, M.; Zhang, J.; Wu, Y.; Jiang, H. Bioinspired Moisture-Driven Soft Actuators Based on MXene/Aramid Nanofiber Nanocomposite Films. *ACS Appl. Nano Mater.* **2024**, *7* (5), 5587−5597.
(20) Hantanasirisakul, K.; Zhao, M.-Q.; Urbankowski, P.; Halim, J.; Anasori, B.; Kota, S.; Ren, C. E.; Barsoum, M. W.; Gogotsi, Y. Fabrication of $Ti_3C_2T_x$ MXene Transparent Thin Films with Tunable Optoelectronic Properties. *Adv. Electron. Mater.* **2016**, *2* (6), No. 1600050.
(21) Mistry, H.; Varela, A. S.; Kühl, S.; Strasser, P.; Cuenya, B. R. Nanostructured Electrocatalysts with Tunable Activity and Selectivity. *Nat. Rev. Mater.* **2016**, *1* (4), No. 16009.
(22) Johnson, D.; Hansen, K.; Yoo, R.; Djire, A. Elucidating the Charge Storage Mechanism on Ti_3C_2 MXene through In Situ Raman Spectroelectrochemistry. *ChemElectroChem* **2022**, *9* (18), No. e202200555.
(23) Lee, S.; Kim, E. H.; Yu, S.; Kim, H.; Park, C.; Lee, S. W.; Han, H.; Jin, W.; Lee, K.; Lee, C. E.; Jang, J.; Koo, C. M.; Park, C. Polymer-Laminated $Ti_3C_2T_x$ MXene Electrodes for Transparent and Flexible Field-Driven Electronics. *ACS Nano* **2021**, *15* (5), 8940−8952.
(24) Li, H.; Chen, S.; Boukhvalov, D. W.; Yu, Z.; Humphrey, M. G.; Huang, Z.; Zhang, C. Switching the Nonlinear Optical Absorption of Titanium Carbide MXene by Modulation of the Surface Terminations. *ACS Nano* **2022**, *16* (1), 394−404.
(25) Maleski, K.; Ren, C. E.; Zhao, M.-Q.; Anasori, B.; Gogotsi, Y. Size-Dependent Physical and Electrochemical Properties of Two-Dimensional MXene Flakes. *ACS Appl. Mater. Interfaces* **2018**, *10* (29), 24491−24498.
(26) Chertopalov, S.; Mochalin, V. N. Environment-Sensitive Photoresponse of Spontaneously Partially Oxidized Ti_3C_2 MXene Thin Films. *ACS Nano* **2018**, *12* (6), 6109−6116.
(27) Ghassemi, H.; Harlow, W.; Mashtalir, O.; Beidaghi, M.; Lukatskaya, M. R.; Gogotsi, Y.; Taheri, M. L. In Situ Environmental Transmission Electron Microscopy Study of Oxidation of Two-Dimensional Ti_3C_2 and Formation of Carbon-Supported TiO_2. *J. Mater. Chem. A* **2014**, *2* (35), 14339−14343.
(28) Hong, J.; Paeng, C.; Park, S.; In, I.; Lee, H.; Velhal, N. B.; Yun, T. H.; Jo, C.; Yim, C. Flashlight Treatment for Instantaneous Structuring of Dense MXene Film into Porous MXene/TiO_2 Nanocomposite for Lithium-Ion Battery Anodes. *Chem. Eng. J.* **2024**, *484*, No. 149598.
(29) Kumar, S.; Aftab, S.; Singh, T.; Kumar, M.; Kumar, S.; Seo, Y. Charge Storage Improvement in Uniformly Grown TiO_2 on $Ti_3C_2T_x$ MXene Surface. *J. Alloys Compd.* **2023**, *968*, No. 172181.
(30) Liu, Y.; Zhang, H.; Zhu, D.; Duan, J.; Miruka, A. C.; Tang, L.; Li, P.; Cai, L. Enhanced Degradation of Tetracycline by TiO_2 @ MXene with Peroxydisulfate under Visible Light Irradiation. *Sep. Purif. Technol.* **2024**, *343*, No. 127122.
(31) Mathis, T. S.; Maleski, K.; Goad, A.; Sarycheva, A.; Anayee, M.; Foucher, A. C.; Hantanasirisakul, K.; Shuck, C. E.; Stach, E. A.; Gogotsi, Y. Modified MAX Phase Synthesis for Environmentally Stable and Highly Conductive Ti_3C_2 MXene. *ACS Nano* **2021**, *15* (4), 6420−6429.
(32) Zhang, C. J.; Pinilla, S.; McEvoy, N.; Cullen, C. P.; Anasori, B.; Long, E.; Park, S.-H.; Seral-Ascaso, A.; Shmeliov, A.; Krishnan, D.; Morant, C.; Liu, X.; Duesberg, G. S.; Gogotsi, Y.; Nicolosi, V. Oxidation Stability of Colloidal Two-Dimensional Titanium Carbides (MXenes). *Chem. Mater.* **2017**, *29* (11), 4848−4856.
(33) Kumar, S.; Park, H. M.; Nguyen, V. H.; Kim, M.; Nasir, N.; Suleman, M.; Lee, S.; Seo, Y. Oxidation-Driven Auto-Conversion of $Ti_3C_2T_x$ MXene to TiO_2 Nanoparticles for Photocatalytic Applications. *J. Alloys Compd.* **2024**, *976*, No. 173399.
(34) Alsaffar, F.; Alodan, S.; Alrasheed, A.; Alhussain, A.; Alrubaiq, N.; Abbas, A.; Amer, M. R. Raman Sensitive Degradation and Etching Dynamics of Exfoliated Black Phosphorus. *Sci. Rep.* **2017**, *7* (1), No. 44540.
(35) Shimizu, M.; Koya, T.; Nakahigashi, A.; Urakami, N.; Yamakami, T.; Arai, S. Kinetics Study and Degradation Analysis through Raman Spectroscopy of Graphite as a Negative-Electrode Material for Potassium-Ion Batteries. *J. Phys. Chem. C* **2020**, *124* (24), 13008−13016.
(36) Lin, Z.; Guo, X.; He, Z.; Liang, X.; Wang, M.; Jin, G. Thermal Degradation Kinetics Study of Molten Polylactide Based on Raman Spectroscopy. *Polym. Eng. Sci.* **2021**, *61* (1), 201−210.
(37) Mikulics, M.; Adam, R.; Sobolewski, R.; Heidtfeld, S.; Cao, D.; Bürgler, D. E.; Schneider, C. M.; Mayer, J.; Hardtdegen, H. H. Nano-LED Driven Phase Change Evolution of Layered Chalcogenides for Raman Spectroscopy Investigations. *FlatChem* **2022**, *36*, No. 100447.
(38) Xue, W.; Yan, H.; He, Y.; Wu, L.; Zhang, X.; Wu, Y.; Xu, J.; He, J.; Yan, C.; Meng, H. Identifying the Molecular Origins of Green BN-TADF Material Degradation and Device Stability via in Situ Raman Spectroscopy. *Chem. - Eur. J.* **2022**, *28* (36), No. e202201006.
(39) Mikulics, M.; Adam, R.; Chen, G.; Chakraborty, D.; Cheng, J.; Pericolo, A.; Komissarov, I.; Bürgler, D. E.; Heidtfeld, S. F.; Serafini, J.; et al. Determination of Thermal Damage Threshold in THz Photomixers Using Raman Spectroscopy. *Crystals* **2023**, *13* (8), No. 1267.
(40) Naqvi, F. H.; Ko, J.-H. Structural Phase Transitions and Thermal Degradation Process of $MAPbCl_3$ Single Crystals Studied by Raman and Brillouin Scattering. *Materials* **2022**, *15* (22), No. 8151.
(41) Hu, T.; Hu, M.; Gao, B.; Li, W.; Wang, X. Screening Surface Structure of MXenes by High-Throughput Computation and Vibrational Spectroscopic Confirmation. *J. Phys. Chem. C* **2018**, *122* (32), 18501−18509.
(42) Sarycheva, A.; Gogotsi, Y. Raman Spectroscopy Analysis of the Structure and Surface Chemistry of $Ti_3C_2T_x$ MXene. *Chem. Mater.* **2020**, *32* (8), 3480−3488.
(43) Benchakar, M.; Loupias, L.; Garnero, C.; Bilyk, T.; Morais, C.; Canaff, C.; Guignard, N.; Morisset, S.; Pazniak, H.; Hurand, S.; Chartier, P.; Pacaud, J.; Mauchamp, V.; Barsoum, M. W.; Habrioux, A.; Célérier, S. One MAX Phase, Different MXenes: A Guideline to Understand the Crucial Role of Etching Conditions on $Ti_3C_2T_x$ Surface Chemistry. *Appl. Surf. Sci.* **2020**, *530*, No. 147209.
(44) Naguib, M.; Mashtalir, O.; Lukatskaya, M. R.; Dyatkin, B.; Zhang, C.; Presser, V.; Gogotsi, Y.; Barsoum, M. W. One-Step Synthesis of Nanocrystalline Transition Metal Oxides on Thin Sheets of Disordered Graphitic Carbon by Oxidation of MXenes. *Chem. Commun.* **2014**, *50* (56), 7420−7423.
(45) Salles, P.; Pinto, D.; Hantanasirisakul, K.; Maleski, K.; Shuck, C. E.; Gogotsi, Y. Electrochromic Effect in Titanium Carbide MXene Thin Films Produced by Dip-Coating. *Adv. Funct. Mater.* **2019**, *29* (17), No. 1809223.
(46) Lorencova, L.; Bertok, T.; Dosekova, E.; Holazova, A.; Paprckova, D.; Vikartovska, A.; Sasinkova, V.; Filip, J.; Kasak, P.; Jerigova, M.; Velic, D.; Mahmoud, K. A.; Tkac, J. Electrochemical Performance of $Ti_3C_2T_x$ MXene in Aqueous Media: Towards Ultrasensitive H_2O_2 Sensing. *Electrochim. Acta* **2017**, *235*, 471−479.
(47) Lipatov, A.; Alhabeb, M.; Lukatskaya, M. R.; Boson, A.; Gogotsi, Y.; Sinitskii, A. Effect of Synthesis on Quality, Electronic

https://doi.org/10.1021/acsnano.4c02150
ACS Nano XXXX, XXX, XXX−XXX

Properties and Environmental Stability of Individual Monolayer Ti_3C_2 MXene Flakes. *Adv. Electron. Mater.* **2016**, *2* (12), No. 1600255.
(48) Gonçalves, M.; Melikyan, A.; Minassian, H.; Makaryan, T.; Petrosyan, P.; Sargsian, T. Interband, Surface Plasmon and Fano Resonances in Titanium Carbide (MXene) Nanoparticles in the Visible to Infrared Range. *Photonics* **2021**, *8* (2), No. 36.
(49) Hu, T.; Wang, J.; Zhang, H.; Li, Z.; Hu, M.; Wang, X. Vibrational Properties of Ti_3C_2 and $Ti_3C_2T_2$ (T = O, F, OH) Monosheets by First-Principles Calculations: A Comparative Study. *Phys. Chem. Chem. Phys.* **2015**, *17* (15), 9997−10003.
(50) Björk, J.; Rosen, J. Functionalizing MXenes by Tailoring Surface Terminations in Different Chemical Environments. *Chem. Mater.* **2021**, *33* (23), 9108−9118.
(51) Berger, E.; Lv, Z.-P.; Komsa, H.-P. Raman Spectra of 2D Titanium Carbide MXene from Machine-Learning Force Field Molecular Dynamics. *J. Mater. Chem. C* **2023**, *11* (4), 1311−1319.
(52) Ibragimova, R.; Erhart, P.; Rinke, P.; Komsa, H.-P. Surface Functionalization of 2D MXenes: Trends in Distribution, Composition, and Electronic Properties. *J. Phys. Chem. Lett.* **2021**, *12* (9), 2377−2384.
(53) Wang, H.-W.; Naguib, M.; Page, K.; Wesolowski, D. J.; Gogotsi, Y. Resolving the Structure of $Ti_3C_2T_x$ MXenes through Multilevel Structural Modeling of the Atomic Pair Distribution Function. *Chem. Mater.* **2016**, *28* (1), 349−359.
(54) Bashir, T.; Ismail, S. A.; Wang, J.; Zhu, W.; Zhao, J.; Gao, L. MXene Terminating Groups O, −F or −OH, −F or O, −OH, −F, or O, −OH, −Cl? *J. Energy Chem.* **2023**, *76*, 90−104.
(55) Shi, C.; Beidaghi, M.; Naguib, M.; Mashtalir, O.; Gogotsi, Y.; Billinge, S. J. L. Structure of Nanocrystalline Ti_3C_2 MXene Using Atomic Pair Distribution Function. *Phys. Rev. Lett.* **2014**, *112* (12), No. 125501.
(56) Zhang, Z.; Yao, Z.; Zhang, X.; Jiang, Z. 2D Carbide MXene under Postetch Low-Temperature Annealing for High−Performance Supercapacitor Electrode. *Electrochim. Acta* **2020**, *359*, No. 136960.
(57) Han, M.; Yin, X.; Wu, H.; Hou, Z.; Song, C.; Li, X.; Zhang, L.; Cheng, L. Ti_3C_2 MXenes with Modified Surface for High-Performance Electromagnetic Absorption and Shielding in the X-Band. *ACS Appl. Mater. Interfaces* **2016**, *8* (32), 21011−21019.
(58) Halim, J.; Persson, I.; Eklund, P.; Persson, P. O. Å.; Rosen, J. Sodium Hydroxide and Vacuum Annealing Modifications of the Surface Terminations of a Ti_3C_2 (MXene) Epitaxial Thin Film. *RSC Adv.* **2018**, *8* (64), 36785−36790.
(59) Hart, J. L.; Hantanasirisakul, K.; Lang, A. C.; Anasori, B.; Pinto, D.; Pivak, Y.; van Omme, J. T.; May, S. J.; Gogotsi, Y.; Taheri, M. L. Control of MXenes' Electronic Properties through Termination and Intercalation. *Nat. Commun.* **2019**, *10* (1), No. 522.
(60) Alhabeb, M.; Maleski, K.; Anasori, B.; Lelyukh, P.; Clark, L.; Sin, S.; Gogotsi, Y. Guidelines for Synthesis and Processing of Two-Dimensional Titanium Carbide ($Ti_3C_2T_x$ MXene). *Chem. Mater.* **2017**, *29* (18), 7633−7644.
(61) Dillon, A. D.; Ghidiu, M. J.; Krick, A. L.; Griggs, J.; May, S. J.; Gogotsi, Y.; Barsoum, M. W.; Fafarman, A. T. Highly Conductive Optical Quality Solution-Processed Films of 2D Titanium Carbide. *Adv. Funct Mater.* **2016**, *26* (23), 4162−4168.
(62) Kang, Z.; Ma, Y.; Tan, X.; Zhu, M.; Zheng, Z.; Liu, N.; Li, L.; Zou, Z.; Jiang, X.; Zhai, T.; Gao, Y. MXene−Silicon Van Der Waals Heterostructures for High-Speed Self-Driven Photodetectors. *Adv. Electron. Mater.* **2017**, *3* (9), No. 1700165.
(63) Mauchamp, V.; Bugnet, M.; Bellido, E. P.; Botton, G. A.; Moreau, P.; Magne, D.; Naguib, M.; Cabioc'h, T.; Barsoum, M. W. Enhanced and Tunable Surface Plasmons in Two-Dimensional Ti_3C_2 Stacks: Electronic Structure versus Boundary Effects. *Phys. Rev. B* **2014**, *89* (23), No. 235428.
(64) Kiefer, W. *Surface Enhanced Raman Spectroscopy: Analytical, Biophysical and Life Science Applications*; John Wiley & Sons, 2011.
(65) Le Ru, E.; Etchegoin, P. *Principles of Surface-Enhanced Raman Spectroscopy: And Related Plasmonic Effects*; Elsevier, 2008.
(66) Xia, F.; Lao, J.; Yu, R.; Sang, X.; Luo, J.; Li, Y.; Wu, J. Ambient Oxidation of Ti_3C_2 MXene Initialized by Atomic Defects. *Nanoscale* **2019**, *11* (48), 23330−23337.
(67) Kumar, S.; Park, H. M.; Singh, T.; Kumar, M.; Seo, Y. Long-Term Stability Studies and Applications of $Ti_3C_2T_x$ MXene. *Int. J. Energy Res.* **2023**, *2023*, No. 5275439.
(68) Lotfi, R.; Naguib, M.; Yilmaz, D. E.; Nanda, J.; van Duin, A. C. T. A Comparative Study on the Oxidation of Two-Dimensional Ti_3C_2 MXene Structures in Different Environments. *J. Mater. Chem. A* **2018**, *6* (26), 12733−12743.
(69) Smith, M. W.; Dallmeyer, I.; Johnson, T. J.; Brauer, C. S.; McEwen, J. S.; Espinal, J. F.; Garcia-Perez, M. Structural Analysis of Char by Raman Spectroscopy: Improving Band Assignments through Computational Calculations from First Principles. *Carbon* **2016**, *100*, 678−692.
(70) Childres, I.; Jauregui, L. A.; Park, W.; Cao, H.; Chen, Y. P. Raman Spectroscopy of Graphene and Related Materials. In *New Developments in Photon and Materials Research*; Citeseer, 2013; Vol. *1*, pp 1−20.
(71) Ma, J.; Li, W.; Morgan, B. J.; Świątowska, J.; Baddour-Hadjean, R.; Body, M.; Legein, C.; Borkiewicz, O. J.; Leclerc, S.; Groult, H.; Lantelme, F.; Laberty-Robert, C.; Dambournet, D. Lithium Intercalation in Anatase Titanium Vacancies and the Role of Local Anionic Environment. *Chem. Mater.* **2018**, *30* (9), 3078−3089.
(72) Hou, C.; Xie, J.; Yang, H.; Chen, S.; Liu, H. Preparation of Cu_2O@$TiOF_2$/TiO_2 and Its Photocatalytic Degradation of Tetracycline Hydrochloride Wastewater. *RSC Adv.* **2019**, *9* (65), 37911−37918.
(73) Liu, S.; Yu, J.; Wang, W. Effects of Annealing on the Microstructures and Photoactivity of Fluorinated N-Doped TiO_2. *Phys. Chem. Chem. Phys.* **2010**, *12* (38), 12308−12315.
(74) Louvain, N.; Karkar, Z.; El-Ghozzi, M.; Bonnet, P.; Guérin, K.; Willmann, P. Fluorination of Anatase TiO_2 towards Titanium Oxyfluoride $TiOF_2$: A Novel Synthesis Approach and Proof of the Li-Insertion Mechanism. *J. Mater. Chem. A* **2014**, *2* (37), 15308−15315.

https://doi.org/10.1021/acsnano.4c02150
ACS Nano XXXX, XXX, XXX−XXX

Development of Silver Halide Fiber-Based SEIRA Approach for Detection of Pollutants in Aqueous Environment

Sonata Adomaviciute-Grabusove,[1,*] Olga Bibikova,[2] Tatiana Sakharova,[3] Viacheslav Artyushenko,[3] Valdas Sablinskas[1]

1 Institute of Chemical Physics, Vilnius University, Sauletekio av. 3, LT-10257 Vilnius, Lithuania
2 Kavli Institute for Nanoscience Discovery, Oxford University, OX13QU, Oxford, the United Kingdom
3 art photonics GmbH, Rudower Chaussee 46, 12489 Berlin, Germany
* Correspondence: sonata.adomaviciute@ff.vu.lt (S.A.-G.)

ABSTRACT

The Surface Enhanced Infrared Absorption (SEIRA) spectroscopy under highly-controlled, laboratory conditions has been extensively applied and is important in many areas of material analysis and sensor development. However, its direct application in aqueous environments remains a significant challenge. Addressing this, our study presents a fiber-based SEIRA technique that utilizes replaceable silver halide polycrystalline infrared (PIR) fiber loops. These fiber loops were modified with silver-polyvinylpyrrolidone (Ag-PVP) nanoparticles and applied for acquiring SEIRA spectra of naphthalene, a model polycyclic aromatic hydrocarbon. It was demonstrated that naphthalene dissolved in water at a concentration of 50 μM can be detected directly in aqueous environments under *in situ* conditions. The distinctive spectral band at 783 cm^{-1} was used to identify naphthalene in water. An exploratory computational study was conducted to investigate the effect of silver interaction on the naphthalene SEIRA spectrum. The computational and experimental results indicate the absence of covalent bond of naphthalene to the Ag-PVP nanoparticles, with only physisorption being observed. This study facilitates the applicability of SEIRA to practical, real-world scenarios, including the detection of low-solubility toxic compounds like naphthalene, which are pertinent to environmental contamination.

KEYWORDS: ATR, SEIRA, naphthalene, fiber, silver nanoparticles, silver halide, polycrystalline fiber, ATR sensor

INTRODUCTION

Surface-Enhanced Infrared Absorption (SEIRA) effect was first demonstrated in the 1980s and uncovered new possibilities for the field of infrared (IR) spectroscopy.[1] Nevertheless, much attention was focused on another enhancement technique of vibrational spectroscopy – Surface Enhanced Raman Scattering (SERS), which underwent much faster development. This is partly because the SERS signal enhancement is proportional to the fourth power of the electric field (E^4) of the Raman effect,[2,3] and due to the use of metal nanoparticles with localized surface plasmon resonance (LSPR) in the visible range. Essentially, the plasmon resonance of these nanoparticles aligns with the Raman excitation frequency, greatly amplifying the enhancement. These resonance conditions generate extremely high enhancement factor in SERS spectroscopy.[3–6] Although the infrared absorption cross-section is significantly higher than that of Raman scattering,[7–9] the enhancement achieved in SEIRA is somewhat more restrained, scaling the electric field

enhancement factor by only two orders of magnitude.[3] Nonetheless, this enhancement, while not as significant as in Raman spectroscopy, holds great promise for advancing the capabilities of infrared spectroscopy. Notably, similar enhancement mechanisms are at play in infrared spectroscopy, despite the inherent differences. Mainly, the electric field near the molecular species gets enhanced due to oscillations of free charges present in the plasmonic material. In case of Raman spectroscopy for visible light, metals like gold, silver, copper, aluminum are used since their plasmon resonance frequencies lie in the visible range.[2,6,10,11] For the infrared spectroscopy, materials like III–V group semiconductors,[12] graphene nanostructures,[13,14] hexagonal boron nitride,[15] etc., have been adopted. Enhancement of SEIRA has also been demonstrated using metal nanostructures.[16–18] Specifically, the tuning of plasmonic resonances in metal antennas to the infrared range,[17,19–22] as well as the dipolar resonances among interparticle coupled structures of multiple nanoshells in the mid-infrared region, have been shown.[16]

Regardless of recent improvements in SEIRA spectroscopy, application of SEIRA in aqueous environments remains challenging. The technique, which has proven effective in highly controlled laboratory conditions, faces limitations when applied to more practical approaches. The integration of optical fibers into Fourier transform infrared (FTIR) spectrometers opens up exciting possibilities for *in situ* sample measurements, bridging the gap between classical spectroscopic techniques and real-world applications. Our approach addresses this gap by demonstrating attenuated total reflection (ATR) enabled SEIRA effect in aqueous environment using infrared fiber probe attachment - the replaceable silver halide polycrystalline infrared (PIR) fiber loops that allow low-cost ATR-spectroscopy. This has enabled the implementation of the SEIRA method for direct and remote applications, even in challenging setups.

It is particularly useful in scenarios where certain toxic chemical compounds, such as naphthalene, have extremely low solubility in water, yet their presence can still contribute to contamination. Naphthalene can serve as a target molecule to demonstrate the capability of fiber-based SEIRA sensors in detecting specific types of organic compounds, particularly those with aromatic rings which are common in many pollutants.[23,24] Naphthalene is a polycyclic aromatic hydrocarbon (PAH) that is commonly found in industrial areas and can be a significant pollutant in water sources due to its widespread use and stability.[25,26] As a common industrial chemical,[27–29] naphthalene is a relevant target for environmental monitoring.[25,30–32] Its detection is important for assessing water quality and the effectiveness of water treatment processes.[32] Exposure to naphthalene by ingestion or inhalation has been linked to adverse disturbance of one's health such as changes in respiratory and olfactory epithelium,[31,33,34] occurrence of cancer.[34–38]

In this work, naphthalene compound was investigated by means of fiber-based SEIRA spectroscopy. Naphthalene is a toxic material soluble in ethanol (solubility 0.6 M) and hardly soluble in water (solubility in water – 0.2 mM). Utilizing the fiber-based SEIRA method, an intense spectral band at approximately 783 cm^{-1} was used as a distinctive spectral marker for naphthalene. It is notable that naphthalene was not detectable in water using conventional/standard infrared absorption technique.

RESULTS

Characterization of Silver Nanoparticles. Silver nanoparticles stabilized with polyvinylpyrrolidone (Ag-PVP) were synthesized by adapting the Aherne method for the synthesis of triangular silver nanoplates.[39] Polyvinylpyrrolidone (PVP) has extensive applications as both a surfactant and a stabilizer in nanoparticle synthesis.[39–46] Additionally, it serves as an agent that

promotes the anisotropic growth of silver nanoparticles.[40–43,47] Stabilization of nanoparticles coated with PVP results from steric effects reducing the interactions with ions in the solution that can lead to nanoparticle aggregation.[47–49] PVP is a nonionic polymer consisting of a highly polar amide group in the pyrrolidone ring, facilitating the formation of polymer/metal-ion complexes.[50] The hydrophobic part of the PVP monomer, the alkyl backbone, is directed towards the solution and the hydrophilic part, the pyrrolidone ring, bonded to the nanoparticle surface.[42,47] Experimental results indicate that PVP binds to silver surface *via* the oxygen[51–55] and, possibly, *via* the nitrogen atoms.[53,54] This effectively improves the stability of the colloidal solution even in adverse media at high concentrations, high ionic strength and over a wide pH range.[49] Another advantage of the PVP coated nanoparticles lies in their biocompatibility. Since PVP is biocompatible[56], it can play a role in reducing the toxicity associated with the silver nanoparticle material.[49,57–60] Further SEIRA experiments were conducted using these Ag-PVP nanoparticles.

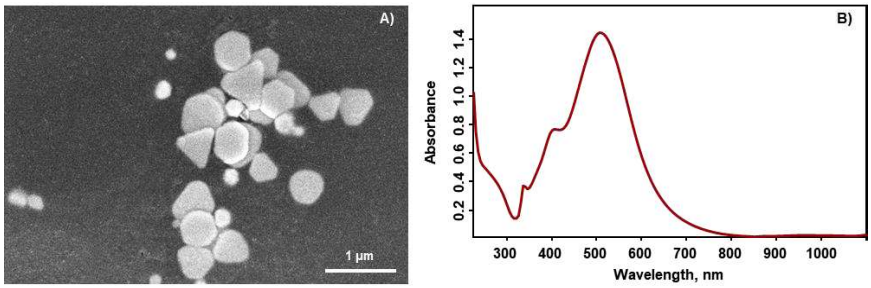

Figure 1. SEM image (A) and optical absorption spectrum (B) of Ag-PVP nanoparticles.

The nanoparticle synthesis yielded a heterogeneous mixture of triangular nanoplates, truncated triangular nanoplates and spherical nanoparticles, as can be seen from Figure 1A. This observation is consistent with findings reported in the literature.[39,61–63] Figure 1A illustrates that the synthesized nanoparticles exhibited a size range from 35 to 85 nm, with an average size of 50 ± 10 nm. The optical properties of silver nanoparticles are significantly influenced by their size, shape, and aggregation state. Consequently, the optical absorption spectrum observed is a cumulative representation of the various nanoparticle types present. In terms of optical properties, the solution of Ag-PVP nanoparticles exhibits several absorption peaks that resemble longitudinal (in-plane) dipole and quadrupole resonances, together with transversal (out-of-plane) quadrupole plasmon resonance typical for triangular nanoplates.[39,61,62,64–68] The peak at 625 nm is assigned to the in-plane dipole resonance, the sole one present for spherical silver nanoparticles up to 50 nm.[69] For larger nanoparticles or non-spherical triangular nanoplates, this resonance is redshifted from 410 to 625 nm due to the phase retardation effect between the incident electromagnetic field and the induced oscillations of electrons in the nanoparticles. As the size of the nanoparticle increases, the phase retardation inside the particle becomes more significant, influencing the resonance frequency of the plasmon oscillation. The observed FWHM (full width at half maximum) of this band is approximately 190 nm. The widening of this band is commonly attributed to the increased radiation damping and increased nonradiative decay.[39,62] In case of triangular nanoplates, the degree of snipped tip of the truncated nanoplates also influence this bandwidth.[68] Another peak at 405 nm can be assigned to in-plane quadrupole resonance which can be induced due to the phase retardation of the electric field within the particle.[61] Besides the dipole resonance, a quadrupole mode has been

theoretically and experimentally identified in nanoparticles ranging from 50 to 150 nm and non-spherical nanoparticles. The out-of-plane quadrupole resonance is visible at 335 nm.[39,62,64–68]

Preparation of Fiber Loop Tips for SEIRA. The polycrystalline nature of the silver halide fiber is apparent in the SEM (scanning electron microscope) images (Figure 2 A, B), which show micro-sized grains. Typically, the grain size in polycrystalline fibers varies widely, generally ranging from 1 μm to 5 μm.[70] In our case, the grain size at the fiber surface was found to be approximately 730 ± 250 nm. Due to the soft nature of the fiber material, it demonstrates excellent flexibility, allowing it to be bent at low bending ratios without incurring damage to the fiber itself. This characteristic is particularly advantageous for the PIR-fiber loop, which, due to its small bending radius, facilitates ATR effect and allows for infrared absorption due to the evanescent wave that penetrates the sample. This infrared absorption technique is highly regarded in modern spectroscopy as it is convenient for easy sample preparation.[71–73]

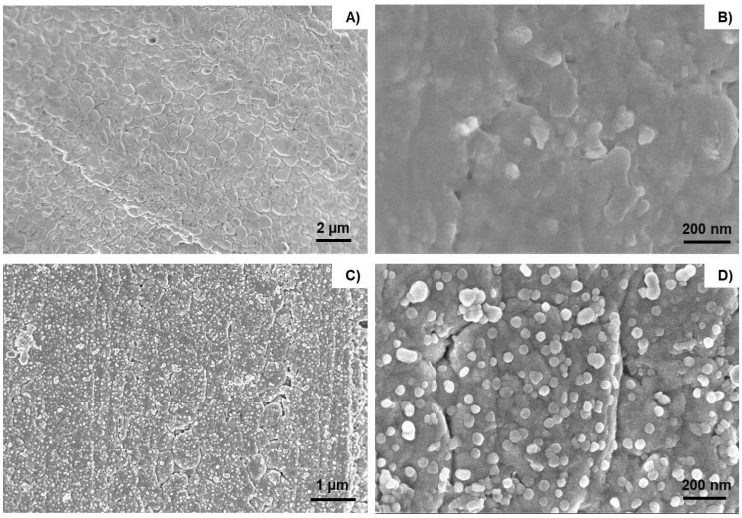

Figure 2. SEM images of PIR-fiber loops without nanoparticles (A, B) and with the deposited Ag-PVP nanoparticles (C, D).

Our methodology to facilitate SEIRA includes the deposition of PVP-coated silver nanoparticles from a colloidal solution. This deposition process relies on the interaction between PVP and the AgCl/AgBr fiber surface. PVP exhibits a pronounced affinity for adsorption onto silver halide crystals,[74,75] which consequently impedes the growth of silver halide structure.[74–77] SEM images, presented in Figures 2C and 2D reveal the presence of assembled Ag-PVP nanoparticles on the PIR-fiber loop after the treatment with the initially synthesized nanoparticles. The size distribution of nanoparticles on the fiber loop tip is similar to that of colloidal Ag-PVP nanoparticles (50 ± 10 nm). The nanosized silver structures on the loop tip enhance the infrared absorption signal of the molecules at close proximity and enable SEIRA.

Naphthalene standard ATR Measurements. Naphthalene ($C_{10}H_8$) is a volatile polycyclic aromatic hydrocarbon. The two-ring molecular structure of naphthalene is depicted in Figure 3. To date, due to its extremely low solubility in water and high volatility, naphthalene has been primarily studied in the gas phase,[78–80] isolated in solid matrices,[81–83] and in crystalline form using KBr

(potassium bromide) pellet technique.[84,85] In aqueous environments, the interaction between naphthalene molecules and water matrix has been investigated by infrared absorption.[86] Another study has explored the detection of dissolved naphthalene under high pressure and temperature conditions using an ATR sensor with a thin polymer cap.[87]

To our knowledge, direct detection of dissolved in water naphthalene has not yet been reported. The primary challenges are its very low solubility in water, approximately 200 µM,[88,89] and the intense spectral background due to water absorption. These factors hinder the use of infrared absorption methods in aqueous environments for the direct detection of negligible-solubility molecules, such as naphthalene. Figure 3 A shows 90 mM concentration of naphthalene dissolved in ethanol, since the solubility of naphthalene in alcohol is much greater than in water. The naphthalene is identified by an intense spectral band at 787 cm^{-1} in the ethanol solution, corresponding to the out-of-plane C–H deformation. Additional weak naphthalene spectral bands at 843 and 949 cm^{-1} corresponding to other C–H deformational vibrations are also visible. The spectral band at 880 cm^{-1} is attributed to the symmetric ν(C–C–O) vibrational mode of ethanol.[90]

Unfortunately, the most pronounced spectral band of naphthalene in our study coincides with the librational modes of water molecules, as indicated by references.[91–93] This results in a broad water spectral band centered at 750 cm^{-1}, which overlaps with naphthalene band. This overlap complicates the detection of naphthalene in aqueous solutions and contributes to an elevated noise level in the lower wavenumber region of the spectra. Therefore, the conventional fiber ATR absorption method failed to detect naphthalene dissolved in water at a concentration of 150 µM (Figure 3 B).

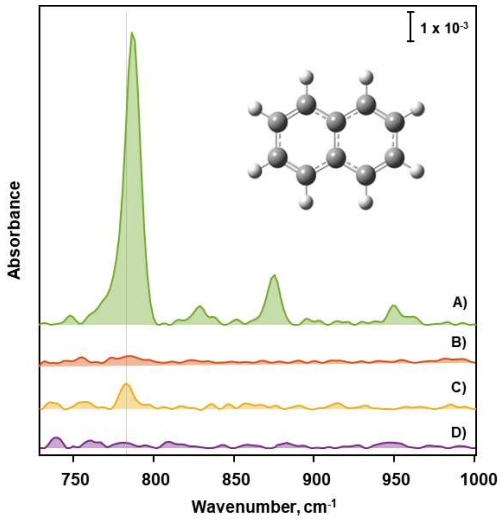

Figure 3. Standard ATR spectra of (A) 0.09 M naphthalene solution in ethanol and (B) 150 µM naphthalene solution in water (B); fiber-based SEIRA spectrum of (C) 150 µM naphthalene solution in water and (D) pure water for comparison. Inset shows naphthalene molecular structure.

Fiber-Based SEIRA Approach for Naphthalene Detection. The fiber-based SEIRA approach has enabled direct detection of naphthalene in water. By introducing nanoparticles to the fiber loop tip, we enhanced the absorption signal of naphthalene molecules, making the absorption band at 783 cm^{-1} observable in an aqueous environment (Figure 3 C). For a quantitative estimation, we evaluated the signal-to-noise ratio (SNR) of naphthalene in the fiber-based SEIRA approach, resulting in an SNR value of 15. The SNR of naphthalene in water measured with an untreated fiber loop was only 1, which is equivalent to the reference water spectrum (Figure 3 B, D). This clearly indicates that the untreated fiber loop is not sufficiently sensitive in this case.

Other spectral bands of naphthalene dissolved in water were not observed, due to lower intensity. The literature suggests that the relative intensity of the band at 783 cm^{-1} is approximately 15 times higher than intensity of other bands.[86] The study of the dissolved naphthalene detection in water in extreme pressures and temperatures revealed naphthalene spectral band at 782 cm^{-1},[87] aligning with the band position observed in our study. Our results reveal the blueshift of 3 cm^{-1} from the crystalline form of naphthalene that also coincides with previous study.[86,87] The dependence of naphthalene spectral band positions on nearby molecules have been demonstrated in matrix isolation study, leading to a shift of up to 8 cm^{-1} based on the amorphous or ordered phase of water molecules.[86] To delve deeper into the interactions between naphthalene and silver atoms and the resultant effects on absorption band shifts, a computational study was conducted (the details of which are presented further).

We aimed to evaluate the enhancement factor achieved using Ag-PVP nanoparticles in the fiber-based SEIRA approach. However, straightforward evaluation was challenging because no naphthalene was detected under the same experimental conditions without Ag-PVP nanoparticles. To address this, the intensity of the spectral band of naphthalene, dissolved in ethanol at a concentration of 90 mM, was measured in the same experimental setup. Notably, ethanol does not exhibit high absorption in the spectral range around 780 cm^{-1}, making the naphthalene band more pronounced. The analytical enhancement factor (AEF) was than evaluated as follows:

$$AEF = \frac{I_{IR\ EtOH} \times c_{IR\ EtOH}}{I_{SEIRA} \times c_{SEIRA}}.$$

Where $I_{IR\ EtOH}$ and $c_{IR\ EtOH}$ correspond to the intensity and concentration (90 mM) of the 787 cm^{-1} band of naphthalene dissolved in ethanol, respectively; I_{SEIRA} and c_{SEIRA} represent the intensity of the corresponding band and the concentration (150 µM) of naphthalene dissolved in water in the SEIRA approach. The AEF calculated by the suggested method was 90.

The concentration of dissolved naphthalene was further reduced to determine the lowest detectable concentration in water using the fiber-based SEIRA approach. As depicted in Figure 4, the measured SEIRA spectra for different naphthalene concentrations in water are presented. After background correction, the spectra reveal a diminishing naphthalene spectral band at 783 cm^{-1}. The lowest reliably detectable concentration of naphthalene was determined to be 50 µM (Figure 4), yielding a SNR value of 4. At a concentration of 25 µM, the naphthalene band becomes indiscernible, rendering this concentration below the limit of detection (LOD). In all cases, SNR was calculated by dividing the intensity of the spectral band at 783 cm^{-1} by the standard deviation of the noise in the 700-870 cm^{-1} range.

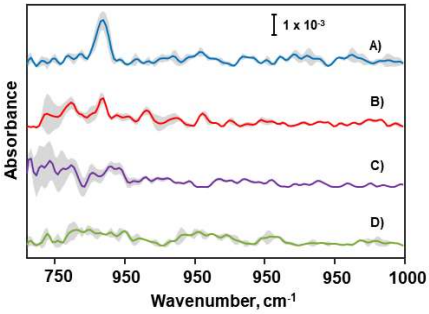

Figure 4. Fiber-based SEIRA spectra of 150 µM naphthalene (A); 50 µM naphthalene (B); 25 µM naphthalene (C); water (D).

Reproducibility of SEIRA Signal. The stability and reproducibility of the fiber-based SEIRA signal, using Ag-PVP nanoparticles, were assessed. For this purpose, ten consecutive measurements of naphthalene dissolved in water were conducted using the same fiber loop. Between measurements, the loop was rinsed with extra pure deionized water, and subsequently, the spectrum of pure water was recorded. In Figure 5 A, the fiber-based SEIRA spectrum of naphthalene is shown for each successive measurement, with the number of measurements increasing from the bottom. We observed that the noise level increased and the intensity of the naphthalene band decreased as the number of measurements progressed, a trend attributed to the potential washout of Ag-PVP nanoparticles by the deionized water. Despite the interaction of PVP with the silver halide surface, the lack of electrostatic forces in deionized water may facilitate the detachment of Ag-PVP nanoparticles from the fiber surface. Moreover, after rinsing step and measuring the pure water spectra, the absence of a naphthalene signal suggests that naphthalene molecules do not adsorb onto the Ag-PVP nanoparticle-coated silver halide surface. The calculated SNR showed an almost linear trend, dropping from a value of 7 to 2.

The application of this method for *in situ* measurements in natural water environments may result in different outcomes due to the presence of varying electrostatic forces. However, the findings suggest that the fiber-based SEIRA loops are best suited for one-time use and should be replaced for subsequent measurements. The straightforward replacement process of these loops ensures consistent measurements using silver halide fiber loops.

It is important to highlight that another technique for nanoparticle deposition on fiber loops has been investigated. This method, which entails synthesizing nanoparticles directly on PIR fibers, mirrors conventional techniques used for mirror coatings.[94] Initial attempts at this synthesis yielded both a higher signal and a higher noise level, leading to a similar SNR for naphthalene; therefore, it was not continued. Notably, nanoparticles coated with PVP not only offer increased biocompatibility but also enable the creation of non-spherical nanoparticles. These are anticipated to enhance the SEIRA signal and, as such, hold high potential for further application. The most favorable outcomes were observed with metal nanorods or nanoantennas.[17,19–22] Furthermore, the synthesis conditions for Ag-PVP nanoparticles were modified slightly. During the growth phase, varying amounts of seed solution were employed: (I) 40 µl, (II) 50 µl, (III) 80 µl and (IV) 90 µl. These variations resulted in different ratios of ascorbic acid to silver (Table S1). Although these adjustments were expected to alter the nanoparticle concentration and size within the final colloidal solution, no significant changes in SEIRA intensity or SNR were detected (Figure S2).

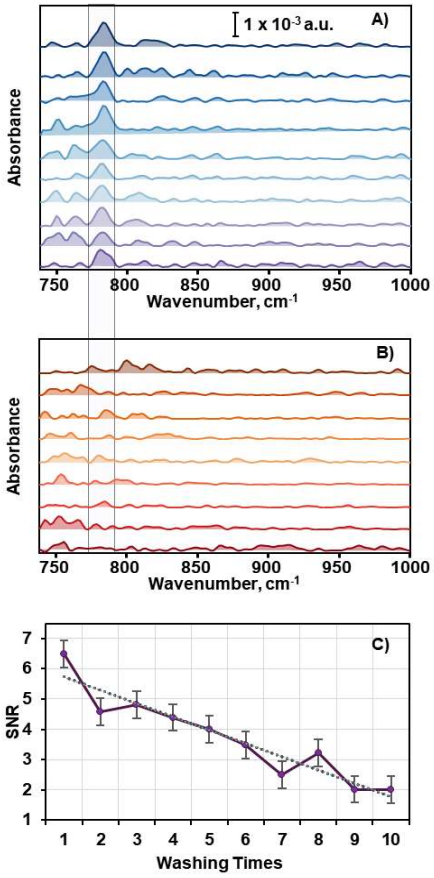

Figure 5. Signal reproducibility during 10 successive measurements: of 150 µM naphthalene fiber-based SEIRA spectra (A); the corresponding water spectra (B); and SNR dependence of 150 µM naphthalene on washing times (C). The number of measurements increases from the top to bottom.

Computational Study of Silver – Naphthalene Interaction. Experimental evidence from multiple studies has demonstrated SERS activity for naphthalene, confirming that interactions between naphthalene and both gold and silver surfaces indeed occur.[95–99] Previous computational studies have explored the behavior of naphthalene on different metal surfaces.[96,100] These studies have led to a diverse understanding of the interaction, with some suggesting a charge transfer effect with silver clusters,[100] while others propose a primarily physical adsorption on gold surfaces.[96] Therefore, we do not include detailed computational results in our paper (for more information see Supporting Information).

Our research aimed to investigate the adsorption behavior of naphthalene (Naph) on a silver (Ag) cluster, particularly its influence on spectral band shifts and intensity enhancements. Density functional theory (DFT) computations were performed using the B3LYP hybrid functional and LANL2dZ/DGDZVP basis sets. Our findings suggest that despite initial variations in the orientation of the naphthalene molecule towards the cluster, it reoriented after geometry optimization, positioning the ring towards the Ag cluster (Figure 6). This reorientation is consistent with other studies that suggest aromatic hydrocarbons interact with silver via the π-electron system in the ring.[100–102] Briefly, this study demonstrated that the shortest computed C – Ag bond distance was 2.62 Å, which is greater than the reported C – Ag bond lengths, indicating that no covalent bond forms between the Ag and C atoms in naphthalene molecule and interaction is physical in nature.[103,104] This finding aligns with the observed minimal molecular overlap in the Naph – Ag_5 complex (Figure S1 in Supporting Information).

Despite this, the calculated natural charge transfer (Δq) and binding energy (ΔE) suggest an interaction between the electron densities of naphthalene and the silver cluster, as indicated in Table 1. The ΔE of Naph – Ag_5 was found to be -0.38 eV, which, while not substantial, supports the likelihood of a physical interaction. The basis set superposition error has been taken into account. The Δq is defined as the total natural charge on the silver cluster, calculated by summing the natural charges of each atom within the cluster. With a value of -0.12 *e*, Δq quantifies the charge transferred from the silver cluster to the naphthalene molecule, which was also found to be minimal. This reinforces the theory that the adsorption of the naphthalene molecule onto the metal surface is physical in nature. Interestingly, a similar charge transfer value was observed for the adsorption of naphthalene on the Au surface.[96] Other parameters, such as static polarizability (α_0) and bandgap energy, exhibited more pronounced changes. The initial response of electron density to electric fields is measured as α_0, which is essential for predicting molecular interactions and their behavior in the presence of field. It increased. Notably, the bandgap of naphthalene, originally 4.72 eV as listed in Table 1, is significantly reduced to 1.63 eV upon introducing the silver cluster (1.63 eV with DGDZVP basis set calculations).

Based on our calculations and experimental results, we propose that naphthalene likely engages with the silver cluster through electrostatic forces, *i.e.* physisorption. However, this interaction does not establish a bond, which is expected given the inherent stability of the naphthalene molecule. Supporting this, experimental observations revealed an absence of naphthalene signal after extracting the SEIRA loop from naphthalene solution, suggesting a mere weak interaction with the nanoparticles. Notably, our study did not incorporate solvent effects or the possible interactions involving the capping PVP agent and naphthalene. The presence of the PVP capping agent could sterically hinder or otherwise influence the interaction capabilities of naphthalene.

Table 1. Bandgap (HOMO-LUMO), Static Polarizability (α_0), the Natural Charge Transfer (Δq) and Binding energy (ΔE) for the Naphthalene and Naph-Ag_5 complex.

	Bandgap, eV	α_0, au.	Δq, *e*	ΔE, eV
Naphthalene	4.72	116.65		
Naph – Ag_5 (LanL2DZ)	1.42	361.57	-0.031	-0.425
Naph – Ag_5 (DGDZVP)	1.63	369.51	-0.12	-0.38

The theoretical computations of vibrational frequencies of naphthalene molecule revealed that the scaled wavenumber spectral values closely match those observed experimentally (Figure 6). The scaling of computed vibrational frequency values is necessary for high-accuracy prediction of organic compound spectrum and accounts for the discrepancies in the electron correlation coefficient, basis set deficiencies, and anharmonicity effects.[105] Interestingly, no significant enhancement of the bands was observed when introducing the silver cluster into the calculations, with the only observable band in the experimentally acquired fiber-based SEIRA spectra located at 783 cm^{-1}. Our computational study indicates a blueshift of this band by 2 cm^{-1} using the DGDZVP basis set and by 18 cm^{-1} using the LanL2DZ basis set. Since the interaction between naphthalene and silver occurs more significantly *via* the tails of the molecular orbitals, we suspect that the inclusion of polarization in this case cannot be neglected.[106] Therefore, the DGDZVP basis set is considered more accurate for determining changes in the SEIRA spectrum. The calculated band shift was not significant and correlates well with the experimentally observed blueshift of 3 cm^{-1}.

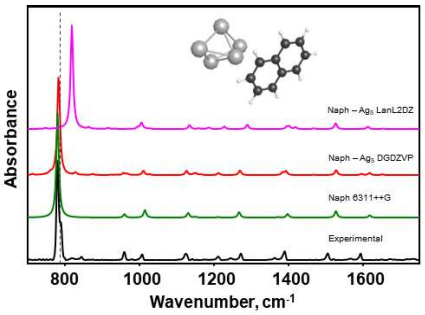

Figure 6. Scaled theoretical and experimental infrared absorption spectra of naphthalene, along with the spectra of the naphthalene-silver cluster (Naph – Ag_5) calculated using the DGDZVP and LanL2DZ basis sets. The calculated spectra have been scaled to account for theoretical and experimental discrepancies. The inset visualizes the optimized structure of the Naph – Ag_5.

DISCUSSION

Fiber-based spectroscopic techniques, such as the one employed in our study, offer a multitude of advantages that are particularly beneficial for rapid and on-site environmental analysis. Vibrational spectra of samples can be obtained within 2 to 5 minutes, with immediate availability of results. Moreover, it allows for the simultaneous detection of various contaminants, provided that spectral markers for specific molecules have been established. ATR sensors, which utilize silver

halide fibers, have already demonstrated the ability to detect volatile organic compounds (VOCs) at parts per billion (ppb) levels in *in situ* approach. The concept behind ATR sensors involves creating multiple internal reflections on the active surface, which interact with sample molecules. Additionally, capping the surface with a hydrophobic polymer prevents water molecule diffusion within the active area, enabling only VOC target molecules to approach the sensor closely.[107,108]

The integration of SEIRA approach into fiber-based ATR technique has enabled *in situ* sample measurements, expanding the potential applications of spectroscopic analysis. In our study, naphthalene with negligible-solubility was directly and straightforwardly detected in water at concentrations of 150 and 50 μM using the fiber-based SEIRA method. In contrast, previous infrared absorption studies of naphthalene in water were performed only under laboratory conditions[86,87] and did not utilize the *in situ* capabilities of fiber-based techniques. Infrared absorption study of naphthalene under extreme pressures and temperatures have revealed a dissolved naphthalene band at 782 cm^{-1}. Our study yielded consistent results, with the observation of the naphthalene band at 783 cm^{-1} upon interaction with Ag-PVP nanoparticles in water. Compared with theoretical computations, a slight blueshift of this band from its crystalline form is observed, which most likely occurs due to naphthalene's interaction with water molecules or silver atoms.

While SEIRA-based detection of naphthalene has not been previously demonstrated to our knowledge, SERS-based detection has been shown in several studies.[95–98,109] It is believed that naphthalene likely adsorbs onto metal surfaces through electrostatic interactions, a hypothesis supported by these SERS studies. This is further supported by our observation that naphthalene could be easily rinsed from the fiber-based SEIRA loops, indicating a lack of strong chemical bonding. Previous SERS studies have demonstrated excellent detection capabilities for naphthalene, with a detection limit of 10 ppb using ligand-functionalized mesoporous Au nanoparticles,[109] approximately 6 ppm using colloidal nanoparticles;[96] and 1 ppm (parts per million) employing polystyrene beads coated with gold nanoparticles.[98] None of the previous studies utilized fiber-based techniques, which limited *in situ* detection capabilities. Our achieved LOD is comparable, reaching 50 μM or approximately 6 ppm. Further optimization of the nanoparticle concentration, shape, capping agent of the fiber loop tips might enhance this LOD and lead to even better performance. It is worth noting that the SNR obtained in our study, which was 15, which can be improved through higher acquisition times and averaging of the acquired spectra. Additionally, the analytical enhancement factor determined by our method was found to be 90, indicating a significant enhancement in spectral signal from the sample molecules.

CONCLUSION

Our research has established that the fiber-based SEIRA method, which employs silver halide polycrystalline fiber loops, is a promising technique for detecting polycyclic aromatic hydrocarbons such as naphthalene in aqueous samples. The LOD for naphthalene in water was determined to be 50 μM (approximately 6 ppm). Notably, the fiber-based SEIRA approach yielded a significant enhancement factor of 90 in the spectral signal of the sample molecules, with the characteristic naphthalene band at 783 cm^{-1}. The adsorption detected is predominantly attributed to electrostatic interactions, which is supported by the ease of rinsing naphthalene from the SEIRA loop tips, indicating a non-covalent nature of the molecule-surface interaction. Theoretical calculations further corroborated these findings, with the minimum computed C–Ag bond length of 2.62 Å suggesting the absence of chemisorption. Moreover, no significant band shift of the characteristic naphthalene band was observed. This study not only demonstrates the efficacy of the

fiber-based SEIRA method in real-world environmental conditions but also provides a foundation for future research to refine and expand the capabilities of SEIRA spectroscopy for the detection of a wide range of substances in aqueous environment.

EXPERIMENTAL SECTION

Preparation of Fiber Optic ATR Loop for Fiber-Based SEIRA Experiments. Fiber optic Detachable Loop probe (*Art Photonics*, Germany) consists of two PIR fibers 900/1000 µm core/clad diameter and replaceable loop tips of 700 µm diameter unclad PIR fiber as ATR sensitive element. PIR fiber has $AgCl_{0.25}Br_{0.75}/AgCl_{0.5}Br_{0.5}$ core/clad composition and fiber loop has $AgCl_{0.25}Br_{0.75}$ core only composition. For convenience, the ATR loop tips are designed for easy replacement within the Fiber Optic ATR Loop Probe. The principal scheme of ATR-Loop Probe setup is given in Figure 7 A. The replaceable loop tip is aligned with the input and output fibers at the probe shaft. The proper alignment is ensured by a slot in the shaft. The loop tip is secured by adding the fixing cap and tightening it to the nut on the probe. Subsequently, the probe legs can be connected to the FTIR MATRIX-MF spectrometer equipped with liquid nitrogen cooled mercury cadmium telluride (MCT) detector (*Bruker*, USA) for measurements.

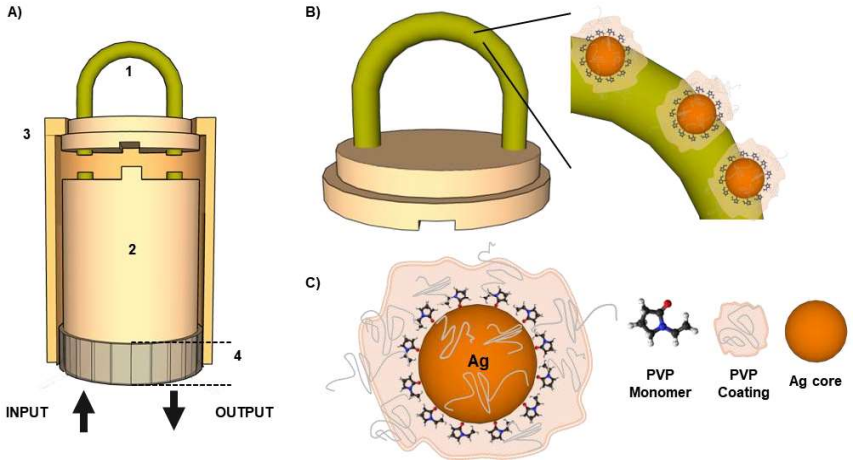

Figure 7. The principal components of the fiber-based SEIRA experimental setup. (A) Principal scheme of the ATR Loop Probe with replaceable PIR-fiber tip: 1 – ATR loop PIR-fiber tip; 2 – ATR probe shaft; 3 – Fixing cap; 4 – Fixing nut. (B) Schematic representation of fiber-based SEIRA tip covered with Ag-PVP nanoparticles. (C) Structure of Ag-PVP nanoparticle.

Deposition of Nanoparticles onto SEIRA Loops: Methodology and Process. To fabricate fiber-based SEIRA tips, PIR-fiber loops were covered with silver nanoparticles. The silver nanoparticles coated with polyvinylpyrrolidone (PVP) polymer layer (Ag-PVP) were synthesized separately. Synthesis for Ag-PVP nanoparticles was adapted from Aherne et al. protocol.[39] The initial step involved producing a seed solution. This was achieved by reducing a mixture that contained 30 mM PVP and 15 mM silver nitrate ($AgNO_3$) in a volume of 3 ml, using a 10 mM sodium borohydride ($NaBH_4$) solution of 90 µl. The growth phase for the Ag-PVP nanoparticles

introduced a minor variation. Specifically, the quantities of the seed solution used were (I) 40 µl, (II) 50 µl, (III) 80 µl and (IV) 90 µl. This seed solution was mixed with 5 ml of pure water, then 1 ml of 10 mM L-ascorbic acid ($C_6H_8O_6$), and finally with 0.5 mM of silver nitrate solution 3 ml, all under continuous stirring.

Prior to the nanoparticle deposition on the PIR-fiber loops, the loops were cleaned with ethanol and acetone. Fiber loops were then submerged in the Ag-PVP nanoparticle solution and left for 48 h. Subsequently, the loops were removed, washed with deionized water (18.2 MΩ × cm), and left to dry. This process resulted in a deposition of Ag-PVP nanoparticles on the fiber-based loop tips. We propose a graphic representation for the formation of Ag-PVP nanoparticle layer on the fiber-based SEIRA loop and Ag-PVP nanoparticle structure (Figure 7 B, C).

Ag-PVP Nanoparticle Characterization. Nanoparticles were characterized using scanning electron microscope (SEM; Helios Nanolab 650, FEI, Netherlands). The SEM images of the Ag-PVP nanoparticles were taken both before and after their deposition onto the PIR-fiber loop tip. The size and size deviation of the nanoparticles were determined using ImageJ software. In parallel, optical absorption spectrometer Lambda 1050 (Perkin Elmer, USA) was employed to analyze the optical properties of the colloidal Ag-PVP nanoparticle solution.

Standard ATR and ATR-SEIRA Measurements. Standard (or conventional) ATR and ATR-SEIRA spectra of naphthalene solutions were measured using a FTIR MATRIX-MF spectrometer (Bruker, USA) equipped with a liquid nitrogen - cooled MCT detector. The Alpha FTIR spectrometer (Bruker Optik GmbH, Germany) with a diamond ATR module and a room-temperature deuterated triglycine sulfate (DTGS) detector was utilized for crystalline naphthalene measurements. The spectra were recorded in the spectral range of 600 – 3500 cm^{-1} with a resolution of 4 cm^{-1}. For each measurement, 128 scans were averaged to improve the signal-to-noise ratio (SNR). In this paper, all spectra are presented in the 700 – 1000 cm^{-1} range for the sake of relevance.

For the ATR-SEIRA measurements, fiber-based SEIRA loop was connected to the probe and the background spectra were measured in deionized water (18.2 MΩ × cm). Afterwards, the SEIRA loop probe was immersed in a 150 µM naphthalene solution in water. The spectra of naphthalene were obtained by subtracting the water spectrum. The subtraction coefficients were optimized to minimize the water absorption bands in the resulting spectra. The difference spectra of naphthalene minus water were constructed using Opus 8.2 software (Bruker, Germany) and further background subtracted using Rubberband/Baseline-correction method. For the experiments of LOD, naphthalene concentration was lowered to 50 and 25 µM. The repeatability of the SEIRA signal was evaluated by immersing the fiber loop tip in a 150 µM naphthalene solution for spectral measurements, then rinsed with and immersed in deionized water for acquiring water spectra. These steps were repeated several times, and the SNR was evaluated. In all cases, the SNR was calculated by dividing the intensity of the spectral band at approximately 783 cm^{-1} by the standard deviation of the noise in the 700 – 870 cm^{-1} range.

For standard ATR measurements of naphthalene solution, a PIR-fiber loop tip was used without Ag-PVP nanoparticles. The same procedure as for ATR-SEIRA measurements was followed. The 90 mM naphthalene solution in ethanol was measured as a reference for comparison with the ATR-SEIRA spectra.

Computational study. Gaussian 16 software package was used for the DFT calculations. Molecules and silver cluster, consisting of five atoms (Ag_5), were constructed, and visualized using GaussView 5 software. Computations were performed using the Becke three hybrid exchange and Lee-Yang-Par correlation functional B3LYP with 6311++G(d,p) basis set for geometry optimization and evaluation of vibrational frequencies of naphthalene molecule. For the geometry

optimization of Ag_5 cluster and naphthalene-silver complex (Naph-Ag_5), B3LYP functional and DGDZVP or LanL2DZ basis sets were used. Geometry was optimized for each complex species separately, then the complex was constructed and optimized. For this, several initial positions of naphthalene molecule in accordance with silver cluster were tested. The calculated infrared absorption spectra were adjusted on the wavenumber axis by subtracting an offset of 20 cm^{-1}. The intensity was scaled by 8×10^{-4} to match the experimental crystalline naphthalene spectrum.

For the assessment of binding energy, B3LYP / DGDZVP and B3LYP / LanL2DZ levels of theory were used for computations. The counterpoise method was implemented for the correction of basis set superposition error. Together with a large basis set, this should reduce the error and present valid energies. Binding energies, minimal C – Ag bond distance, static polarizability (α_0), natural charge transfer (Δq) was evaluated. The frontier molecular orbitals and the molecular electrostatic potential surface in the ground state were obtained without imposing any symmetry constraints.

Acknowledgment: Authors are grateful to Dr. Algirdas Selskis for scanning electron microscopy imaging. Computations were performed on resources at the High-Performance Computing Center, "HPC Sauletekis" (Faculty of Physics, Vilnius University, Lithuania).

Supporting Information

Supporting Information Available: The DFT study provided the molecular orbitals and molecular electrostatic potential surfaces of the naphthalene and the naphthalene-silver composition, accompanied by an analysis. The protocol for the direct synthesis of silver nanoparticles. Fiber-based SEIRA spectra of a naphthalene solution in water obtained using SEIRA loop tips coated with silver nanoparticles, which were synthesized using various seed solution concentrations.

References

(1) Hartstein, A.; Kirtley, J. R.; Tsang, J. C. Enhancement of the Infrared Absorption from Molecular Monolayers with Thin Metal Overlayers. *Phys. Rev. Lett.* **1980**, *45* (3), 201–204. https://doi.org/10.1103/PhysRevLett.45.201.

(2) Amer, M. S. *Raman Spectroscopy for Soft Matter Applications*; Wiley, 2009.

(3) Wang, H. L.; You, E. M.; Panneerselvam, R.; Ding, S. Y.; Tian, Z. Q. Advances of Surface-Enhanced Raman and IR Spectroscopies: From Nano/Microstructures to Macro-Optical Design. *Light Sci Appl.* **2021**, *10* (1), 161. https://doi.org/10.1038/s41377-021-00599-2.

(4) Chang, X.; Vijay, S.; Zhao, Y.; Oliveira, N. J.; Chan, K.; Xu, B. Understanding the Complementarities of Surface-Enhanced Infrared and Raman Spectroscopies in CO Adsorption and Electrochemical Reduction. *Nat Commun* **2022**, *13* (1), 2656. https://doi.org/10.1038/s41467-022-30262-2.

(5) Osawa, M. Surface-Enhanced Infrared Absorption. In *Near-Field Optics and Surface Plasmon Polaritons*; Springer Berlin Heidelberg: Berlin, Heidelberg, 2001; Vol. 81, pp 163–187. https://doi.org/10.1007/3-540-44552-8_9.

(6) Aroca, Ricardo. *Surface Enhanced Vibrational Spectroscopy*; Wiley, 2006.

(7) Oksenberg, E.; Shlesinger, I.; Tek, G.; Koenderink, A. F.; Garnett, E. C. Complementary Surface-Enhanced Raman Scattering (SERS) and IR Absorption Spectroscopy (SEIRAS) with Nanorods-on-a-Mirror. *Adv Funct Mater* **2023**, *33* (8). https://doi.org/10.1002/adfm.202211154.

(8) Li, S.; Li, Y.; Yi, R.; Liu, L.; Qu, J. Coherent Anti-Stokes Raman Scattering Microscopy and Its Applications. *Front Phys* **2020**, *8*. https://doi.org/10.3389/fphy.2020.598420.

(9) Bazhenov, A. V; Kveder, V. V; Maksimov, A. A.; Tartakovski, I. I.; Oganyan, R. A.; Ossipyan, Y. A.; Shalynin, A. I. Raman Scattering of Light and IR Absorption in Carbon Nanotubes. *Journal of Experimental and Theoretical Physics* **1998**, *86*, 1030–1034.

(10) Zhang, J.; Zhang, L. Nanostructures for Surface Plasmons. *Adv Opt Photonics* **2012**, *4* (2), 157. https://doi.org/10.1364/aop.4.000157.

(11) Barnes, W. L.; Dereux, A.; Ebbesen, T. W. Surface Plasmon Subwavelength Optics`. *Nature* **2003**, 824–830.

(12) Zhong, Y.; Malagari, S. D.; Hamilton, T.; Wasserman, D.; Malagari, D. Review of Mid-Infrared Plasmonic Materials. *J Nanophotonics* **2015**, *9* (1). https://doi.org/10.1117/1.JNP.9.093791.

(13) De Abajo, F. J. G. Graphene Plasmonics: Challenges and Opportunities. *ACS Photonics* **2014**, *1* (3), 133–152. https://doi.org/10.1021/ph400147y.

(14) Bartlett, N. W.; Tolley, M. T.; Overvelde, J. T. B.; Weaver, J. C.; Mosadegh, B.; Bertoldi, K.; Whitesides, G. M.; Wood, R. J. A 3D-Printed, Functionally Graded Soft Robot Powered by Combustion. *Science (1979)* **2015**, *349* (6244), 161–165. https://doi.org/10.1126/science.aab0129.

(15) Autore, M.; Li, P.; Dolado, I.; Alfaro-Mozaz, F. J.; Esteban, R.; Atxabal, A.; Casanova, F.; Hueso, L. E.; Alonso-González, P.; Aizpurua, J.; Nikitin, A. Y.; Vélez, S.; Hillenbrand, R. Boron Nitride Nanoresonators for Phonon-Enhanced Molecular Vibrational Spectroscopy at the Strong Coupling Limit. *Light Sci Appl* **2018**, *7* (4). https://doi.org/10.1038/lsa.2017.172.

(16) Le, F.; Brandl, D. W.; Urzhumov, Y. A.; Wang, H.; Kundu, J.; Halas, N. J.; Aizpurua, J.; Nordlander, P. Metallic Nanoparticle Arrays: A Common Substrate for Both Surface-Enhanced Raman Scattering and Surface-Enhanced Infrared Absorption. *ACS Nano* **2008**, *2* (4), 707–718. https://doi.org/10.1021/nn800047e.

(17) Neubrech, F.; Huck, C.; Weber, K.; Pucci, A.; Giessen, H. Surface-Enhanced Infrared Spectroscopy Using Resonant Nanoantennas. *Chem Rev* **2017**, *117* (7), 5110–5145. https://doi.org/10.1021/acs.chemrev.6b00743.

(18) Ataka, K.; Stripp, S. T.; Heberle, J. Surface-Enhanced Infrared Absorption Spectroscopy (SEIRAS) to Probe Monolayers of Membrane Proteins. *Biochim Biophys Acta Biomembr* **2013**, *1828* (10), 2283–2293. https://doi.org/10.1016/j.bbamem.2013.04.026.

(19) Neuman, T.; Alonso-González, P.; Garcia-Etxarri, A.; Schnell, M.; Hillenbrand, R.; Aizpurua, J. Mapping the near Fields of Plasmonic Nanoantennas by Scattering-Type Scanning near-Field Optical Microscopy. *Laser Photon Rev* **2015**, *9* (6), 637–649. https://doi.org/10.1002/lpor.201500031.

(20) Olmon, R. L.; Krenz, P. M.; Jones, A. C.; Boreman, G. D.; Raschke, M. B. Near-Field Imaging of Optical Antenna Modes in the Mid-Infrared. *Opt Express* **2008**, *16* (25), 20295–20305. https://doi.org/10.1364/OE.16.020295.

(21) Alonso-González, P.; Albella, P.; Neubrech, F.; Huck, C.; Chen, J.; Golmar, F.; Casanova, F.; Hueso, L. E.; Pucci, A.; Aizpurua, J.; Hillenbrand, R. Experimental Verification of the Spectral Shift between Near- and Far-Field Peak Intensities of Plasmonic Infrared Nanoantennas. *Phys Rev Lett* **2013**, *110* (20). https://doi.org/10.1103/PhysRevLett.110.203902.

(22) Neubrech, F.; Weber, D.; Lovrincic, R.; Pucci, A.; Lopes, M.; Toury, T.; De La Chapelle, M. L. Resonances of Individual Lithographic Gold Nanowires in the Infrared. *Appl Phys Lett* **2008**, *93* (16). https://doi.org/10.1063/1.3003870.

(23) Pereira, L.; Mondal, P. K.; Alves, M. Aromatic Amines Sources, Environmental Impact and Remediation. In *Pollutants in Buildings, Water and Living Organisms*; 2015. https://doi.org/10.1007/978-3-319-19276-5_7.

(24) Kirkok, S. K.; Kibet, J. K.; Kinyanjui, T. K.; Okanga, F. I. A Review of Persistent Organic Pollutants: Dioxins, Furans, and Their Associated Nitrogenated Analogues. *SN Appl Sci* **2020**, *2* (10). https://doi.org/10.1007/s42452-020-03551-y.

(25) Jia, C.; Batterman, S. A Critical Review of Naphthalene Sources and Exposures Relevant to Indoor and Outdoor Air. *Int J Environ Res Public Health* **2010**, *7* (7). https://doi.org/10.3390/ijerph7072903.

(26) Donohue J M. *Health Effects Support Document for Naphthalene*; 2003.

(27) Price, C. C.; Ciskowski, J. M. The Alkylation of Naphthalene with Alcohols and Boron Fluoride. The Mechanism of the Reaction. *J Am Chem Soc* **1938**, *60* (10). https://doi.org/10.1021/ja01277a062.

(28) Hourani, M. J.; Hessell, T.; Abramshe, R. A.; Liang, J. Alkylated Naphthalenes as High-Performance Synthetic Lubricating Fluids. *Tribology Transactions* **2007**, *50* (1). https://doi.org/10.1080/10402000601105581.

(29) Phthalic Anhydride: Worldwide Markets to 2023. *Focus on Catalysts*. 2019. https://doi.org/10.1016/j.focat.2019.02.014.

(30) Howard, P. H. *Handbook of Environmental Fate and Exposure Data for Organic Chemicals*; 1991. https://doi.org/10.1201/9780203719305.

(31) Buckpitt, A.; Boland, B.; Isbell, M.; Morin, D.; Shultz, M.; Baldwin, R.; Chan, K.; Karlsson, A.; Lin, C.; Taff, A.; West, J.; Fanucchi, M.; Van Winkle, L.; Plopper, C. Naphthalene-Induced Respiratory Tract Toxicity: Metabolic Mechanisms of Toxicity. *Drug Metab Rev* **2002**, *34* (4). https://doi.org/10.1081/DMR-120015694.

(32) Lee, B.-D.; Hosomi, M. Ethanol Washing of PAH-Contaminated Soil and Fenton Oxidation of Washing Solution. *Journal of Material Cycles and Waste Management* **2000**, *2*, 24–30. https://doi.org/10.1007/s10163-999-0012-7.

(33) Schreiner, C. A. Genetic Toxicity of Naphthalene: A Review. *Journal of Toxicology and Environmental Health - Part B: Critical Reviews*. March 2003, pp 161–183. https://doi.org/10.1080/10937400306472.

(34) Bogen, K. T.; Benson, J. M.; Yost, G. S.; Morris, J. B.; Dahl, A. R.; Clewell, H. J.; Krishnan, K.; Omiecinski, C. J. Naphthalene Metabolism in Relation to Target Tissue Anatomy, Physiology, Cytotoxicity and Tumorigenic Mechanism of Action. *Regulatory Toxicology and Pharmacology* **2008**, *51* (2 SUPLL), 27–36. https://doi.org/10.1016/j.yrtph.2007.10.018.

(35) *Toxicology and Carcinogenesis Studies of Naphthalene (CAS No. 91-20-3) in B6C3F1 Mice (Inhalation Studies)*; 1992.

(36) IARC Working Group on the Evaluation of Carcinogenic Risks to Humans.; World Health Organization.; International Agency for Research on Cancer. *Cobalt in Hard Metals and Cobalt Sulfate, Gallium Arsenide, Indium Phosphide, and Vanadium Pentoxide*; International Agency for Research on Cancer, 2006.

(37) Yost, E. E.; Galizia, A.; Kapraun, D. F.; Persad, A. S.; Vulimiri, S. V.; Angrish, M.; Lee, J. S.; Druwe, I. L. Health Effects of Naphthalene Exposure: A Systematic Evidence Map and Analysis of Potential Considerations for Dose–Response Evaluation. *Environmental Health Perspectives*. Public Health Services, US Dept of Health and Human Services July 1, 2021. https://doi.org/10.1289/EHP7381.

(38) of Environmental Health Hazard Assessment, O. *Long-Term Health Effects of Exposure to Naphthalene Background and Status of Naphthalene as a Toxic Air Contaminant and Potential*.

(39) Aherne, D.; Ledwith, D. M.; Gara, M.; Kelly, J. M. Optical Properties and Growth Aspects of Silver Nanoprisms Produced by a Highly Reproducible and Rapid Synthesis at Room Temperature. *Adv Funct Mater* **2008**, *18* (14), 2005–2016. https://doi.org/10.1002/adfm.200800233.

(40) Hoppe, C. E.; Lazzari, M.; Pardiñas-Blanco, I.; López-Quintela, M. A. One-Step Synthesis of Gold and Silver Hydrosols Using Poly(N-Vinyl-2- Pyrrolidone) as a Reducing Agent. *Langmuir* **2006**, *22* (16), 7027–7034. https://doi.org/10.1021/la060885d.

(41) Sun, Y.; Xia, Y. Mechanistic Study on the Replacement Reaction between Silver Nanostructures and Chloroauric Acid in Aqueous Medium. *J Am Chem Soc* **2004**, *126* (12), 3892–3901. https://doi.org/10.1021/ja039734c.

(42) Ren, M.; Jin, Y.; Chen, W.; Huang, W. Rich Capping Ligand-Ag Colloid Interactions. *Journal of Physical Chemistry C* **2015**, *119* (49), 27588–27593. https://doi.org/10.1021/acs.jpcc.5b09958.

(43) Yugang Sun; Younan Xia. Shape-Controlled Synthesis of Gold and Silver Nanoparticles. *Science (1979)* **2002**, *298* (5061), 2179–2179. https://doi.org/10.1126/science.1077229.

(44) Kedia, A.; Kumar, P. S. Solvent-Adaptable Poly(Vinylpyrrolidone) Binding Induced Anisotropic Shape Control of Gold Nanostructures. *Journal of Physical Chemistry C* **2012**, *116* (44), 23721–23728. https://doi.org/10.1021/jp306952d.

(45) Sotnichuk, S. V.; Skryabina, O. V.; Shishkin, A. G.; Bakurskiy, S. V.; Kupriyanov, M. Y.; Stolyarov, V. S.; Napolskii, K. S. Long Single Au Nanowires in Nb/Au/Nb Josephson Junctions: Implications for Superconducting Microelectronics. *ACS Appl Nano Mater* **2022**, *5* (11), 17059–17066. https://doi.org/10.1021/acsanm.2c03837.

(46) Zhang, D.; You, H.; Zhang, L.; Fang, J. Facile Surface Modification of Mesoporous Au Nanoparticles for Highly Sensitive SERS Detection. *Anal Chem* **2020**, *92* (23), 15379–15387. https://doi.org/10.1021/acs.analchem.0c02781.

(47) Saidi, W. A.; Feng, H.; Fichthorn, K. A. Binding of Polyvinylpyrrolidone to Ag Surfaces: Insight into a Structure-Directing Agent from Dispersion-Corrected Density Functional Theory. *Journal of Physical Chemistry C* **2013**, *117* (2), 1163–1171. https://doi.org/10.1021/jp309867n.

(48) Kyrychenko, A.; Korsun, O. M.; Gubin, I. I.; Kovalenko, S. M.; Kalugin, O. N. Atomistic Simulations of Coating of Silver Nanoparticles with Poly(Vinylpyrrolidone) Oligomers: Effect of Oligomer Chain

Length. *Journal of Physical Chemistry C* **2015**, *119* (14), 7888–7899. https://doi.org/10.1021/jp510369a.

(49) Tejamaya, M.; Römer, I.; Merrifield, R. C.; Lead, J. R. Stability of Citrate, PVP, and PEG Coated Silver Nanoparticles in Ecotoxicology Media. *Environ Sci Technol* **2012**, *46* (13), 7011–7017. https://doi.org/10.1021/es2038596.

(50) Al-Saidi, W. A.; Feng, H.; Fichthorn, K. A. Adsorption of Polyvinylpyrrolidone on Ag Surfaces: Insight into a Structure-Directing Agent. *Nano Lett* **2012**, *12* (2), 997–1001. https://doi.org/10.1021/nl2041113.

(51) Bonet, F.; Tekaia-elhsissen, K.; Vijaya Sarathy, K. Study of Interaction of Ethylene Glycol/PVP Phase on Noble Metal Powders Prepared by Polyol Process. *Bulletin of Materials Science* **2000**, *23* (3), 165–168. https://doi.org/10.1007/BF02719903.

(52) Huang, H. H.; Ni, X. P.; Loy, G. L.; Chew, C. H.; Tan, K. L.; Loh, F. C.; Deng, J. F.; Xu, G. Q. Photochemical Formation of Silver Nanoparticles in Poly(N-Vinylpyrrolidone). *Langmuir* **1996**, *12* (4), 909–912. https://doi.org/10.1021/la950435d.

(53) Mdluli, P. S.; Sosibo, N. M.; Revaprasadu, N.; Karamanis, P.; Leszczynski, J. Surface Enhanced Raman Spectroscopy (SERS) and Density Functional Theory (DFT) Study for Understanding the Regioselective Adsorption of Pyrrolidinone on the Surface of Silver and Gold Colloids. *J Mol Struct* **2009**, *935* (1–3), 32–38. https://doi.org/10.1016/j.molstruc.2009.06.039.

(54) Zhang, Z.; Zhao, B.; Hu, L. PVP Protective Mechanism of Ultrafine Silver Powder Synthesized by Chemical Reduction Processes. *J Solid State Chem* **1996**, *121*, 105–110. https://doi.org/10.1006/jssc.1996.0015.

(55) Gao, Y.; Jiang, P.; Liu, D. F.; Yuan, H. J.; Yan, X. Q.; Zhou, Z. P.; Wang, J. X.; Song, L.; Liu, L. F.; Zhou, W. Y.; Wang, G.; Wang, C. Y.; Xie, S. S.; Zhang, J. M.; Shen, D. Y. Evidence for the Monolayer Assembly of Poly(Vinylpyrrolidone) on the Surfaces of Silver Nanowires. *Journal of Physical Chemistry B* **2004**, *108* (34), 12877–12881. https://doi.org/10.1021/jp037116c.

(56) Higa, O. Z.; Rogero, S. O.; Machado, L. D. B.; Mathor, M. B.; Lugão, A. B. Biocompatibility Study for PVP Wound Dressing Obtained in Different Conditions. *Radiation Physics and Chemistry* **1999**, *55* (5–6), 705–707. https://doi.org/10.1016/S0969-806X(99)00215-7.

(57) Greulich, C.; Kittler, S.; Epple, M.; Muhr, G.; Köller, M. Studies on the Biocompatibility and the Interaction of Silver Nanoparticles with Human Mesenchymal Stem Cells (HMSCs). *Langenbecks Arch Surg* **2009**, *394* (3), 495–502. https://doi.org/10.1007/s00423-009-0472-1.

(58) Gupta, G.; Hamawandi, B.; Sheward, D. J.; Murrell, B.; Hanke, L.; McInerney, G.; Blosi, M.; Costa, A. L.; Toprak, M. S.; Fadeel, B. Silver Nanoparticles with Excellent Biocompatibility Block Pseudotyped SARS-CoV-2 in the Presence of Lung Surfactant. *Front Bioeng Biotechnol* **2022**, *10*. https://doi.org/10.3389/fbioe.2022.1083232.

(59) Gliga, A. R.; Skoglund, S.; Odnevall Wallinder, I.; Fadeel, B.; Karlsson, H. L. Size-Dependent Cytotoxicity of Silver Nanoparticles in Human Lung Cells: The Role of Cellular Uptake, Agglomeration and Ag Release. *Part Fibre Toxicol* **2014**, *11* (1). https://doi.org/10.1186/1743-8977-11-11.

(60) Wang, X.; Ji, Z.; Chang, C. H.; Zhang, H.; Wang, M.; Liao, Y. P.; Lin, S.; Meng, H.; Li, R.; Sun, B.; Winkle, L. Van; Pinkerton, K. E.; Zink, J. I.; Xia, T.; Nel, A. E. Use of Coated Silver Nanoparticles to Understand

the Relationship of Particle Dissolution and Bioavailability to Cell and Lung Toxicological Potential. *Small* **2014**, *10* (2), 385–398. https://doi.org/10.1002/smll.201301597.

(61) Zhang, Q.; Li, N.; Goebl, J.; Lu, Z.; Yin, Y. A Systematic Study of the Synthesis of Silver Nanoplates: Is Citrate a "Magic" Reagent? *J Am Chem Soc* **2011**, *133* (46), 18931–18939. https://doi.org/10.1021/ja2080345.

(62) Munechika, K.; Smith, J. M.; Chen, Y.; Ginger, D. S. Plasmon Line Widths of Single Silver Nanoprisms as a Function of Particle Size and Plasmon Peak Position. *Journal of Physical Chemistry C* **2007**, *111* (51), 18906–18911. https://doi.org/10.1021/jp076099e.

(63) Wu, C.; Zhou, X.; Wei, J. Localized Surface Plasmon Resonance of Silver Nanotriangles Synthesized by a Versatile Solution Reaction. *Nanoscale Res Lett* **2015**, *10* (1). https://doi.org/10.1186/s11671-015-1058-1.

(64) Kelly, K. L.; Coronado, E.; Zhao, L. L.; Schatz, G. C. The Optical Properties of Metal Nanoparticles: The Influence of Size, Shape, and Dielectric Environment. *Journal of Physical Chemistry B* **2003**, *107* (3), 668–677. https://doi.org/10.1021/jp026731y.

(65) Jin, R.; Cao, Y.; Mirkin, C. A.; Kelly, K. L.; Schatz, G. C.; Zheng, J. G. Photoinduced Conversion of Silver Nanospheres to Nanoprisms. *Science (1979)* **2001**, *294* (5548), 1901–1903. https://doi.org/10.1126/science.1066541.

(66) Sun, Y.; Xia, Y. Triangular Nanoplates of Silver: Synthesis, Characterization, and Use as Sacrificial Templates For Generating Triangular Nanorings of Gold. *Advanced Materials* **2003**, *15* (9), 695–699. https://doi.org/10.1002/adma.200304652.

(67) Samanta, S.; Sarkar, P.; Pyne, S.; Sahoo, G. P.; Misra, A. Synthesis of Silver Nanodiscs and Triangular Nanoplates in PVP Matrix: Photophysical Study and Simulation of UV–Vis Extinction Spectra Using DDA Method. *J Mol Liq* **2012**, *165*, 21–26. https://doi.org/10.1016/j.molliq.2011.10.002.

(68) Sherry, L. J.; Jin, R.; Mirkin, C. A.; Schatz, G. C.; Van Duyne, R. P. Localized Surface Plasmon Resonance Spectroscopy of Single Silver Triangular Nanoprisms. *Nano Lett* **2006**, *6* (9), 2060–2065. https://doi.org/10.1021/nl061286u.

(69) Zhang, Q.; Li, N.; Goebl, J.; Lu, Z.; Yin, Y. A Systematic Study of the Synthesis of Silver Nanoplates: Is Citrate a "Magic" Reagent? *J Am Chem Soc* **2011**, *133* (46), 18931–18939. https://doi.org/10.1021/ja2080345.

(70) Lindad. Crystalline Fiber Optics. In *Infrared Fibers and Their Applications*; SPIE: 1000 20th Street, Bellingham, WA 98227-0010 USA; pp 105–137. https://doi.org/10.1117/3.540899.ch6.

(71) Kazarian, S. G.; Chan, K. L. A. ATR-FTIR Spectroscopic Imaging: Recent Advances and Applications to Biological Systems. *Analyst* **2013**, *138* (7), 1940. https://doi.org/10.1039/c3an36865c.

(72) Ramer, G.; Lendl, B. Attenuated Total Reflection Fourier Transform Infrared Spectroscopy. In *Encyclopedia of Analytical Chemistry*; Wiley, 2013. https://doi.org/10.1002/9780470027318.a9287.

(73) Milosevic, M. Internal Reflection and ATR Spectroscopy. *Appl Spectrosc Rev* **2004**, *39* (3), 365–384. https://doi.org/10.1081/ASR-200030195.

(74) Jukić, M.; Sviben, I.; Zorić, Z.; Milardović, S. Effect of Polyvinylpyrrolidone on the Formation AgBr Grains in Gelatine Media. *Croatica Chemica Acta* **2012**, *85* (3), 269–276. https://doi.org/10.5562/cca1919.

(75) Chen, D.; Chen, Q.; Zhang, W.; Ge, L.; Shao, G.; Fan, B.; Lu, H.; Zhang, R.; Yang, D.; Shao, G. Freeze-Dried PVP-Ag+ Precursors to Novel AgBr/AgCl-Ag Hybrid Nanocrystals for Visible-Light-Driven Photodegradation of Organic Pollutants. *Superlattices Microstruct* **2015**, *80*, 136–150. https://doi.org/10.1016/j.spmi.2015.01.004.

(76) 2216-9980-1-CE.

(77) Pueskuelev, G.; Zarnorechki, O.; Kabaivanov, Vi. On the Influence of Polyvinylpyrrolidone (PVP) during the Synthesis of Ultrafine Emulsions. *The Journal of Photographic Science* **1974**, *22* (5), 235–238. https://doi.org/10.1080/00223638.1974.11737785.

(78) Constantinidis, P.; Schmitt, H. C.; Fischer, I.; Yan, B.; Rijs, A. M. Formation of Polycyclic Aromatic Hydrocarbons from Bimolecular Reactions of Phenyl Radicals at High Temperatures. *Physical Chemistry Chemical Physics* **2015**, *17* (43), 29064–29071. https://doi.org/10.1039/c5cp05354d.

(79) Scharko, N. K.; Oeck, A. M.; Tonkyn, R. G.; Baker, S. P.; Lincoln, E. N.; Chong, J.; Corcoran, B. M.; Burke, G. M.; Weise, D. R.; Myers, T. L.; Banach, C. A.; Griffith, D. W. T.; Johnson, T. J. Identification of Gas-Phase Pyrolysis Products in a Prescribed Fire: First Detections Using Infrared Spectroscopy for Naphthalene, Methyl Nitrite, Allene, Acrolein and Acetaldehyde. *Atmos Meas Tech* **2019**, *12* (1), 763–776. https://doi.org/10.5194/amt-12-763-2019.

(80) Lemmens, A. K.; Ferrari, P.; Loru, D.; Batra, G.; Steber, A. L.; Redlich, B.; Schnell, M.; Martinez-Haya, B. Wetting of a Hydrophobic Surface: Far-IR Action Spectroscopy and Dynamics of Microhydrated Naphthalene. *Journal of Physical Chemistry Letters* **2023**, *14* (48), 10794–10802. https://doi.org/10.1021/acs.jpclett.3c02854.

(81) Hudgins, D. M.; Sandford, S. A.; Allamandola, L. J. Infrared Spectroscopy of Polycyclic Aromatic Hydrocarbon Cations. 1. Matrix-Isolated Naphthalene and Perdeuterated Naphthalene. *J Phys Chem* **1994**, *98* (16), 4243–4253. https://doi.org/10.1021/j100067a008.

(82) Hudgins, D. M.; Sandford, S. A. Infrared Spectroscopy of Matrix Isolated Polycyclic Aromatic Hydrocarbons. 1. PAHs Containing Two to Four Rings. *J Phys Chem A* **1998**, *102* (2), 329–343. https://doi.org/10.1021/jp9834816.

(83) Szczepanski, J.; Roser, D.; Personette, W.; Eyring, M.; Pellow, R.; Vala, M. Infrared Spectrum of Matrix-Isolated Naphthalene Radical Cation. *J Phys Chem* **1992**, *96* (20), 7876–7881. https://doi.org/10.1021/j100199a010.

(84) Suthan, T.; Rajesh, N. P.; Dhanaraj, P. V.; Mahadevan, C. K. Growth and Characterization of Naphthalene Single Crystals Grown by Modified Vertical Bridgman Method. *Spectrochim Acta A Mol Biomol Spectrosc* **2010**, *75* (1), 69–73. https://doi.org/10.1016/j.saa.2009.09.041.

(85) Gurusamy, S.; Krishnaveni, K.; Sankarganesh, M.; Sathish, V.; Thanasekaran, P.; Mathavan, A. Multiple Target Detection and Binding Properties of Naphthalene-Derived Schiff-Base Chemosensor. *J Mol Liq* **2021**, *325*. https://doi.org/10.1016/j.molliq.2020.115190.

(86) Sandford, S. A.; Bernstein, M. P.; Allamandola, L. J. The Mid-Infrared Laboratory Spectra of Naphthalene ($C_{10}H_8$) in Solid H_2O. *Astrophys J* **2004**, *607* (1), 346–360. https://doi.org/10.1086/383461.

(87) Heath, C.; Myers, M.; Pejcic, B. The Effect of Pressure and Temperature on Mid-Infrared Sensing of Dissolved Hydrocarbons in Water. *Anal Chem* **2017**, *89* (24), 13391–13397. https://doi.org/10.1021/acs.analchem.7b03623.

(88) Shiu, W. Y.; Bobra, M.; Bobra, A. M.; Maijanen, A.; Suntio, L.; Mackay, D. The Water Solubility of Crude Oils and Petroleum Products. *Oil and Chemical Pollution* **1990**, *7* (1), 57–84. https://doi.org/10.1016/S0269-8579(05)80034-6.

(89) Page, C. A.; Bonner, J. S.; Sumner, P. L.; Autenrieth, R. L. Solubility of Petroleum Hydrocarbons in Oil/Water Systems. *Mar Chem* **2000**, *70* (1–3), 79–87. https://doi.org/10.1016/S0304-4203(00)00016-5.

(90) Berryman, P. J.; Faux, D. A.; Dunstan, D. J. Solvation Pressure in Ethanol by Molecular Dynamics Simulations. *Phys Rev B Condens Matter Mater Phys* **2007**, *76* (10). https://doi.org/10.1103/PhysRevB.76.104303.

(91) Perakis, F.; De Marco, L.; Shalit, A.; Tang, F.; Kann, Z. R.; Kühne, T. D.; Torre, R.; Bonn, M.; Nagata, Y. Vibrational Spectroscopy and Dynamics of Water. *Chem Rev* **2016**, *116* (13), 7590–7607. https://doi.org/10.1021/acs.chemrev.5b00640.

(92) Verma, P. K.; Kundu, A.; Puretz, M. S.; Dhoonmoon, C.; Chegwidden, O. S.; Londergan, C. H.; Cho, M. The Bend+Libration Combination Band Is an Intrinsic, Collective, and Strongly Solute-Dependent Reporter on the Hydrogen Bonding Network of Liquid Water. *J Phys Chem B* **2018**, *122* (9), 2587–2599. https://doi.org/10.1021/acs.jpcb.7b09641.

(93) Ramasesha, K.; De Marco, L.; Mandal, A.; Tokmakoff, A. Water Vibrations Have Strongly Mixed Intra- and Intermolecular Character. *Nat Chem* **2013**, *5* (11), 935–940. https://doi.org/10.1038/nchem.1757.

(94) Jiang, B.; Li, M.; Bai, F.; Yu, H.; Mwenya, T.; Li, Y.; Song, D. Morphology-Controlled Synthesis of Silver Nanoparticles on the Silicon Substrate by a Facile Silver Mirror Reaction. *AIP Adv* **2013**, *3* (3). https://doi.org/10.1063/1.4794956.

(95) Li, C.; Zhang, Y.; Ye, Z.; Bell, S. E. J.; Xu, Y. Combining Surface-Accessible Ag and Au Colloidal Nanomaterials with SERS for in Situ Analysis of Molecule–Metal Interactions in Complex Solution Environments. *Nat Protoc* **2023**, *18* (9), 2717–2744. https://doi.org/10.1038/s41596-023-00851-6.

(96) Li, C.; Chen, Z.; Huang, Y.; Zhang, Y.; Li, X.; Ye, Z.; Xu, X.; Bell, S. E. J.; Xu, Y. Uncovering Strong π-Metal Interactions on Ag and Au Nanosurfaces under Ambient Conditions via in-Situ Surface-Enhanced Raman Spectroscopy. *Chem* **2022**, *8* (9), 2514–2528. https://doi.org/10.1016/j.chempr.2022.06.008.

(97) Naqvi, S. M. Z. A.; Awais, M.; Wei, Z.; Wu, J.; Raghavan, V.; Hu, J.; Khan, M. I. Chemical Processing and Waste Management Using SERS: A Nanovative Gateway for Sustainable and Robust Bioremediation for Agricultural Lands. *Biomass Convers Biorefin* **2024**. https://doi.org/10.1007/s13399-024-05433-4.

(98) Péron, O.; Rinnert, E.; Toury, T.; Lamy De La Chapelle, M.; Compère, C. Quantitative SERS Sensors for Environmental Analysis of Naphthalene. *Analyst* **2011**, *136* (5), 1018–1022. https://doi.org/10.1039/c0an00797h.

(99) Haruna, K.; Saleh, T. A.; Hossain, M. K.; Al-Saadi, A. A. Hydroxylamine Reduced Silver Colloid for Naphthalene and Phenanthrene Detection Using Surface-Enhanced Raman Spectroscopy. *Chemical Engineering Journal* **2016**, *304*, 141–148. https://doi.org/10.1016/j.cej.2016.06.050.

(100) Rekha, T. N.; Umadevi, M.; Rajkumar, B. J. M. Structural and Spectroscopic Study of Adsorption of Naphthalene on Silver. *J Mol Struct* **2015**, *1079*, 155–162. https://doi.org/10.1016/j.molstruc.2014.09.022.

(101) Rekha, T. N.; Rajkumar, B. J. M. Spectroscopic and Structural Study of Adsorption of Benzene on Silver Using DFT. *J Comput Electron* **2016**, *15* (3), 729–740. https://doi.org/10.1007/s10825-016-0841-2.

(102) Gottfried, J. M.; Vestergaard, E. K.; Bera, P.; Campbell, C. T. Heat of Adsorption of Naphthalene on Pt(111) Measured by Adsorption Calorimetry. *Journal of Physical Chemistry B* **2006**, *110* (35), 17539–17545. https://doi.org/10.1021/jp062659i.

(103) Boukhvalov, D. W.; Zhidkov, I. S.; Kurmaev, E. Z.; Fazio, E.; Cholakh, S. O.; D'Urso, L. Atomic and Electronic Structures of Stable Linear Carbon Chains on Ag-Nanoparticles. *Carbon N Y* **2018**, *128*, 296–301. https://doi.org/10.1016/j.carbon.2017.11.044.

(104) Hibble, S. J.; Cheyne, S. M.; Hannon, A. C.; Eversfield, S. G. Beyond Bragg Scattering: The Structure of AgCN Determined from Total Neutron Diffraction. *Inorg Chem* **2002**, *41* (5), 1042–1044. https://doi.org/10.1021/ic015610u.

(105) Blom, C. E.; Altona, C. Application of Self-Consistent-Field Abinitio Calculations to Organic Molecules Ii. Scale Factor Method for the Calculation of Vibrational Frequencies from Ab Initio Force Constants: Ethane, Propane and Cyclopropane. *Mol Phys* **1976**, *31* (5), 1377–1391. https://doi.org/10.1080/00268977600101081.

(106) Tsuzuki, S.; Kaneko, T.; Sodeyama, K. Accuracy of Intermolecular Interaction Energies, Particularly Those of Hetero Atom Containing Molecules Obtained by van Der Waals DFT Calculations. *ChemistrySelect* **2023**, *8* (6). https://doi.org/10.1002/slct.202203754.

(107) Walsh, J. E.; MacCraith, B. D.; Meaney, M.; Vos, J. G.; Regan, F.; Lancia, A.; Artjushenko, S. Sensing of Chlorinated Hydrocarbons and Pesticides in Water Using Polymer Coated Mid-Infrared Optical Fibres. *Analyst* **1996**, *121* (6), 789. https://doi.org/10.1039/an9962100789.

(108) Lu, R.; Li, W.-W.; Mizaikoff, B.; Katzir, A.; Raichlin, Y.; Sheng, G.-P.; Yu, H.-Q. High-Sensitivity Infrared Attenuated Total Reflectance Sensors for in Situ Multicomponent Detection of Volatile Organic Compounds in Water. *Nat Protoc* **2016**, *11* (2), 377–386. https://doi.org/10.1038/nprot.2016.013.

(109) Zhang, D.; Hao, R.; Zhang, L.; You, H.; Fang, J. Ratiometric Sensing of Polycyclic Aromatic Hydrocarbons Using Capturing Ligand Functionalized Mesoporous Au Nanoparticles as a Surface-Enhanced Raman Scattering Substrate. *Langmuir* **2020**, *36* (38), 11366–11373. https://doi.org/10.1021/acs.langmuir.0c02271.

Research Article | Vol. 12, No. 1 / 1 Jan 2022 / Optical Materials Express 34
Optical Materials EXPRESS

Microstructuring of the end-surface for silver halide polycrystalline fibers to suppress Fresnel reflection

Sonata Adomavičiūtė-Grabusovė,[1,2] Jonas Hinkel,[2,3] Iskander Usenov,[2,4] Alexander S. Novikov,[2,4,*] Tatiana Sakharova,[2] Torsten Döhler,[3] Ute Geißler,[3] Elena Feliksberger,[2] and Viacheslav Artyushenko[2]

[1]Institute of Chemical Physics, Vilnius University, Sauletekio av. 3, LT- 10257 Vilnius, Lithuania
[2]Art photonics GmbH, Rudower Chaussee 46, 12489 Berlin, Germany
[3]Technical University of Applied Science Wildau, Hochschulring 1, 15745 Wildau, Germany
[4]Technische Universität Berlin, Institute of Optics and Atomic Physics, Straße des 17. Juni 135, 10623 Berlin, Germany
*an@artphotonics.de

Abstract: Silver halide polycrystalline infrared fibers (PIR) have unique properties such as excellent transmittance in the spectral range from 3 to 17 μm, while also being highly flexible, non-toxic, and non-hygroscopic. They are used in industry and medicine for CO_2-laser power delivery, flexible infrared imaging, and remote process spectroscopy. While PIR fibers possess a quite low attenuation (0.1-0.5 dB/m) in the 8-12 μm range, their total transmittance is limited by significant Fresnel reflections at the fiber end faces due to the high refractive index of silver halide (>2.1). Functionalization of these surfaces with specially designed Anti-Reflective Microstructures (ARMs) enables a striking enhancement of fiber transmittance. In this work, direct imprinting (or embossing) of microstructures to fiber ends and their profiling with a microstructured knife was applied to fabricate such ARMs. The resulting two-dimensional Moth-eye microstructures and one-dimensional microgrooves at the PIR-fiber ends enable to an increase of fiber transmittance in a broadband range of (5-17 μm) as well as to reach up to 20% improvement for PIR-fiber laser cables used for power delivery of CO_2-lasers at 10.6 μm.

1. Introduction

Polycrystalline infrared (PIR) fibers made by extrusion from solid solutions of silver halides ($AgCl_{1-x}Br_x$) possess excellent transmission values in the spectral range from 3 to 17 μm [1,2]. The applications for PIR fibers include flexible power delivery for CO, CO_2 and quantum cascade laser systems [3–5] in addition to mid-infrared (mid-IR) spectroscopy [2], flexible infrared imaging [6,7], and pyrometry [8,9].

While PIR fibers have low intrinsic losses in the mid-IR range, Fresnel reflectance losses at the fiber ends significantly reduce overall transmission due to the high-refractive index contrast between the fiber material ($n_{fiber} \approx 2.15$ for infrared region) and air ($n_{air} = 1$). Data on the refractive index dispersion and the attenuation for AgClBr solid solutions are scarce and in the case of the refractive index not fully consistent (e.g. compare the summarized data in [10] with [11]). Most probably, both depend on the material manufacturing process to some extent. In this paper, we estimated the refractive index dispersion for $AgCl_{0.25}Br_{0.75}$ and $AgCl_{0.5}Br_{0.5}$ compositions used as core and clad of PIR fibers, respectively. This data were used to calculate the optical properties of PIR fibers in the mid-IR range. The refractive index of 2.15 for PIR fibers at wavelengths of 3-16 μm corresponds to Fresnel reflection losses of approximately 13% from one surface. Thus about 25% Fresnel reflection at two surfaces of PIR fiber piece notably

#439904 https://doi.org/10.1364/OME.439904
Journal © 2022 Received 11 Aug 2021; revised 24 Oct 2021; accepted 23 Nov 2021; published 3 Dec 2021

Optical Materials EXPRESS

impede high-power delivery for laser radiation. For complex systems that contain multiple PIR fibers, this value is significantly higher and can be estimated as $1 - (1 - R)^k$, where R is a Fresnel coefficient of power reflectance and k is the number of interfaces. For example, PIR fibers are the main component in Attenuated Total Reflectance (ATR)-probes that are used for real-time reaction monitoring in the Chemical, Petrochemical, Atomic, Biopharmaceutical and Food industries [12,13]. ATR probes consist of at least two fibers and thus four interfaces that result in 43% power losses due to Fresnel reflection. Eliminating or reducing these losses would result in a significantly increased signal to noise ratio and improved sensitivity of the probe and thus the whole spectroscopic system. Therefore, improving single-surface transmittance for PIR fibers is very important, especially for laser power delivery and spectroscopic systems.

There are different methods of surface modification to reduce Fresnel reflection losses, and the most used one is thin film coating [14–16]. Despite being the most frequently implemented on various fiber materials and for numerous applications, the anti-reflection thin film shows some drawbacks. Insufficiently wide spectral range for spectroscopy applications and low laser induced threshold for laser optics applications limit the use of fibers treated with anti-reflection coating [17–19]. Moreover, in the case of high-power laser radiation, differences in thermal expansion coefficients of the fiber core, cladding and coating material can lead to cracks in the coating [18]. This, together with the high refractive index of AgClBr fiber, makes the choice of coating material difficult. In addition, the sensitivity of AgClBr material to the heat exposure (above 140 °C) and UV irradiation also limits the number of suitable coating techniques [10]. Furthermore, the softness of the AgClBr makes polishing impossible and the plasticity of the AgClBr material prevents perfect cleavage, at the same time a slicing technique used to prepare the fiber surface still results in non-perfect flatness which leads to a poor coating quality. Nevertheless, there are some examples of using anti-reflection coatings for silver halide fibers in literature [20–22].

An entirely different approach to the reduction of Fresnel reflection is the creation of anti-reflective microstructures (ARMs). The difference from antireflection coating approach is that an effective refractive index at the fiber surface is created by a sub-wavelength profiled structure [15,23,24]. The best known of the profiled anti-reflective structures is named after its biomimicry, the “moth’s eye". These nano-textures create an effective light trap, which theoretically reduces the reflection down to 0.1% [25]. This light trapping effect also occurs in the short wavelength range, where the period of the structure is greater than the wavelength [10]. Profiled anti-reflection structures have some advantages, in particular, they can be made of the substrate material and therefore have a higher mechanical strength and a higher laser-induced damage threshold [26]. They can be designed for a broad spectral and angular range [27]. There are a number of techniques to create ARMs on the optics, e.g. lithography [28,29], laser ablation [29,30], etching [31], molding [32–34], etc. [24,35]. Not all of them are suitable in our case for PIR fiber end faces due to the reasons discussed before. However, the most straightforward and simply implemented ones are a direct imprinting (in some cases also called embossing or stamping), and profiling with a microstructured knife (also called a Special Microstructure Anti-Reflection Treatment (SMART) in [1]). The former allows the fabrication of two-dimensional ARMs on a fiber tip via direct contact with a master plate, while the latter creates one-dimensional grooves by profiling the fiber tip. These structures gradually reduce the refractive index of the fiber surface and allow to obtain a better optical impedance match.

Here, we investigate the surface modification of the polycrystalline silver halide fiber tip using direct imprinting and profiling methods. The possibility of direct formation of ARMs at room temperature (about 22 °C) is demonstrated with respective spectral and profile characterizations. Two methods for ARM formation are demonstrated - imprinting on the PIR fiber end face using a master plate with Moth-eye structure and direct profiling with a microstructured knife that creates microgrooves.

Optical Materials EXPRESS

2. Experimental methods

2.1. Computational methods

In order to substantiate the measurements and to gain a deeper understanding of the anti-reflection performance of the produced ARMs, these structures were simulated using the finite difference frequency domain method implemented in COMSOL Multiphysics. The refractive indices used for the simulations were obtained by fitting measurement data (estimated) and a Sellmeier equation for the visible range, both published in [11].

All calculations of transmission were performed using experimental data of the microstructures. The dimensions of the microstructures on the master plate and imprinted fiber ends were measured with a three-dimensional profilometer.

2.2. Profile measurements

To measure profiles of the fiber end faces after modification, the laser confocal optical profilometer VK-X1100 from KEYENCE was used with a 100x objective (NA = 0.8, working distance of 2 mm, nominal resolution of 12 nm in height and 40 nm laterally). The original ARMs and the ones created on the fibers were measured in three randomly chosen spots in different directions obtaining at least three data points in each direction and overall at least 27 data points. Obtained data were averaged and standard deviation was calculated.

2.3. Materials

Imprinting was performed using 0.9 m long polycrystalline fibers with 900/1000 μm core/clad diameters and $AgCl_{0.25}Br_{0.75}/AgCl_{0.5}Br_{0.5}$ core/clad composition (Art Photonics, Germany). A diamond mold plate with anti-reflective Moth-eye structure (Telaztec, USA) was used as a master plate to obtain two-dimensional patterns. One-dimensional profiling was done using a special knife made from a cleaved silicon wafer with grooves. The geometry of the micro grooved one-dimensional silicon knife and two-dimensional Moth-eye microstructures was specifically optimized for high anti-reflectance performance in the range 8-12 μm.

Before usage, the master plate was cleaned from previous $AgCl_{1-x}Br_x$ fiber residues. Cleaning was performed by 15 minutes sonication in concentrated hydrochloric acid solution. After that, the master plate was rinsed with ethanol and dried with a nitrogen flow.

2.4. Imprinting of moth-eye microstructures (2D-imprinting)

Moth-eye impress is a two-dimensional (2D) microstructured surface that is embossed on the fiber end faces by using a master plate. During the imprinting experiments, the fiber was secured in the plastic tubing with the fiber ends tightened in the ferrule using a squeeze connector. This squeeze connector allows securing of the fiber inside a ferrule and prevents its movement during the imprinting process.

A setup was built for the imprinting of the Moth-eye ARMs on the fiber end (general scheme is shown in Fig. 1). In the setup, the ferrule is tightened in a special holder and the relative position between the fiber and the master plate can be changed in x, y and z directions using micrometer drives. The master plate was then pressed onto the fiber. Imprinting was performed at room temperature (about 22 °C).

2.5. Fiber end face profiling with the microstructured knife (1D-profiling)

The 1D-profiling is the creation of one-dimensional microstructures - grooves and ridges - as a result of shaving (slicing, scraping) with a profiled knife made of a cleaved silicon substrate with grooves. The microstructures on the knife surface were produced using grayscale photolithography. The geometry of these microstructures was approximately trapezoidal-shaped, with parameters,

Optical Materials EXPRESS

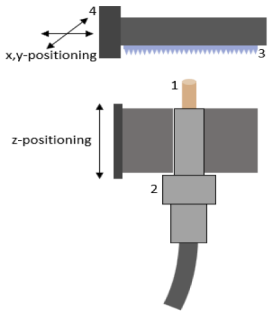

Fig. 1. General scheme of the setup for imprinting of ARMs to the fiber end. Setup parts are indicated by numbers: 1 – fiber; 2 – squeeze connector; 3 – master plate; 4 – holder for a master plate.

shown at Fig. 5. The 1D-profiling was performed by slicing the fiber tip surface with the structured knife edge at room temperature (about 22 °C).

2.6. Temperature and force measurements for 2D-imprinting

As the efficient imprinting of the Moth-eye ARMs on the fiber end depends on the mechanical properties of the material and consequently, on the temperature of the fiber material [36–38], it is necessary to understand the amount of force required for a successful result. As follows, the next setup was built to investigate the temperature influence on the required force for the imprinting process (see Fig. 2). For this, the master plate with Moth-eye structure was fixed on a hot plate (Kyntel, Peru). The fiber was tightly glued inside the ferrule and pressed to the master plate heated from the bottom. Thus the heating of the fiber occured only on the surface in physical contact with the master plate. The temperature of the master plate was measured with a thermocouple. Force was applied by pressing the load cell onto the fiber (moving in z direction) and measured with a load cell. The load cell with the signal amplifier and microcontroller was connected to the computer.

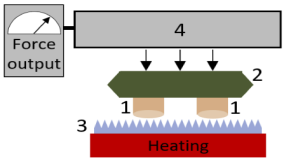

Fig. 2. Experimental setup for force versus temperature measurements. Setup parts are indicated by numbers: 1 – fiber; 2 – fiber capsule; 3 – master plate; 4 - load cell.

2.7. Transmission measurements

For the measurements of fiber performance, two optical setups were used. The first setup contained a CO_2-laser source with a maximum 10 W output power (Diamond C-40 air-cooled laser GEM 40A Circular, Coherent Inc., USA) and necessary optical components to guide the laser beam and a power meter to measure transmitted power. The second setup used a mid-IR spectrometer (Fourier transform infrared (FTIR) spectrometer ReactIR 1000 with Mercury-Cadmium-Telluride (MCT) detector) to measure changes in transmission over a broad wavelength range. The

Optical Materials EXPRESS

measurements of optical power and fiber transmission were performed on the initial fiber and afterwards the same fiber with formed ARMs on its ends. The scheme of the measurements is shown in Fig. 3. As percentages are already used to represent the fiber transmittance, here the improvement in transmittance is presented in terms of relative enhancement in fiber transmission, i.e. the ratio between the transmittance of treated and untreated fiber (also using percentages).

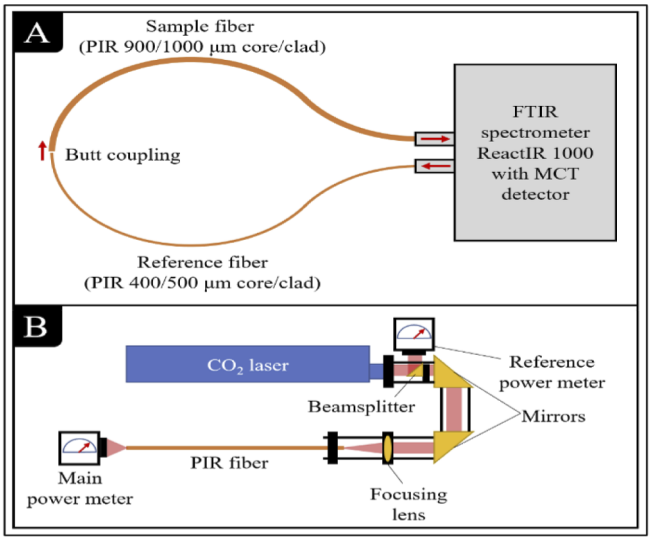

Fig. 3. Scheme of the transmission measurements using a CO_2-laser for 10.6 μm wavelength transmission (a) and a FTIR spectrometer for broad wavelength range (b).

3. Results

3.1. Imprinting of the moth-eye microstructures (2D-imprinting)

The best achieved replication of the Moth-eye microstructure, i.e. when the whole fiber end surface area was imprinted and covered by ARMs, was achieved only after the optimisation of the imprinting process. The master Moth-eye plate features a similar structure of truncated cones arranged in a hexagonal array present in the eyes of moths [39,40]. These structures are known to be anti-reflective. Depending on the height (H), period (Λ) and structure size at the top (D) and bottom (B) (Fig. 4), the anti-reflective performance can be shifted from visible light to infrared and mid-IR range [41–43]. Effectively, such structures create a gradually changing refractive index when the wavelength of incident radiation is comparably longer than the dimensions of the structure [44]. For imprinting of the ARMs onto $AgCl_{1-x}Br_x$ fibers we used cone type Moth-eye microstructures fabricated on the diamond plate. Three-dimensional optical profilometer images of the master plate (Fig. 4(a)) revealed a Λ of 3.06±0.18 μm, the D of 1.05±0.26 μm, the B of 0.6±0.4 μm. The H of Moth-eye microstructures was 1.22±0.3 μm.

After the imprinting of the master structure onto the fiber end face, the negative shape (an inversion of the master plate structure) is left behind. Nevertheless, some discrepancies from the expected inverse structure occur. This is due to mechanical properties of the material, such as stiffness, strength, viscoelasticity, toughness, viscosity, i.e. due to elastic response of the fiber material and insufficient time given for complete material flow [45,46].

Optical Materials EXPRESS

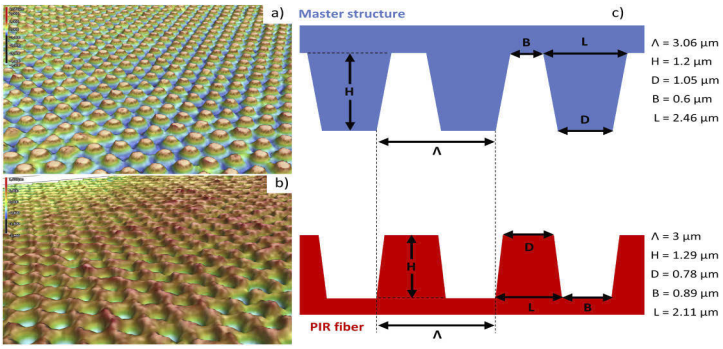

Fig. 4. The 3D profilometer images of the master plate (a) and imprinted fiber surface (b); geometrical parameters of the master plate profile and imprinted fiber end (c).

With our sample, when increase in CO_2 laser transmission by 28.6% was observed, the size D of the imprinted microstructures on the fiber was 0.78±0.16 μm (corresponding to the B of 0.6±0.4 μm on the master plate), B - 0.89±0.14 μm (corresponding to the D of 1.05±0.26 μm on the master plate), Λ was 3±0.09 μm and H increased to 1.29±0.2 μm (Fig. 4(c)). The increase in the structure height compared with the master structure is unexpected and can be attributed to the sticking of the fiber residues to the master plate after previous imprinting due to more favorable adhesion. Nevertheless, the bottom dimension of Moth-eye ARMs changed from D = 1.05±0.26 μm to 0.89±0.14 μm when imprinted. Decrease of the size D might also have occurred because of elastic deformation and incomplete imprinting.

All things considered, we expected some decrease in the structure height H due to the incomplete embossing. Because of the limited plasticity, the required time for fiber material to flow under the cavities depends on the material properties and dimensions of the master structure [47]. Nevertheless, a slight increase in structure height was observed experimentally. The size deviation between the individual protrusions and cavities might also have increased because of inhomogeneous pressure on the whole fiber surface – some areas underwent more pressure than others. However, three-dimensional profilometer data reveal apparent microstructures over the entire fiber surface (Fig. 4(b)) after imprinting.

3.2. Fiber surface profiling with a microstructured knife (1D-profiling)

One-dimensional profile of the microstructured knife and related fiber surface pattern are presented in Fig. 5. For this profile, the transmittance for CO_2-laser increased up to 24% after treatment of both fiber end faces. After the treatment, the fiber surface acquires almost the same structure geometry as the knife edge, but inverted. The resulting height of the structure on the fiber surface profile (approximately 1.75 μm) is less compared to that on the knife (2.15 μm). Also, it can be noted that the top corner of the ridges became sharper on the fiber edge, while the groove bottom width or distance between ridges became slightly larger than on the knife. This can be explained by incomplete profiling, i.e. not the whole height of the knife grooves was used.

3.3. Transmission measurements

After the 2D-imprinting of ARMs, the fiber transmission (0.9 m length, 900/1000 μm core/clad diameter) was measured in a broad spectral range using the FTIR spectrometer. After the Moth-eye 2D-imprinting (structure corresponding to Fig. 4), the fiber transmittance increased in the spectral range 5-17 μm (Fig. 6(a)) and decreased in the short wavelength range of 2-5

Optical Materials EXPRESS

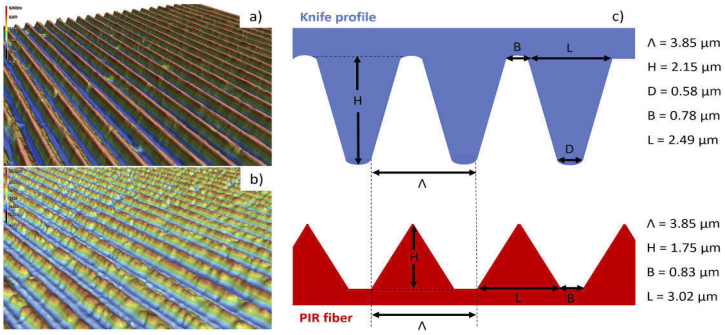

Fig. 5. The 3D profilometer images of grating on the knife edge (a) and microstructured fiber surface after slicing (b); geometrical parameters of the knife profile and fiber end structure after treating (c).

μm due to the diffraction. The transmission at 10.6 μm wavelength increased by 5% after the treatment of one fiber end surface and by 14% after both fiber end surfaces treated, resulting in total transmission increase from 60.5% to 68.8% for two surfaces being treated. Further attempts of Moth-eye imprinting enabled to achieve the transmission increase as high as 25.1% (up to 75.7% on 10.6 μm wavelength) when both fiber ends were micro-structured (shown in Fig. 6(a) - dashed line). Unfortunately, there was no possibility to measure the corresponding structures with a profilometer. An interesting observation is that after the Moth-eye treatment, the fiber end visually looked almost black (as shown in the Fig. 6 legend inlay).

The transmission increase in in 7.5 μm - 17 μm spectral range (the cut-off wavelength being approximately 7.5 μm) was observed for 1D-profiled fiber surfaces (structure corresponding to Fig. 5). The transmission at 10.6 μm increased by 22.3% from 62.7% to 76.7% after the treatment of both fiber end surfaces (Fig. 6(b)).

The effect of diffraction on the transmittance in short wavelengths range is observed experimentally for both Moth-eye imprinting and profiling of the fiber surface (Fig. 6). The cut-off wavelengths for this effect are different due to the difference of geometrical dimensions for both 1D-profile and 2D Moth-eye structures.

Fibers with 2D-imprinted ARMs were also examined by measuring their transmission with a CO_2-laser. Data on CO_2-laser transmission and FTIR measurements for 10.6 μm from several samples are summarized in Table 1.

The increase of CO_2-laser transmission is about by 25% (up to 30% in some attempts) at Moth-eye imprinting and about 19%-24% at profiling after both fiber end surfaces treated. The fiber transmittance measurements with FTIR-spectrometer show lower values due to a higher input numerical aperture [27,48], but are in a good agreement with laser transmission results.

Comparison of the 1D-profiling and 2D-imprinting treatment of the fiber shows a similar increase in the transmittance over a broad wavelength range (Fig. 7). At 10.6 μm the ratio between the transmissions of treated fiber/initial flat surface is 1.25 and 1.22 for 2D-imprinting and 1D-profiling treatment, respectively. However, with the other 2D-imprinting Moth-eye treatment attempt, the ratio reached only 1.14 (corresponds to Fig. 4). The best results correspond to a single-surface reflectance of 3% (2D-imprinted moth-eye ARM) and 4% (1D-profiling) at 10.6 μm wavelength (13% is for untreated surface).

Optical Materials EXPRESS

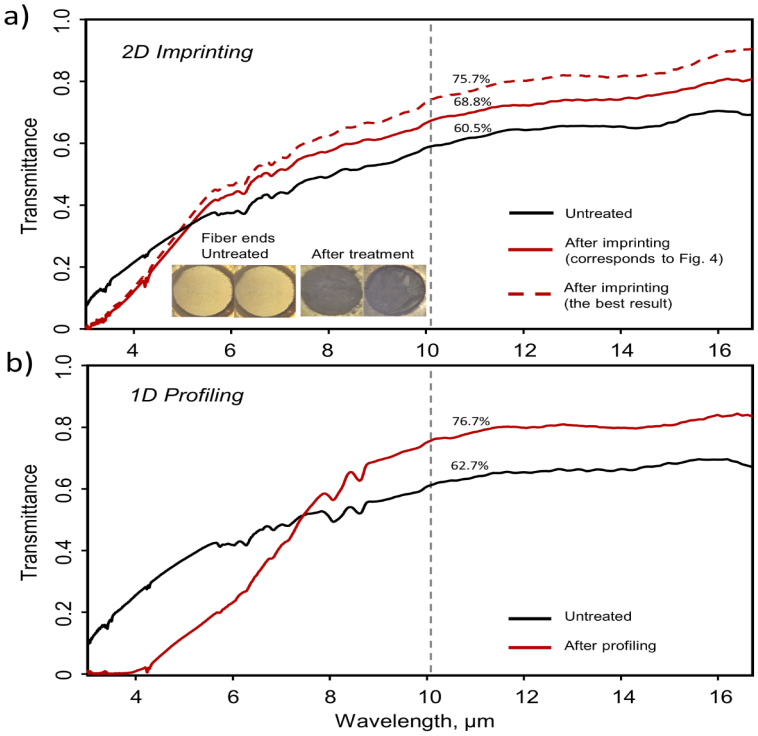

Fig. 6. The measured transmission before and after the 2D Moth-eye imprinting (a) and 1D-profiling (b). In case of Moth-eye treatment (a) dashed line indicates the best result, whereas the solid line shows the result for the structure described at Fig. 4. The legend inlay shows optical microscope pictures of both flat fiber ends (upper), one imprinted fiber end in the input (middle) and both imprinted fiber ends (bottom).

Table 1. Results of ARMs treated fiber transmission at 10.6 μm wavelength measured with CO_2-laser and FTIR spectrometer.

Sample No	Treatment type	Increase in CO_2-laser transmission, %		Transmission with both ends treated, %	
		One end treated	Both ends treated	CO_2-laser	Spectrometer
1	Non-treated	-	-	69	60.5
2	2D imprinted	14	30	90	75.7
3	2D imprinted	13	29	89	73.5
4	2D imprinted	13	29	89	74.4
5	2D imprinted	12	28	88	70.1
6	2D imprinted	10	25	86	68.8
7	2D imprinted	10	25	86	68.9
8	Non-treated	-	-	67	62.7
9	1D profiled	-	24	83	76.7
10	1D profiled	-	19	80	75.2

Optical Materials EXPRESS

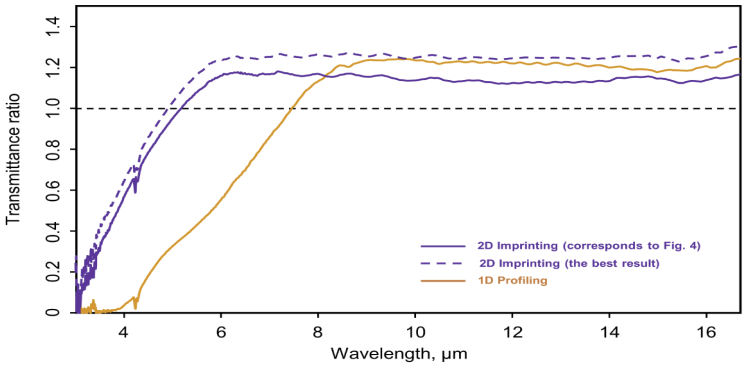

Fig. 7. Comparison of the increase in fiber transmittance ratio for 2D-imprinted Moth-eye microstructures and 1D profiled grooves on both fiber ends.

3.4. Transmission calculation

The refractive indices used for the simulations are obtained by fitting measurement data (estimated) and a Sellmeier equation for the visible range, both published in [11]. For the input function of the fit, a known Sellmeier equation for the component silver chloride, published in [49] was used (Fig. 8). In the fitted function (1) the wavelength λ is given in micrometers.

$$n_{AgCl_{0.25}:AgBr_{0.75}}(\lambda) = \sqrt{4.66 + \frac{78 \cdot 10^{-3}}{\lambda^2 - 32.4 \cdot 10^{-3}} - 1.93 \cdot 10^{-3} \cdot \lambda^2 + 4 \cdot 10^{-6} \cdot \lambda^4} \quad (1)$$

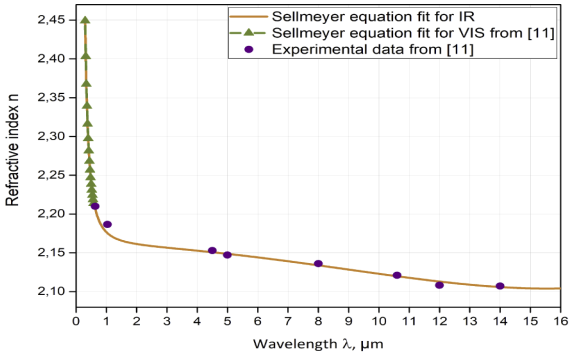

Fig. 8. Sellmeier equation fitted for PIR fiber core material using data obtained from [11] and the Sellmeier equation from [49] as an input function.

Transmission calculations were performed for Moth-eye and groove structures with geometry and sizes specified in Fig. 4 and Fig. 5. According to computational results for Moth-eye ARM treatment (2D-imprinting), increase in the transmission due to anti-reflective contribution occurs in a wide range of wavelengths from 5 μm to 16 μm (Fig. 9(a)). The reflection from the single plain air/fiber interface diminishes the transmission to ≈87% as calculated from the Fresnel

Optical Materials EXPRESS

equations. Whereas, when the ideal Moth-eye ARMs based on the mold geometry are imprinted on the plain fiber end, the single surface transmission at 10.6 μm wavelength increases to 92.5%. When the incident wavelength is close to the dimensions of an ideal Moth-eye ARM ($\Lambda \approx 3$ μm), the anti-reflective performance is not noticeable anymore. Because of this effect, the transmission of the radiation is suppressed due to the diffraction in the range of 3-5 μm. Nevertheless, the simulations based on the geometry of experimentally obtained structures after imprinting show that reduced reflection should lead to 93% transmission at 10.6 μm wavelength.

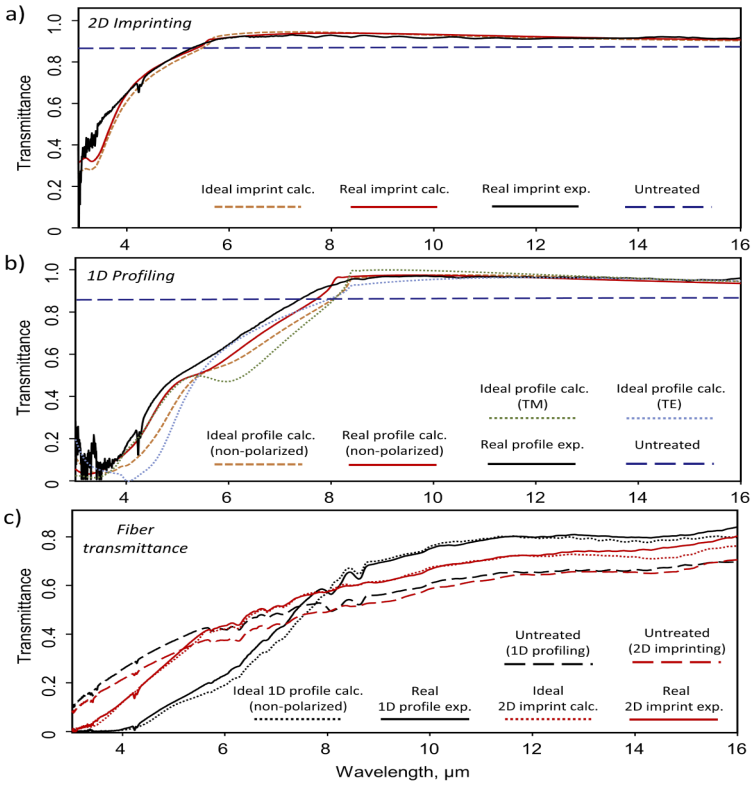

Fig. 9. Comparison between the calculated (calc.) and experimental (exp.) performances of the 1D-profiling and 2D-imprinting, in accordance with data from Fig. 4 and Fig. 5. A) Single surface transmittance of 2D-imprinted fiber tip with Moth-eye ARMs. B) Single surface transmittance of 1D-profiled fiber tip. C) Calculated and measured fiber transmittance in case of treatment of both fiber end faces. Used fibers are PIR fibers with 0.9 m length and 900/1000 μm core/clad diameters. "Ideal" imprint and profile refer to the inverted structures from the master plate and knife, respectively. "Real" imprint and profile refer to the structures measured on the profilometer.

Similar results were observed with the one-dimensional groove simulations (1D-profiling, Fig. 9(b)). A transmission of 97.4% for 10.6 μm should be achieved after a perfect treatment (when an ideal inverted structure is attained on the fiber using the knife profile described in Fig. 5). Overall, simulated transmittance for groove ARMs is slightly better than that for the

Optical Materials EXPRESS

Moth-eye ARMs, though the cut-off wavelength is higher, providing a more narrow anti-reflective range. For the groove microstructures, the high transmittance is achieved in the range 8-17 μm.

The simulated transmission of single treated fiber surface was compared with the experimental results (Fig. 9(a, b)). For this purpose, an internal attenuation from the raw transmission data of the fiber was excluded and the transmission of single ARMs treated air/fiber interface was evaluated. The obtained experimental results correspond well to the simulations. Nevertheless, transmission values observed in the short wavelength range were better than expected. Although it is not clear yet, this improved transmittance could be explained by neglected interaction between the diffracted radiation and the fiber material. Generally, the transmission losses in the polycrystalline fibers at shorter wavelengths are caused by complex interactions between the Rayleigh-Gans scattering from the micro-grains at the fiber structure and Brillouin scattering, resulting in a λ^{-2} dependency [10,25]. The possible interaction between the short wavelength radiation (approximately 6 μm and shorter) passing through the ARM treated fiber surface and the micro-grains of the fiber material could be the reason for the improved transmission in the short wavelength range observed in the experiments. Such interaction was not accounted for when experimental single ARMs were evaluated.

The transmittance of the whole 0.9 m length fiber was simulated for the cases of the ideal Moth-eye and ideal grooved ARMs obtained by imprinting/profiling the fiber, i.e. the ARMs on the fiber tips are inverted ARMs from the master plate/knife. The simulated transmittance is compared to the experimentally obtained spectra in Fig. 9(c). Experimental transmission for the used fiber with flat ends is 60.5% (in case of 2D-imprinting) - 62.7% (in case of 1D profiling) at 10.6 μm. If the Moth-eye structure obtained by imprinting would be on both fiber ends instead of the flat ends, the transmission would reach 69%. The experimentally obtained value - 68.8% is similar to the expected one. The simulated transmission for the groove ARMs obtained by profiling the fiber should also be similar to the one obtained experimentally and reach 77.9% (experimentally obtained value is 76.7%). In this way, the transmission should increase by 14% after the Moth-eye imprinting (experimentally observed increase is 14%) and by 24% after profiling both ends of the fiber (experimental increase - 22%).

3.5. Temperature and force measurements for 2D-imprinting

The 2D-imprinting described above was performed at room temperature (about 22 °C). However, it was found that the force required for imprinting the whole fiber (with 900/1000 μm core/clad diameters) surface area, i.e. with maximum surface coverage efficiency, can be reduced if the process is performed under higher temperatures. When the heated master plate gets in contact with the fiber end face, the temperature of the fiber end increases that leads to increased plasticity of the fiber material. According to our results, the force needed for imprinting of the whole fiber end area decreased from 90 N at room temperature (about 22 °C) to approximately 45 N when the master plate heated to 150-200 °C.

4. Discussion

1D-profiling and Moth-eye ARMs treatments lead to similar transmittance improvement of polycrystalline optical fiber in the spectral range 7.5 - 17 μm (see Fig. 7). The main difference is that the resulting transmission increase starts from about 5 μm for Moth-eye ARMs and from 7.5 μm for profiling treatment. The dependency of cut-off wavelength and the amount of reflected radiation on the microstructure dimensions (height, period, top and bottom width) is complex [50,51]. For the Moth-eye ordered microstructures, the height of the relief affects how much the reflectance is suppressed. But the cut-off wavelength does not depend on the height, only on the period. The reduction of the period results in a shift of the cut-off wavelength into the range of shorter wavelengths [30,44,51].

Optical Materials EXPRESS

The profilometric measurements show that the resulting geometrical dimensions of the fiber surface profile are different from the surfaces of the profiled knife edge or the moth-eye master plate. This is due to the low plasticity of the fiber material that also tends to stick to the master plate or microstructured knife during the treatment. For further improvement in replicating of ARMs on the fiber surface by embossing technique, an increase in pressure and temperature will be attempted. The higher loading at the contact of the fiber end and master plate should lead to better replication of the microstructures. Moreover, higher temperatures should soften the fiber material and allow to reduce the required force. However, PIR fibers should avoid being heated for a prolonged period of time as it leads to substantial grain growth and increased optical losses [10,26]. Thus, the embossing process will be further optimised. In case of 1D-profiling we believe that the quality of 1D-profiled surface on fiber end face is mainly determined by the silicon knife quality. Thus, for the improvement in the profiling process, the importance to the quality of silicon knives and the whole cutting arrangement should be paid.

While producing one-dimensional structures with 1D-profiling is more cost-effective and simpler, their transmittance is polarisation dependent [52,53] with accordance to our calculations. Of course, in case of non-polarised radiation (for example, in spectroscopy) this property does not produce a notable effect. The 2D-imprinting technique allows the production of 2D gratings with the advantage of polarisation-independent transmittance. This method is more advanced, requires an application of force and temperature to the master plate and needs to be done more accurately and precisely to achieve a good imprint on the fiber end face. In addition, master plates with 2D anti-reflective “moth-eye" structure are much more expensive in comparison to 1D grating used in the previous method. The contamination of the master plate with the polycrystalline fiber material is another problem which leads to reducing the quality of the resulting structure on the fiber end face. The cleaning of the master plate is possible with a method described above, however, it is difficult to get rid of all contaminants because of the fine relief of the structure.

Another significant problem during the imprinting is that usually it is very hard to cleave the fiber end face perfectly perpendicular to the fiber axis. It leads to incomplete physical contact between fiber and master plate during the embossing and results in a non-uniform covering of the ARM structure over the fiber end face.

Despite the problems described above, thermomechanical imprinting and 1D-profiling remain the most straightforward method of fabricating ARMs on the fiber end face.

5. Conclusion

Simple and straightforward methods to suppress Fresnel reflection and increase the transmittance of $AgCl_{1-x}Br_x$ fibers (in a broad spectral range and at CO_2-laser radiation wavelength, particularly) have been proposed and investigated. Both of these treatments were implemented at room temperature. The shaving of the fiber end with a profiled silicon knife produces one-dimensional anti-reflective grating. Another method is the imprinting of a two-dimensional so called Moth-eye microstructured master plate onto the fiber end face. The theoretical reducing of Fresnel reflection for two structures has been calculated, the experimental results are in a good agreement with calculated values. The transmission spectra of treated optical fibers in the spectral range from 3 μm to 17 μm show the effect of diffraction at the surface microstructure on the fiber transmission. The significant transmission increase has been measured in the spectral range from 7 to 17 μm. Measurement with CO_2-laser (10.6 μm wavelength) showed the transmission increase by 25-30% for both fiber surfaces treated. The advantage of 1D-profiling technique is the availability and relatively low cost whereas 2D-imprinting is more promising for broadband anti-reflection treatment with polarisation independence.

Disclosures. The authors declare no conflicts of interest.

Data availability. Data underlying the results presented in this paper are available from the authors upon reasonable request.

Optical Materials EXPRESS

References

1. V. Artyushenko, A. Bocharnikov, T. Sakharova, and I. Usenov, "Mid-infrared fiber optics for 1 – 18 μm range," Opt. Photonik **9**(4), 35–39 (2014).
2. A. Yuzhakova, A. Lvov, D. Salimgareev, A. Korsakov, and L. Zhukova, "Infrared silver halide fiber for medicine application," in *2020 Ural Symposium on Biomedical Engineering, Radioelectronics and Information Technology (USBEREIT)* (2020), pp. 0136–0138.
3. L. N. Butvina, A. G. Okhrimchuk, A. L. Butvina, E. M. Dianov, N. V. Lichkova, and V. N. Zagorodnev, "Low loss micro and nano structured single mode crystalline fibers for 5-15 μm," in *Advances in Optical Materials* (Optical Society of America, 2011), p. AIThD4.
4. S. Israeli and A. Katzir, "Optical losses of AgClBr crystals and fibers in the middle infrared," Opt. Mater. **33**(11), 1825–1828 (2011).
5. L. N. Butvina, E. M. Dianov, N. V. Lichkova, V. N. Zavgorodnev, and L. Kuepper, "Crystalline silver halide fibers with optical losses lower than 50 dB/km in broad IR region," in *Infrared Optical Fibers and Their Applications*, vol. 3849 M. Saad and J. A. Harrington, eds., International Society for Optics and Photonics (SPIE, 1999), pp. 181–188.
6. E. Korsakova, S. Markham, A. Mani, C. Silien, J. Bauer, S. Tofail, L. Zhukova, and A. Korsakov, "MIR imaging bundles of ordered silver halide polycrystalline fibres for thermal transmission and imaging," J. Therm. Anal. Calorim. **142**(1), 245–253 (2020).
7. S. Delbeck, B. Schmitz, A. Nabers, K. Gerwert, A. Habermehl, U. Lemmer, and H. M. Heise, "Applications of tapered flat silver halide fibers chemically modified by 12-mercaptododecanoic acid NHS ester for infrared biospectroscopy with prospects for medical diagnostics," in *Optical Fibers and Sensors for Medical Diagnostics and Treatment Applications XIX*, vol. 10872 I. Gannot, ed., International Society for Optics and Photonics (SPIE, 2019), pp. 141–151.
8. S. Sade, O. Eyal, V. Scharf, and A. Katzir, "Fiber-optic infrared radiometer for accurate temperature measurements," Appl. Opt. **41**(10), 1908–1914 (2002).
9. B. Lee, W. J. Yoo, D. H. Cho, K. W. Jang, S.-C. Chung, and G.-R. Tack, "Low-temperature radiometric measurements using a silver halide optical fiber and infrared optical devices," Opt. Rev. **14**(5), 355–357 (2007).
10. J. A. Harrington, *Infrared Fibers and their Applications* (SPIE-International Society for Optical Engineering, 2003).
11. A. S. Korsakov, D. S. Vrublevsky, A. E. Lvov, and L. V. Zhukova, "Refractive index dispersion of $AgCl_1{-}xBr_x$; $(0{\le}x{\le}1)$ and $Ag_1{-}xTl_xBr_1 - xI_x$; $(0{\le}x{\le}0.05)$," Opt. Mater. **64**, 40–46 (2017).
12. A. Bogomolov, M. Heßling, U. Wenzel, S. Princz, T. Hellmuth, M. J. B. Bernal, T. Sakharova, I. Usenov, V. Artyushenko, and H. Meyer, "Development and testing of mid-infrared sensors for in-line process monitoring in biotechnology," Sens. Actuators, B **221**, 1601–1610 (2015).
13. A. Bogomolov, "Developing multisensory approach to the optical spectral analysis," Sensors **21**(10), 3541 (2021).
14. Y. Matsuoka, S. Mathonnèire, S. Peters, and W. T. Masselink, "Broadband multilayer anti-reflection coating for mid-infrared range from 7 μm to 12 μm," Appl. Opt. **57**(7), 1645–1649 (2018).
15. H. K. Raut, V. A. Ganesh, A. S. Nair, and S. Ramakrishna, "Anti-reflective coatings: a critical, in-depth review," Energy Environ. Sci. **4**(10), 3779–3804 (2011).
16. K. C. Krogman, T. Druffel, and M. K. Sunkara, "Anti-reflective optical coatings incorporating nanoparticles," Nanotechnology **16**(7), S338–S343 (2005).
17. B. Mangote, L. Gallais, M. Commandré, M. Mende, L. Jensen, H. Ehlers, M. Jupé, D. Ristau, A. Melninkaitis, J. Mirauskas, V. Sirutkaitis, S. Kičas, T. Tolenis, and R. Drazdys, "Femtosecond laser damage resistance of oxide and mixture oxide optical coatings," Opt. Lett. **37**(9), 1478–1480 (2012).
18. A. Sincore, J. Cook, F. Tan, A. E. Halawany, A. Riggins, S. McDaniel, G. Cook, D. V. Martyshkin, V. V. Fedorov, S. B. Mirov, L. Shah, A. F. Abouraddy, M. C. Richardson, and K. L. Schepler, "High power single-mode delivery of mid-infrared sources through chalcogenide fiber," Opt. Express **26**(6), 7313–7323 (2018).
19. J. Sun, X. Cui, C. Zhang, C. Zhang, R. Ding, and Y. Xu, "A broadband antireflective coating based on a double-layer system containing mesoporous silica and nanoporous silica," J. Mater. Chem. C **3**(27), 7187–7194 (2015).
20. L. Nagli, A. German, A. Katzir, J. Tschepe, V. Prapavat, H.-G. Eberle, and G. J. Mueller, "Optical catheters based on silver halide infrared fibers," in *Medical and Fiber Optic Sensors and Delivery Systems*, vol. 2631 N. I. Croitoru, M. Miyagi, G. Orellana, A. V. Scheggi, and H. J. C. M. Sterenborg, eds., International Society for Optics and Photonics (SPIE, 1995), pp. 208–215.
21. V. N. Glebov, P. G. Leonov, A. M. Malyutin, and V. P. Yakunin, "Protective antireflection coatings for optical IR fibers based on silver halogenides," in *Seventh International Conference on Laser and Laser-Information Technologies*, vol. 4644 V. Y. Panchenko and V. S. Golubev, eds., International Society for Optics and Photonics (SPIE, 2002), pp. 363–365.
22. O. Wallner, V. G. Artjuschenko, and R. Flatscher, "Development of silver-halide single-mode fibers for modal filtering in the mid-infrared," in *New Frontiers in Stellar Interferometry*, vol. 5491 W. A. Traub, ed., International Society for Optics and Photonics (SPIE, 2004), pp. 636–646.
23. Z. Han, Z. Wang, X. Feng, B. Li, Z. Mu, J. Zhang, S. Niu, and L. Ren, "Antireflective surface inspired from biology: A review," Biosurface and Biotribology **2**(4), 137–150 (2016).
24. D. S. Hobbs and B. D. MacLeod, "Design, fabrication, and measured performance of anti-reflecting surface textures in infrared transmitting materials," in *Window and Dome Technologies and Materials IX*, vol. 5786 R. W. Tustison, ed., International Society for Optics and Photonics (SPIE, 2005), pp. 349–364.
25. J. Sanghera and I. D. Aggarwal, *Infrared Fiber Optics* (CRC Press, 1998).

Optical Materials EXPRESS

26. D. Bunimovich, S. Shalem, and A. Katzir, "Effects of thermal treatment on the infrared transmission of polycrystalline silver halide fibers," Appl. Opt. **36**(1), 285–290 (1997).
27. I. R. Lewis and H. Edwards, *Handbook of Raman Spectroscopy: From the Research Laboratory to the Process Line* (CRC press, 2001).
28. D. S. Hobbs, B. D. McLeod, A. F. Kelsey, M. A. Leclerc, and E. S. III, "Automated-interference-lithography-based systems for generation of submicron-feature size patterns," in *Micromachine Technology for Diffractive and Holographic Optics*, vol. 3879 S. H. Lee and J. A. Cox, eds., International Society for Optics and Photonics (SPIE, 1999), pp. 124–135.
29. Y. Fu, M. Soldera, W. Wang, B. Voisiat, and A. F. Lasagni, "Picosecond laser interference patterning of periodical micro-architectures on metallic molds for hot embossing," Materials **12**(20), 3409 (2019).
30. M. K. Tarabrin, A. A. Bushunov, A. A. Teslenko, T. Sakharova, J. Hinkel, I. Usenov, T. Döhler, U. Geißler, V. Artyushenko, and V. A. Lazarev, "Fabrication of an antireflection microstructure on AgClBr polycrystalline fiber by single pulse femtosecond laser ablation," Opt. Mater. Express **11**(2), 487–496 (2021).
31. D. S. Hobbs, B. D. MacLeod, A. D. Manni, and S. M. Consoles, "Pulsed laser damage resistance of nano-structured polarizers for 1064nm," in *Laser-Induced Damage in Optical Materials 2018: 50th Anniversary Conference*, vol. 10805 C. W. Carr, G. J. Exarhos, V. E. Gruzdev, D. Ristau, and M. Soileau, eds., International Society for Optics and Photonics (SPIE, 2018), pp. 159–170.
32. K. Yamada, M. Umetani, T. Tamura, Y. Tanaka, and J. Nishii, "Formation of antireflective structure on the surface of optical glass by molding," in *Advanced Fabrication Technologies for Micro/Nano Optics and Photonics*, vol. 6883 T. J. Suleski, W. V. Schoenfeld, and J. J. Wang, eds., International Society for Optics and Photonics (SPIE, 2008), pp. 23–30.
33. G. Du, Q. Yang, F. Chen, H. Liu, Z. Deng, H. Bian, S. He, J. Si, X. Meng, and X. Hou, "Direct fabrication of seamless roller molds with gapless and shaped-controlled concave microlens arrays," Opt. Lett. **37**(21), 4404–4406 (2012).
34. A. Rank, V. Lang, and A. F. Lasagni, "High-speed roll-to-roll hot embossing of micrometer and sub micrometer structures using seamless direct laser interference patterning treated sleeves," Adv. Eng. Mater. **19**(11), 1700201 (2017).
35. A. A. Bushunov, M. K. Tarabrin, and V. A. Lazarev, "Review of surface modification technologies for mid-infrared antireflection microstructures fabrication," Laser Photonics Rev. **15**(5), 2000202 (2021).
36. A. Jacobo-Martín, M. Rueda, J. J. Hernández, I. Navarro-Baena, M. A. Monclús, J. M. Molina-Aldareguia, and I. Rodríguez, "Bioinspired antireflective flexible films with optimized mechanical resistance fabricated by roll to roll thermal nanoimprint," Sci. Rep. **11**(1), 2419 (2021).
37. J. Sanghera, C. Florea, L. Busse, B. Shaw, F. Miklos, and I. Aggarwal, "Reduced Fresnel losses in chalcogenide fibers by using anti-reflective surface structures on fiber end faces," Opt. Express **18**(25), 26760–26768 (2010).
38. M. R. Lotz, C. R. Petersen, C. Markos, O. Bang, M. H. Jakobsen, and R. Taboryski, "Direct nanoimprinting of moth-eye structures in chalcogenide glass for broadband antireflection in the mid-infrared," Optica **5**(5), 557–563 (2018).
39. A. R. Parker and H. E. Townley, "Biomimetics of photonic nanostructures," Nat. Nanotechnol. **2**(6), 347–353 (2007).
40. S. Wilson and M. Hutley, "The optical properties of 'moth eye' antireflection surfaces," Opt. Acta **29**(7), 993–1009 (1982).
41. A. A. Bushunov, M. K. Tarabrin, V. A. Lazarev, V. E. Karasik, Y. V. Korostelin, M. P. Frolov, Y. K. Skasyrsky, and V. I. Kozlovsky, "Fabrication of anti-reflective microstructures on chalcogenide crystals by femtosecond laser ablation," Opt. Mater. Express **9**(4), 1689–1697 (2019).
42. D. S. Hobbs, "Laser damage threshold measurements of anti-reflection microstructures operating in the near UV and mid-infrared," *Laser-Induced Damage in Optical Materials: 2010*, vol. 7842 G. J. Exarhos, V. E. Gruzdev, J. A. Menapace, D. Ristau, and M. J. Soileau, eds., International Society for Optics and Photonics (SPIE, 2010), pp. 509–521.
43. B. D. MacLeod and D. S. Hobbs, "Long life, high performance anti-reflection treatment for HgCdTe infrared focal plane arrays," *Infrared Technology and Applications XXXIV*, vol. 6940 B. F. Andresen, G. F. Fulop, and P. R. Norton, eds., International Society for Optics and Photonics (SPIE, 2008), pp. 318–333.
44. S. A. Boden and D. M. Bagnall, *Moth-eye antireflective structures* (Springer, 2012).
45. L. Heyderman, H. Schift, C. David, J. Gobrecht, and T. Schweizer, "Flow behaviour of thin polymer films used for hot embossing lithography," Microelectron. Eng. **54**(3-4), 229–245 (2000).
46. N. Bogdanski, M. Wissen, S. Möllenbeck, and H.-C. Scheer, "Structure size dependent recovery of thin polystyrene layers in thermal imprint lithography," Microelectron. Eng. **84**(5-8), 860–863 (2007).
47. H. Schift and A. Kristensen, *Nanoimprint Lithography* (Springer Berlin Heidelberg, 2007), pp. 239–278.
48. O. Stevens, I. E. I. Petterson, J. C. Day, and N. Stone, "Developing fibre optic Raman probes for applications in clinical spectroscopy," Chem. Soc. Rev. **45**(7), 1919–1934 (2016).
49. L. W. Tilton, E. K. Plyler, and R. E. Stephens, "Refractive index of silver chloride for visible and infra-red radiant energy*," J. Opt. Soc. Am. **40**(8), 540–543 (1950).
50. K. Han and C.-H. Chang, "Numerical Modeling of sub-wavelength anti-reflective structures for solar module applications," Nanomaterials **4**(1), 87–128 (2014).
51. R. J. Weiblen, C. R. Menyuk, L. E. Busse, L. B. Shaw, J. S. Sanghera, and I. D. Aggarwal, "Optimized moth-eye anti-reflective structures for As_2S_3 chalcogenide optical fibers," Opt. Express **24**(10), 10172–10187 (2016).

Optical Materials EXPRESS

52. Y. Yang, S.-C. Liu, Y. Wang, M. Long, C.-M. Dai, S. Chen, B. Zhang, Z. Sun, Z. Sun, C. Hu, S. Zhang, L. Tong, G. Zhang, D.-J. Xue, and J.-S. Hu, "In-plane optical anisotropy of low-symmetry 2D GeSe," Adv. Opt. Mater. **7**(4), 1801311 (2019).
53. J. Zheng, Z.-C. Ye, N.-L. Sun, R. Zhang, Z.-M. Sheng, H.-P. D. Shieh, and J. Zhang, "Highly anisotropic metasurface: a polarized beam splitter and hologram," Sci. Rep. **4**(1), 6491 (2014).

Received: 20 November 2019 | Revised: 11 January 2020 | Accepted: 4 February 2020

DOI: 10.1002/jrs.5853

RESEARCH ARTICLE

Journal of RAMAN SPECTROSCOPY WILEY

Detection of aspirin traces in blood by means of surface-enhanced Raman scattering spectroscopy

Sonata Adomavičiūtė | Martynas Velička | Valdas Šablinskas

Institute of Chemical Physics, Vilnius University, Vilnius, Lithuania

Correspondence
Valdas Sablinskas, Institute of Chemical Physics, Vilnius University, Saulėtekio al. 3, LT-10257 Vilnius, Lithuania.
Email: valdas.sablinskas@ff.vu.lt

Funding information
Research Council of Lithuania, Grant/Award Number: SEN-16/2015

Abstract

Aspirin being freely available as an over the counter drug has a high overdose risk and can cause severe health symptoms. The methods used in clinics for the detection of such drugs (pharmaceuticals) in bodily fluids are mostly based on liquid chromatography and mass spectroscopy. These methods are known to be precise; however, they both require long and laborious sample preparation; thus, it takes time to acquire the required information. Because in the case of an overdose, the time has high importance, and faster methods would be beneficial. This work presents an application of a Surface-enhanced Raman scattering (SERS) spectroscopic method for the detection of salicylic acid as a metabolite of aspirin in the blood serum of the patient under examination. In this research, the various colloidal solutions were employed for the preparation of SERS active substrates. The choice of the most efficient colloidal solution and the challenges of collecting SERS spectra of whole blood or its components are discussed. The spectra of both the model and the real-life blood samples containing metabolite of aspirin were collected with a Fourier transform Raman spectrometer. The analysis of the collected spectra revealed that label-free SERS can be used for the detection of salicylic acid with concentration down to 3 mM in blood serum corresponding to consumption of at least eight standard pills of aspirin (equivalent to mild toxicity). The proposed diagnostic method could be applied faster than the standard methods and could allow sensitive and fast diagnosis of aspirin consumption in the human blood.

KEYWORDS

aspirin, blood, colloidal SERS, salicylic acid, serum

1 | INTRODUCTION

In the age of technology, when vast amounts of various information, including medical, is freely available, it is quite tempting to self-evaluate one's health and match the felt symptoms to the specific diagnosis, which previously was prerogative of the medical experts.[1] Unfortunately, without the proper regulation and validation of such information, there is no guarantee that the diagnosis is truly correct. The flawed diagnosis and unguided self-medication often leads to serious health risks and other more serious problems related to the misuse of pharmaceuticals such as organ function failure or death.[2] Although every medicine brings forth a risk of being abused, over the counter drugs are more frequently misused due to their availability in the market. Out of the latter, probably the most commonly abused drug is acetylsalicylic acid also known as aspirin. Usually, in

general public, this nonsteroidal anti-inflammatory drug is the first choice for a fast relief. When used, aspirin is rapidly deacetylated to salicylic acid (SA) in the blood and is thought to affect us in several ways.[3] The overdosing of aspirin is not so simple because quite a large amount of the drug should be taken. However, many patients are prescribed and use a constant daily dose of aspirin both in pure doses or as a constituent of some other pharmaceuticals. For treatment of pain, arthritis, migraine, and insomnia, it is often used together with acetaminophen, caffeine, salicylamide, and so forth. Chronic ingestion of aspirin can result in buildup of SA in the blood (salicylate poisoning) and is especially common among elders. The mild toxicity of SA (40–80 mg/dl or 3–6 mM) already has an effect on health whereas high toxicity can cause such symptoms as dysfunctions in renal and hepatic activity.[4–6] In order to ensure the best possible treatment for the overdosed patient, it is important to make a fast assessment of the pharmaceutical because the treatment is most effective in the early stages of the overdose. This is mainly done by drug screening via blood or urine chemical tests. The most widely used methods for detection of pharmaceuticals or their metabolites in blood are liquid chromatography tandem mass spectrometry and gas chromatography coupled with mass spectrometry.[7–9] These methods are quite sensitive and allow the detection of SA with concentration down to 0.04 mg/l (30 μM). However, the drawback of these methods is the lack of simplicity. The preparation of the sample involves several steps and the use of different chemical standards that leads to prolonged testing times. The need for improved SA detection methods initiated the development of various screening methods based on different sensing techniques. Surface-enhanced Raman scattering (SERS) spectroscopy is one of the methods that has potential to be used for a faster drug detection in bodily fluids. It is notable that this method is based on the analysis of molecular vibrations and is sensitive to the chemical structure of molecule under study thus providing exceptionally high chemical specificity. Additionally, SERS is an extremely sensitive method that can be used for the detection of molecules with concentration down to parts per million. The SERS method has already been successfully adapted to studies of human blood and detection of certain biomolecules and pharmaceuticals.[10] It has been shown that the sensitivity of the SERS method employed via colloidal nanoparticle (nanoparticle) solutions and aggregating salts can be compared with (or can even surpass) the sensitivity of the gas chromatography coupled with mass spectrometry.[11] The SERS method is also versatile and allows various technical approaches for the enhancement of the Raman scattering signal.[12] Thus, SERS is being proposed as a cheaper alternative for detection and monitoring of various drugs.[13,14] Previously, the SERS method employing microgels containing agglomerates of silver nanocubes was used for the detection of aspirin in the blood.[15] However, the method was tested only on rat blood that was spiked with 30 mg/dl (1.7 mM) of aspirin. Thus, a true representation of the diagnostic problem was not investigated in this research because consumed aspirin is quickly metabolized to SA in blood. Therefore, the aspirin spiked blood is not suitable to simulate the real-life samples.

In this work, we propose a method for a faster and sensitive detection of SA in blood using label-free SERS spectroscopy by employing colloidal solutions of silver and gold nanoparticles. Such solutions can be used to create active substrates for the enhancement of the Raman scattering signal. Several different colloidal synthesis procedures for the creation of such substrates were considered in this work. Advantages and disadvantages of using colloidal solutions, with steric and electrostatic stabilization of nanoparticles, are discussed. The best experimental conditions—the ones that would give the highest enhancement factor and the spectrum free of the influence of the substrate—were determined using model solutions of SA in whole blood (or its components). Samples simulating real-life conditions were used for testing the sensitivity of the method and its application for point-of-care analysis. The fluorescence-free spectra were recorded with an Fourier transform Raman spectrometer using a near infrared spectroscopy laser for the excitation.

2 | EXPERIMENTAL SECTION

2.1 | Materials

Chemicals used for synthesis of the nanoparticles: extra pure silver nitrate ($AgNO_3$), tetrachloroauric (III) acid trihydrate 99.5 % purity ($HAuCl_4{\cdot}3H_2O$), and anhydrous trisodium citrate ($C_6H_5Na_3O_7$) were bought from the *Merck Group* (Germany), and polyvinylpyrrolidone K30 (PVP; $C_6H_9NO)_n$ and sodium borohydride ($NaBH_4$) were bought from *Carl Roth* (Germany). Pure SA ($C_7H_6O_3$) was purchased from *Sigma-Aldrich* (USA); *o*-acetylsalicylic acid ($C_9H_8O_4$) 99% purity was purchased from *Alfa Aesar* (Germany); uric acid (UA; $C_5H_4N_4O_3$) 99% purity was purchased from Sigma-Aldrich (USA). Sample pH was altered with a solution of 2 M sodium hydroxide (NaOH) bought from Carl Roth (Germany). For serum separation from the whole blood coagulation agent—dicynone (etamsylate) was used (*Lek Pharmaceutical and Chemical Company*). Deionized ultrapure water

(18.2 $M\Omega cm^{-1}$) was used in the preparations of all aqueous solutions. All glassware was cleaned using Aqua Regia solution (3:1 hydrochloric acid to nitric acid) and washed with deionized water. Samples were prepared on aluminum substrates cleaned with methanol and deionized water. Human blood serum was bought from *Thermo Fisher Scientific* (USA).

2.2 | Synthesis of nanoparticles

Different synthesis methods have been employed in order to find the colloidal solution of the nanoparticles that most suited for detection of aspirin traces in human blood. We used different surface chemistry approaches for preparation of the nanoparticles. Different capping agents used in these approaches alter interactions between the analyte molecules and the nanoparticles. For example, nanoparticles prepared by the approach described by Lee and Meisel are stabilized by citrate, and such stabilization is based on the electrostatic forces. Adsorption of analyte molecules can occur on the surface of citrate-stabilized nanoparticles by substitution of citrate molecules on the silver surface or by the interaction of the analyte molecules with the citrate molecules.[16] Another method for stabilization of nanoparticles based on steric polymer repulsion is also possible. In order to realize such stabilization, we have employed PVP. Due to the different adsorption properties of the PVP, it is also possible to realize the faster growth of the nanoparticles in certain directions defined by the crystal structure.[17] Such directional growth leads to the formation of nonspherical nanoparticles that might lead to higher SERS intensities. Additionally, analyte molecules can interact with polymer differently; thus, it can alter adsorption of analyte molecules. Silver and gold are usually used for the enhancement of Raman scattering of molecules. Generally, in the majority of cases, silver gives a higher enhancement factor for SERS than gold; however, it is not as stable as gold, which in certain cases could be a better solution.[18]

Solutions of colloidal gold and silver nanoparticles were prepared by employing five different approaches. The following silver nanoparticles were obtained (a) citrate-stabilized nanoparticles (Ag-cit), (b) polymer-stabilized nanoparticles (Ag-PVP) synthesized by polyol process that should lead to the formation of spherical nanoparticles, and (c) reduced sodium borohydride and PVP-stabilized nanoparticles (Ag-BH_4), in order to yield nonspherical nanoparticles. Additionally, two colloidal solutions of gold nanoparticles were synthesized and examined: (e) citrate-stabilized (Au-cit) and (f) polymer-stabilized gold nanoparticles were (Au-PVP) also synthesized by polyol process that should lead to the formation of icosahedral nanoparticles.

Colloidal solution of Ag-cit nanoparticles was prepared according to the Lee-Meisel synthesis method by reducing and stabilizing nanoparticles with trisodium citrate.[19] In brief, 100 ml of 1 mM $AgNO_3$ solution was heated until boiling and, 4 ml of 1% trisodium citrate solution was added to the heated $AgNO_3$ solution. The resulting solution was kept at a boiling point for 1 hour under constant stirring.

Ag-PVP nanoparticles were synthesized in the following manner by polyol process with PVP that should yield spherical nanoparticles stabilized by PVP.[20] The mass of 1 g of PVP K30 was dissolved in 20 ml of deionized water. Then, a prepared PVP solution was heated under constant stirring. Finally, 1 g of $AgNO_3$ was added to the solution. The final solution of nanoparticles was stirred for an additional hour at the temperature of 80°C.

Reduced sodium borohydride and PVP-stabilized silver nanoparticles (Ag-BH_4) were prepared by a two-step procedure adapted from Aherne et al.[21] This synthesis method should yield nonspherical nanoparticles because PVP is known to reduce nanoparticle growth in certain crystallographic axes.[17] At first, seed preparation was done by heating 0.12 M PVP solution (2 ml) to boiling. Then, a solution of 1 mM of $AgNO_3$ (4 ml) and a solution of 2.5 mM of citrate (2 ml) were added to the 2 ml of the previously prepared PVP solution. Finally, 10 mM of freshly prepared sodium borohydride solution (0.06 ml) was added under stirring. The next preparation step of nanoparticles solution preparation is the nanoparticle growth. For this step, the seed solution was diluted 6 times. Then, a solution of 10 mM of ascorbic acid (75 μl) was added to 3 ml of the diluted seed solution following addition of a solution of 0.5 mM of $AgNO_3$ (3 ml).

A colloidal solution of citrate-stabilized and reduced gold nanoparticles (Au-cit) was prepared according to synthesis protocol described by Turkevich et al.[22] At first, a solution of 5 mM of $HAuCl_4$ (100 ml) was brought to boiling. Afterwards, 5 ml of 1% trisodium citrate solution was added to tetrachloroauric acid solution and kept under boiling temperature for an additional hour while stirring constantly.

Au-PVP nanoparticles were prepared by the polyol synthesis method[23] covering gold nanoparticles with polymeric surface. First, a solution of 0.12 mM of PVP (25 ml) was heated to boiling temperature. Second, a solution of 1 mM of tetrachloroauric acid (25 ml) preheated to 60°C was added under stirring to the boiling solution. The colloidal solution was kept at boiling point for another hour. After the synthesis, excess amount of PVP was removed by diluting the colloidal

solution with deionized water, centrifuging and discarding supernatant afterwards. The washing step was repeated 3 times.

2.3 | Collection of blood

Fresh blood for the SERS experiments was obtained by collecting it from the fingers of volunteers after overnight fasting using a standard fingerstick sampling technique. The samples of blood or its serum were diluted 20 times with deionized water and mixed with SA acquiring concentrations of the drug as stated. In such a way, the model blood samples containing SA were prepared. Real pharmacokinetic samples were prepared by collecting blood from the volunteers before and after taking a bolus dose of 3.2 g of soluble aspirin (Aspirin-C). The blood samples were preprocessed by mixing 400 μl of blood with one drop (50 μl) of dicynone and centrifuging the mixture for 10 min. A centrifugal force of 5,000 × *g* was applied in order to separate blood serum from the whole blood.

2.4 | Instrumental

After the synthesis of the nanoparticles, the colloidal solution was concentrated by centrifuging 30 ml of the solution with a centrifugal force of 6,000 × *g* for 10 min. Afterwards, 10 ml of supernatant was discarded from the solution. SERS active layers of nanoparticles for the spectroscopic measurements were prepared by drying 25 μl of concentrated colloidal solution on the precleaned aluminum substrate. Upon measurements, one drop (25 μL) of sample solution was put on the prepared substrate. All spectra were acquired with a Bruker *MultiRAM* Fourier transformed Raman spectrometer equipped with a 1064-nm Nd:YAG laser. A liquid nitrogen-cooled Ge diode detector was used for detection of the SERS spectra. Sample excitation and collection of scattered light was performed using microscopy stage of the spectrometer equipped with reflecting objective—a 90° angle gold plated parabolic mirror. All spectra were collected using a laser power of 300 mW, which was found to give the best intensity of the spectra without overheating the sample. Excitation beam was focused to a 100-μm-diameter spot that gives the intensity of $4.8 \cdot 10^8$ W/m^2. The spectra were measured with the 4-cm^{-1} spectral resolution. The resulting spectrum was taken as an average of 300 interferograms that were Fourier transformed using a Blackman-Harris 3 term apodization function and a zero filling factor of 2.

3 | RESULTS

In this work, traces of SA as an active metabolite of acetylsalicylic acid (aspirin) in blood were detected. Aspirin is absorbed into the bloodstream mainly unhydrolyzed although some amount is hydrolyzed in the gastrointestinal mucosa and liver and is subsequently absorbed into the blood in the metabolized form—SA. Further, acetylsalicylic acid in blood is rapidly converted to SA by carboxyl esterases; thus, it can be detected hydrolyzed in blood only for a short period of time.[24] The half-life for aspirin in the blood plasma is about 20 min. For example, after consumption of 1 g (therapeutic doze) of aspirin, almost all acetylsalicylic acid (27–30% of acetylsalicylic acid is still present in blood) is hydrolyzed to SA after 20 min.[24–26] The aspirin is known to bind to platelets and to cyclooxygenase-1 (and to cyclooxygenase-2, depending on the intake dose of aspirin). Consequently, 80–90 % of aspirin is found as irreversibly bounded after 1 h[24,26] in blood and remains in the bloodstream for platelets turnover time. Concentration of free acetylsalicylic acid in blood by that time usually is too low for detection. For this reason, toxicity and dose of aspirin is determined not directly but from the concentration of salicylate in blood.[27] In fact, anticoagulating as well as analgesic and anti-inflammatory functions of aspirin are established to be dependent on acetylation of such chemical molecules. SA has a much longer half-life than that of aspirin which may vary between 3 hr at antiplatelet doses and 30 hr at therapeutic doses or intoxication. Also, SA is known to have anti-inflammatory, therapeutic properties and the capability to bind to other molecules. For instance, it is mostly detected in blood (or its serum) as protein bounded. Percentage of the bounded SA molecules can be up to 90% when SA concentration in blood is low and can be down to 30% when SA concentration is high.[28,29] The calculations of geometries and normal vibrational modes of SA in this work were performed by *ab initio* methods using Gaussian 09 software.[30] Density functional theory calculations were made at B3LYP/6-311G++ level of theory. The optimized structure of the most stable tautomer of SA molecule is presented in Figure 1. The most stable SA tautomer is a planar molecule with hydroxyl facing toward carbonyl group, which agrees well with the literature data.[31] The calculated energy differences between the most stable tautomers are in the range of 56.5–62.7 kcal/mol.

SA is composed of benzene ring, hydroxy, and carboxylic functional groups. The pKa value of SA is 2.98, so in biological pH, SA is either protonated or bounded to proteins.

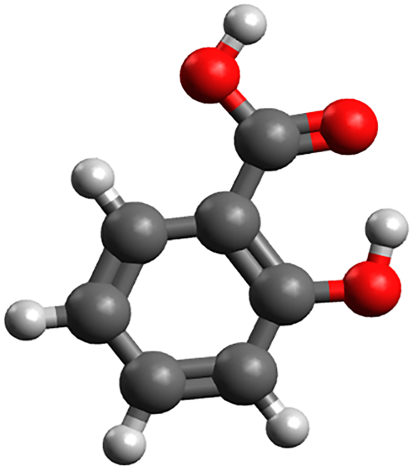

FIGURE 1 Theoretically calculated (B3LYP/6-311G++) structure of salicylic acid—$C_7H_6O_3$ [Colour figure can be viewed at wileyonlinelibrary.com]

SA or a group of chemicals that are related to SA by their chemical structure or their anti-inflammatory effects (also known as salicylates) are excreted with urine from the body. In customary doses of aspirin (from 325 to 500 mg), the half-life of SA in blood is ranging from 3 to 5 hr. If the intake dose of aspirin is higher (3.6 g), pharmacokinetics of SA is slowed down, and SA concentration in blood drops twice only after 12–16 h.[32,33] Maximum concentration of SA in blood (0.3 mM) after consumption of a 640-mg dose of aspirin is reached after 0.5–1 h.[34] After the intake of 1.2 g of aspirin, maximum concentration of SA in blood (0.7 mM) is reached after 1 h.[35] Salicylates can also be detected from other biological fluids such as synovial fluid, cerebrospinal fluid, and perilymph. It is notable that in other bodily fluids, SA is usually available in smaller concentrations than in blood. For example, concentration of SA in synovial fluid is 50% lower than in blood. Five times lower concentration of SA is detected in cerebrospinal fluid and perilymph in respect to that in blood.[36]

When determination of the lowest detectible concentration of SA in human blood is concerned (as in our case), pharmacokinetic properties of aspirin as well as concentration of SA in blood should be considered. Furthermore, if blood concentration of SA is higher than 4 mM after the intake of aspirin, it is considered to be dangerous, whereas concentrations below 3 mM are considered to be therapeutic and anti-inflammatory. Concentration of SA is considered lethal when it exceeds 5 mM in human blood.

3.1 | Selection of the nanoparticles

In order to test the capability of SA detection in biological fluids such as whole blood or serum by means of SERS, SERS-efficiency of various metal nanoparticles has to be estimated. Whole blood has many SERS active constituents such as UA, proteins, and so forth, which are formed during various metabolic reactions. These constituents may interfere and even weaken the SERS signal of drug molecules (or their metabolites) that we seek to detect. In order to reach the highest possible SERS signal from SA molecules, as well as the highest signal-to-noise ratio, solutions of different nanoparticles were tested. It is well established that molecules of SA are adsorbed on the citrate-capped nanoparticles through the carboxylic group.[37] Because SERS intensity strongly depends on the distance between the nanoparticle and molecule under study, chemical adsorption usually leads to high intensity of the SERS signals of the adsorbates,[38] and thus, adsorption is aspired.

In this work, gold nanoparticles were synthesized by the citrate reduction (Au-cit) and by the polyol synthesis (Au-PVP) protocols. Colloidal solutions of silver nanoparticles were prepared using the following methods: the citrate reduction synthesis (Ag-cit), the polyol process (Ag-PVP), and the reduction with sodium borohydride (Ag-BH_4). Ultraviolet–visible spectroscopy absorption spectra of the nanoparticles are presented in Figure 2.

The spectra presented in Figure 2 reveal that Ag-cit nanoparticles are the most concentrated in the colloidal solution, and the absorption maximum is located at 412 nm, which corresponds to the absorption of spherical nanoparticles approximately 60 nm in diameter.[39,40] The transmission electron microscopy images of Ag-cit nanoparticles presented in Figure 2 have confirmed these Ultraviolet–visible spectroscopy results and have showed that the average size of the synthesized nanoparticles was indeed ~60 nm. The images also reveal that the colloidal solution is not monodispersed. The size of the nanoparticles ranges from 10 to 100 nm. Also, single differently shaped nanoparticles (e.g., rod shaped nanoparticles) are present. Variation in size of the nanoparticles prevents formation of the uniform SERS substrate. However, the size of nanoparticles does not affect positions of the SERS spectral bands (only the SERS intensity can be affected depending on the size of the nanoparticles). This is not a problem if the spectral marker for the detection of certain molecules is the

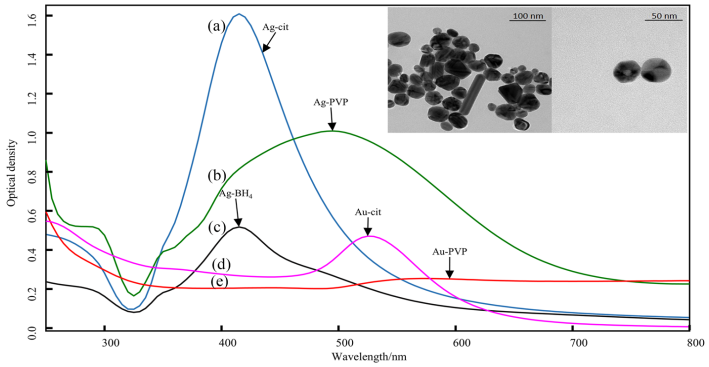

FIGURE 2 The ultraviolet–visible spectroscopy absorption spectra of various colloidal solutions of silver nanoparticles: (a) ag-cit, (b) ag-PVP, (c) ag-BH_4 PVP and gold nanoparticles: (d) au-cit, (e) au-PVP. The transmission electron microscopy images of ag-cit nanoparticles (top right) [Colour figure can be viewed at wileyonlinelibrary.com]

relative intensity of the spectral bands. In this study, absolute intensity of SERS spectral bands was not relevant because the collected spectra were normalized, and only relative intensities of spectral bands of SA and UA were considered.

The absorption band related to plasmon resonance frequency of polymer capped silver nanoparticles Ag-PVP is located at ~500 nm. The band of Ultraviolet–visible spectroscopy absorption spectrum of Au-PVP nanoparticles is located at longer wavelengths, which means that nanoparticles are either large or not spherically shaped. Actually, according to the transmission electron microscopy images, the Au-PVP nanoparticles were triangular shaped see Figure S1 (Supporting Information).

The lower frequency of the plasmon resonance is advantageous in the case of a near infrared laser used for the SERS excitation. This is due to the fact that plasmon resonance frequency is usually desired to be close to the excitation laser frequency in order to achieve higher SERS enhancement by the nanoparticles. However, this requirement is not critical when the highly concentrated colloidal solution is used. In such a colloidal solution, metal nanoparticles strongly interact with each other. The interaction of electromagnetic fields of different nanoparticles creates so called "dark modes" of enhanced electromagnetic fields and thus can enhance Raman signal even when employed laser excitation frequency is far from the plasmon resonance.[41] In our work, we used concentrated colloidal solutions with strongly interacting metal nanoparticles and 1,064-nm excitation wavelength with corresponding frequency being rather far from the plasmon resonance frequency of the nanoparticles, so the differences in plasmon resonance frequency had little impact on the enhancement capabilities of the nanoparticles. This excitation frequency was chosen in order to suppress fluorescence background from blood constituents and because the Fourier transformed Raman system that was used in this work was optimized for this frequency.

SERS spectra of aqueous solution of SA (1 mM) collected using different colloidal nanoparticles are presented in Figure 3. Analytical Raman scattering enhancement factor (E) and signal-to-noise ratio (S/N) were calculated for each spectrum and are presented in figure 3. Analytical Raman scattering enhancement factor was calculated by comparing the intensity of SERS spectrum I_{SERS} of a solution with a certain concentration of SA c_{SERS} with Raman signal intensity I_{Raman} of c_{Raman} concentration under the same conditions—laser wavelength and power, laser spot area, and so forth. An analytical signal enhancement factor was calculated by the following relation:

$$E = \frac{I_{SERS} \cdot c_{Raman}}{I_{Raman} \cdot c_{SERS}}.$$

As can be seen from the spectra (see Figure 3), the highest analytical enhancement factor ($E = 2.4 \cdot 10^4$) and signal to noise ratio ($S/N = 216$) is reached in case of Ag-cit nanoparticles. Whereas Au nanoparticles display a 40 times lower S/N ratio and 10 times lower enhancement of Raman spectral bands. Whenever Au nanoparticles are used for the SERS experiments, the analytical enhancement factor does not exceed $3.8 \cdot 10^3$, which is too low for detection of SA in blood serum. Additionally, SERS spectra of SA collected using the substrates prepared from the Au-cit and Au-PVP nanoparticles reveal extraneous arising of the spectral bands from the colloids. The SERS spectra of SA on Au-cit nanoparticles contains additional spectral bands from carboxylate group of sodium citrate: symmetric vibration (ν_{sym} [COO^-]) at 1,390 and 1,368 cm^{-1}, asymmetric vibration (ν_{asym} [COO^-]) at 1,565 cm^{-1}, and

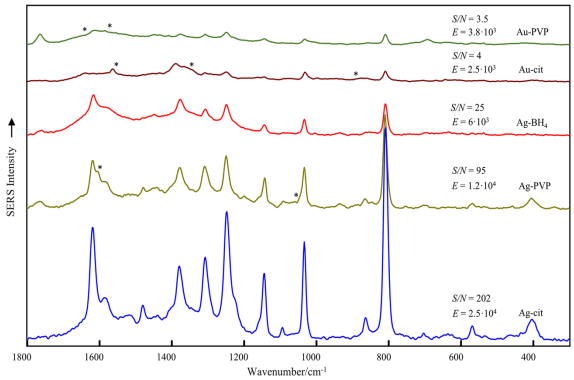

FIGURE 3 SERS spectra of the aqueous salicylic acid solution (1 mM) collected using different silver and gold nanoparticles. The analytical enhancement factor (*E*) and signal to noise ratio (*S/N*) were calculated for the spectral band located at 1034 cm^{-1}. Extraneous bands arising from the colloidal solutions are indicated with an asterisk. SERS, surface-enhanced Raman spectroscopy [Colour figure can be viewed at wileyonlinelibrary.com]

deformational vibration (δ [COO^-]) at 892 cm^{-1}.[42,43] Likewise, distinct wide spectral bands at 1,615 cm^{-1} to 1,585 cm^{-1} appear when Au-PVP nanoparticles are used. These bands may be attributed to ν(C—N) and ν(C═O) vibrations of lactam ring in the PVP.[44] Considering that PVP can be adsorbed on the surface of nanoparticle through the oxygen of carbonyl group,[45,46] the occurring spectral bands implicate that PVP is not adsorbed on Au surface firmly or that the amount of PVP is excessive. When PVP is adsorbed on the surface of nanoparticle, these vibrational bands should not be visible.[45,46]

Contrary to the case of Au nanoparticles, SERS spectra of SA collected using Ag-PVP nanoparticles was more intense but still less intense than in the case of the Ag-cit nanoparticles. Furthermore, PVP may not be stable when high laser power is used, and the dissociation products give rise to the spectral band located at 1039 cm^{-1}. This band may be attributed to the oxidation products forming between PVP and Ag.[45,46] Besides the mentioned cons, preparation of Ag-PVP and Au-PVP nanoparticles is also more complicated because extensive washing is required in order to excess PVP.

The use of other type of silver nanoparticles (Ag-BH_4) in this study did not give satisfactory results: (a) preparation of the Ag-BH_4 is too laborious because it consists of two steps, and (b) Ag-BH_4 nanoparticles did not produce the best *E* value.

Because of the above mentioned findings, Ag-cit nanoparticles were chosen for further experiments.

3.2 | Spectral experiments with SA in whole blood and blood serum

There are several computational studies of SA that determine adsorption of SA on a nanoparticle's surface through a ionized carboxyl group[47–49] that is well in accordance with experimental spectra where Ag—O stretching vibration is observed.[47] Assignment of the spectral bands in the SERS spectrum of SA indicates that the molecule is chemically adsorbed on the metal nanoparticle through its carboxylic group.[47–49] The most intense SERS bands are 809 cm^{-1} corresponding to the ring stretching + (C—COO) scissor vibration, 1248 cm^{-1} corresponding to δ(C—H) bending + ν (C—O), 1,034 cm^{-1} corresponding to δ (CH) bending + ring stretching, and 1,612 cm^{-1} corresponding to ring stretching + O—H bending. It is well established that the most efficiently enhanced spectral bands are those that are related to the vibrations of chemical groups being near the surface of nanoparticle and having the vibrational transition moment perpendicular to the nanoparticle's surface.[38,50,51] Intensities of such spectral bands are convenient to use as spectral markers in case when they are not overlapped with the spectral bands of the blood constituents. In order to check what bands could be used as spectral markers in whole blood sample after an overdose of acetylsalicylic acid, we have prepared samples of fresh human blood spiked with high concentration of SA. In this experiment, the pH of SA solution in the blood was increased (by adding calculated amounts of sodium hydroxide) to 6.5 to resemble the pH of blood with this concentration of SA[52]). SERS spectra of fresh human blood, its serum, and their mixtures with a concentration of 5 mM of SA are presented in Figure 4.

Overall, SERS spectra of whole human blood is difficult to interpret, because the spectra of blood from the same patient can vary with time Figure S2 (Supporting Information). Most likely, this is the result of chemical decomposition of cells and cellular metabolites, proteins, and amino acids that are present in blood. As can be seen from Figure 4, the most evident difference between a SERS spectrum of whole blood and the spectrum of SA solution in whole blood is the appearance of the spectral

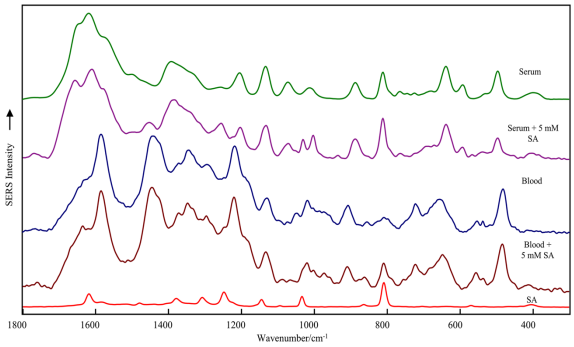

FIGURE 4 SERS spectra of (from the top): Serum, solution of SA in serum (5 mM), whole blood, solution of SA in whole blood (5 mM), and aqueous solution of SA (1 mM). SA, salicylic acid; SERS, surface-enhanced Raman spectroscopy [Colour figure can be viewed at wileyonlinelibrary.com]

band located at 809 cm^{-1} (corresponding to the normal vibration related to the ring stretching + (C—COO) scissor vibration). It should be noted that the spectral variation of the SERS spectrum of blood in the spectral region of the band is high. Standard deviation was calculated from the data of 11 blood samples. The standard deviation of the intensity of the band located at 809 cm^{-1} was divided by the averaged intensity values of the band at the same wavenumber giving the value of 54 % (Figure S2). Such high value of the relative standard deviation means that this region is not suitable for the detection of SA in blood (SA spectral band is not prominent for detection in this region). When the concentration of SA in blood does not reach 5 mM, we cannot state that SA is present in blood. In order to use this band (809 cm^{-1}) for the detection of SA in blood with a concentration lower than 5 mM, much more spectra should be collected, and statistical methods should be employed.

In this respect, blood serum is a biological fluid better suited for the detection of SA than the whole blood because blood cells are absent in the serum. Human serum consists of more than 4,000 chemical components, but the most SERS active is UA. This circumstance makes a SERS spectrum of human serum relatively simple. At normal conditions, UA concentration in blood serum varies between 140 μM and 420 μM depending on the diet, overall health, physical activity, and so forth. This concentration is low compared with that of SA after consumption of aspirin, but a UA molecule is extremely SERS active and thus can be detected by means of SERS even at very low concentrations down to micromoles.[53,54] In our case, such SERS activity of UA is inconvenient, and it has negative influence to the detection limit of SA in human serum. By comparing SERS spectra of serum and mixture of serum with SA, we have identified the possible spectral markers for SA in human serum. Such markers are the intense spectral band of SA located at 1,032 cm^{-1} (δ [CH] bending + ring stretching) and decreased integral intensity ratio of spectral band doublet at 1,073 and 1,012 cm^{-1} respectively. It is notable that the vibrational band of SA in water solution was located at 1,034 cm^{-1}, but when in blood, this band is red shifted to 1,032 cm^{-1}.

The other strong SERS spectral band of SA is located at 809 cm^{-1} (ring stretching + (C—COO) scissor vibration), but it is completely overlapped by the serum spectral band at 811 cm^{-1} (UA molecule vibrations – ν(C—N) + ring). Therefore, dependence of the intensity of the band on the SA concentration was not investigated. Similar behavior is observed for another intense spectral band in the SERS spectrum of SA located at 1,248 cm^{-1}. This band cannot be detected in the SERS spectra of serum when concentration of SA is low (see figure 5).

Another important observation is that SERS spectrum of the blood serum changes when concentration of SA is high. The intensity of the spectral bands associated with UA tends to decrease, and the intensity of spectral bands located 1,003, 1,447 and 1,694 cm^{-1} increases. These spectral bands are also observed in Raman spectra of serum; meaning that, high concentration of SA (more accurately—the changes in serum pH) leads to weaker adsorption of UA molecules on the surface of nanoparticles and to stronger adsorption of some other substituents of serum. As can be seen from Figure 4, when SA concentration in serum is high (5 mM), more intense spectral markers of SA can be observed together with the other spectral markers—relatively weaker spectral bands of UA. To conclude, SERS spectra of serum seems to be more promising for detection of SA traces than the whole blood spectra. Sensitivity of the spectral markers to concentration of SA in human serum and the lowest detectable concentration of SA in human serum is shown in Figure 5.

When concentration of SA in serum is high, the spectral band of SA located at 1,032 cm^{-1} is prominent. In case of low concentration of SA, the intensity of this

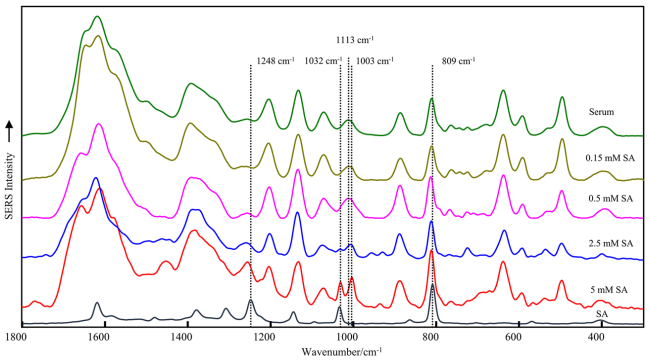

FIGURE 5 SERS spectra of: Blood serum—Top, SA and blood serum mixtures with different concentration of SA, aqueous solution of SA (1 mM)—Bottom. SA, salicylic acid; SERS, surface-enhanced Raman spectroscopy [Colour figure can be viewed at wileyonlinelibrary.com]

spectral band decreases and can be detected only as shoulder of the spectral band of serum at 1,012 cm^{-1}. Further in this work, we employed a contour separation method to identify SA spectral band located at 1032 cm^{-1}.

Another interesting observation is that the intensity of the serum spectral band at 1,012 cm^{-1} gets stronger with increasing concentrations of SA. It is thought that this increase in intensity resulted by a more intense spectral band at 1,003 cm^{-1} (asymmetric ring vibrations). This spectral band is the most intense band of phenylalanine, which is also observable in the Raman spectrum of serum. The intensity of a bands of the SERS spectrum of UA is high, when this molecule is chemically adsorbed on the nanoparticle. In the contrary, we observe the spectral bands of other molecules such as SA or phenylalanine in the SERS spectrum of blood serum when the adsorption of UA is hindered. As mentioned before, SA molecule is adsorbed on the citrate-capped nanoparticle's surface through a carboxyl group. Calculations of UA showed that UA molecule is adsorbed on the nanoparticle's surface through an ionized amide group.[53,54] Different molecular structures and binding sites influence adsorption affinity of molecules differently when conditions (for example pH) of samples change. Indeed, SERS is a surface-sensitive spectroscopy, meaning that the Raman signal will be enhanced only for the molecules that are adsorbed or close to the surface of nanoparticles. Because nanoparticles are relatively stable and their surface area does not change, molecules compete for the adsorption. Properties of the solution, such as pH or an electrostatic field on nanoparticles surface may reason better adsorption of some molecules.

SA and UA molecules compete for adsorption space on nanoparticles surface; therefore, the dependence of the intensity of UA spectral bands on the concentration of SA is nonlinear (contrary to the linear increase in the intensity of the spectral bands due to increased concentration). Such nonlinearity is demonstrated in Figure 6a, where dependence of relative intensity (I_{UA}/I_{SA}) of UA SERS spectral bands on the concentration of SA in UA–SA–water mixture is presented. Concentration of UA was kept stable—200 μM. SA concentration was changed from 10 to 0.25 mM, and dependence of the relative intensity of UA spectral bands on SA concentration was measured.

Due to the weakened adsorption of UA on the surface of nanoparticles, the intensity of the SERS spectral bands of UA decreases and the spectral bands of phenylalanine or other molecules can be observed.

It is known that phenylalanine is present in serum proteins (phenylalanine makes up 5% of all human serum albumin protein[55]) and as a free amino acid in serum usually up to 120 μM concentration. The spectral band at 1,003 cm^{-1} is the most intense band in the Raman spectrum of serum that does not fully overlap with a SERS spectral band of UA. So, when UA is not effectively adsorbed on Ag nanoparticles surface, the spectral band of phenylalanine gets stronger. Thus, such behavior of the spectral band can be resulted by serum acidity changes upon increased concentration of SA. Increase of acidity of the solutions is followed by the changes of intensity ratio of the serum spectral bands at 1,073 and 1,012 cm^{-1}. Thus, this ratio can be used as an indirect spectral marker for detection of SA in serum. In fact, the ratio of the spectral bands located at 1,073 and 1,012 cm^{-1} decreases from 1.8 (in pure serum) to 0.7 (when SA concentration in serum and SA mixture is 5 mM). The lowest concentration of SA in serum that was detected is 0.15 mM, which corresponds to the ratio of spectral bands equal to 1.67. At this concentration, SA was detected as a shoulder of the spectral band located at 1,032 cm^{-1} and from the intensity ratio of the spectral doublet that was mentioned earlier. Such concentration (0.15 mM) in the sample under study corresponds to

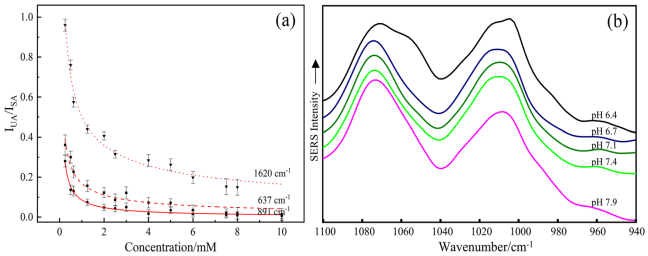

FIGURE 6 The dependence of relative intensity (I_{UA}/I_{SA}) between the SERS spectral bands of uric acid (1620 cm^{-1}, 637 cm^{-1}, 891 cm^{-1}) and salicylic acid (1031 cm^{-1})—(a); SERS spectra of human blood serum at different pH values—(b). SERS, surface-enhanced Raman spectroscopy [Colour figure can be viewed at wileyonlinelibrary.com]

3 mM of SA concentration in undiluted human serum and corresponds to a mild toxicity level.

In order to affirm our hypothesis that intensity ratio of spectral bands at 1,073 and 1,012 cm^{-1} is caused by changes in serum acidity, SERS spectra of serum with different pH values were measured. Serum pH was changed by addition of different amount of 1 M of H_2SO_4 solution to 5 ml of 20 times diluted blood serum. SERS spectra of serum with different pH values is presented in Figure 6b.

As can be seen from Figure 6b, changes in relative intensity of the serum spectral bands at 1,073 and 1,012 cm^{-1} are observed when pH of serum decreases (acidity increases). When serum pH drops down to 6.4 the arising of phenylalanine spectral band at 1,003 cm^{-1} can be observed. More precise positions of the spectral bands are provided in Figure S3. Such behavior of the bands can be explained by the burdened adsorption of UA molecules on nanoparticles' surface. The burdened adsorption causes lower intensity of the SERS spectral bands of UA and therefore higher intensity of phenylalanine SERS spectral bands. It is clearly seen that changes in the solution pH are reasoning the changes in relative intensity of this doublet.

The increase in intensity can be observed not only for the spectral band of phenylalanine but also for the spectral band of UA located at 1,013 and 983 cm^{-1}. Additionally, the serum spectral band at 1,073 cm^{-1} splits in two bands at 1,069 and 1,059 cm^{-1}. These two spectral changes occurring upon changing of pH of the solution can be related to tautomeric changes of UA.

The pKa value of neat UA is 5.4, and it is higher than that of SA. Such pH value of UA means that half of UA molecules are protonated. Further increase of the pH values denotes deprotonation of even more UA molecules. Increase of SA concentration in blood is followed by higher abundance of protonated UA. It is known from other studies that UA displays tautomerism.[56–60] Theoretically it is established that UA can form up to 35 tautomers[57] in which proton can be either bonded to an oxygen atom, forming an OH group (enol tautomer) or to nitrogen atom, forming an NH group (keto tautomer). Theoretical calculations revealed that the most stable tautomer of UA is a triketo form.[57] Nevertheless, there might be other three possible tautomers, which have slightly higher potential energy with $\Delta H = 2 - 6$ kcal/mol. These tautomeric forms are diketo or monoketo where the hydrogen is attached to the oxygen atom of imidazole or pyrimidine rings. Monoanion is formed when a N—H bond of UA is deprotonated.[57] The most stable monoanion is UA3 (see Fig. S5 in Supplementary materials) that is formed from the most stable triketo tautomer by deprotonation of pyrimidine ring. Other stable monoanion is UA9 with $\Delta H = 1 - 3$ kcal/mol, which is formed by deprotonation of the imidazole ring. The calculations predict that at normal pH, UA in aqueous solution exists as mixture of UA3 form and UA9 form. The other monoanionic forms have much less stability and is considered not to be present in the solution.[59,60] More monoanions of UA are getting transformed to a protonated neutral UA molecular form when pH of UA solution decreases. A hydrogen atom is bonded to a nitrogen atom of an imidazole or pyrimidine ring, and the concentration of the most stable UA tautomer, trikeo, increases. Our *ab initio* calculations of the most stable UA neutral tautomers and monoanions with a five atom silver cluster revealed that redistribution of intensity of spectral bands at 1,073 and 1,012 cm^{-1} is present in the most stable triketo form of UA. In this form, the intensity ratio of C—N/N—C—C ring vibration at 1,012 cm^{-1} and C—N/N—C—C stretching/OH bending at 1,073 cm^{-1} is 1.4, whereas in monoanionic forms it is about 0.2 or even less. Calculated intensities of the mentioned vibrational bands of the UA tautomers are presented in Figure S4. The increase of vibrational transition dipole moment for the band at 1,012 cm^{-1} causes intensity changes in SERS spectra of UA at acidic pH. The red shift from 1,073 to 1,059 cm^{-1} that is present in mixed normal vibrations: C—N/N—C—C stretching/OH bending,[54] can be related to increase of mass of the pyridine ring when it is protonated. The increase of the reduced mass causes a red shift of the corresponding spectral band.[58] It should be noted that the calculations we have performed showed that the

strength of the interaction between the SA (or different tautomers of UA) and the Ag cluster is in the order of 120 kcal/mol that also corresponds to the previously calculated values for the UA and Ag complexes.[53] This value is suggesting that real chemical bond is formed between the silver cluster and the molecule. Dispersion forces give a meaningful influence only when the weak chemical interactions occur. We did not include the dispersion term in our semiempirical calculations; because in our case, the influence of dispersion term is overshadowed by the forming of the chemical bond.

3.3 | Real-life experiments

In order to check the viability of aspirin detection based on our proposed method, SERS spectra of blood serum were measured after consumption of 3.2 g of aspirin (maximum daily dose is 4 g). The kinetics of SA in blood is presented after 30 min, 1 and 2 hr of consumption of bolus dose of aspirin. Serum was separated from whole blood and immediately that SERS spectra were measured (see Figure 7).

As can be seen from the spectra, the intensity ratio of the spectral band doublet at 1,073 and at 1,012 cm^{-1} (highlighted in the Figure 7) decreases noticeably and has a minimum value of 1.23 after 1 hr. In these spectra, the shoulder of SA spectral band can also be observed at 1,032 cm^{-1}. The intensity ratio is increased again to 1.53 in the SERS spectra of the sample after 2 hr, but the spectral band of SA can still be separated from other UA bands by a contour separation method (see Figure 8).

The contour separation was done via the data analysis and graphing software "OriginPro 2018."[61] Because the spectral bands are broadened due to different effects reasoning either Gaussian or Lorenz contours, the starting contour for the fitting was chosen to be Voigt. However, upon software assisted fitting procedure, the contribution of Gaussian and Lorenz contour to the overall band shape was changed. Thus, the final result of the fitting

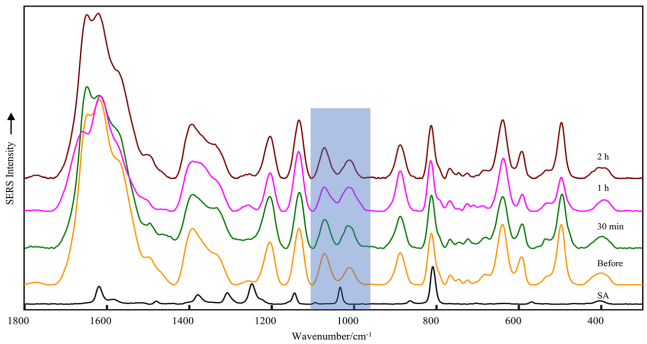

FIGURE 7 The SERS spectra of the blood serum collected at different times of aspirin consumption, and aqueous solution of SA (1 mM)—Bottom. SA, salicylic acid; SERS, surface-enhanced Raman spectroscopy [Colour figure can be viewed at wileyonlinelibrary.com]

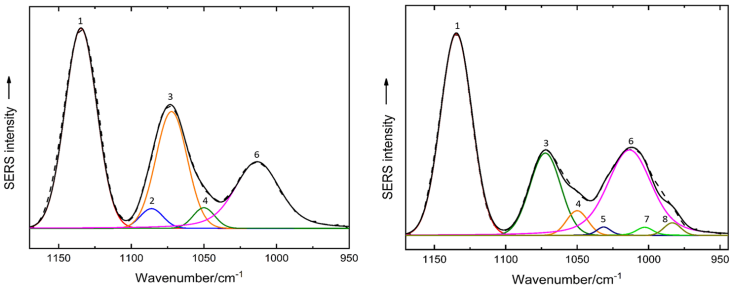

FIGURE 8 Experimental and fitted SERS spectra of blood serum before and after aspirin intake shown in the spectral range of 1,200–950 cm^{-1}. The approximated spectra—Solid line; experimental spectra—Dotted line. Approximated bands are numbered as follows: 1, 1,135 cm^{-1} (UA), 2, 1,085 cm^{-1} (UA); 3, 1,072 cm^{-1} (UA); 4, 1,050 cm^{-1} (UA); 5, 1,031 cm^{-1} (SA); 6, 1,013 cm^{-1} (UA); 7, 1,003 cm^{-1} (Phe); 8, 983 cm^{-1} (UA). Phe, phenylalanine; SA, SA; SERS, surface-enhanced Raman spectroscopy; UA, uric acid [Colour figure can be viewed at wileyonlinelibrary.com]

can, for example, be dominated by the Gaussian or by Lorenz contour. The parameters of the spectra calculated during the fitting procedure are presented in Figure S3. The fitted contours belong to the UA spectral bands at 1,085, 1,072, and 1,050 cm^{-1}, which are also observable in SERS spectra of UA as a complex band. Other combined spectral band of UA is a combination of two bands at 1,013 and 983 cm^{-1}. SA spectral band is fitted by contour located at 1,031 cm^{-1} and phenylalanine spectral band—at 1,003 cm^{-1}.

4 | CONCLUSIONS

This research has shown that label-free colloidal SERS using near infrared laser excitation can be effectively employed for the detection of SA in human blood. SA is a metabolite of one of the most common drug—aspirin, and concentration of the SA in whole blood or in its components can be used for assessment of usage of aspirin. It was proven that serum in comparison with whole blood is the best choice of the media for the determination of SA because it contains less chemical constituents that could interfere with the SERS spectra. Several colloidal solutions made from both silver and gold nanoparticles were tested. Out of these, the best approach, giving the highest SERS enhancement with least interference, was determined. Such SERS active colloidal solution is the one that contains the citrate-capped spherically shaped silver nanoparticles with the average diameter of 60 nm. The detection limit reached using this approach was 3 mM of SA in the blood what according to the clinical standards corresponds to the mild toxicity. Calibration curve—dependence of the intensity ratio of UA and SA spectral bands on SA concentration was made. Nonlinearity of the curve was found and can be explained due to the fact of competing adsorption between SA and UA. For the first time, it was found that the increase of concentration of SA in blood drastically affects the adsorption process of UA, which in turn leads to the better adsorption of SA itself as well as adsorption of some other molecules like phenylalanine. It was proved that intensity of the SERS band of the phenylalanine located at 1,003 cm^{-1} can be used as indirect spectral marker related to concentration of SA in blood. This marker is even more reliable than direct marker related to the spectral band of SA at 1,031 cm^{-1}. In conclusion, the proposed method for detection of aspirin usage is not yet sensitive enough to replace the standard drug testing methods like liquid chromatography tandem mass spectrometry and gas chromatography tandem mass spectrometry. However, this method can be applied faster and easier, which saves time and resources. Also, the hardware needed to implement SERS analysis and its maintenance is cheaper than liquid chromatography or mass spectroscopy devices; thus, the method is approachable for more clinics and medical centers. Having this in mind, we can assume that this method could be a valuable tool in the cases where fast information to decide further treatment is needed or could be used for a point-of-care analysis of aspirin use. Improvements and new developments of the method could also lead to higher sensitivity, and it could one day become a cheaper alternative to the standard clinical methods of the drug testing.

ACKNOWLEDGMENTS

This research was partly funded by a grant (SEN-16/2015) from the Research Council of Lithuania.

ORCID

Valdas Šablinskas https://orcid.org/0000-0001-6865-4797

REFERENCES

[1] D. Limaye, V. Limaye, G. Krause, G. Fortwengel, *Ann Med Health Sci Res* **2017**, *7*, 5.
[2] M. E. Ruiz, *Curr Drug Saf* **2010**, *5*, 9.
[3] J. R. Vane, R. M. Botting, *Thromb. Res.* **2010**, *110*, 4.
[4] E. J. M. Campbell, R. E. Maclaurin, *Br. Med. J.* **1958**, *1*, 3.
[5] A. Enejder, T. W. Koo, J. Oh, M. Hunter, S. Šašić, M. S. Feld, G. L. Horowitz, *Opt. Lett.* **2002**, *27*, 3.
[6] S. Feng, D. Lin, Y. Li, Z. Huang, Y. Wu, Y. Wang, J. Lin, R. Chen, *J Biomed Eng* **2012**, *29*, 5.
[7] Y. Kim, J. Y. Jeon, S. H. Han, N. Ha, K. Jang, M. G. Kim, *Transl Clin Pharmacol* **2018**, *26*, 6.
[8] D. Sirok, M. Patfalusi, G. Szeleczky, G. Somorjai, D. Greskovits, K. Monostory, *Microchem. J.* **2018**, *136*, 9.
[9] J. B. Stephenson, M. L. Flater, L. T. Bain, *J. Anal. Toxicol.* **2016**, *40*, 4.
[10] C. Chen, W. Liu, S. Tian, T. Hong, *ACS Sens* **2019**, *19*, 21.
[11] V. Turzhitsky, L. Zhang, G. L. Horowitz, E. Vitkin, U. Khan, Y. Zakharov, L. Qiu, I. Itzkan, L. T. Perelman, *Small* **2018**, *14*, 11.
[12] L. Ouyang, W. Ren, L. Zhu, J. Irudayaraj, *Rev. Anal. Chem.* **2016**, *36*, 22.
[13] S. S. Panikar, G. Ramírez-García, S. Sidhik, T. Lopez-Luke, C. Rodriguez-Gonzalez, I. H. Ciapara, P. S. Castillo, T. Camacho-Villegas, E. De la Rosa, *Anal. Chem.* **2018**, *91*, 12.
[14] A. Subaihi, H. Muhamadali, S. T. Mutter, E. Blanch, D. I. Ellisa, R. Goodacre, *Analyst* **2017**, *142*, 7.
[15] D. J. Kim, T. Y. Jeon, S. G. Park, H. J. Han, S. H. Im, D. H. Kim, S. H. Kim, *Small* **2017**, *13*, 8.
[16] M. Rani, L. Moudgil, B. Singh, A. Kaushal, A. Mittal, G. S. S. Saini, S. K. Triphati, G. Singh, A. Kaura, *RSC Adv.* **2016**, *6*, 11.
[17] Y. Sun, X. Younan, *Science* **2002**, *298*, 4.
[18] A. D. S. Indrasekara, S. Meyers, S. Shubeita, L. C. Feldman, T. Gustafsson, L. Fabris, *Nanoscale* **2014**, *6*, 15.

[19] P. C. Lee, D. Meisel, *J Phys Chem* **1982**, *86*, 5.
[20] Y. Sun, X. Younan, *Science* **2002**, *298*, 4.
[21] D. Aherne, D. M. Ledwith, M. Gara, J. M. Kelly, *Adv. Funct. Mater.* **2008**, *18*, 12.
[22] J. Kimling, M. Maier, B. Okenve, V. Kotaidis, H. Ballot, A. Plech, *J Phys Chem B* **2006**, *110*, 8.
[23] M. Zhou, S. Chen, S. Zhao, *J. Phys. Chem. Lett.* **2006**, *110*, 4.
[24] A. G. Gilman, T. W. Rall, A. S. Nies, P. Tylor, *The Pharmaceutical Basis of Therapeutics*, 8th ed., Pergamon Press, USA **1990**.
[25] V. Cotty, F. Zurzola, T. Beezley, A. Rodgers, *J. Pharm. Sci.* **1965**, *54*, 3.
[26] J. Nagelschmitz, M. Blunck, J. Kraetzschmar, M. Ludwig, G. Wensing, T. Hohlfeld, *Clin Pharm* **2014**, *6*, 9.
[27] C. Dale, A. A. M. Aulaqi, J. Baker, R. C. Hobbs, M. E. L. Tan, C. Tovey, I. A. L. Walker, J. A. Henry, *QJM* **2005**, *98*, 6.
[28] Y. M. Jean, Y. Yamamoto, R. B. Gaynor, *Nature* **1998**, *396*, 4.
[29] S. Lee, D. Johnson, J. Klein, J. Eppler, *Vet Hum Toxicol* **1995**, *37*, 2.
[30] Gaussian 16, Revision D.01, M. J. Frisch, G. W. Trucks, H. B. Schlegel, G. E. Scuseria, M. A. Robb, J. R. Cheeseman, G. Scalmani, V. Barone, G. A. Petersson, H. Nakatsuji, X. Li, M. Caricato, A. V. Marenich, J. Bloino, B. G. Janesko, R. Gomperts, B. Mennucci, H. P. Hratchian, J. V. Ortiz, A. F. Izmaylov, J. L. Sonnenberg, D. Williams-Young, F. Ding, F. Lipparini, F. Egidi, J. Goings, B. Peng, A. Petrone, T. Henderson, D. Ranasinghe, V. G. Zakrzewski, J. Gao, N. Rega, G. Zheng, W. Liang, M. Hada, M. Ehara, K. Toyota, R. Fukuda, J. Hasegawa, M. Ishida, T. Nakajima, Y. Honda, O. Kitao, H. Nakai, T. Vreven, K. Throssell, J. A. Montgomery Jr., J. E. Peralta, F. Ogliaro, M. J. Bearpark, J. J. Heyd, E. N. Brothers, K. N. Kudin, V. N. Staroverov, T. A. Keith, R. Kobayashi, J. Normand, K. Raghavachari, A. P. Rendell, J. C. Burant, S. S. Iyengar, J. Tomasi, M. Cossi, J. M. Millam, M. Klene, C. Adamo, R. Cammi, J. W. Ochterski, R. L. Martin, K. Morokuma, O. Farkas, J. B. Foresman, D. J. Fox, *Gaussian, Inc*, Wallingford CT **2016**.
[31] L. Gao, Y. Hu, H. Zhang, Y. Liu, Z. Song, Y. Dai, *J. Mol. Struct.* **2016**, *1116*, 6.
[32] A. K. Done, *Pediatrics* **1960**, *26*, 8.
[33] N. Muir, J. D. Nichols, J. M. Clifford, M. R. Stillings, R. C. Hoare, *Curr Med Res Opin* **1997**, *13*, 7.
[34] W. D. Masonx, N. Winer, *J. Pharm. Sci.* **1981**, *70*, 4.
[35] L. Ross-Lee, M. Elms, B. Cham, F. Bochner, I. Bunce, *M Eur J Clin Pharmacol* **1982**, *23*, 7.
[36] K. Schrör, *Acetylsalicylic acid*, John Wiley & Sons, Germany **2016**.
[37] P. J. G. Goulet, R. F. Aroca, *Can. J. Chem.* **2004**, *82*, 11.
[38] P. L. Stiles, J. A. Dieringer, N. C. Shah, R. P. Van Duyne, *Annu Rev Anal Chem* **2008**, *1*, 26.
[39] W. Haiss, N. T. Thanh, J. Aveyard, D. G. Fernig, *Anal. Chem.* **2007**, *79*, 7.
[40] Y. Q. He, S. P. Liu, L. Kong, Z. F. Liu, *Spectrochim. Acta, Part a* **2005**, *61*, 6.
[41] D. Solis Jr., B. Willingham, S. L. Nauert, L. S. Slaughter, J. Olson, P. Swanglap, A. Paul, W. S. Chang, S. Link, *Nano Lett.* **2012**, *12*, 5.
[42] F. D. C. Vega, P. G. M. Torres, J. P. Molina, N. M. G. Ortiz, V. G. Hadjiev, J. Z. Medina, F. C. R. Hernandez, *J. Mater. Chem. C* **2017**, *5*, 8.
[43] P. Wulandari, T. Nagahiro, N. Fukada, Y. Kimura, M. Niwano, K. Tamada, J. Colloid Interface, *Forensic Sci* **2015**, *438*, 5.
[44] M. Verma, A. Kedia, M. B. Newmai, P. S. Kumar, *RSC Adv.* **2016**, *6*, 12.
[45] P. S. Mdluli, N. M. Sosibo, P. N. Mashazi, T. Nyokong, R. T. Tshikhudo, A. Skepu, E. van der Lingen, *J. Mol. Struct.* **2011**, *1004*, 7.
[46] C. Wu, B. P. Mosher, K. Lyons, T. Zeng, *J. Nanosci. Nanotechnol.* **2010**, *10*, 6.
[47] J. L. Castro, J. F. Arenas, M. R. López-Ramírez, J. C. Otero, *Biopolymers* **2006**, *82*, 5.
[48] J. L. Castro, M. R. López-Ramirez, J. F. Arenas, J. Soto, J. C. Otero, *Langmuir* **2012**, *28*, 7.
[49] P. J. Goulet, R. F. Aroca, *Can. J. Chem.* **2004**, *82*, 11.
[50] E. C. Le Ru, M. Meyer, E. Blackie, P. G. Etchegoin, J. Raman, *Spectrosc* **2018**, *39*, 8.
[51] M. Moskovits, *J Chem Phys* **1982**, *77*, 9.
[52] J. Y. Qu, B. C. Wilson, D. Suria, *Appl. Opt.* **1999**, *38*, 8.
[53] Y. Lu, C. Wu, R. You, Y. Wu, H. Shen, L. Zhu, S. Feng, *Biomed Opt Express* **2018**, *9*, 10.
[54] M. Pucetaite, M. Velicka, J. Pilipavicius, A. Beganskiene, J. Ceponkus, V. Sablinskas, J. Raman, *Spectrosc* **2016**, *47*, 6.
[55] P. F. Spahr, J. T. Edsall, *J Biol Chem* **1964**, *239*, 5.
[56] M. Altarsha, G. Monard, B. Castro, *J. Mol. Struct.: THEOCHEM* **2006**, *761*, 5.
[57] M. Altarsha, G. Monard, B. Castro, *Int. J. Quantum Chem.* **2007**, *107*, 10.
[58] B. Nie, J. Stutzman, A. Xie, *Biophys. J.* **2005**, *88*, 15.
[59] H. Ringertz, *Acta Crystallogr* **1966**, *20*, 7.
[60] M. K. Shukla, P. C. Mishra, *J. Mol. Struct.* **1996**, *377*, 13.
[61] OriginPro, *OriginLab Corporation*, Northampton, MA, USA **2018**.

SUPPORTING INFORMATION

Additional supporting information may be found online in the Supporting Information section at the end of this article.

How to cite this article: Adomavičiūtė S, Velička M, Šablinskas V. Detection of aspirin traces in blood by means of surface-enhanced Raman scattering spectroscopy. *J Raman Spectrosc*. 2020;1–13. https://doi.org/10.1002/jrs.5853

NOTES

NOTES

NOTES

Vilniaus universiteto leidykla
Saulėtekio al. 9, III rūmai, LT-10222 Vilnius
El. p. info@leidykla.vu.lt, www.leidykla.vu.lt
bookshop.vu.lt, journals.vu.lt
Tiražas 30 egz.